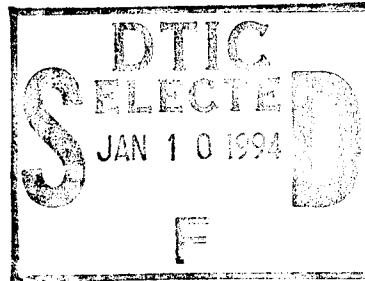


RADIATION PRODUCTION FROM STAGNATING COMPACT TOROIDS EMPLOYING A NONEQUILIBRIUM RADIATION DIFFUSION MODEL

Melissa Rae Douglas

December 1994



Final Report

19950109 056

Approved for public release; distribution is unlimited.



**PHILLIPS LABORATORY
Advanced Weapons and Survivability Directorate
AIR FORCE MATERIEL COMMAND
KIRTLAND AIR FORCE BASE, NM 87117-5776**

This final report was prepared by the Phillips Laboratory, Kirtland Air Force Base, New Mexico, under Job Order 5797AQ01. Melissa Rae Douglas (WSP) was the Laboratory Project Officer-in-Charge.

When Government drawings, specifications, or other data are used for any purpose other than in connection with a definitely Government-related procurement, the United States Government incurs no responsibility or any obligation whatsoever. The fact that the Government may have formulated or in any way supplied the said drawings, specifications, or other data, is not to be regarded by implication, or otherwise in any manner construed, as licensing the holder, or any other person or corporation; or as conveying any rights or permission to manufacture, use, or sell any patented invention that may in any way be related thereto.

This report has been authored by an employee of the United States Government. Accordingly, the United States Government retains a nonexclusive, royalty-free license to publish or reproduce the material contained herein, or allow others to do so, for the United States Government purposes.

This report has been reviewed by the Public Affairs Office and is releasable to the National Technical Information Service (NTIS). At NTIS, it will be available to the general public, including foreign nationals.

If your address has changed, if you wish to be removed from the mailing list, or if your organization no longer employs the addressee, please notify PL/WSP, Kirtland AFB, NM 87117-5776 to help maintain a current mailing list.

This technical report has been reviewed and is approved for publication.

Melissa Rae Douglas

MELISSA RAE DOUGLAS
Project Officer

FOR THE COMMANDER



DR THOMAS W. HUSSEY
Chief, High Energy Plasma
Division

William L. Baker

WILLIAM L. BAKER, GM-15
Acting Director, Advanced Weapons and
Survivability Directorate

REPORT DOCUMENTATION PAGE			Form Approved OMB No. 0704-0188	
Public reporting burden for this collection of information is estimated to average 1 hour per response, including the time for reviewing instructions, searching existing data sources, gathering and maintaining the data needed, and completing and reviewing the collection of information. Send comments regarding this burden estimate or any other aspect of this collection of information, including suggestions for reducing this burden, to Washington Headquarters Services, Directorate for Information Operations and Reports, 1215 Jefferson Davis Highway, Suite 1204, Arlington, VA 22202-4302, and to the Office of Management and Budget, Paperwork Reduction Project (0704-0188), Washington, DC 20503.				
1. AGENCY USE ONLY (Leave blank)		2. REPORT DATE December 1994		3. REPORT TYPE AND DATES COVERED Final; Sep 90 - May 94
4. TITLE AND SUBTITLE RADIATION PRODUCTION FROM STAGNATING COMPACT TOROIDS EMPLOYING A NONEQUILIBRIUM RADIATION DIFFUSION MODEL			5. FUNDING NUMBERS PE: 62601F PR: 5797 TA: AQ WU: 01	
6. AUTHOR(S) Melissa Rae Douglas				
7. PERFORMING ORGANIZATION NAME(S) AND ADDRESS(ES) Phillips Laboratory 3550 Aberdeen Avenue SE Kirtland AFB, NM 87117-5776			8. PERFORMING ORGANIZATION REPORT NUMBER PL-TR--94-1126	
9. SPONSORING / MONITORING AGENCY NAME(S) AND ADDRESS(ES)			10. SPONSORING / MONITORING AGENCY REPORT NUMBER	
11. SUPPLEMENTARY NOTES Publication of this technical report does not constitute approval or disapproval of the ideas or findings. It is published in the interest of STINFO exchange. The established procedures for editing reports were not followed for this report.				
12a. DISTRIBUTION / AVAILABILITY STATEMENT Approved for public release; distribution is unlimited.			12b. DISTRIBUTION CODE	
13. ABSTRACT (Maximum 200 words) The stagnation of a high Z, high velocity compact toroidal plasma against a stationary object has been shown computationally to be an efficient radiation source. To obtain a better understanding of the stagnation process and the influence of various prestagnation properties on radiation production, the 2 1/2 dimensional radiation magnetohydrodynamic code, MACH2, was used to simulate the stagnation physics. To perform these calculations, a flux-limited nonequilibrium radiation diffusion model was incorporated into the MACH2 code. In this model the radiation field evolves separately from the material components of the fluid and is described by a Plankian distribution at the radiation temperature, T_R . This introduced a dynamic equation for the radiation field and modifications to both the momentum and electron energy equations. A flux-limited version of the radiative conductivity was formulated to extend this model into the optically thin regime. Detailed benchmarking of the radiation diffusion and electron-radiation coupling using a set of radiation MHD test problems was conducted.				
14. SUBJECT TERMS Compact Toroids, Radiation Magnetohydrodynamics, Radiation Production, Nonequilibrium Radiation Diffusion, Stagnation, Plasma			15. NUMBER OF PAGES 260	
			16. PRICE CODE	
17. SECURITY CLASSIFICATION OF REPORT Unclassified	18. SECURITY CLASSIFICATION OF THIS PAGE Unclassified	19. SECURITY CLASSIFICATION OF ABSTRACT Unclassified	20. LIMITATION OF ABSTRACT	

© Copyright by Melissa Rae Douglas

This work is dedicated to my parents, George and Charlotte Dittmar, who taught me, through their own lives, that dreams are attainable if you have the courage to reach for them.

Accession For	
NTIS CRA&I	<input checked="" type="checkbox"/>
DTIC TAB	<input type="checkbox"/>
Unannounced	<input type="checkbox"/>
Justification	
By	
Distribution/	
Availability Codes	
Dist	Avail. or Special
A-1	

ACKNOWLEDGEMENTS

It is a honor for me to acknowledge those people that have influenced my life, and in one way or another, have contributed toward this accomplishment. I would like to begin by thanking the members of my dissertation committee, Dr. Nebojsa Duric, Dr. Norman Roderick, Dr. Bob Peterkin Jr., and Dr. Derek Swinson. Much appreciation goes to Neb Duric for his guidance in my early graduate years. I am amazed at the amount of support and patience that he provided to me during that time, and also later, when I decided to do research in computational plasma physics. Special thanks to Norm Roderick for his technical supervision of this work and for taking on a graduate student from another department that he initially knew very little about. Every student should be as fortunate as I to have an advisor who truly cares not just about the quality of the work, but the person doing the work. I thank him for keeping me focused, for the many, many detailed discussions on physics, for the moral support, and especially for his availability. In addition, his insight and deep-founded understanding of the computational and physics issues involved was invaluable.

I would like to thank Bob Peterkin for the helpful hints concerning code development and his expertise on MACH2. His demand for excellence seems to set a standard for all those who work with him and I was no exception. His constructive criticism throughout this work and particularly with the written document was immeasurable. I have no doubt that I will take what I have learned from this experience wherever I go. My appreciation also goes out to Derek Swinson for his kindness, his interest in this work, and his advice concerning the final copy of the dissertation. I also thank Mike Frese of NumerEx and Richard Bowers at Los Alamos National Laboratory for their assistance in

interpretating both numerical and physical aspects of the simulations. I am extremely grateful to Richard for his help on the electron-radiation coupling and flux-limiter problems, and also his suggestions for benchmarking.

Working at the Phillips Laboratory has indeed been a great opportunity for me. I wish to thank Bill Mullins for his interest in the CoOp program at the laboratory and his work in getting me through the system. I also want to thank the folks in WSP for providing me with a fantastic workstation and endless technical support. Special thanks to Janice Sanchez, who was continually getting me out of messes and to Dave Bell, for just knowing a heck of alot about computers and physics. I would like to express my gratitude to Ann Nelson, who made sure I didn't have to mess with the beauracratc confusion of the laboratory, and to Tom Hussey for putting in a good word for me on numerous occassions. Overwhelming smiles to those fun crazies, Thad and Sue Englert, for making my day on many occassions.

Trudging through graduate school would have been far more difficult if I didn't have the support of friends. I am truly indebted to the lunch "gang" - Renae Dellinger, Yvonne Alvarez, David Scholfield, Charles Davis, Alex Pilipowskyj - for putting up with all my nonsense and for getting me through the more trying times of the dissertation. Special thanks to my dear friends, Dave and Charles, for their wit and their abilitiy to put the situation into perspective when I started taking things far too seriously. For those that have been praying for me continuously over the past few years, Judy Leone, Robert and Debbie Christy, Gene and Janice Koskey, Tom and Henrietta King, thanks so much. I am extremely grateful for your love and concern for me. For the friends at UNM, Mike Ledlow, Susan Durham, Rob Price, David and Jodi Clarke, it was a pleasure to suffer with you. Thanks for being an inspiration to me. Also, undying gratitude to Barby Woods and Alan Noyes for all of their

administrative assistance and their sympathy.

I would like to thank a number of other people whose influence has strongly affected the direction of my life. My appreciation goes out to Bob Reall, for getting me interested in running thereby keeping me out of trouble in adolescence. For making Astronomy so intriguing and the world of science so appealing, I thank Roger Grossenbacher. I would also like to express my gratitude to Dr. Charles Shirkey at Bowling Green State University for his willingness to explain physics to me and for his overwhelming support. And finally, I want to thank Steve Gregory for being my friend and believing in me when I could not believe in myself.

Lastly, and most importantly, I would like to gratefully acknowledge my family for their love and emotional support. My sister, Rebecca, has been an inspiration to me through her success as a woman in a scientific field and as a mother. I appreciate her honesty, her friendship, and admire her incredible tenacity. I thank my brother and my friend, Mark, for sharing my love of science among many other things. The memories of those nights on the porch swing talking of our dreams has often kept me going in the rough times of my career. Sincerest gratitude to my husband David, who took the journey with me, knowing full well the sacrifices. Thank you for being my friend and for never giving up on me. For my two beloved canine companions, Hamlet and Casey, I don't think "mudder" could have survived this without you. The hikes, the daily walks, and your faithful listening ears kept me from losing my sanity. And for my parents, my greatest supporters, my role models, I cannot emphasize enough how important you have been to me. Thank you for your financial support, your moral support, and giving me the freedom to find my own path in life, wherever it may take me. Your many sacrifices have not gone unnoticed. It is truly a privilege to have you as my parents.

*Blessed be the Lord,
Because He has heard the voice
of my supplications!
The Lord is my strength and my shield;
My heart trusted in Him, and
I am helped;
Therefore my heart greatly rejoices,
And with my song I will praise Him.*

Psalm 28:6,7

Radiation Production from Stagnating Compact Toroids Employing a Nonequilibrium Radiation Diffusion Model

Melissa Rae Douglas

B.S. Physics and Mathematics - Bowling Green State University, 1985

M.S. Physics - University of New Mexico, 1990

Ph.D. Physics - University of New Mexico, 1994

The stagnation of a high Z , high velocity compact toroidal plasma against a stationary object has been shown computationally to be an efficient radiation source. To obtain a better understanding of the stagnation process and the influence of various prestagnation properties on radiation production, the 2 1/2 dimensional radiation magnetohydrodynamic code, MACH2, was used to simulate the stagnation physics. To perform these calculations, a flux-limited nonequilibrium radiation diffusion model was incorporated into the MACH2 code. In this model the radiation field evolves separately from the material components of the fluid and is described by a Plankian distribution at the radiation temperature, T_R . This introduced a dynamic equation for the radiation field and modifications to both the momentum and electron energy equations. A flux-limited version of the radiative conductivity was formulated to extend this model into the optically thin regime. Detailed benchmarking of the radiation diffusion and electron-radiation coupling using a set of radiation MHD test problems was conducted.

An extensive analysis of a stagnation calculation was carried out for a 10 mg, nominally 1 cm in diameter compact toroid at a velocity of 100 cm/ μ s, or a directed kinetic energy of 5 MJ. This calculation indicated that 4.6 MJ of radi-

ation was emitted over a 10 ns period, a high conversion efficiency of directed kinetic energy into thermal energy and then radiation. The effects of numerical resolution, radiation boundary conditions, and extent of the computational domain on the stagnation physics were included in this analysis.

In the stagnation process, radiation production depends on the directed kinetic energy of the toroid, the conversion of this energy into ion thermal energy, and the efficiency of the ion-electron and electron-radiation coupling. An investigation was performed on the influence of magnetic field strength, toroid velocity, toroid mass, more compact stagnation geometry, and toroid material on these properties. Overall, a number of trends were observed. With increasing magnetic field strength, a larger fraction of the initial kinetic energy of the toroid goes into compressing the magnetic field and the material compression itself decreases. This results in lower densities and lower conversion efficiencies. In the most extreme case considered, magnetic energy 50% of the kinetic energy, the radiated yield was 3.2 MJ. With increasing mass, the total kinetic energy is increased as is the material density. Coupling is improved, the conversion efficiency rises as does the total radiated energy, while the photon distribution remain essentially the same. With increasing velocity, the directed kinetic energy per particle is increased, and the radiated energy, peak radiated power and distribution of photon energies are higher.

With a more compact geometry, the magnetic field effects compete with the improved coupling resulting from higher densities and the radiation production declines. In moving to a lower Z toroid, the material experiences "burn through" and the electron-radiation coupling drops significantly as does the energy spectrum of the produced radiation. The results of this parameter study indicate that the desired radiated yield, radiated power and photon spectrum can be constructed by optimizing the various prestagnation quantities.

TABLE OF CONTENTS

ACKNOWLEDGEMENTS	v
ABSTRACT	x
LIST OF FIGURES	xiv
LIST OF TABLES	xxi
CHAPTER 1. INTRODUCTION	1
1.1 Radiation Models	3
1.2 Compact Toroid Stagnation	7
1.3 Present Study	14
CHAPTER 2. THE NONEQUILIBRIUM RADIATION DIFFUSION APPROXIMATION	15
2.1 The Moment Equations in Cylindrical Coordinates	17
2.2 The First Order Equilibrium Diffusion Approximation	23
2.3 The Nonequilibrium Diffusion Approximation	25
2.4 The Validity of the Diffusion Approximation and Flux-Limited Diffusion	29
CHAPTER 3. IMPLEMENTING THE RADIATION ENERGY EQUATION INTO MACH2	31
3.1 The MACH2 Code	32
3.2 Adding the Radiation Energy Equation to MACH2	43
3.3 Finite Difference Formulation of the Radiation Energy Equation ...	48
3.4 Limits of the Nonequilibrium Diffusion Approximation and a Comparison to the Emission and Equilibrium Diffusion Models in MACH2	58
CHAPTER 4. THE MARAUDER COMPACT TOROID EXPERIMENT	61

CHAPTER 5. BENCHMARKING	76
5.1 Numerical Stability and Accuracy	77
5.2 Radiation Diffusion	85
5.3 Electron-Radiation Coupling	101
5.4 Additional Benchmarking	118
CHAPTER 6. COMPACT TOROID STAGNATION	128
6.1 Numerical Simulations: Baseline Calculation	129
6.1.1 Role of Numerical Resolution in the Baseline Case	165
6.1.2 The Role of Radiation Boundary Conditions and Computational Geometry on the Baseline Case	171
6.2 Numerical Simulations: Parameter Survey	180
6.2.1 Magnetic Field Strength Variation.....	182
6.2.2 Constant Mass, Velocity Variation	189
6.2.3 Constant Velocity, Mass Variation	194
6.2.4 Mass Variation, Velocity Variation.....	200
6.2.5 Stagnation Geometry and Toroid Material Variation	205
CHAPTER 7. SUMMARY AND CONCLUSIONS	210
APPENDIX A. ANALYTIC COMPRESSION RATIOS OF PHYSICAL PARAMETERS FOR ISENTROPIC COMPRESSION	217
APPENDIX B: ANALYTIC SOLUTIONS OF THE DIFFUSION EQUATION	220
APPENDIX C: CONSERVING ENERGY IN THE STAGNATION PROBLEM	231
REFERENCES	234

LIST OF FIGURES

Figure 1.1. Illustration of a spheromak class of compact toroid. The compact toroid is comprised of both poloidal and toroidal magnetic fields as depicted. The plasma resides within the magnetic field structure [10].	8
Figure 3.1. Centering of the fluid variables in MACH2. In general, the grid lines need not be parallel to the coordinate directions, and the cell need not be orthogonal.	36
Figure 3.2. Spatial positions of arbitrary points on the MACH2 computational domain.	37
Figure 3.3. Technical schematic of the physical processes calculated in MACH2.	40
Figure 3.4. Technical schematic of the physical processes calculated in MACH2 with the changes required to add the nonequilibrium radiation diffusion treatment.	49
Figure 3.5. MACH2 notation used in the finite volume differencing of the various fluid equations. The indexing corresponds to the cell-centered values, while the arrows indicate the directions of positive flow for vertex-centered fluxes.	53
Figure 4.1. The MARAUDER experiment. Gas is injected into a magnetized plasma gun and a discharge applied. This breaks down the gas and pushes mass and field into the formation volume, creating a compact toroid. The toroid relaxes into a Taylor state [47]. The second discharge is then applied, compressing the toroid to high density. During this time magnetic flux accumulates behind the plasma ring accelerating it to high velocities. Radiation is produced as the fast, high density compact toroid stagnates against an end plate.	62
Figure 4.2. Schematic of the first MARAUDER 3:1 radial compression experiment [41].	64
Figure 4.3. A schematic of the formation process. (a) Initial bias field and toroidal field. (b) Expansion into the expansion region. (c) Formation of compact toroid with reconnection of poloidal field lines [42].	66
Figure 4.4. Computationally predicted 2-D mass distribution prior to the formation discharge. This is arrived at by superimposing the gas distributions resulting from all 60 gas valves using a MACH2 calculation modelling the mass distribution from a single valve. The superposition of the 60 distributions is averaged over the azimuthal angle to obtain the 2-D mass contours shown above. The contours are logarithmic, ranging from approximately $5.0 \times 10^{16} / \text{cm}^3$	

in the region adjacent to the nozzle and thinning out to $1.0 \times 10^{11} / \text{cm}^3$ in the outermost gun regions [49].	69
Figure 4.5. Initial magnetic field configuration shown above as poloidal magnetic flux contours. This is derived from a time-dependent electromagnetic code which calculates the diffusion of magnetic flux produced by currents in the solenoid coils exterior to the gun through the gun electrodes [49].	70
Figure 4.6. A MACH2 simulation showing the formation, compression, and acceleration down the stovepipe region of a compact toroid. Pictured are the poloidal magnetic flux lines at (a) 0 ms, (b) 4 ms, (c) 6 ms, (d) 15 ms, (e) 17 ms, and (f) 20 ms [54].	75
Figure 5.1. Radiation energy distribution for one dimensional radiation diffusion in the y-direction with 4 cells. Curves plot the energy as a function of vertical distance for $1 \times 10^{-4}\text{s}$, $5 \times 10^{-4}\text{s}$, $1 \times 10^{-3}\text{s}$, $3 \times 10^{-3}\text{s}$, $5 \times 10^{-3}\text{s}$, $8 \times 10^{-3}\text{s}$, $1 \times 10^{-2}\text{s}$, $3 \times 10^{-2}\text{s}$, and $5 \times 10^{-2}\text{s}$ using a calculational timestep of (a) 10^{-6}s and (b) 10^{-3}s . The solid lines represent the analytic solution, while the open circles represent the numerical solution.	91
Figure 5.2. Radiation energy distribution for one dimensional radiation diffusion in the y-direction with 8 cells. Curves plot the energy as a function of vertical distance for $1 \times 10^{-4}\text{s}$, $5 \times 10^{-4}\text{s}$, $1 \times 10^{-3}\text{s}$, $3 \times 10^{-3}\text{s}$, $5 \times 10^{-3}\text{s}$, $8 \times 10^{-3}\text{s}$, $1 \times 10^{-2}\text{s}$, $3 \times 10^{-2}\text{s}$, and $5 \times 10^{-2}\text{s}$ using a calculational timestep of (a) 10^{-6}s and (b) 10^{-3}s . The solid lines represent the analytic solution, while the open circles represent the numerical solution.	92
Figure 5.3. Radiation energy distribution for one dimensional radiation diffusion in the y-direction with 16 cells. Curves plot the energy as a function of vertical distance for $1 \times 10^{-4}\text{s}$, $5 \times 10^{-4}\text{s}$, $1 \times 10^{-3}\text{s}$, $3 \times 10^{-3}\text{s}$, $5 \times 10^{-3}\text{s}$, $8 \times 10^{-3}\text{s}$, $1 \times 10^{-2}\text{s}$, $3 \times 10^{-2}\text{s}$, and $5 \times 10^{-2}\text{s}$ using a calculational timestep of (a) 10^{-6}s and (b) 10^{-3}s . The solid lines represent the analytic solution, while the open circles represent the numerical solution.	93
Figure 5.4. Radiation energy distribution for one dimensional radiation diffusion in the y-direction with 32 cells. Curves plot the energy as a function of vertical distance for $1 \times 10^{-4}\text{s}$, $5 \times 10^{-4}\text{s}$, $1 \times 10^{-3}\text{s}$, $3 \times 10^{-3}\text{s}$, $5 \times 10^{-3}\text{s}$, $8 \times 10^{-3}\text{s}$, $1 \times 10^{-2}\text{s}$, $3 \times 10^{-2}\text{s}$, and $5 \times 10^{-2}\text{s}$ using a calculational timestep of (a) 10^{-6}s and (b) 10^{-3}s . The solid lines represent the analytic solution, while the open circles represent the numerical solution.	94
Figure 5.5. MACH2 radiation energy density profiles for the square 2 dimensional diffusion problem at (a) $5 \times 10^{-4}\text{s}$ and (b) $5 \times 10^{-3}\text{s}$. Initial conditions are a uniform interior radiation temperature of $T_R=10\text{ eV}$, and $T_R=0$ at boundaries. Cell resolution is 16 cells x 16 cells.	97

- Figure 5.6.** Radiation energy density profile for the square two dimensional diffusion problem. Curves plot the energy as a function of vertical distance along the y-axis for 5×10^{-4} s, 1×10^{-3} s, 5×10^{-3} s, and 1×10^{-2} s. The solid lines represent the analytic solution, while the open circles represent the numerical solution.98
- Figure 5.7.** MACH2 radiation energy density profiles for the rectangular 2 dimensional diffusion problem at (a) 5×10^{-4} s and (b) 5×10^{-3} s. Initial conditions are a uniform interior radiation temperature of $T_R=10$ eV, and $T_R=0$ at boundaries. Cell resolution is 16 cells x 32 cells.99
- Figure 5.8.** Radiation energy density profile for the rectangular two dimensional diffusion problem. Curves plot the energy as a function of (a) horizontal distance along the x-axis for vertical position at cell 16 (b) vertical distance along the y-axis for horizontal position at cell 8, for 5×10^{-4} s, 1×10^{-3} s, 5×10^{-3} s, and 1×10^{-2} s. The solid lines represent the analytic solution, while the open circles represent the numerical solution.100
- Figure 5.9.** Material, Radiation temperature vs. time for a density of 10^{-2} kg/m³ using the explicit difference form given by Eqns. (79) and (80) with timesteps of (a) 10^{-2} s, (b) 10^{-4} s, and (c) 10^{-6} s.109
- Figure 5.10.** Material, Radiation temperature vs. time for a density of 10^{-2} kg/m³ using the implicit difference form given by Eqns. (41), (42) and (43) with timesteps of (a) 10^{-2} s, (b) 10^{-4} s, and (c) 10^{-6} s.110
- Figure 5.11.** Material, Radiation temperature vs. time for a density of 1 kg/m³ using the explicit difference form given by Eqns. (79) and (80) with timesteps of (a) 10^{-6} s, (b) 10^{-8} s, and (c) 10^{-10} s.111
- Figure 5.12.** Material, Radiation temperature vs. time for a density of 1 kg/m³ using the implicit difference form given by Eqns. (41), (42) and (43) with timesteps of (a) 10^{-6} s, (b) 10^{-8} s, and (c) 10^{-10} s.112
- Figure 5.13.** Material, Radiation temperature vs. time for a density of 10^2 kg/m³ using the explicit difference form given by Eqns. (79) and (80) with timesteps of (a) 10^{-10} s, (b) 10^{-12} s, and (c) 10^{-14} s.113
- Figure 5.14.** Material, Radiation temperature vs. time for a density of 10^2 kg/m³ using the implicit difference form given by Eqns. (41), (42) and (43) with timesteps of (a) 10^{-10} s, (b) 10^{-12} s, and (c) 10^{-14} s.114
- Figure 5.15.** Material, Radiation energy density vs. time for (a) density of 10^{-2} kg/m³ at a timestep of 10^{-6} s, (b) density of 1 kg/m³ at a timestep of 10^{-10} s, and (c) density of 10^2 kg/m³ at a timestep of 10^{-14} s for the explicit difference form given by Eqns. (79) and (80).115

- Figure 5.16.** Time evolution of Material, Radiation (a) temperatures and (b) energy densities for initial material temperature of 100 eV, initial radiation temperature of 10 eV, timestep 10^{-14} s for the implicit difference form given by Eqns. (41), (42) and (43). Material density is $5. \times 10^{-2} \text{ kg/m}^3$116
- Figure 5.17.** Time evolution of Material, Radiation (a) temperatures and (b) energy densities for initial material temperature of 10 eV, initial radiation temperature of 100 eV, timestep 10^{-14} s for the implicit difference form given by Eqns. (41), (42) and (43). Material density is $5. \times 10^{-2} \text{ kg/m}^3$117
- Figure 5.18.** Distribution of radiation energy density along a slice in the x-direction at (a) 1.0×10^{-6} s, (b) 5.0×10^{-6} s, (c) 1.0×10^{-5} s, and (d) 3.0×10^{-5} s for the Marshak Wave problem. Material density is 10 kg/m^3 and the material temperature is initially 100 eV. The wall is at a radiation temperature of 150 eV.123
- Figure 5.19.** Slice plots of (a) the material temperature, (b) the radiation temperature, (c) the photon mean free path, and (d) the radiative flux at 1×10^{-5} s for the Marshak Wave problem. Material density is 10 kg/m^3 and the material temperature is initially 100 eV. The wall is at a radiation temperature of 150 eV.124
- Figure 5.20.** Slice plots of (a) the radiation energy density, (b) the photon mean free path, (c) the material density, and (d) the material velocity along the direction of the diffused radiation field, at 1×10^{-5} s for the “Marshak wave” problem allowing for dynamic fluid effects. Material density is 10 kg/m^3 and the material temperature is initially 100 eV. The wall is at a radiation temperature of 150 eV.125
- Figure 5.21.** Radiation profiles showing the propagation of radiation through a thin material with the initial conditions defined using the Marshak Wave problem but with a fluid density of 0.001 kg/m^3 . The plots are at (a) 2.0×10^{-8} s, (b) 4.0×10^{-8} s, (c) 6.0×10^{-8} s, and (d) 8.0×10^{-8} s. The radiation and material temperature are originally set to 100 eV. The wall is at a radiation temperature of 150 eV.126
- Figure 5.22.** Slice plots of (a) the radiation energy density, (b) the radiation temperature, (c) the flux-limited diffusion coefficient, and (d) the radiative flux at 5.0×10^{-8} s for the thin problem illustrated in Figure 5.21. The material density is set to 0.001 kg/m^3 with the initial material and radiation temperatures at 100 eV. The wall is at a radiation temperature at 150 eV.127
- Figure 6.1.** Compact Toroid Stagnation Geometry. Prior to stagnation, the compact toroid has been compressed and/or focused down to an 0.89 cm diameter. Depicted is the toroid at the end of the stovepipe ready to impact the end wall. The compact toroid spans the annular region formed by extending the

conducting walls out of the computational plane about the centerline. This produces a structure consisting of concentric cylinders. The box at the upper right of the diagram shows the region contained in the simulations.	133
Figure 6.2. Initial conditions of compact toroid prior to stagnation, (a) directed velocity, (b) density.	135
Figure 6.3. Initial conditions of compact toroid prior to stagnation, (a) poloidal magnetic flux, (b) out of plane component of magnetic field.	136
Figure 6.4. Evolution of stagnation process for 5 MJ compact toroid baseline case. Shown are out-of -plane magnetic field lines.	140
Figure 6.5. Contour plots of the (a) density and (b) radiation temperature at 1.0 ns.	142
Figure 6.6. Slice plots of the (a) density, (b) pressure, (c) electron temperature, and (d) ion temperature at 1.0 ns. The slices are taken along the direction of motion through the center of the toroid. The right boundary defines the target wall, while the left boundary is the open boundary at the bottom of the computational box of Figure 6.1.	143
Figure 6.7. Contour plots of the (a) density, (b) out-of -plane component of the magnetic field, (c) radiation temperature, and (d) radiation flux at peak compression - 6.2 ns.	145
Figure 6.8. Slice plots of the (a) density, (b) pressure, (c) electron temperature, and (d) ion temperature at 6.2 ns. The slices are taken along the direction of motion through the center of the toroid.	146
Figure 6.9. Contour plots of (a) density and (b) radiation temperature at 10 ns.	150
Figure 6.10.(a),(b). Plot of (a) Radiated Power vs. Time for the 5 MJ kinetic energy baseline case and (b) Plank distribution at 4.2 ns, time at which radiated power peaks. Electron temperature here is 164 eV.	153
Figure 6.10 (c),(d). Slice plots of the ion average charge state and Plank mean free path at (c) 1 ns and (d) 1.4 ns into stagnation. The slices are through the center of the toroid with the right side of the figures defining the stagnation wall and the left side, the open flowthru boundary. The plots indicate that in going from an ionization state of $\bar{Z} \sim 43$ to a state with $\bar{Z} \approx 31$ (from a filled L shell to a partially filled M shell), the bound electron distribution significantly modifies (increases) the opacity and the Plank mean free path drops rapidly from 8 cm down to 1 cm.	154
Figure 6.11. Plot of the Radiated Power vs. Time for the runs ct1,ct2, and ct3.	159

Figure 6.12. Plot of the Radiated Power vs. Time for the runs ct4 and ct5.	161
Figure 6.13. Plot of the Radiated Power vs. Time for the runs ct1 and ct6.	162
Figure 6.14. Contour plots of (a) electron and (b) ion temperature at 0.1 ns.	164
Figure 6.15. Density profiles at 1.0, 3.0 and 6.0 ns for (a) 16 and (b) 64 cell resolution.	168
Figure 6.16. Plots of the radiative flux indicating radiation boundary conditions with (a) one radiating boundary and (b) three radiating boundaries.	172
Figure 6.17. Plot of the Radiated Power vs. Time for the calculation of the baseline case with one flowthru radiating boundary and the calculation with three flowthru radiating boundaries.	173
Figure 6.18. Stagnation geometry in which the inner and outer conducting walls have been extended an additional 2.24 cm. The plot also illustrates the boundaries through which radiation is permitted to flowthru.	175
Figure 6.19. Plot of the (a) initial density and (b) initial toroidal field profiles for the calculation using the extended stagnation geometry.	176
Figure 6.20. Plot of the (a) density and (b) radiation temperature at peak compression for the calculation using the extended stagnation geometry.	177
Figure 6.21. Plot of the Radiated Power vs. time for the calculation of the baseline case with both the standard stagnation geometry and the extended geometry (denoted as 3 block since three computational blocks were used to model this problem)	179
Figure 6.22. Toroidal Magnetic field and density contours at peak compression for (a) the baseline case where the magnetic energy is 2% of the kinetic energy and (b) the case where the magnetic energy is 50% of the kinetic energy.	185
Figure 6.23. Radiated Yield as a function of magnetic energy to kinetic energy.	187
Figure 6.24. Plot of the Radiated Power vs. time for varying initial magnetic field strengths, and thus magnetic energies.	188
Figure 6.25. Radiated Power vs. Time for the (a) 45 cm/ μ s velocity run, 1 MJ directed kinetic energy and (b) 142 cm/ μ s run, 10 MJ directed kinetic energy. ...	192
Figure 6.26. Radiated Power vs. Time for the (a) 20 mg and 40 mg runs at 10 MJ and 20 MJ directed kinetic energy, respectively, and (b) 2 mg run at 1 MJ directed kinetic energy.	197

Figure 6.27. Plot of the Radiated Power vs. Time for a 5 MJ toroid with varying initial mass and velocity.	202
Figure 6.28. Radiated Power vs. time for (a) more compact geometry with outer conducting wall only, and (b) Argon filled toroid.	208
Figure C.1. Plots of (a) the total energy (including radiation energy leaving the bottom boundary of the problem) vs. time and (b) radiated power (radiation rate) vs. time for the baseline 5 MJ calculation.	233

LIST OF TABLES

Table 5.1. N_C for cell size and timestep	88
Table 5.2. Electron-Radiation coupling parameter survey	105
Table 6.1. Initial parameters for 5 MJ baseline case	132
Table 6.2. Initial temperatures for each run	158
Table 6.3. Total radiated yield for each run	158
Table 6.4. Resolution parameters for each run	166
Table 6.5. Results of resolution calculations	166
Table 6.6. Initial field parameters for magnetic field strength survey	184
Table 6.7. Results at peak compression for magnetic field strength survey	184
Table 6.8. Results of radiation production from magnetic strength survey	187
Table 6.9. Initial parameters for velocity survey	190
Table 6.10. Results from velocity survey: peak compression, radiation production	190
Table 6.11. Initial parameters of mass survey	195
Table 6.12. Results from mass survey: peak compression, radiation production	195
Table 6.13. Initial parameters for 5 MJ survey: varying initial mass and velocity	201
Table 6.14. Results from 5 MJ survey: peak compression, radiation production	201

CHAPTER 1. INTRODUCTION

In high temperature fluids, such as plasmas, the existence of the radiation field will often effect the thermodynamic properties of the fluid and its dynamic evolution. Plasmas not only emit radiation, but they also interact with surrounding radiation through absorption and scattering. The processes of absorption and scattering involve exchanges of energy and momentum between photons and the constituents of the fluid (specifically, the electrons). It is this coupling between the radiation field and the material which governs the manner in which radiative properties such as energy density, momentum density, and stress (i.e., pressure) contribute to the spatial and temporal development of the fluid. Such contributions are manifest through radiation-electron energy exchange, radiation pressure, and the continual evolution of the radiation field. If these radiative properties are significant compared to the corresponding fluid properties, or if the dominant mode of energy exchange is through radiation-electron coupling, then the radiation field will be an important player in the evolution of the fluid. In many instances, magnetic fields are also present within the fluid and must be taken into account. Under such conditions, it is necessary to solve the conservation laws which describe the evolution of the radiation field simultaneously with the conservation equations of a magnetized fluid to obtain a complete description of the fluid physics.

In a dense plasma regime, where the fluid is optically thick to radiation, the conservation equations for the radiation field can be reduced to a single evolution equation for the radiation energy density. In this case, the evolution of the radiation field is accomplished by including one additional equation to a set of existing MHD equations. Many problems of interest occur in this

regime, particularly in the areas of laboratory plasma physics and plasma astrophysics. Plasma pinches, imploding liners, compact toroids, thermal arc jets, and the inertial confinement process are among the laboratory experiments that have applications in the dense plasma regime. In the arena of astrophysics, such applications include astrophysical jets, the snowplow treatment of supernovae expansion, and accretion discs surrounding young stellar objects or neutron stars.

The assumptions that arise out of thick fluid conditions and which lead to the radiation energy equation encompass what is traditionally called the diffusion approximation. It is the purpose of this dissertation to incorporate a nonequilibrium diffusion approximation into a 2-1/2 dimensional, nonideal magnetohydrodynamic (MHD) code, MACH2 [34], and apply this code to laboratory radiating plasmas. Specifically, this code will be used to simulate the stagnation of a high velocity compact toroid. The stagnation process involves the compressional evolution of a dense radiating plasma confined by a complex magnetic field structure. MACH2 has the capabilities necessary to model this process, including resistive decay of fields and the evolution of all three vector components of velocity and magnetic field. With the implementation of the advanced nonequilibrium radiation diffusion treatment, the MACH2 code is able to simulate the dense radiating fluid regime typical of the compact toroids considered here.

1.1 Radiation Models

The propagation, or transport, of radiation through a material is described by the radiation transport equation. This equation can be rigorously derived from a statistical treatment, by forming an evolution equation for the photon distribution function [1]. The photon distribution function defines the probable number density of photons in phase space as determined by three spatial coordinates, \bar{x} , two directional coordinates, \hat{n} , and frequency ν (these latter three variables take the place of momentum). A conservation equation for the number density of photons is then constructed taking into account the processes of emission, absorption, and scattering. This results in what is known as the transport equation or the photon Boltzmann equation. A general form of the transport equation is given by [2]

$$\frac{1}{c} \frac{\partial I(\bar{x}, t, \hat{n}, \nu)}{\partial t} + \hat{n} \cdot \nabla I(\bar{x}, t, \hat{n}, \nu) = \eta(\bar{x}, t, \hat{n}, \nu) - \chi(\bar{x}, t, \hat{n}, \nu) I(\bar{x}, t, \hat{n}, \nu) \quad (1)$$

where the intensity I is a physically measurable quantity and is related to the photon distribution function through a factor of $ch\nu$. Here c refers to the speed of light, and $h\nu$, the photon energy. The terms on the right hand side describe the emission and absorption properties of the material, respectively, and include the effects of scattering. The term η is defined as the material emissivity, while χ is the opacity or the total absorption coefficient.

The conservation, or evolution, equations for the radiation field are mathematically derived by calculating angular moments of the radiation transport equation. Taking the zeroth and first order moments of the transport equation, two moment equations are formed which describe the dynamical evolution of the radiation field in terms of defined radiation quantities. These

quantities are the radiation energy density E , the radiative flux F , and the radiation pressure tensor P . When written in component form, the two moment equations expand to four equations with ten unknown quantities. Thus, solving the moment equations in terms of the radiation quantities requires six additional equations, which in effect are closure relations. This analysis is analogous to the generation of the fluid equations by taking moments of the Boltzmann equation. In this case, the fluid equations are closed by equations of state relating the material gas pressure to the material density and energy and a caloric equation of state.

The closure of the radiation moment equations is typically achieved by relating the radiation pressure tensor to the radiation energy density. There are two approaches that are used to determine this relationship. One approach is to solve the transport equation for the intensity, extracting from it the relationship between P_{ij} and E . Methods based on this treatment include the S-N (Discrete Ordinate) Method [1], the P-N (Spherical Harmonic) Method [1], and the Method of Characteristics (Variable Eddington Method) [3]. Under physical conditions where the material is optically thick, the radiation field is nearly isotropic, and the pressure tensor is reduced to a scalar form in which $P = 1/3 E$ [2,4]. The moment equations are then closed with this simple relationship instead. This approach is valid in an opaque medium and is commonly referred to as the diffusion approximation.

Solving the transport equation is based on the assumption that problems of interest occur on fluid flow time scales as opposed to radiation flow time scales. In other words, the radiation field at any position is assumed to adjust instantaneously to changes in surrounding material conditions. When solved by a computer code, the fluid is thus considered to be in a particular state at each calculational timestep and the static transfer equation is solved to com-

pute the radiation field propagating through the material at that instant. Depending on the method used and the level of accuracy desired, this often calls for large amounts of computational memory and time. The numerical solution to the transport equation requires not only spatial resolution, but also angular resolution, making it necessary to have an additional radiation grid and database containing pertinent information for each grid point (i.e., angular coordinates, material properties, photon energy distributions). Once the radiation field is determined for each grid point, it must then be used to calculate the radiation variables needed to close the two dynamic moment equations. Clearly, this calls for an extensive database and a substantial increase in calculations, making these methods computationally difficult and expensive.

There are a number of ways in which these stringent computational requirements are reduced, resulting in obtainable and affordable solutions to the transfer equation. One choice is to assume the material is in local thermodynamic equilibrium (LTE) [3] so that opacities and emissivities are functions of the local material properties as defined statistically by the Boltzmann and Saha equations. Other choices include decreasing the number of transport equations by utilizing as few photon energy and angular distributions groups as possible or using coordinate-dependent transfer equation solvers [1]. In all instances, accuracy is sacrificed for efficiency.

The underlying premise of the diffusion approximation is that the material is optically thick to radiation. This implies that the radiation pressure tensor can be written a priori as an isotropic scalar quantity with $P=1/3 E$, providing the necessary closure relationship. Applying this along with the necessary approximations (associated with the diffusion approximation) to the moment equations, a single dynamic evolution equation for the radiation field is pro-

duced. By reducing the moment and transport equations to this one equation, reasonable memory requirements and computational times can be obtained compared to the transport method. In this instance, there is only one additional equation to be solved as opposed to three, and the equation does not require a radiation grid on which to perform calculations.

Less severe computational requirements make this approximation an appealing approach to closing the moment equations. Moreover, there are few restrictions on the form of the radiation field allowing flexibility in the distribution of radiation being transported and its relationship to the local fluid. In particular, the radiation field does not have to be in equilibrium with the material, a situation which may arise when the radiation field varies too rapidly for the material to compensate instantaneously or when the material is driven through hydrodynamic processes faster than it can relax radiatively. This latter model is often denoted as the nonequilibrium radiation diffusion approximation [2].

By its very definition, the diffusion approximation neglects any anisotropic effects in the radiation field which can result in excessive radiation energy transport. However, smooth, qualitative corrections to the radiative flux can be used where such effects may dominate the physics. Specifically, in regimes where the photon mean free path becomes comparable to a characteristic dimension of interest (i.e., a defined region of flow), the overprediction of energy transport is compensated for by introducing a flux-limiter. Based on this and the properties described above, a flux-limited form of the nonequilibrium diffusion approximation is preferable to the transport closure method for problems associated with dense plasma configurations of interest.

1.2 Compact Toroid Stagnation

The concept of a compact toroid was first introduced by Hans Alfven in 1958 [5]. It is a toroidal plasma confinement scheme which maintains a high-density plasma within a compact ring structure by a strong magnetic field. In general such configurations appear to be highly stable against many plasma instabilities and are conducive to plasma confinement on dynamic timescales. Compact toroids have their roots in fusion technology, where their compact nature and confinement capabilities provide a number of advantages over traditional confinement schemes [6,7]. Because of these properties, they have also been proposed for a variety of other applications [8].

Compact toroids encompass FRC (field-reversed configuration) [6], RFP (reverse-field pinch) [6], and spheromak [7] magnetic field configurations. Of particular interest is the spheromak class in which the magnetic field structure is self contained and is comprised of both toroidal and poloidal field components (See Figure 1.1). The combination of fields results in magnetic shear, and produces a plasma configuration stable to acceleration-driven instabilities such as the Rayleigh Taylor instability [9]. Stability permits the acceleration of the confined plasma to high velocities and hence high directed kinetic energies. Compact toroids can also be compressed, a property that is advantageous for increasing power densities and energy coupling efficiencies between driver and recipient toroid. These factors can lead to applications requiring high energy densities and include such possibilities as an accelerating charge-neutral ion beam, a photon or neutron source, plasma flow switch, microwave compressor, inertial fusion driver, and a fuel and/or heating source of fusion reactors. For the purpose of this dissertation, the term compact toroid will denote the spheromak class of compact toroids associated with such applications.

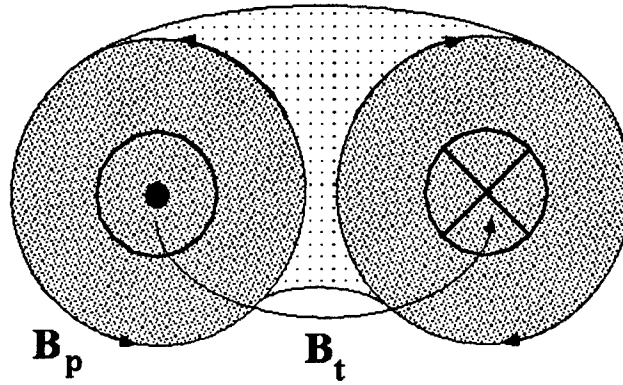


Figure 1.1. Illustration of a spheromak class of compact toroid. The compact toroid is comprised of both poloidal and toroidal magnetic fields as depicted. The plasma resides within the magnetic field structure [10].

One application, which is under investigation at the Phillips Laboratory, uses the compact toroid as a radiation source that may be capable of emitting photons up through the 100 keV energy range. Such a source would aid in testing the hardness of electronics and other structures to harsh radiation environments. There are a number of devices that are currently used as radiation sources at the 1 to 3 keV level. Among these are the classic Z-pinch, the wire or fiber pinch, and the imploding liner. The possible advantage of the compact toroid is the extension of the photon energy range to 10 keV and higher.

The classic Z-pinch, the wire pinch, and the fiber pinch are physical processes which involve the collapse of a column of plasma on axis [11]. Typically a plasma column is formed through the ionization of a gas column or an injected gas puff. The application of a voltage difference across the ends of the column produces an axial current, which in turn, creates a toroidal magnetic field. The current and the induced field then interact producing a $\vec{J} \times \vec{B}$ compressional force exterior to the plasma column. When this compressional force is on the order of the plasma particle pressure, nkT , the plasma undergoes a quasistatic compression, commonly referred to as an equilibrium pinch or a Bennet pinch. When the compressional force is much larger than the pressure forces, the plasma rapidly collapses inward towards its axis in a dynamic pinch. During collapse, a significant fraction of the stored electric energy of the driving system is converted into kinetic energy associated with the implosion velocity; upon impact on axis, the kinetic energy is converted into material internal energy and the plasma is thermalized. Observations indicate that the resulting radiation spectrum is limited to a continuum corresponding to plasma temperatures on the order of 1 keV and K shell line radiation of a few keV indicative of the plasma composition [7].

While undergoing compression, some of the directed kinetic energy of the plasma column is converted into internal compressional heating of particles. This is accompanied by ohmic heating. Both compressional and ohmic heating of the plasma is necessary to produce a radiation source with photon energies in the x-ray regime. Because this heating occurs throughout the implosion process, the plasma loses specific internal energy via radiation on an implosion timescale. Thus at maximum compression, the plasma is cooler than it would have been if it had not been able to radiate. This lowers the energy spectrum. In this case, obtaining a higher energy spectrum requires compression to even higher densities or keeping radiation losses prior to impact on axis as low as possible. Compression to higher densities can be achieved by using smaller radius wire and fiber pinches. For a given current, the compressional magnetic field increases as $1/r$, making the imploding force large enough to collapse to even smaller radii and larger densities.

Regardless of their preionization configuration, standard pinches based on the implosion of plasma columns partition their energy during compression between kinetic, internal, and radiation energies. To keep the coupling between the kinetic and the internal energy of the plasma at a minimum throughout most of the collapse, and hence radiative losses at a minimum, imploding liners are used. Imploding liners are dynamic pinches involving the compression of an annular plasma as opposed to a filled column of plasma. They usually take the form of foils, wires, or annular gas puffs. Although the processes involved in initial ionization and implosion dynamics are essentially the same as that of standard pinches, imploding liners are able to obtain large kinetic energies with little internal energy conversion. As a result, they provide an energy store which efficiently couples to the plasma during compression. For a range of kinetic energies, these systems can then produce a higher

energy spectrum of photon emission.

In terms of radiation production, the compact toroid has some advantages over these contemporary radiation sources. Like the imploding liner, the compact toroid is an efficient energy store which couples to the plasma primarily during its compression. However, where liners are limited to velocities on the order of tens of cm/ μ s in order to avoid Rayleigh Taylor instabilities [7], compact toroids have been experimentally produced with velocities in the hundreds of cm/ μ s regime. It is these higher specific directed kinetic energies that provide an access to even higher photon energies.

If the particle density is sufficiently large, a high-Z compact toroid can produce keV range radiation by colliding with a target. The collision and the associated physical processes is often referred to as stagnation. For applications of current interest, this target is a wall and the compact toroid has a directed kinetic energy on the order of a few MJ. During the stagnation, the compact toroid collides against the wall, first compressing and then expanding outward from the target. At these energies, the compression is a supersonic process. Thus, the initial compression will produce a shock wave at the toroid-wall interface, heating the ion constituents of the toroid. The ions in turn couple with the electrons which then couple with the radiation field. If the shock heating of the ions is an efficient process and the ion-electron and electron-photon coupling time scales are small compared to the stagnation time, the compact toroid will radiate via bound-bound, free-bound and free-free radiation. The level of radiation production is essentially determined by the coupling efficiency and the shock strength which depend upon such parameters as the directed velocity, material density, and magnetic field strength. The role that such parameters play in the stagnation process and consequent radiation production widely varies and is of general interest.

Previous work on the compact toroid stagnation process is limited to a set of computational simulations performed by M. Gee, et. al. [12,13] at the Lawrence Livermore National Laboratory. These calculations use a one-dimensional slab geometry to model the stagnation of a uniform density, multi-MJ directed kinetic energy xenon plasma. One component of the magnetic field is used in these calculations, the toroidal component, which has an initial uniform magnitude. Material properties are based on a range of atomic physics models and the radiation treatment is flux-limited multigroup diffusion. Parameter studies with a 5 MJ kinetic energy toroid include (1) calculations using LTE, non-LTE average atom model and Detailed Configuration Accounting (DCA) atomic physics, (2) DCA calculations with and without magnetic field, and (3) calculations with a perfectly conducting target and a copper target.

Numerical simulations assist in the understanding of the physics of the stagnation process and provide clues concerning the ability of this process to produce an effective radiator. As indicated above, prior analysis has focused on atomic physics and radiation transport with little emphasis on the magnetic field structure. However, compact toroids consist of a complex three dimensional magnetic field structure which should be taken into account if the physics is to be modelled properly. During stagnation, the magnetic fields are compressed along with the material, and an increase in magnetic pressure is observed in the stagnation region. As a result, some of the initial kinetic energy must be partitioned into compressing against the magnetic pressure. Clearly, this effects the radiation production.

With the nonequilibrium radiation diffusion approximation in the MACH2 code, the stagnation process is a natural choice for an application. MACH2 is equipped to model complicated field structures and uses all three components

of vector quantities such as velocity and magnetic field. A survey of the literature indicates that MACH2 is the only 2 -1/2 dimensional MHD code which can handle all three field components in complex geometries with LTE atomic physics and radiation. In this case, the MACH2 calculations would provide a sophisticated treatment of magnetic fields and a somewhat simplified treatment of the atomic physics in contrast to the calculations of M. Gee, et. al,. Furthermore, a number of stagnation experiments are just beginning with the MARAUDER effort at the Phillips Laboratory and will provide, in the near future, actual experimental data to compare with numerical results. For these reasons, this new radiation code development will first be used to investigate the compact toroid stagnation process.

1.3 Present Study

The remainder of this dissertation is concerned with the development of the nonequilibrium radiation diffusion approximation, its implementation into the code MACH2, the subsequent benchmarking of the code, and the application of this code to the radiation production of the stagnating compact toroid. In Chapter 2, the derivation of the nonequilibrium radiation diffusion approximation is detailed starting from a general form of the moment equations and continuing through the steps leading to the final energy equation used here. Chapter 3 addresses the incorporation of this radiation treatment into MACH2, including additional terms added to the MHD equations and the atomic physics available in MACH2. A description of the MARAUDER compact toroid experiment at the Phillips Laboratory upon which the stagnation application is based is found in Chapter 4. Chapter 5 covers the testing of the radiation algorithms by benchmarking with analytic solutions and other numerically known solutions. Chapter 6 then discusses the results of a detailed analysis and parameter study performed on the stagnation process using the nonequilibrium radiation diffusion approximation. Finally, in Chapter 7, a summary and conclusions are presented along with thoughts for future work.

CHAPTER 2. THE NONEQUILIBRIUM RADIATION DIFFUSION APPROXIMATION

The radiation moment equations together with the material conservation laws define the equations of radiation hydrodynamics [14]. These equations may be written in a variety of forms, depending on the chosen reference frame and the manner in which one treats the radiation-material coupling. The choice of reference frame is often dictated by the physics to be modelled along with computational and physical simplicity. For the diffusion regime, the equations are almost always expressed in the comoving reference frame where the material is instantaneously at rest. In the relativistic sense, this frame is the proper frame; material properties are isotropic and are defined on a microscopic level from thermodynamics and statistical mechanics.

With the derivation of the radiation transport equation in the comoving frame, $O(v/c)$ and higher frame-dependent terms surface and propagate through to the moment equations of the radiating fluid. These terms are the result of a Lorentz transformation of radiation quantities and derivatives from an Eulerian frame to a comoving frame and depend upon the fluid velocity \bar{v} and the speed of light, c . Although the higher order terms are negligible and can be ignored for small v/c , the terms of $O(v/c)$ can become important in certain physical regimes and may actually dominate over all other terms in the equations [2]. To account for such contributions, it is necessary to make an order of magnitude comparison between terms in each equation in all physical regimes, keeping those $O(v/c)$ terms that play a relevant role in any given regime. The resulting transport and moment equations are referred to as the first order comoving frame transport and moment equations.

The derivation of the comoving frame transport equation, the subsequent

moment equations, and the first order analysis of these equations can be found in the literature. The equations are derived in either a covariant form which is then used to extract specific coordinate and symmetry dependent equations (Buchler [15], Muir and Weaver [16]), or in a form which is already based on a particular geometry (Mihalas and Mihalas [2], Castor [17]). In this chapter, the comoving frame moment equations for cylindrical geometry with azimuthal symmetry are used as a starting point from which to derive a general form of the radiation diffusion equation.

2.1 The Moment Equations in Cylindrical Coordinates

The MACH2 code has the capability to simulate physical problems in either cylindrical or planar geometry. It is therefore beneficial to write the moment equations in either cylindrical or cartesian coordinates. Because of their initial complexity, the moment equations in cylindrical geometry will be discussed in this section. From Muir and Weaver [16], the radiation energy and momentum equations in cylindrical coordinates (with azimuthal symmetry in which $\partial s / \partial \theta = 0$ for any scalar field s) are:
energy equation:

$$\begin{aligned} & \frac{dE_o}{dt} + E_o \left[\frac{1}{r} \frac{\partial (rv^r)}{\partial r} + \frac{\partial v^z}{\partial z} \right] + \left[\frac{v^r}{c^2} \frac{\partial F_o^r}{\partial t} + \frac{v_z}{c^2} \frac{\partial F_o^z}{\partial t} \right] \\ & + \frac{1}{r} \frac{\partial (rF_o^r)}{\partial r} + \frac{\partial F_o^z}{\partial z} + \frac{a_r}{c^2} F_o^r + \frac{a_z}{c^2} F_o^z - v_o \left[\frac{a_r}{c^2} \frac{\partial F_o^r}{\partial v_o} + \frac{a_z}{c^2} \frac{\partial F_o^z}{\partial v_o} \right] \\ & - v_o \left[\frac{\partial v_r}{\partial r} \frac{\partial P_o^{rr}}{\partial v_o} + \frac{v_r}{r} \frac{\partial P_o^{\theta\theta}}{\partial v_o} + \frac{\partial v_z}{\partial z} \frac{\partial P_o^{zz}}{\partial v_o} + \frac{\partial v_z}{\partial r} \frac{\partial P_o^{rz}}{\partial v_o} + \frac{\partial v_r}{\partial z} \frac{\partial P_o^{rz}}{\partial v_o} \right] \\ & = 4\pi\eta_o - c\chi_o E_o, \end{aligned} \quad (2)$$

r-component of the momentum equation:

$$\begin{aligned} & \frac{1}{c} \frac{dF_o^r}{dt} + \frac{F_o^r}{c} \left[\frac{1}{r} \frac{\partial (rv^r)}{\partial r} + \frac{\partial v^z}{\partial z} \right] + \left[\frac{v_r}{c} \frac{\partial P_o^{rr}}{\partial t} + \frac{v_z}{c} \frac{\partial P_o^{rz}}{\partial t} \right] + \left[\frac{a_r}{c} P_o^{rr} + \frac{a_z}{c} P_o^{rz} \right] \\ & + c \left[\frac{1}{r} \frac{\partial (rP_o^{rr})}{\partial r} + \frac{\partial P_o^{rz}}{\partial z} - \frac{P_o^{\theta\theta}}{r} \right] + \frac{a_r}{c} E_o + \left[\frac{F_o^r}{c} \frac{\partial v^r}{\partial r} + \frac{F_o^z}{c} \frac{\partial v^r}{\partial z} \right] \\ & - \frac{1}{c} \frac{\partial v_r}{\partial r} \frac{\partial}{\partial v_o} (v_o Q_o^{rrr}) - \frac{1}{c} \frac{\partial v_z}{\partial z} \frac{\partial}{\partial v_o} (v_o Q_o^{rzz}) \\ & - \frac{v_r}{cr} \frac{\partial}{\partial v_o} (v_o Q_o^{r\theta\theta}) - \frac{1}{c} \left(\frac{\partial v_r}{\partial z} + \frac{\partial v_z}{\partial r} \right) \frac{\partial}{\partial v_o} (v_o Q_o^{rrz}) \\ & - \frac{a_r}{c} \frac{\partial}{\partial v_o} (v_o P_o^{rr}) - \frac{a_z}{c} \frac{\partial}{\partial v_o} (v_o P_o^{rz}) = -\chi_o F_o^r, \end{aligned} \quad (3)$$

z-component of the momentum equation:

$$\begin{aligned}
& \frac{1}{c} \frac{dF_o^z}{dt} + \frac{F_o^z}{c} \left[\frac{1}{r} \frac{\partial (rv^r)}{\partial r} + \frac{\partial v^z}{\partial z} \right] + \left[\frac{v_r}{c} \frac{\partial P_o^{zr}}{\partial t} + \frac{v_z}{c} \frac{\partial P_o^{zz}}{\partial t} \right] + \left[\frac{a_r}{c} P_o^{zr} + \frac{a_z}{c} P_o^{zz} \right] \\
& + c \left[\frac{1}{r} \frac{\partial (rP_o^{zr})}{\partial r} + \frac{\partial P_o^{zz}}{\partial z} \right] + \frac{a^z}{c} E_o + \left[\frac{F_o^r}{c} \frac{\partial v^z}{\partial r} + \frac{F_o^z}{c} \frac{\partial v^r}{\partial z} \right] \\
& - \frac{1}{c} \frac{\partial v_r}{\partial r} \frac{\partial}{\partial v_o} (v_o Q_o^{zrr}) - \frac{1}{c} \frac{\partial v_z}{\partial z} \frac{\partial}{\partial v_o} (v_o Q_o^{zzz}) \\
& - \frac{v_r}{cr} \frac{\partial}{\partial v_o} (v_o Q_o^{z\theta\theta}) - \frac{1}{c} \left(\frac{\partial v_r}{\partial z} + \frac{\partial v_z}{\partial r} \right) \frac{\partial}{\partial v_o} (v_o Q_o^{zzr}) \\
& - \frac{a_r}{c} \frac{\partial}{\partial v_o} (v_o P_o^{zr}) - \frac{a_z}{c} \frac{\partial}{\partial v_o} (v_o P_o^{zz}) = -\chi_o F_o^z . \tag{4}
\end{aligned}$$

The quantities E_o , F_o , P_o , and Q_o , are the zeroth, first, second, and third moments, respectively, of the integrated intensity over solid angle. E_o , F_o , and P_o physically correspond to the comoving radiation energy density, flux, and stress tensor. The variables η_o and χ_o define the comoving material emissivity and absorption coefficient, while v and a are the fluid velocity and acceleration. The radiation variables are measured in the comoving frame as denoted by the subscript, and are frequency dependent.

The underlying stipulation of the diffusion approximation is that the photon mean free path, λ_p , must be much less than some characteristic length, l , of the physical system in which it interacts. This implies that on the scale of l , the material component of the system appears opaque to radiation. Under these conditions, the photons will be absorbed, emitted, or scattered independent of direction, resulting in an isotropic photon distribution. This is desirable since isotropy simplifies the radiation equations by forcing the linear relationship $P_o = 1/3 E_o$:

$$\begin{aligned}
& \text{isotropy} \\
& I(\bar{x}, t; \hat{n}, \nu) \Rightarrow I(\bar{x}, t; \nu)
\end{aligned}$$

Then

$$E_v = \int I(\bar{x}, t; v) d\Omega = I(\bar{x}, t; v) \int d\Omega = 4\pi I(\bar{x}, t; v)$$

$$P_v = \int I(x, t; v) \hat{n} \hat{n} d\Omega = I(\bar{x}, t; v) \int \hat{n} \hat{n} d\Omega = \frac{4\pi}{3} I(\bar{x}, t; v) = \frac{1}{3} E_v$$

$$\text{or } P = \int P_v dv = \frac{1}{3} \int E_v dv = \frac{1}{3} E$$

(Because this simplification is desirable, the diffusion approximation is used often and quite liberally for many physical applications.)

The assumption of an isotropic radiation field can be maintained even if material inhomogeneities exist in the system as long as the inhomogeneities vary slowly on the spatial scale of the system. In general, this is commonly referred to as the first order diffusion approximation. The inhomogeneity of the material is then taken into account by allowing it to perturb an isotropic radiation field. By keeping only the lowest order terms in the momentum equation, a non zero but small value for the radiation flux emerges which is independent of angle and related to the gradient of the radiation energy density. This is introduced into the energy equation as the lowest perturbing term in the evolution of an isotropic radiation energy distribution.

Although the condition $\lambda_p \ll l$ is a necessary assumption for the diffusion approximation, it may be insufficient when the fluid is moving. A moving fluid can modify the photon distribution to such a degree that a breakdown of the diffusion approximation is possible even if $\lambda_p \ll l$. This will happen if the fluid flows rapidly enough to change local material conditions on the scale of a photon interaction time.

To illustrate this, consider the existence of an isotropic field in a local homogeneous region of dimension l . Within this region, let the material motion be either non-existent or small compared to the timescale on which the photons interact with their surroundings. Photons are then re-emitted at essentially

the same location in which they were absorbed, and the photon distribution is, as assumed, isotropic. However, if the fluid velocity becomes large enough that the fluid flow time is comparable to or exceeds the photon-material collision times, the photon distribution left behind may see a somewhat different physical environment than it originally had; local material conditions may have been modified drastically by the fluid flow. Thus, in this simplified picture, the assumption of isotropy may no longer be valid under certain conditions and leads to the breakdown of the diffusion approximation. To insure that isotropy be maintained, it is necessary to also require that the photon interaction time be much less than the fluid flow time. If this is the case, the photons are able to adjust quickly enough to the modifications introduced into their local area to insure an isotropic photon distribution [2].

The criterion just defined is used to obtain the first order diffusion approximation. With $t_{\text{photon mfp}} \sim \lambda_p / c$ and $t_{\text{fluid flow}} \sim l / v$, the requirement that the photon interaction time be much less than the fluid flow time is equivalent to $(\lambda_p / c) \ll l / v$ or $(\lambda_p / l) (v / c) \ll 1$. This can be used to reduce the momentum equation by performing a dimensional analysis of its various components on a fluid flow time scale. Replacing $\partial / \partial t$ with v / l where $v \sim v_r \sim v_\theta$ is the fluid flow velocity, $\partial / \partial r, \partial / \partial z$ with $1 / l$, the terms in the radiation momentum equations (3-4) are each in turn proportional to:

$$\frac{1}{c} \frac{v}{l} F_o : \frac{1}{c} \frac{v}{l} F_o : \frac{v^2}{c} \frac{1}{l} P_o : \frac{a}{c} P_o : c \frac{1}{l} P_o : \frac{a}{c} E_o : \frac{1}{c} \frac{v}{l} F_o : \frac{1}{c} \frac{v}{l} Q_o : \frac{a}{c} P_o : \frac{1}{\lambda_p} F_o \quad (5)$$

Note that the quantities within a set of brackets in the momentum equations, (3) and (4), are of the same dimensionality and are regarded as a single entity in the scaling, as are all terms containing the third moment Q . Comparing terms with like radiation quantities:

$$F_o \text{ terms : } \frac{\lambda_p v}{l c} : \frac{\lambda_p v}{l c} : \frac{\lambda_p v}{l c} : 1$$

$$P_o \text{ terms : } \frac{v^2}{c^2} : \frac{al}{c^2} : 1 : \frac{al}{c^2}$$

Of the F_o terms, the first three are negligible compared to the last and may be dropped. A comparison of the pressure terms show that the time derivative quantities are found to be $O(v^2/c^2)$ to the divergence of the pressure tensor and hence may be ignored. The acceleration terms are of order al/c^2 and are also assumed to be small compared to unity. For the purpose of this work, the terms containing the third moments may be dropped because they vanish when the momentum equation is integrated over frequency. The terms remaining from Equations (3) and (4) then give the reduced momentum equation in the isotropic limit ($P_o = 1/3 E_o$):

$$\begin{aligned} \text{r-component : } \quad & \frac{c}{3} \left[\frac{1}{r} \frac{\partial}{\partial r} (r E_o) - \frac{E_o}{r} \right] = -\chi_o F_o^r \\ \text{z-component : } \quad & \frac{c}{3} \frac{\partial E_o}{\partial z} = -\chi_o F_o^z \end{aligned} \tag{6}$$

$$\text{or} \quad \bar{F}_o = -\frac{c}{3\chi_o} \nabla E_o . \tag{7}$$

(A comparison between the radiation moments F_o and P_o would not be correct at this time since there is no way of knowing a priori how these quantities relate to each other as far as dimensionality, and thus magnitude, is concerned.) Using the isotropic prescription $P_o = 1/3 E_o$, it is convenient to rewrite the energy equation (2) in the following form:

$$\begin{aligned} \frac{dE_o}{dt} + E_o \left[\frac{1}{r} \frac{\partial}{\partial r} (rv^r) + \frac{\partial v^z}{\partial z} \right] + \frac{1}{r} \frac{\partial}{\partial r} (r F_o^r) + \frac{\partial F_o^z}{\partial z} + \frac{E_o}{3} \left[\frac{\partial v_r}{\partial r} + \frac{v_r}{r} + \frac{\partial v_z}{\partial z} \right] \\ - \frac{\partial}{\partial v_o} \left[v_o \cdot \frac{E_o}{3} \cdot \left[\frac{\partial v_r}{\partial r} + \frac{v_r}{r} + \frac{\partial v_z}{\partial z} \right] \right] = 4\pi\eta_o - c\chi_o E_o . \end{aligned} \tag{8}$$

Here the $\partial F/\partial t$ terms have been dropped since they are of $O(v^2/c^2)$ on a fluid flow time scale and their inclusion leads only to a forced diffusion equation for a transparent medium [2].

Substituting the result from the reduced momentum equation (7) into the energy equation (2):

$$\begin{aligned} \frac{dE_o}{dt} + E_o \left[\frac{1}{r} \frac{\partial}{\partial r} (rv^r) + \frac{\partial v^z}{\partial z} \right] + \frac{1}{r} \frac{\partial}{\partial r} \left[-\frac{c}{3\chi_o} \left(\frac{\partial}{\partial r} (rE_o) - E_o \right) \right] + \frac{\partial}{\partial z} \left(-\frac{c}{3\chi_o} \frac{\partial E_o}{\partial z} \right) \\ + \frac{E_o}{3} \left[\frac{\partial v^r}{\partial r} + \frac{v_r}{r} + \frac{\partial v_z}{\partial z} \right] - \frac{\partial}{\partial v_o} \left\{ v_o \frac{E_o}{3} \left[\frac{\partial v_r}{\partial r} + \frac{v_r}{r} + \frac{\partial v_z}{\partial z} \right] \right\} = 4\pi\eta_o - c\chi_o E_o . \end{aligned} \quad (9)$$

The sum of the quantities in the brackets of the second and fifth terms is the divergence of the velocity, and the sum of the third and fourth terms is the divergence of the energy flux, $\nabla \cdot (c/3\chi_o) \nabla E_o$. Condensing terms in brackets and rewriting in operator form one finds:

$$\frac{dE_o}{dt} + \frac{4}{3} E_o \nabla \cdot \bar{v} - \nabla \cdot \frac{c}{3\chi_o} \nabla E_o - \frac{1}{3} \frac{\partial}{\partial v_o} [v_o E_o \nabla \cdot \bar{v}] = 4\pi\eta_o - c\chi_o E_o . \quad (10)$$

This can be written in a slightly different fashion using a variation of the continuity equation, $\nabla \cdot \bar{v} = \rho \, d/dt(1/\rho)$ and $dE_o/dt = -\rho E_o \, d/dt(1/\rho) + d/dt(E_o/\rho)$:

$$\rho \left[\frac{d}{dt} \left(\frac{E_o}{\rho} \right) + \frac{1}{3} \left\{ E_o - \frac{\partial}{\partial v_o} [v_o E_o] \right\} \frac{d}{dt} \left(\frac{1}{\rho} \right) \right] = \nabla \cdot \frac{c}{3\chi_o} \nabla E_o + 4\pi\eta_o - c\chi_o E_o . \quad (11)$$

This is the general form of the radiation energy equation in the diffusion approximation.

2.2 The First Order Equilibrium Diffusion Approximation

In the diffusion approximation, material properties and dynamics are such that the prescription of an isotropic photon distribution is maintained on a local scale. Photons can travel no more than a few mean free paths before they are absorbed or scattered and their energy distribution is indicative of the material temperatures in the surrounding vicinity. If the material temperature changes slowly over a distance of a few mean free paths, the radiation distribution at any given point is defined by the local material temperature through the Plank function [18]. Under these conditions, the radiation field and the material components of a radiating fluid are said to be in local thermal equilibrium with each other. This leads to the following equilibrium diffusion approximation.

Integrating the energy equation over frequency

$$\begin{aligned} \rho \left[\frac{d}{dt} \left(\frac{E_o}{\rho} \right) + \frac{1}{3} E_o \frac{d}{dt} \left(\frac{1}{\rho} \right) \right] &= \nabla \cdot \int_0^\infty \frac{c}{3\chi_o(v_o)} \nabla E_o(v_o) dv_o \\ &\quad + \int_0^\infty [4\pi\eta_o(v_o) - c\chi_o(v_o)E_o(v_o)] dv_o \\ &= \nabla \cdot \frac{c}{3\chi_R^o} \nabla E_o + \int_0^\infty [4\pi\eta_o(v_o) - c\chi_o(v_o)E_o(v_o)] dv_o. \end{aligned}$$

Here χ_R^o is the Rosseland mean opacity defined by

$$\chi_R^{-1} = \frac{\int_0^\infty \frac{1}{\chi_o(v_o)} \nabla E_o(v_o) dv_o}{\int_0^\infty \nabla E_o(v_o) dv_o} = \frac{\int_0^\infty \frac{1}{\chi_o(v_o)} \nabla E_o(v_o) dv_o}{\nabla E_o}.$$

Defining a radiation energy density at the material temperature by $E_o = a_R T^4$,

where a_R is Stefan's constant, the radiation energy equation becomes

$$\begin{aligned} \frac{d}{dt} \left(\frac{a_R T^4}{\rho} \right) + \frac{1}{3} a_R T^4 \frac{d}{dt} \left(\frac{1}{\rho} \right) = \nabla \cdot \frac{4a_R c T^3}{3\chi_R} \nabla T \\ + \int_0^\infty [4\pi\eta_o(v_o) - c\chi_o(v_o) E_o(v_o)] dv_o . \end{aligned} \quad (12)$$

Combining this with the material energy equation (fluid with no magnetic field)

$$\rho \left[\frac{de}{dt} + \rho \frac{d}{dt} \left(\frac{1}{\rho} \right) + \frac{1}{\rho} \nabla \cdot \kappa \nabla T \right] = - \int_0^\infty [4\pi\eta_o(v_o) - c\chi_o(v_o) E_o(v_o)] dv_o \quad (13)$$

the following law of thermodynamics for the material is obtained:

$$\frac{d}{dt} \left(e + \frac{a_R T^4}{\rho} \right) + \left(p + \frac{1}{3} a_R T^4 \right) \frac{d}{dt} \left(\frac{1}{\rho} \right) = \frac{1}{\rho} \nabla \cdot \left(\left(\kappa + \frac{4a_R c T^3}{3\chi_R \rho} \right) \nabla T \right) . \quad (14)$$

This states that the rate of change of the total (material + radiation) energy density in a fluid element plus the rate of work done by the total pressure in the element equals the rate of energy loss by transport to adjacent fluid elements. Here e is the specific internal energy of the electron fluid and is a function only of material temperature as described by the equation of state for a perfect gas $e = c_v T$ (LTE). The variables p and κ correspond to the electron pressure and the electron thermal conductivity, respectively. The presence of the radiation field also effects the fluid momentum which is modified through an additional "pressure" term in the electron momentum equation:[2,14]

$$\rho \left[\frac{\partial \bar{v}}{\partial t} + \bar{v} \cdot \nabla \bar{v} \right] = - \nabla \left(p + \frac{1}{3} a_R T^4 \right) + \nabla \cdot \bar{\bar{\sigma}} . \quad (15)$$

Here $\bar{\bar{\sigma}}$ is defined as the viscous stress tensor.

2.3 The Nonequilibrium Diffusion Approximation

The application of the equilibrium diffusion approximation is limited to physical conditions under which the radiation field and the material are in local thermal equilibrium. However, problems can arise where the diffusion approximation is still appropriate, but the radiation field is not in equilibrium with the material. For example, the photon distribution may be Plankian but at an effective temperature which differs from the local material temperature. This can occur if the radiation field originated from a region with other (but thick) material conditions.

It is possible to treat such problems in the diffusion approximation. To extend the range of applicability, the form of the radiation field may be relaxed to an arbitrary spectral distribution (i.e., non-Plankian) and energy density. Integrating the diffusion energy equation over frequency

$$\begin{aligned} & \int_0^{\infty} \rho \left[\frac{d}{dt} \left(\frac{E_o(v_o)}{\rho} \right) + \frac{1}{3} \left\{ E_o(v_o) - \frac{\partial}{\partial v_o} [v_o E_o(v_o)] \right\} \frac{d}{dt} \left(\frac{1}{\rho} \right) \right] dv_o \\ &= \int_0^{\infty} \nabla \cdot \frac{c}{3\chi_o(v_o)} \nabla E_o(v_o) dv_o + \int_0^{\infty} \chi_o(v_o) [4\pi B(v_o, T) - cE_o(v_o)] dv_o \end{aligned}$$

one obtains the nonequilibrium radiation diffusion equation:

$$\rho \left[\frac{d}{dt} \left(\frac{E_o}{\rho} \right) + \frac{1}{3} E_o \frac{d}{dt} \left(\frac{1}{\rho} \right) \right] = \nabla \cdot \left(\frac{c}{3\bar{\chi}} \nabla E_o \right) + c (\kappa_P a_R T^4 - \kappa_E E_o) \quad (16)$$

where

$$\frac{\nabla E_o}{\bar{\chi}} = \int_0^{\infty} \frac{\nabla E_o(v_o)}{\chi_o(v_o)} dv_o, \quad \kappa_P = \frac{\int_0^{\infty} \chi_o(v_o) B(v_o, T) dv}{\int_0^{\infty} B(v_o, T) dv}$$

and κ_E is the absorption mean

$$\kappa_E = \frac{\int_0^\infty (E_o(v_o)) \chi_o(v_o) dv_o}{E_o}$$

In the above equations, the material is treated as a Plankian emitter (recall the material is in LTE) defined by the Plank function $B(v_o, T)$ at the material temperature, while the existing photon distribution is somewhat arbitrary (but with no angular dependence) as given by $E_o(v_o)$.

As a first approximation, it is common to assume that the radiation field is not strongly out of equilibrium with the material. In this case, the photon distribution takes on a Plankian form at a specific radiation temperature. The coefficients κ_E and $\bar{\chi}$ are then set so that $\bar{\chi} = \chi_R$, the Rosseland mean opacity, and $\kappa_E = \kappa_P$, the Plankian mean opacity, which are evaluated at the material temperature and depend solely upon the absorption (photon-material interactions) property of the material. Because they are averages over the entire photon spectrum, these mean opacities will become an insufficient way to describe the radiation transport and photon distribution when large fluctuations in the absorption coefficients are present; the averaging process tends to wash out physically important features of the opacity spectrum. In such instances, it would be necessary to write the various radiation quantities over specific frequency integrals, thus solving a set of multigroup diffusion equations. For the work in this dissertation, the single group treatment to the diffusion approximation will be used.

As with the equilibrium diffusion approximation, the radiation field provides an additional influence in the material evolution. Its presence is manifest through a pressure term in the momentum equation and a coupling term in the electron energy equation (neglecting magnetic field and with all quanti-

ties measured in the comoving frame):

electron energy equation:

$$\rho \left[\frac{\partial e}{\partial t} + \bar{v} \cdot \nabla e \right] = -p \nabla \cdot \bar{v} - \nabla \cdot (\kappa \nabla T) - a_R c \kappa_P (T^4 - E_o) \quad (17)$$

momentum equation:

$$\rho \left[\frac{\partial \bar{v}}{\partial t} + \bar{v} \cdot \nabla \bar{v} \right] = -\nabla (p + \frac{1}{3} E_o) + \nabla \cdot \bar{\bar{\sigma}} \quad (18)$$

The coupling term in the electron energy equation naturally arises out of a need to conserve energy between the electron fluid and the radiation field. Its existence in the radiation energy equation is a consequence of applying the nonequilibrium diffusion approximation to the $O(v/c)$ moment equations. This term describes the exchange of energy between the free electron population and the radiation field. To maintain energy balance, it must therefore reside in the electron energy equation.

Although physically evident, the existence of the radiation coupling term in the electron energy equation also becomes apparent when one performs an $O(v/c)$ analysis on the comoving frame equations of the radiating fluid. Such an analysis is actually necessary to maintain an $O(v/c)$ consistency among all radiation hydrodynamic equations including the dynamical equations of the fluid. Mihalas and Mihalas [2] carried out an $O(v/c)$ analysis which reveals the presence of a coupling term in the gas energy equation and also a radiation pressure gradient term in the Lagrangian momentum equation. Thus to $O(v/c)$, the inclusion of the radiation energy equation into MACH2 must be accompanied by additional terms in the momentum and electron energy equations.

The nonequilibrium radiation diffusion approximation can describe a wide variety of plasma related physics and represents a vast improvement over an

equilibrium diffusion treatment. Not only does it allow for the possible non-equilibrium between radiation and material, but, utilizing flux-limiting ideas described in the next section, it also has the capacity to cover many physical regimes through which a radiating fluid can dynamically evolve.

2.4 The Validity of the Diffusion Approximation and Flux-Limited Diffusion

By its very derivation, the diffusion approximation for the evolution of the radiation field is no longer valid when carried outside a regime where the isotropy of the photon distribution is no longer maintained. In general, this occurs when the photon mean free path is on the order of or larger than the characteristic size of the system, or when the fluid flow changes the material properties fast enough that the field cannot keep up with the changes.

Inherent in the diffusion approximation is the definition that photons always travel a distance of the order of λ_p irrespective of material properties and without regard to the physically imposed upper bound of the photon free flight distance $c\Delta t$. Such negligence can rapidly lead to a misrepresentation of the radiation physics outside the optically thick regime, the most extreme case occurring in a transparent medium. The radiative flux predicted by diffusion theory is (from Equation(7))

$$F_o = -\frac{c}{3\chi} \nabla E_o \sim -\frac{c}{3} \lambda_p \frac{E_o}{l} \quad (19)$$

where λ_p is the photon mean free path and l is the dimension of the physical system. For a transparent medium, $(\lambda_p/l) \gg 1$, forcing

$$|F| > cE \quad (20)$$

Physically, this is not possible since it implies that the photons are propagating through the material unhindered at a speed greater than c :

$$v_E = \frac{|F|}{E} = \frac{\left| \frac{1}{3} c \lambda_p \nabla E \right|}{E} \sim c \left(\frac{\lambda_p}{3l} \right) \quad (21)$$

This causes the diffusion approximation to predict a radiation energy flux larger than that given for photons in the free streaming limit.

To overcome the limitations of the diffusion approximation, flux-limiting capabilities can be introduced into the radiation energy equation [14]. The idea is to modify the radiative flux term so that in transparent media, the photon flux becomes the free streaming value cE , while in optically thick media, the photon flux is the standard $c/(3\chi)\nabla E_0$. Because this is an ad hoc solution [1] to the problem, its accuracy is not well known. It does however, produce the correct limits and qualitatively correct behavior in the intermediate region, although quantitatively it could be seriously wrong in the intermediate region.

There are a variety of different approaches that are taken to limit the radiative flux [14,19,20]. The approach taken here is similar to that of Lund [21] and will be described in the next chapter.

CHAPTER 3. IMPLEMENTING THE RADIATION ENERGY EQUATION INTO MACH2

In the previous chapter, the moments of the radiation transport equation were shown in the diffusion limit to reduce to a modified form of the radiation energy equation. This energy equation describes the time evolution of the radiation field in the presence of a fluid. Solved self-consistently with the dynamical equations of the fluid, the influence of the radiation field on fluid properties and motion can be treated numerically to some specified level of accuracy. By incorporating a nonequilibrium radiation energy equation into the MACH2 code, the role radiation plays in the evolution of a radiating fluid can thus be addressed.

MACH2 is a 2 1/2 -dimensional, two temperature, nonideal (resistive dissipation of magnetic fields and thermal conduction) magnetohydrodynamics (MHD) code which has been utilized to model a variety of laboratory plasma experiments. The code contains a number of powerful numerical features including an Arbitrary Lagrangian-Eulerian (ALE) approach to grid motion, adaptive mesh capabilities, finite spatial volume differencing, and implicit time differencing of the dynamic fluid equations. It is written in FORTRAN 77 with the CRAY pointer extension and emphasizes clean and modular coding. The addition of a nonequilibrium radiation treatment into MACH2 was carried out in such a way as to conform to the overall structure of the code, employing available algorithms when possible and using notation consistent with that found throughout MACH2. The form of the nonequilibrium radiation diffusion equation reduces to the same physics as the existing emission and equilibrium diffusion models of MACH2, for the physical regimes in which they are appropriate.

3.1 The MACH2 Code

The MACH2 code contains the physics needed to model magnetically embedded plasmas, including resistive diffusion of magnetic fields, thermal conduction, elastic stresses, a multi-material capacity, and the availability of a separate electron and ion fluid temperature treatment. In the absence of radiative processes, the single fluid MHD equations [22] that are solved in MACH2 are (SI units with the temperature measured in eV):

$$\text{mass continuity equation: } \frac{\partial \rho}{\partial t} + \nabla \cdot (\rho \bar{v}) = 0, \quad (22)$$

$$\text{fluid momentum equation: } \rho \left[\frac{\partial \bar{v}}{\partial t} + \bar{v} \cdot \nabla \bar{v} \right] = -\nabla p + \bar{J} \times \bar{B} + \nabla \cdot \bar{\bar{\sigma}}, \quad (23)$$

$$\text{elastic stress equation: } \frac{\partial \bar{\bar{\sigma}}}{\partial t} = 2\mu I - \bar{v} \cdot \nabla \bar{\bar{\sigma}}, \quad (24)$$

specific internal energy equation:

$$\rho \left[\frac{\partial e}{\partial t} + \bar{v} \cdot \nabla e \right] = -p \nabla \cdot \bar{v} + \bar{J} \cdot \bar{E} + \nabla \cdot (\kappa \nabla T), \quad (25)$$

magnetic field transport equation:

$$\frac{\partial \bar{B}}{\partial t} = \nabla \times (\bar{v} \times \bar{B}) - \nabla \times \left(\frac{\eta}{\mu_0} \nabla \times \bar{B} \right) - \nabla \times \frac{1}{q_e n_e} (\bar{J} \times \bar{B}). \quad (26)$$

These are supplemented by equations of state of the plasma:

$$\text{thermal equation of state: } p = p(\rho, T) \quad (27)$$

$$\text{caloric equation of state (perfect gas): } e = e(\rho, T) \quad (28)$$

and exist in either an analytic form (i.e., perfect gas) or a pre-generated tabular form. Here the variables ρ and \bar{v} refer to the fluid density and velocity, respectively, while the material energy is denoted by e . The pressure associ-

ated with the fluid constituents is broken into two parts, one that is associated with normal stresses, p , and one that is associated with shear or tangential surface stresses, the viscous stress tensor, $\bar{\bar{\sigma}}$. The quantity μ in the elastic-stress equation is called the coefficient of viscosity (or shear modulus) and is determined from a strength of material model [23]. The transport coefficients η and κ correspond to the total electric resistivity and the thermal conductivity; these are determined from an analytic equation or obtained from an equation of state (EOS) table that is accessed by MACH2. The constant μ_0 is the permeability of free space, $4\pi \cdot 10^{-7}$, while q_e is the magnitude of the electron charge, and n_e is the electron number density. The variables \bar{J} , \bar{E} , and \bar{B} have their usual meanings of current density, electric field, and magnetic field.

The magnetic field transport equation is the result of combining the MHD approximation (neglect of the displacement current) to Maxwell's equations with Ohm's law for the moving fluid:

$$\text{Maxwell's Equations: } \nabla \times \bar{E} = -\frac{\partial \bar{B}}{\partial t}, \quad \nabla \times \bar{B} = \mu_0 \bar{J} \quad (29)$$

$$\text{Ohm's Law: } \bar{E} = \eta \cdot \bar{J} - \bar{v} \times \bar{B} + \frac{1}{q_e n_e} (\bar{J} \times \bar{B}) \quad (30)$$

It should be noted that the Hall term, which is ignored in many single fluid codes, is present in Ohm's law and the magnetic field transport equation.

The single fluid equations as given above represent a one temperature code in which the electrons and the ions are assumed to be in equilibrium. MACH2 also allows for a physical state of the fluid in which the electron and ion components of the fluid have not yet equilibrated with each other but have reached equilibrium within their own species. In other words, the ion and electron pop-

ulations have separate, distinct Maxwellian velocity distributions that are defined by two separate temperatures, T_e and T_i . The nonequilibrium nature of the two fluid components is handled in MACH2 by introducing two separate energy equations but maintaining a single momentum equation. In this case the single energy equation is replaced by separate ion and electron energy equations which are coupled through a collision term [24]:

ion energy equation:

$$\rho \left[\frac{\partial e_i}{\partial t} + \bar{v} \cdot \nabla e_i \right] = -p_i \nabla \cdot \bar{v} + \nabla \cdot (\kappa_{T_i} \nabla T) + \Phi_{ie}, \quad (31)$$

electron energy equation:

$$\rho \left[\frac{\partial e_e}{\partial t} + \bar{v} \cdot \nabla e_e \right] = -p_e \nabla \cdot \bar{v} + \bar{J} \cdot \bar{E} + \nabla \cdot (\kappa_{T_e} \nabla T_e) + \Phi_{ei}, \quad (32)$$

where $\Phi_{ie} = -\Phi_{ei}$ = the electron-ion coupling term:

$$\frac{\rho}{dt} \frac{(T_e - T_i)}{\frac{1}{c_{v_i}} \left(1 + \frac{1}{dt v_{ei}} \right) + \frac{1}{c_{v_e}}} \quad (33)$$

The subscripts on the thermodynamic variables refer to the fluid species of electron or ion. The parameter $c_{v_{i,e}}$ is the specific heat for each species, while v_{ei} is the electron-ion energy transfer collision frequency and dt is the computational timestep.

As mentioned, tabular values of pressure, energy, electrical resistivities, and thermal conductivities are available in MACH2. These values are obtained from the standardized, computer based SESAME Equation of State Library generated and maintained by the T-4 Group of the Theoretical Division at Los Alamos National Laboratory [25]. The library contains data for over 70 materials and covers a wide range of physical conditions in which a

local thermodynamic treatment of the fluid is appropriate, utilizing both physical models and experimental data. Also contained in this library are values of fractional ionization, Plankian mean opacities and Rosseland mean opacities.

A numerical treatment of the MHD fluid equations involves the conversion of a set of continuous coupled partial differential equations into a discrete system of algebraic "difference" equations defined on a finite grid. In MACH2 finite difference forms of the fluid equations are solved on 2 dimensional grids, simulating problems having either plane parallel geometry or a cylindrical geometry with azimuthal symmetry. A physical problem can be decomposed into one or a number of computational grids, called blocks. In the latter case, these blocks have the ability to communicate with each other. Each computational grid is comprised of zones, or cells, with each mesh point of the grid defining a spatial location. In cartesian coordinates, the grid covers a subset of the x-y plane, while in cylindrical coordinates, it covers a subset of the r-z plane. All dependent variables in the fluid equations are described positionally on the grid, and their evolution is connected to variable conditions in adjacent cells. In general, physical quantities are considered as being located at either cell centers or cell vertices (mesh points). Figure 3.1 displays the spatial centering of various physical quantities in MACH2. For numerical purposes, it is customary to index grid vertices and cells. Figure 3.2 displays the grid indexing notation used in MACH2 for an arbitrary mesh. To account for boundary conditions and communication between blocks, the calculational mesh is surrounded by a band of ghost cells and vertices.

As noted, out of plane symmetry is assumed in MACH2 calculations. However, all components of vectors and tensors are included in the calculations and are permitted to evolve as functions of two spatial coordinates. This has an advantage over strictly two dimensional codes in which vector and tensor

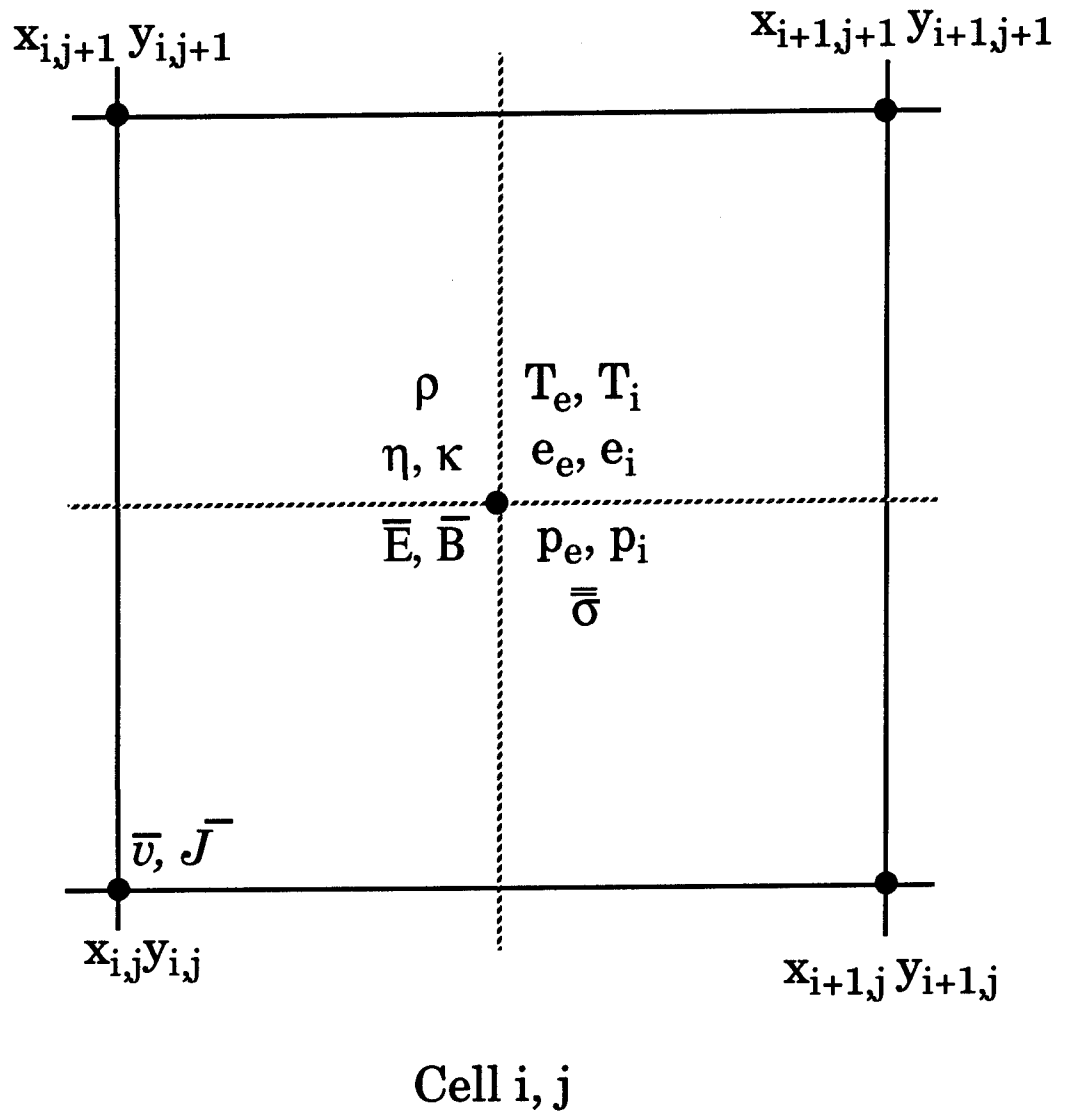


Figure 3.1. Centering of the fluid variables in MACH2. In general, the grid lines need not be parallel to the coordinate directions, and the cell need not be orthogonal.

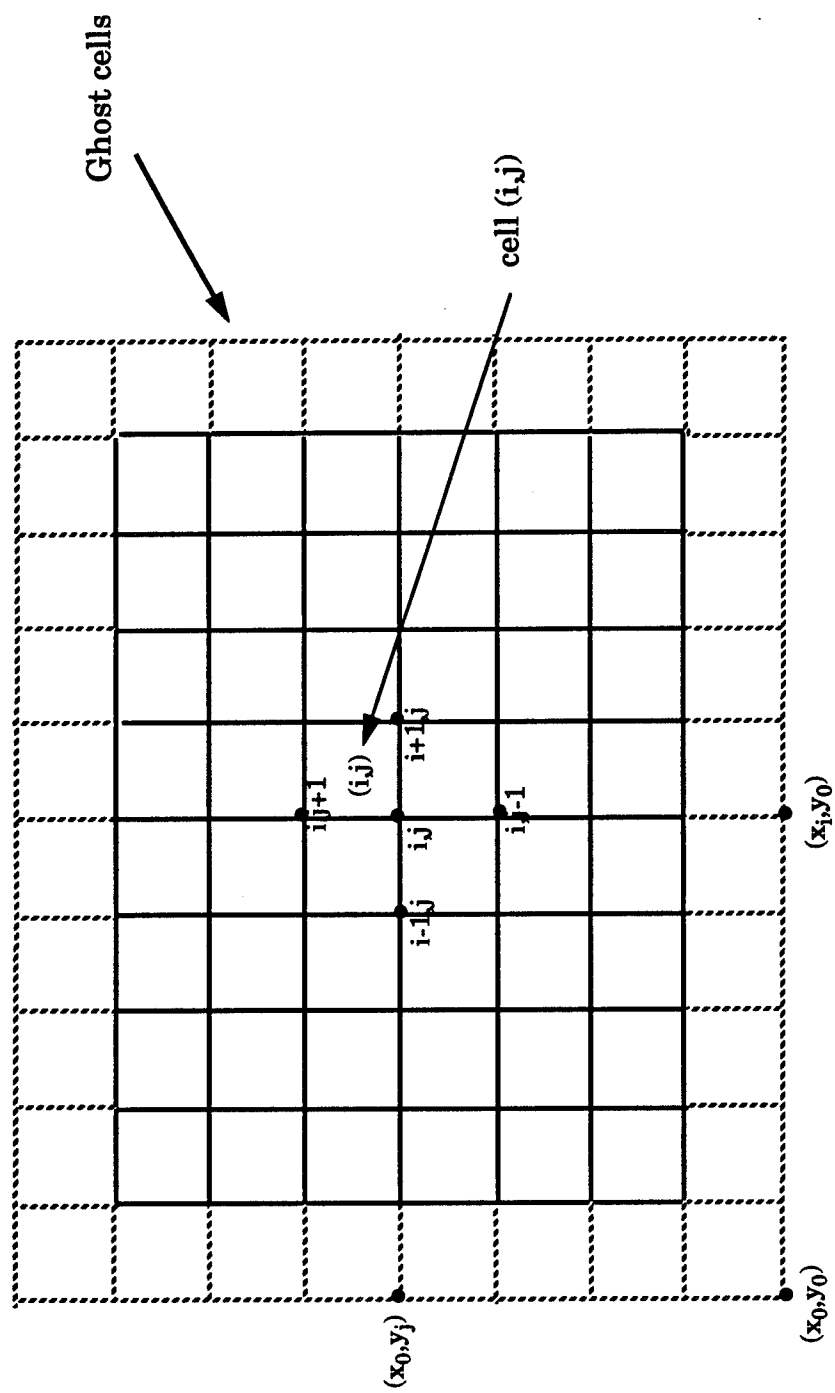


Figure 3.2. Spatial positions of arbitrary points on the MACH2 computational domain.

variables are restricted to components in the two spatial coordinates that span the problem domain. Not only does it permit a more realistic calculation of field component evolution, but it is also essential for the proper treatment of many possible wave modes in MHD [3]. Maintaining all components of vectors in code calculations is often referred to as 2-1/2 dimensional MHD dynamics.

As with all codes that use grids to perform spatial computations, the grid motion in MACH2 plays an important role in the numerical efficiency of the simulation. The ALE aspect of the code is an improvement over purely Eulerian or purely Lagrangian codes. With ALE, the computational grid has the ability to remain stationary or to move in either a Lagrangian or a user-defined fashion with respect to the fluid. Together with the adaptive capability of the mesh, one has a very powerful numerical tool; the user can dictate the mode of calculation for a given problem to avoid the adverse aspects which can arise in either a purely Lagrangian (coordinate distortion) or purely Eulerian (numerical diffusion) calculation while also obtaining higher resolution in regions of physical interest.

In MACH2, during each computational cycle, each vertex of the computational grid may be chosen to remain fixed in the laboratory frame (Eulerian) or be moved with the fluid by a distance defined by the fluid velocity at that vertex, $v_f \Delta t$. An "ideal" mesh may then be constructed which is a smoothed, orthogonalized, and variable-dependent concentrated version of the updated grid. The purpose of the ideal mesh is to minimize strong variations in cell size and area, and to lessen the degree of non-orthogonality in cell internal angles. It also allows for concentration of cells in regions of interest, i.e., where physical variables have the higher density. (Parameters to control the numerically generated grid are specified.) The computational grid is relaxed toward the ideal grid by an amount specified by the user. In general, the new

computational mesh is thus an arbitrarily moving grid which dynamically adapts to the simulation.

Numerically, the dynamic fluid equations are solved in a self-consistent manner using an operator split, or time splitting, approach to advance the equations in time and a finite volume differencing method to perform spatial differencing of operators. A time splitting scheme partitions each of the evolution equations into segments, each segment describing the evolution of a quantity based on a specific physical process. For a given process, all segmented equations pertaining to that process are evaluated and the evolving variables updated. All updated values are then used to solve successive portions of the evolution equations pertaining to additional physics.

The non-radiative physical processes which are timesplit in MACH2 are electron-ion coupling, $\propto \nu_{ei}(T_e - T_i)$, thermal diffusion, $\nabla \cdot \kappa \nabla T$, magnetic resistive diffusion $\nabla \times (\eta/\mu_0 \cdot \nabla \times \mathbf{B})$, the hall effect $\nabla \times (1/(q_e n_e) \bar{\mathbf{J}} \times \bar{\mathbf{B}})$, Lagrangian hydrodynamics, $\nabla \cdot \bar{\mathbf{v}}$, $\nabla \cdot \bar{\mathbf{S}}$, $\nabla \times (\bar{\mathbf{v}} \times \bar{\mathbf{B}})$, and coordinate system motion/convective transport, $\bar{\mathbf{v}} \cdot \nabla$. Here $\bar{\mathbf{S}}$ is the stress tensor whose form is given in [22]. These are performed in the order given, updating the internal energy each step. A flow chart depicting the order in which these processes are calculated along with the graphics and data output are shown in Figure 3.3. The convective transport of all dynamic variables is accomplished by using an explicitly time differenced, second order Van Leer advection scheme [26]. For the case of magnetic field transport, a generalized form of the constrained transport algorithm of Evans and Hawley [28] has also been implemented to insure flux conservation. The thermal and resistive diffusion along with the Lagrangian hydrodynamics are implicitly time differenced. This guarantees the stability of solutions. Although many two dimensional codes perform implicit diffusion, few calculate the hydrodynamic portions of the fluid equa-

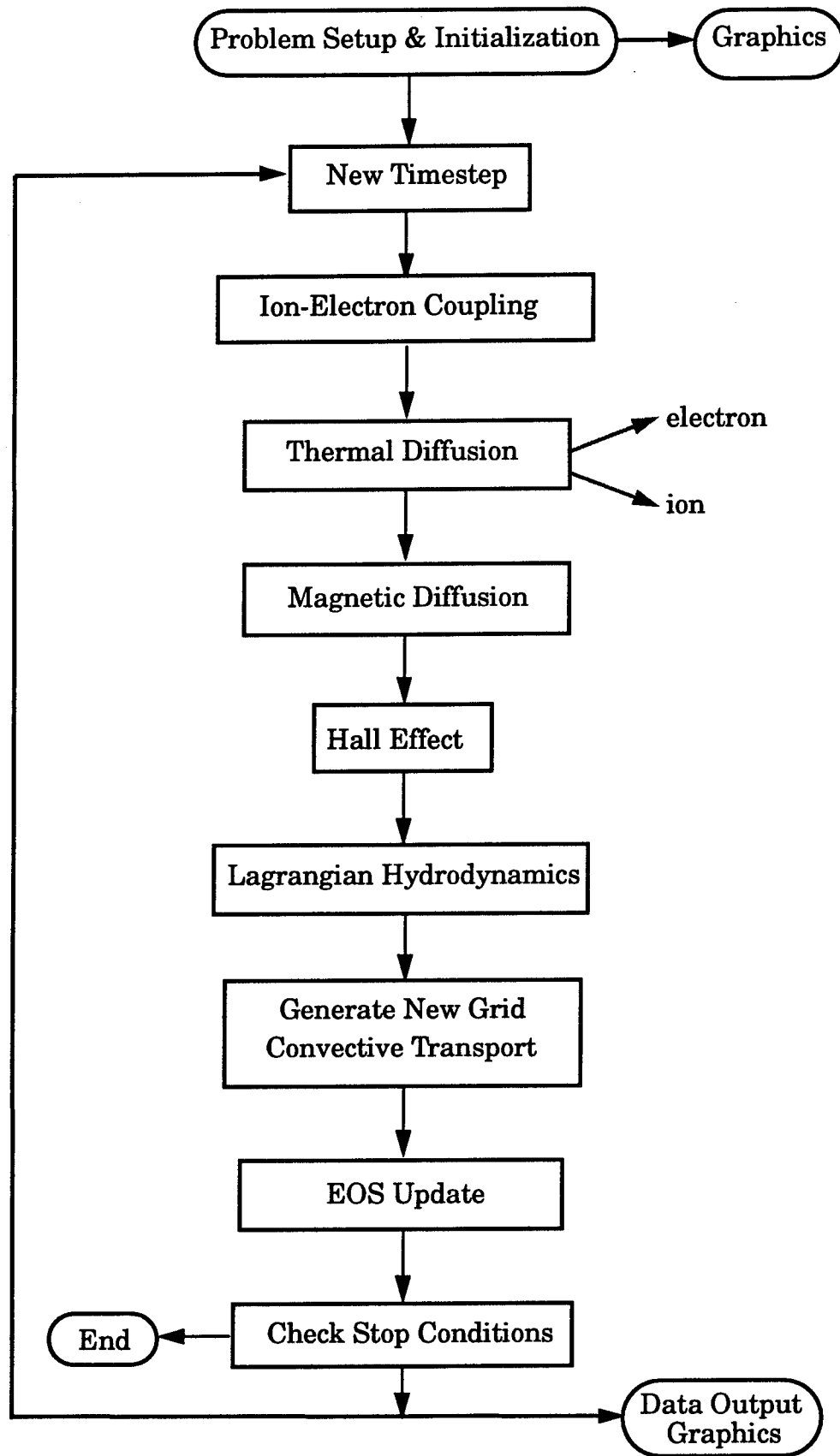


Figure 3.3. Technical schematic of the physical processes calculated in MACH2.

tions implicitly. This can be invaluable under conditions in which the fluid flow is such that unacceptably small values for the computational timestep would be necessary for an explicit calculation.

The diffusion of the magnetic field and that of the material temperature employ essentially the same numerical techniques. In general, a multigrid technique with a relaxation algorithm are together applied to iteratively converge on the solution to the specific diffusion equation [22]. The magnetic field is diffused into the plasma using either analytic models for resistivity, i.e., classical Spitzer (charged particle-particle interaction), or tabular values obtained from the SESAME tables. MACH2 also provides both analytic models and tabular values for microturbulent resistivity (wave-plasma interaction) [29]. A similar approach is taken with the thermal conduction; thermal conductivities are calculated either analytically from a Spitzer model or extracted from a table.

The spatial derivatives that result from the gradient, divergence, and curl operators in the conservation equations for the fluid are treated in MACH2 with the finite volume method. The finite volume differencing scheme in MACH2 utilizes Stoke's theorem to transform volume integrated quantities involving difference operators of physical variables (e.g., divergence) to a difference-free algebraic form involving only the physical variable, cell areas and cell volumes. Like most differencing schemes, the finite volume differencing maps one class of centered quantities into another class of centered quantities, i.e., vertex-centered quantities into cell-centered quantities and vis versa. This centered differencing is desirable since it maintains a physical interpretation of spatial derivatives and also is second order accurate in truncation error. To illustrate the finite volume difference method, the finite difference form for the thermal electron flux $\kappa \nabla T_e$ will be developed. Applying Stokes

theorem to the integrated flux over a volume element:

$$\int_R \kappa \nabla T_e dV = \int_{\partial R} \kappa T_e \hat{n} dA .$$

Here R is the volume over which the flux is calculated, ∂R is the surface area which bounds this volume, and \hat{n} is the unit normal to the surface pointing in an outwardly direction. Taking as our volume of interest the three dimensional cell which is constructed by extending a grid cell an incremental distance out of the grid plane, and assuming that $\kappa \nabla T_e$ and $\kappa T_e \hat{n}$ are uniform over the cell volume and the cell faces, respectively, then

$$(\kappa \nabla T_e)_{ij} dV_{ij} = \sum_{faces} (\kappa T_e \hat{n})_{ij} dA_{ij}$$

or

$$(\kappa \nabla T_e)_{ij} = \frac{1}{dV_{ij}} \sum_{faces} (\kappa T_e \hat{n})_{ij} dA_{ij} ,$$

where the subscripts i,j refer to any arbitrary cell. This is the finite difference form for the thermal flux. Clearly, this scheme invokes writing the difference form of the spatial operators as conservation laws, exactly conserving (at least to roundoff error) the quantities which are based on spatially dependent processes. As a result, this scheme is superior to standard finite difference schemes when the grid deviates from a strictly orthogonal, smooth grid.

3.2 Adding the Radiation Energy Equation to MACH2

Recall the nonequilibrium radiation energy diffusion equation:

$$\rho \left[\frac{d}{dt} \left(\frac{E_o}{\rho} \right) + \frac{1}{3} E_o \frac{d}{dt} \left(\frac{1}{\rho} \right) \right] = \nabla \cdot \left(\frac{c}{3\chi_R} \nabla E_o \right) + c\kappa_P (a_R T_e^4 - E_o) \quad (16)$$

This can be rewritten in a slightly different form to more closely resemble the specific internal energy equation of MACH2. Expanding the first expression in the equation and rewriting the second expression using a variation of the continuity equation, $d/dt(1/\rho) = 1/\rho \nabla \cdot \bar{v}$, the left hand side becomes

$$\begin{aligned} \rho \frac{d}{dt} \left(\frac{E_o}{\rho} \right) + \frac{\rho}{3} E_o \frac{d}{dt} \left(\frac{1}{\rho} \right) &= \frac{d}{dt} (E_o) - \frac{E_o}{\rho} \frac{d\rho}{dt} + \frac{1}{3} E_o (\nabla \cdot \bar{v}) \\ &= \frac{d}{dt} (E_o) + E_o (\nabla \cdot \bar{v}) + \frac{1}{3} E_o (\nabla \cdot \bar{v}) . \end{aligned}$$

Here the contributions attributed to material compression or expansion, $E_o (\nabla \cdot \bar{v})$, are written as two separate quantities. The first term denotes the change in radiation energy density by a finite change in material volume while the second term corresponds to the work done by the radiation field on the material through radiation pressure [30]. Parameterizing the radiation energy density in terms of a radiation temperature T_R so that $E_o = a_R T_R^4$, the radiation energy equation can be written as

$$\begin{aligned} \frac{d}{dt} (a_R T_R^4) + \left(1 + \frac{1}{3}\right) (a_R T_R^4) (\nabla \cdot \bar{v}) \\ = \nabla \cdot \frac{c}{3\chi_R} \nabla (a_R T_R^4) + a_R c \kappa_P (T_e^4 - T_R^4) \end{aligned}$$

or

$$\begin{aligned} \frac{\partial}{\partial t} (a_R T_R^4) &= -\bar{v} \cdot \nabla (a_R T_R^4) - \left(1 + \frac{1}{3}\right) (a_R T_R^4) \nabla \cdot \bar{v} \\ &\quad + \nabla \cdot \frac{c}{3\chi_R} \nabla (a_R T_R^4) + a_R c \kappa_P (T_e^4 - T_R^4) . \quad (34) \end{aligned}$$

This form is very similar to that of the material internal energy Equation (32). The first and third terms on the right hand side characterize the convective transport of radiation and the radiation diffusion through the medium, respectively. These terms, along with the radiation pressure volume work, are the radiation counterparts to the convection, diffusion, and $p dv$ terms found in the electron energy equation. The last expression in Equation (34) describes the exchange of energy between the free electron population and the radiation field.

From the discussions in Sections 2.3 and 2.4, the presence of the radiation field in an opaque medium will lead to additional expressions in the fluid equations. Specifically, the electron energy and momentum equations must be modified to include the contribution from the radiation field. In MACH2, these existing equations are altered accordingly:

electron energy equation:

$$\rho \left[\frac{\partial e_e}{\partial t} + \bar{v} \cdot \nabla e_e \right] = -p_e \nabla \cdot \bar{v} + \bar{J} \cdot \bar{E} + \nabla \cdot (\kappa_{T_e} \nabla T_e) + \Phi_{ei} \quad (32)$$

momentum equation:

$$\rho \left[\frac{\partial \bar{v}}{\partial t} + \bar{v} \cdot \nabla \bar{v} \right] = -\nabla p + \bar{J} \times \bar{B} + \nabla \cdot \bar{\sigma} \quad (23)$$

must be modified to:

electron energy equation:

$$\rho \left[\frac{\partial e_e}{\partial t} + \bar{v} \cdot \nabla e_e \right] = -p_e \nabla \cdot \bar{v} + \bar{J} \cdot \bar{E} + \nabla \cdot (\kappa_{T_e} \nabla T_e) + \Phi_{ei} - a_R c \kappa_P (T_e^4 - T_R^4) \quad (35)$$

momentum equation:

$$\rho \left[\frac{\partial \bar{v}}{\partial t} + \bar{v} \cdot \nabla \bar{v} \right] = -\nabla \left(p + \frac{1}{3} a_R T_R^4 \right) + \bar{J} \times \bar{B} + \nabla \cdot \bar{\sigma} \quad (36)$$

Here the added pressure term in the momentum equation is often referred to as the radiation acceleration [14].

With Equations (34), (35), and (36), the three temperature radiation diffusion treatment can be implemented into MACH2. It is important to remember, however, that this treatment is inappropriate when the diffusion criteria are no longer met. This can lead to excessive radiation energy transport and unphysical radiation pressure effects in regions that are optically thin. To correct this first problem, a flux-limited form of the diffusion equation is needed. As discussed in Section 2.4, the purpose of a flux-limited diffusion equation is to provide the proper behavior of the radiation field in the optically thin limit, where the diffusion approximation is not valid. If formulated properly, it can also enable a qualitative transition from a thick to thin regime.

The flux-limited version of the diffusion equation that is developed here involves the modification of the diffusion coefficient $c/(3\chi_R)$ in the following manner:

$$\kappa_{rad} = \frac{c}{3\chi_R\rho + \frac{|\nabla E|}{E} + \frac{1}{\Delta l}} \quad (37)$$

(Tabular values of opacity in MACH2 are in units that require multiplication by ρ to give the correct dimensions of 1/length.) This gives the proper values of the radiation flux in both thick and thin limits, and permits a smooth transition between these limits when necessary. The addition of the term $|\nabla E|/E$ to $3\chi_R\rho$ enables the radiation energy equation to restrict the speed at which photons can diffuse through a transparent region to the speed of light. When the material is thin, the photon mean free path becomes very large and $3\chi_R\rho$ is negligible in comparison to $|\nabla E|/E$. The flux then becomes proportional to cE . To insure this result is maintained under conditions in which there is

essentially no gradient in the radiation field, but the radiation is still free streaming, the $1/(\Delta l)$ term was included in the denominator of κ_{rad} . This term allows the user to define a length over which a photon can diffuse no faster than the speed of light, such as a computational cell or a fluid characteristic dimension [31]. Its introduction into the flux-limited form of the diffusion coefficient can be considered as a ceiling for the diffusion coefficient in much the same manner as the user defined vacuum magnetic resistivity value in MACH2 [22].

With $1/(\Delta l)$ in the diffusion coefficient, the $|\nabla E|/E$ term can actually be removed, since numerically $1/(\Delta l)$ additionally flux limits the physical regime represented by $|\nabla E|/E$. For the calculations presented in this work, this term is preserved along with $1/(\Delta l)$. This is due partly to that fact that $|\nabla E|/E$ has a physical meaning which is associated with the system that is being modelled. At most, an error of a factor of 2 could result in the value of the radiation diffusion coefficient (when the two terms are of the same magnitude) if both terms are retained and $1/(\Delta l)$ is defined appropriately.

As a fluid transitions from an optically thick to optically thin regime, the radiation field and the material become increasingly decoupled. In the extreme thin case, the radiation field ceases to influence the dynamics of the fluid. To accurately depict this diminishing interaction of the radiation field and fluid, any terms which relate the radiation field and material must vanish in this limit. In particular, the radiation acceleration of the fluid should no longer be a viable force in the momentum equation. As written in Equation (36), this term is present under all physical conditions and results in an artificial radiation pressure contribution as the thin fluid regime is approached. This physical discrepancy can be removed by introducing a multiplicative fac-

tor [14] given by

$$\frac{1}{1 + (\lambda_p/d)} \quad (38)$$

to the radiation acceleration term in the momentum equation. Here λ_p , the photon mean free path, is defined as $1/(\chi_R \rho)$ and d is a user defined distance outside of which the photons are considered to be free streaming. As λ_p becomes larger and eventually overtakes the value of d , the above multiplier decreases until it approximates zero. This allows for a smooth reduction in the radiation acceleration force as the thin limit is approached. The revised momentum equation thus takes the following form:

$$\rho \left[\frac{\partial \bar{v}}{\partial t} + \bar{v} \cdot \nabla \bar{v} \right] = -\nabla \left(p + \frac{1}{3} \left(\frac{1}{1 + (\lambda_p/d)} \right) a_R T_R^4 \right) + \bar{J} \times \bar{B} + \nabla \cdot \bar{\sigma} . \quad (39)$$

To maintain consistency among the evolution equations and conserve energy, the radiation pressure contribution in the radiation energy equation must also contain the multiplier of Equation (38). With this pressure term multiplier and the flux-limited form of the diffusion coefficient, the radiation energy equation is written finally as:

$$\begin{aligned} \frac{\partial}{\partial t} (a_R T_R^4) = & -\bar{v} \cdot \nabla (a_R T_R^4) - \left(1 + \frac{1}{3} \left(\frac{1}{1 + (\lambda_p/d)} \right) \right) (a_R T_R^4) \nabla \cdot \bar{v} \\ & + \nabla \cdot \kappa_{rad} \nabla (a_R T_R^4) + a_R c \kappa_P \rho (T^4 - T_R^4) . \end{aligned} \quad (40)$$

This is the equation that is implemented into the MACH2 code along with the additional terms in the electron energy and momentum equations found in Equations (35) and (39).

3.3 Finite Difference Formulation of the Radiation Energy Equation

Similar to the electron and ion evolution equations, the radiation energy equation contains the physical processes of diffusion, convection and pressure-volume work. Thus, its implementation into the MACH2 code comprises the modification of the existing algorithms for diffusion, convection, and hydrodynamics, along with additional subroutines required to treat certain aspects of the radiation field and the electron-radiation coupling. The radiation energy equation is solved simultaneously with the other MHD fluid equations of MACH2 in an operator split fashion. The following radiation processes are operator split: the electron-radiation coupling, the radiation diffusion, the radiation hydrodynamics, and the convective transport of the radiation field. The implementation of these radiation processes in the overall structure and ordering of the MACH2 code is displayed schematically in Figure 3.4.

The electron-radiation coupling is solved implicitly in time [32,33] and has the following difference form:

$$E_{i,j}^{n+1} = \frac{1}{1 + (k_{eff})_{i,j}^n} \left[E_{i,j}^n + (k_{eff})_{i,j}^n a_R (T_e)_{i,j}^n \right], \quad (41)$$

$$e_{i,j}^{n+1} = e_{i,j}^n - (k_{eff})_{i,j}^n (a_R (T_e)_{i,j}^n - E_{i,j}^{n+1}) / \rho_{i,j}^n, \quad (42)$$

where

$$(k_{eff})_{i,j}^n = \frac{(\kappa_P)_{i,j}^n \rho_{i,j}^n c \Delta t}{1 + \frac{4a_R (\kappa_P)_{i,j}^n c}{(c_v)_{i,j}^n} (T_e^3)_{i,j}^n \Delta t}, \quad (43)$$

with $E = a_R T_R^4$, the radiation energy density, and e , the electron specific internal energy. Here the subscripts i and j have their usual meaning of cell

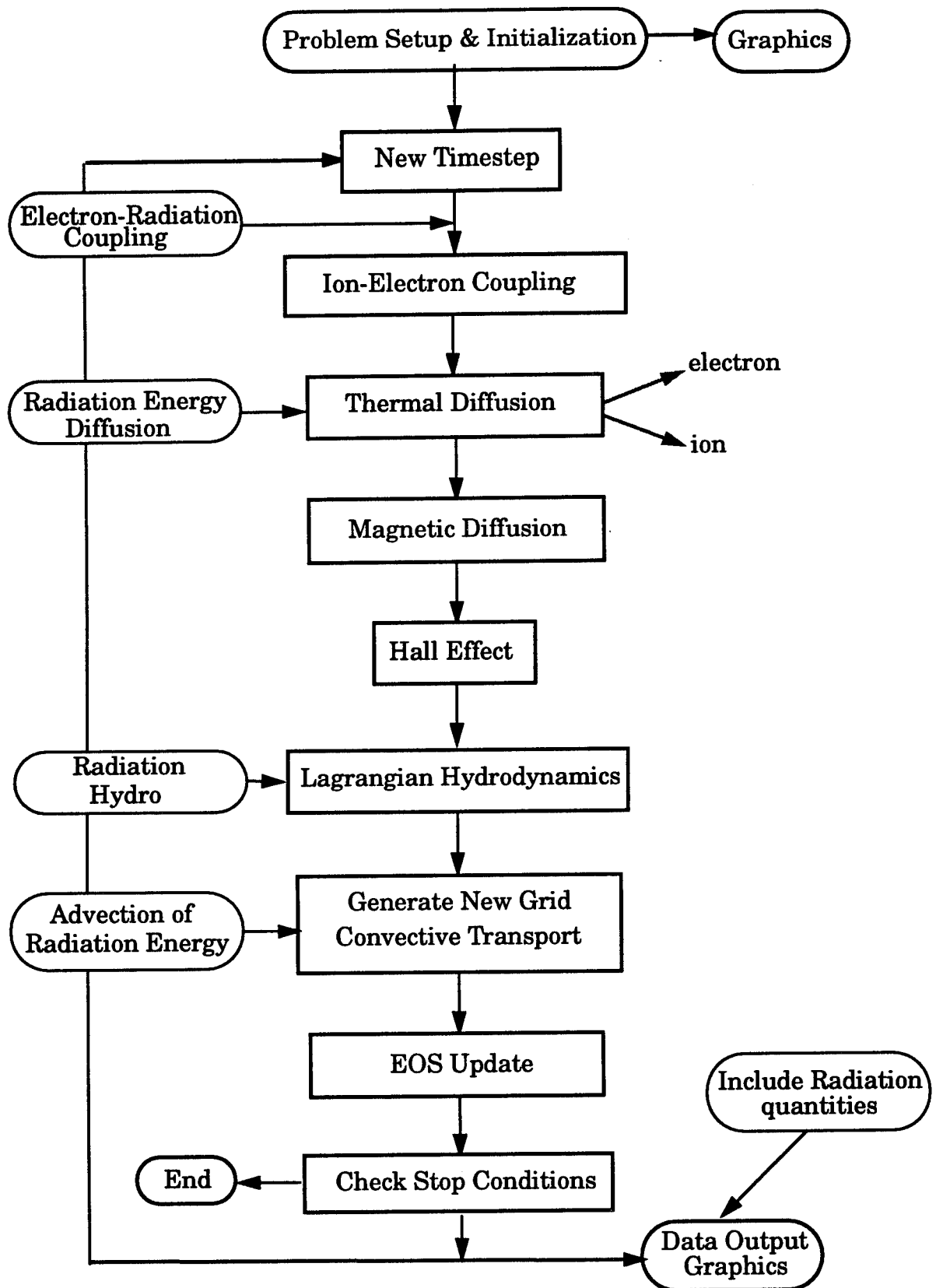


Figure 3.4. Technical schematic of the physical processes calculated in MACH2 with the changes required to add the nonequilibrium radiation diffusion treatment.

indexing and the superscript n is related to the last updated quantity during a problem timestep, Δt . The centering of variables is as discussed in Section 3.1 with the vertex i,j always to the lower left of the cell i,j . The above finite difference form is obtained by writing out the material coupling term

$$\rho c_v \frac{\partial T_e}{\partial t} = -\kappa_p \rho c (a_R T_e^4 - E)$$

implicitly:

$$\rho c_v \frac{(T_e^{n+1} - T_e^n)}{\Delta t} = -\kappa_p \rho c (a_R (T_e^4)^{n+1} - E^{n+1}) .$$

Expanding $(T_e^4)^{n+1}$ on the right hand side of this equation about $(T_e^4)^n$ in a Taylor series expansion and keeping only first order terms,

$$\rho c_v \frac{\partial T_e}{\partial t} = -\kappa_p \rho c \left(a_R (T_e^4)^n + a_R \Delta t \left(\frac{\partial T_e^4}{\partial t} \right) - E^{n+1} \right) .$$

With

$$\left(\frac{\partial T_e^4}{\partial t} \right) \equiv 4 (T_e^3)^n \left(\frac{\partial T_e}{\partial t} \right) ,$$

the above equation becomes

$$\left[1 + \frac{4 a_R \kappa_p c}{c_v} (T_e^3)^n \Delta t \right] \rho c_v \frac{\partial T_e}{\partial t} = -\kappa_p \rho c (a_R (T_e^4)^n - E^{n+1}) .$$

Rearranging and defining k_{eff} as in Equation (43), Equation (42) is obtained.

Using the relationship

$$-\rho c_v \frac{\partial T_e}{\partial t} = \frac{\partial E}{\partial t} = \kappa_p \rho c (a_R T_e^4 - E) ,$$

leads to Equation (41) [14].

The diffusion of the radiation energy density is part of the thermal diffusion routines and follows the calculations of electron and ion thermal diffusion. In a

conserved integral form, the radiation diffusion equation is given by

$$\frac{\partial}{\partial t} \int E dV = \int \nabla \cdot (\kappa \nabla E) dV = \int (\kappa \nabla E) \cdot d\bar{A} .$$

The finite volume difference representation of this equation for a rectangular uniform grid in planar geometry, using the MACH2 definition of area normals [34], and fully implicit in time is given by:

$$\begin{aligned} \frac{E_{i,j}^{n+1} - E_{i,j}^n}{\Delta t} (\Delta x \Delta y \Delta z) = & \left[(\kappa \nabla_y E)_{i,j+1}^{v,n+1} + (\kappa \nabla_y E)_{i+1,j+1}^{v,n+1} \right. \\ & \left. - (\kappa \nabla_y E)_{i+1,j}^{v,n+1} - (\kappa \nabla_y E)_{i,j}^{v,n+1} \right] \frac{1}{2} \Delta x \Delta z \\ & + \left[-(\kappa \nabla_x E)_{i,j+1}^{v,n+1} + (\kappa \nabla_x E)_{i+1,j+1}^{v,n+1} \right. \\ & \left. + (\kappa \nabla_x E)_{i+1,j}^{v,n+1} - (\kappa \nabla_x E)_{i,j}^{v,n+1} \right] \frac{1}{2} \Delta y \Delta z . \end{aligned} \quad (44)$$

The quantities $(\kappa \nabla E)_{i,j}^v$ correspond to the vertex-centered radiative fluxes, and Δx , Δy , and Δz refer to the cell dimensions (Δz extends normal to the computational plane and is taken to be 1 in cartesian geometry.) The finite volume form of the vertex-centered flux is given by

$$(\kappa \nabla_y E)_{i,j}^v = \frac{(\kappa^v)_{i,j}}{\Delta x \Delta y \Delta z} [E_{i-1,j} + E_{i,j} - E_{i,j-1} - E_{i-1,j-1}] \frac{1}{2} \Delta x \Delta z , \quad (45)$$

$$(\kappa \nabla_x E)_{i,j}^v = \frac{(\kappa^v)_{i,j}}{\Delta x \Delta y \Delta z} [-E_{i-1,j} + E_{i,j} + E_{i,j-1} - E_{i-1,j-1}] \frac{1}{2} \Delta y \Delta z . \quad (46)$$

These expressions reduce to the standard finite difference forms for a variety of conditions. Here κ^v is the vertex averaged value of the flux-limited radiation diffusion coefficient determined by averaging the cell-centered radiative conductivity over the four cells adjacent to the vertex denoted by i,j . Positive

values for the radiative fluxes indicate downward flow for the y-component of flux and flow to the left for the x-component. This convention appropriately defines the energy being added to a cell (fluxes are defined at vertices) as a positive value and energy being removed from a cell as a negative value. The indexing notation and directions of positive flow as defined in the MACH2 code are indicated in Figure 3.5.

The finite volume difference form of the diffusion equation as defined by Equations (44), (45), and (46) can be shown to simplify to a finite difference form under certain conditions. Writing Equation (44) in terms of the cell-centered radiation energy densities and assuming a constant κ :

$$\begin{aligned} \frac{E_{i,j}^{n+1} - E_{i,j}^n}{\Delta t} = & \frac{\kappa^v}{4(\Delta y)^2} \left[E_{i-1,j+1}^{n+1} + 2E_{i,j+1}^{n+1} - 4E_{i,j}^{n+1} - 2E_{i-1,j}^{n+1} + E_{i+1,j+1}^{n+1} \right. \\ & \left. - 2E_{i+1,j}^{n+1} + E_{i+1,j-1}^{n+1} + 2E_{i,j-1}^{n+1} + E_{i-1,j-1}^{n+1} \right] \\ & + \frac{\kappa^v}{4(\Delta x)^2} \left[E_{i-1,j+1}^{n+1} - 2E_{i,j+1}^{n+1} - 4E_{i,j}^{n+1} + 2E_{i-1,j}^{n+1} + E_{i+1,j+1}^{n+1} \right. \\ & \left. + 2E_{i+1,j}^{n+1} + E_{i+1,j-1}^{n+1} - 2E_{i,j-1}^{n+1} + E_{i-1,j-1}^{n+1} \right] \quad (47) \end{aligned}$$

For uniform flow in the y-direction, i.e.,

$$E_{i-1,j} = E_{i,j} = E_{i+1,j}, \quad j = j-1, j, j+1$$

the expression in (47) reduces to the familiar finite difference form [32]

$$\frac{E_{i,j}^{n+1} - E_{i,j}^n}{\Delta t} = \frac{\kappa^v}{(\Delta y)^2} [E_{i,j+1}^{n+1} - 2E_{i,j}^{n+1} + E_{i,j-1}^{n+1}] \quad (48)$$

As seen from Equation (47), the diffusion of the radiation energy density in implicit form describes a set of equations written in terms of unknown quantities E^{n+1} and known quantities E^n and boundary conditions. In MACH2, the

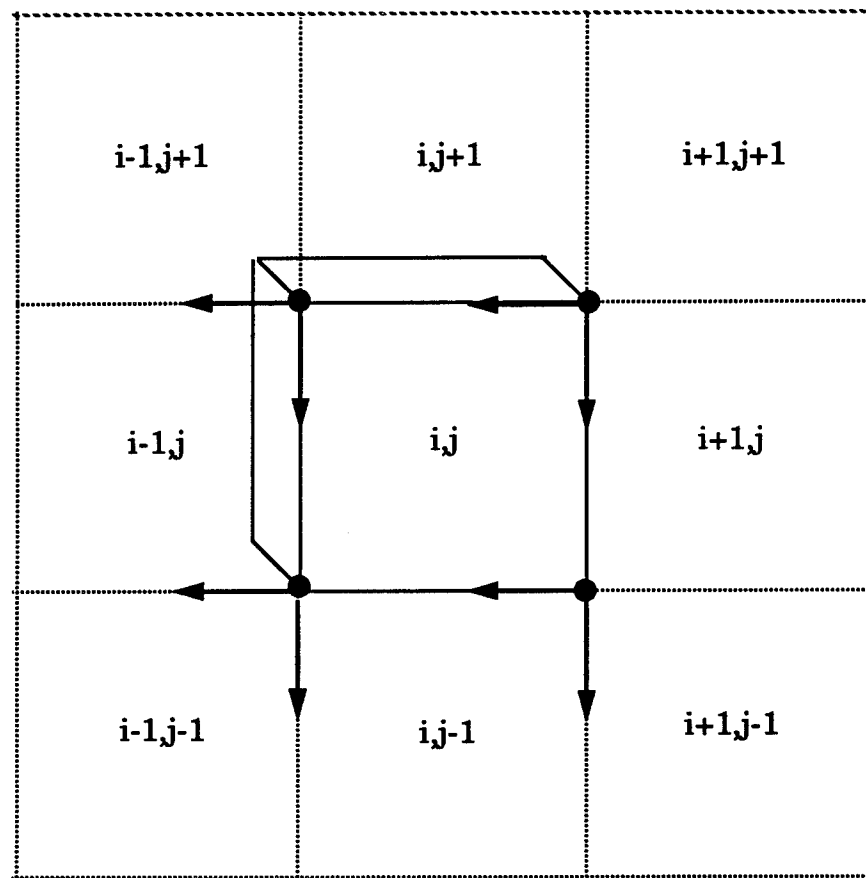


Figure 3.5. MACH2 notation used in the finite volume differencing of the various fluid equations. The indexing corresponds to the cell-centered values, while the arrows indicate the directions of positive flow for vertex-centered fluxes.

solution to this set of equations is carried out using a Jacobi iteration scheme. The efficiency of the iteration algorithm is improved by adding a relaxation capability to decrease the number of iterations needed to reach convergence, and making available a multigrid method to accelerate the convergence [22]. For uniform flow in the y-direction, the Jacobi formula with a relaxation capability can be written as:

$$E_{i,j}^{m+1} = E_{i,j}^m + \frac{\gamma}{a_{jj}} \left[E_{i,j}^n - \sum_{k=1}^N a_{jk} E_{i,k}^m \right] \quad (49)$$

The variable m denotes the m th iteration, while N is the number of mesh points along the y axis and a_{jk} is the value of the coefficients in front of the E^{n+1} terms. The expression in brackets is commonly referred to as the residual and indicates the error in the estimated (iterated) solution to the exact solution [35]. The multiplier γ , which is the relaxation contribution to the expression, is called the relaxation parameter and is restricted to the range $0 < \gamma < 2$ [36]. When $0 < \gamma < 1$ the iteration scheme is said to be under-relaxed, while for $1 < \gamma < 2$, it is considered to be over-relaxed. Under-relaxation can be used to obtain convergence in cases that are not convergent by Jacobi iteration alone. Over-relaxation (SOR- Successive Over-Relaxation) is typically used to accelerate the convergence of problems which already converge by Jacobi iteration [37]. In general, iteration techniques with a relaxation multiplier are called relaxation methods.

For the above iteration scheme, the values of the radiation energy density at the last timestep are used as initial "guesses" (i.e., the zeroth iteration values) in the Jacobi formula and a user specified relaxation parameter is employed to over-relax or under-relax the residual. With each iteration, a convergence test is applied to the residual. Until the convergence criterion is met, a corrective term is added to the last iterative approximation to the solu-

tion. This results in a sequence of approximate solutions which converge to within a specified value to the exact solution.

Typically, the Jacobi iteration scheme is slow to converge and requires a large number of iterations. This can be numerically explained by representing the residual, or error, between the approximate solution and the exact solution by a Fourier series consisting of a superposition of modes of varying wavelengths. Numerical experiments demonstrate that for such a representation, standard relaxation schemes such as Jacobi/SOR remove (or smooth) the high frequency components of the residual rapidly, while reducing the low frequency components at a much slower rate [38]. This results in an overall slow convergence rate.

To improve the rate at which low frequency components are eliminated from the residual, acceleration techniques are commonly applied to standard iteration algorithms [36]. In MACH2, a Full Approximation Storage (FAS) multigrid technique [39] can be used in conjunction with the Jacobi/relaxation scheme to speed up convergence [22]. In general, multigrid methods are based on the observation that low frequency components of the error defined on any given grid become high frequency components on a coarser grid. By going to a coarser grid, these original low frequency components can be removed using standard iterative schemes.

In the FAS "v-cycle" method [36], an approximate solution and residual are initially defined on the finest grid. A designated number of iterations are performed on this grid, quickly smoothing the high frequency components of the residual and approximation. These updated values are computed via a restriction operator onto the first coarser grid level. The iterative procedure, or relaxation, is again carried out at this level, essentially removing the high frequency components of both the approximate solution and the residual.

These new quantities are subsequently determined on the next coarser grid. This process of relaxation and restriction is continued until the coarsest grid is reached. At the coarsest grid level, the approximate solution is solved to the degree specified by the convergence criteria. This solution is then interpolated, or prolonged, onto the next grid level where it undergoes the designated number of relaxations steps. In this manner, a cycle of prolongation and relaxation is repeated until the finest grid is reached and a final solution is obtained.

MACH2 provides the option to accelerate convergence using the FAS multi-grid method in either a “v-cycle” mode as described above or a “converge” mode [22]. With the “converge” mode, the movement from one grid level to another is based on the convergence criteria. At a given grid level, the convergence test is applied to the residual. If the convergence criteria is not met, the code moves to the next coarser grid, and the Jacobi/relaxation algorithm is applied at that level. If the criteria is met, the code proceeds to the next finer level.

Following the diffusion of the radiation energy density and magnetic field, MACH2 calculates updated values for the fluid variables resulting from hydrodynamic processes. In this portion of the code, the velocity, density, and magnetic field are solved implicitly using a block Jacobi iteration scheme with a Newton step [34]. The radiation portion of the hydrodynamics entails adding a radiation pressure term to the electron momentum equation which solves for $\nabla \cdot \bar{v}$, and a pressure term to the radiation energy equation (refer to Section 3.2). A finite volume difference representation for the hydrodynamic portions of the fluid equations can be found in [34], and will not be written out here.

The convection of the radiation energy density is performed along with the convection of the other fluid variables and is similar in form to the finite volume difference notation found in [34]. The advection requires the calculation

of convective fluxes, which are edge-centered quantities. In general, the computation of a convective flux for a cell-centered variable requires the averaging of the cell-centered quantity to the cell edge. MACH2 incorporates two different interpolation schemes for choosing the interface value, a first order donor cell method or a second order van Leer method. A complete discussion of these two methods and results from simulations using each method separately can be found in [27].

3.4 Limits of the Nonequilibrium Diffusion Approximation and a Comparison to the Emission and Equilibrium Diffusion Models in MACH2

Ideally, the flux-limited form of the nonequilibrium radiation diffusion equation should produce the physically correct behavior under optically thin conditions when radiation is free streaming, while reducing to the equilibrium diffusion approximation when the material is opaque and the radiation field and material are in equilibrium with each other. Each of these extreme limits is provided for in the MACH2 code through an additional term in the electron energy equation.

For an optically thick fluid, the material is opaque to photons and radiant energy can be transported only through a diffusion process. Under conditions in which the radiation field and the material are in local thermal equilibrium with each other, the radiation field is Plankian at the material temperature. Radiant energy is then diffused through the fluid at a rate proportional to ∇T_e . In this limit, MACH2 incorporates an equilibrium diffusion model which modifies the electron thermal conductivity to include an additional radiation heat conduction term [22]:

$$\kappa' = \kappa_e + \frac{4a_R c T_e^3}{3\chi\rho}, \quad (50)$$

$$\rho \frac{de}{dt} = -p_e \nabla \cdot \bar{v} + \bar{J} \cdot \bar{E} + \nabla \cdot (\kappa' \nabla T_e) . \quad (51)$$

Consider the nonequilibrium radiation diffusion energy equation written in the following form:

$$\rho \frac{d}{dt} \left(\frac{a_R T_R^4}{\rho} \right) = -\frac{1}{3} (a_R T_R^4) \nabla \cdot \bar{v} + \nabla \cdot \kappa_{rad} \nabla (a_R T_R^4) + a_R c \kappa_P (T_e^4 - T_R^4) \quad (52)$$

In the limit of equilibrium diffusion, $T_R = T_e$, $\kappa_{rad} \rightarrow c/(3\chi\rho)$ and the above equation becomes

$$\rho \frac{d}{dt} \left(\frac{a_R T_e^4}{\rho} \right) = -\frac{1}{3} (a_R T_e^4) \nabla \cdot \bar{v} + \nabla \cdot \frac{4a_R T_e^3 c}{3\chi\rho} \nabla T_e \quad (53)$$

Combining this with the electron energy Equation (35),

$$\begin{aligned} \rho \left[\frac{de}{dt} + \frac{d}{dt} \left(\frac{a_R T_e^4}{\rho} \right) \right] = & - (p_e + \frac{1}{3} a_R T_e^4) (\nabla \cdot \bar{v}) + \bar{J} \cdot \bar{E} \\ & + \nabla \cdot \left(\kappa_{T_e} + \frac{4a_R T_e^3 c}{3\chi\rho} \right) \nabla T_e . \end{aligned} \quad (14)$$

This is the equilibrium diffusion equation of Section 2.2. In systems where the material energy is much larger than the radiation energy density, the rate of change in the energy density and the radiation pressure term have no effect on the energy balance or the motion of the fluid and may be neglected [18]. The equation then reduces to the equilibrium diffusion model of MACH2.

In the free streaming limit, the fluid is optically thin and the radiation field does not couple efficiently with the material. In this case, MACH2 supplies an emission model which simulates radiation cooling caused by photons of various energies leaving the local area. As a fluid radiates, it loses energy. Because the fluid is thin, this radiation can escape the system with little interaction, causing a decrease in electron specific internal energy. The emission model in MACH2 performs the equivalent of this process through an energy loss rate term, $a_R c \chi T_e^4$, in the electron energy Equation [22]. In instances where the material energy is much greater than the radiation energy, or $T_e \gg T_R$, the electron energy Equation (35) becomes:

$$\rho \left[\frac{\partial e_e}{\partial t} + \bar{v} \cdot \nabla e_e \right] = -p_e \nabla \cdot \bar{v} + \bar{J} \cdot \bar{E} + \nabla \cdot (\kappa_{T_e} \nabla T_e) + \Phi_{ei} - a_R c \chi T_e^4 \quad (54)$$

Thus energy is removed from the electron fluid at a rate given by $a_R c \kappa_p T_e^4$, which is the emission model of MACH2. The manner in which this energy is removed from the system as a whole, however, differs between the thin limit of the diffusion approximation and the MACH2 emission model. The coupling term which arises out of the nonequilibrium diffusion approximation causes the loss in electron energy to result in an increase in radiation energy density. The radiation energy density is then transported out of the system through flux-limited diffusion, leaving the system at cE. This is opposed to the emission model, which instantaneously removes this amount of electron energy each calculational timestep.

The emission model and the equilibrium radiation diffusion model of MACH2 are based on the assumption that problems of interest occur at temperatures and densities in which the material energy is always greater than the radiation energy density. Under such conditions, the nonequilibrium radiation diffusion equation reduces to these models in the limits where they are appropriate.

CHAPTER 4. THE MARAUDER COMPACT TOROID EXPERIMENT

The MARAUDER (Magnetically Accelerated Rings to Achieve Ultra-high Directed Energy and Radiation) program at the Phillips Laboratory was designed to study the formation, compression, and acceleration of high energy compact toroids and their applications. This investigation was motivated in part by the RACE (Ring ACcelerator Experiment) effort at the Lawrence Livermore National Laboratory [8], and utilizes many of the same concepts. Both experiments involve the formation of a compact toroid plasma ring via a magnetized coaxial plasma gun, the acceleration and/or compression of the ring as it is pushed through a conical coaxial electrode region, and the optional ability to further accelerate and focus. The MARAUDER experiment differs quantitatively from that of RACE in the amount of mass which resides within the toroidal confinement structure, the accelerating currents which can be applied to the compact toroid, and the specific experimental geometry. Typically, more massive compact toroids and larger accelerating forces are used in MARAUDER. Figure 4.1 is a cartoon illustrating all of the various stages of the MARAUDER experiment including stagnation upon an end plate.

Plausible MARAUDER parameters include a compact toroid mass in the 0.1 to 10 mg range, radial compression ratios ranging from a factor of 3 to a factor of 20, and acceleration to final velocities between 10 and 200 cm/ μ s within a 10 μ sec timespan [40]. At the higher end of this parameter spectrum, compact toroids with directed kinetic energies of a few to ten MJs are obtained. To date, the MARAUDER experiment has successfully formed compact toroids for a variety of plasma species with toroid masses between 1 and 2 mg. A factor of 9 compression has also been achieved, as well as directed kinetic energies from a few hundred kJs up to 1 MJ.

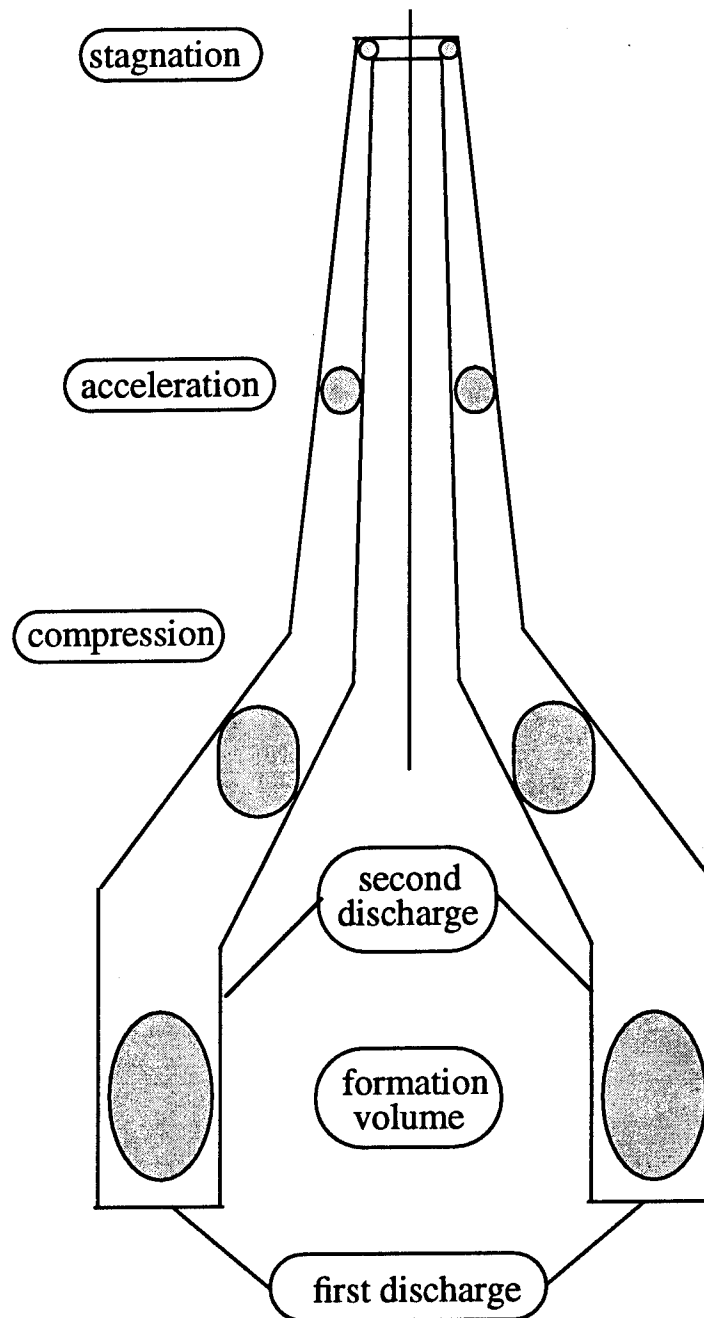


Figure 4.1. The MARAUDER experiment. Gas is injected into a magnetized plasma gun and a discharge applied. This breaks down the gas and pushes mass and field into the formation volume, creating a compact toroid. The toroid relaxes into a Taylor state [47]. The second discharge is then applied, compressing the toroid to high density. During this time magnetic flux accumulates behind the plasma ring accelerating it to high velocities. Radiation is produced as the fast, high density compact toroid stagnates against an end plate.

A schematic of the current MARAUDER experimental configuration is displayed in Figure 4.2. The apparatus can be divided into three sections, each pertaining to a specific evolutionary stage of the compact toroid. The formation section, in which the compact toroid is created, covers the lower portion of the system and consists of a plasma gun and an expansion region. It is connected to a compression section which is defined by a pair of nested cones. Once formed, the toroid is pushed through this compression region, increasing in mass density and magnetic field strength. These increases are necessary to obtain the high material densities and velocities required for many applications. Downstream from the compression zone is a straight coaxial section which provides a region for further acceleration of the toroid apart from compression. This defines the upper portion of the apparatus. To aid in the understanding of the formation and acceleration properties of the compact toroid, another experimental configuration besides that depicted in Figure 4.2 has been used. In this design, the compression and straight coax sections are replaced with a short cylindrical acceleration coax.

The compact toroid formation process is illustrated in Figure 4.3. A neutral gas is injected (puffed) into a coaxial plasma gun with an embedded, nearly radial, bias magnetic field. A voltage is applied to the conducting walls, creating a voltage difference across the electrodes. It is believed that cosmic ray electrons which are present within the plasma gun coaxial region feel the effect of the potential and are accelerated towards the lowest potential conducting wall. These electrons collide with the neutral molecules or atoms comprising the gas, ionizing them. These charged particles in turn, ionize further neutrals within a mean free path distance. This continues until an avalanche effect takes over (this is commonly referred to as the Paschen breakdown), ionizing a large number of the constituents of the gas and producing a plasma.

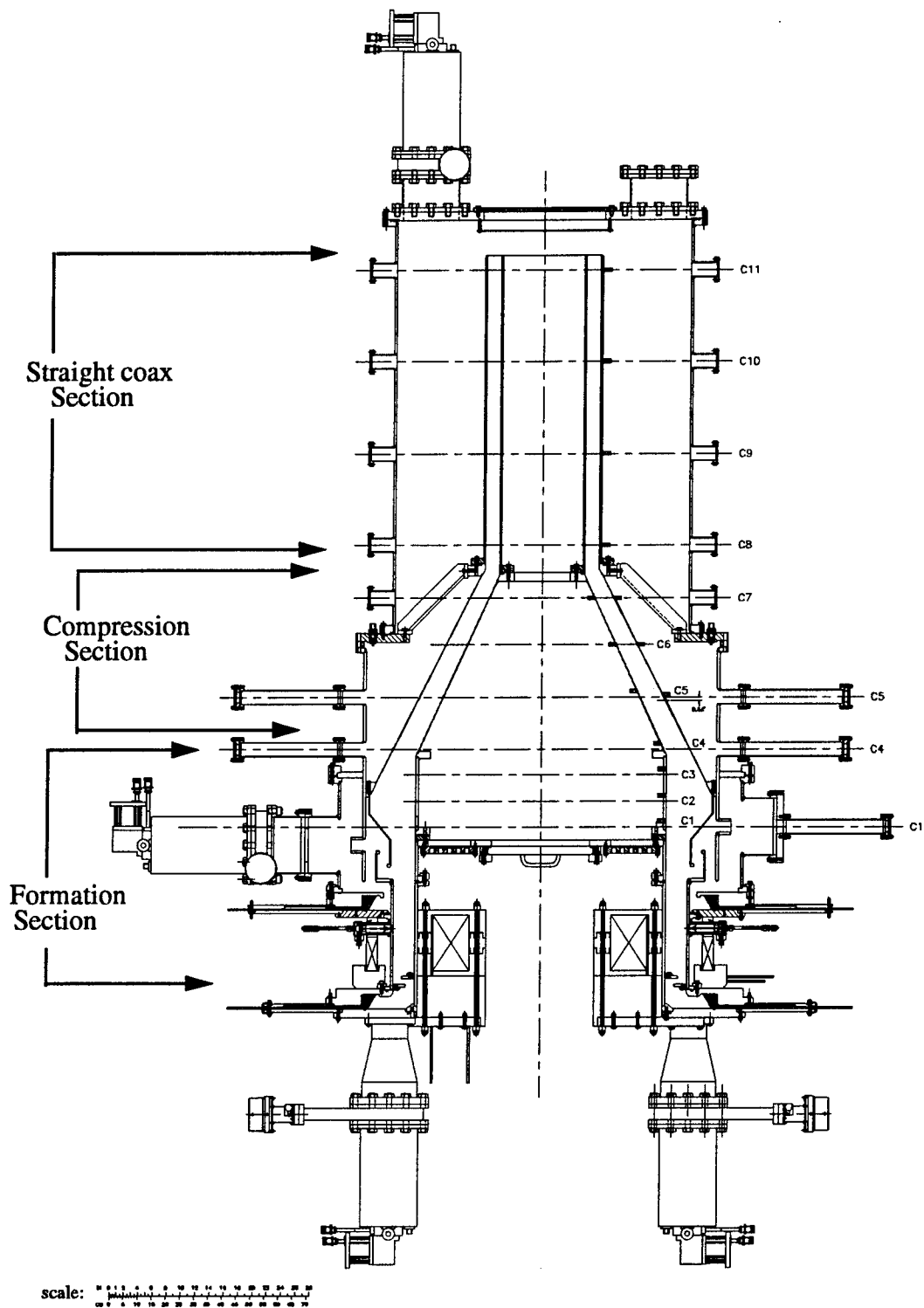


Figure 4.2. Schematic of the first MARAUDER 3:1 radial compression experiment [41].

The voltage difference across the electrodes causes a current flow through the ionized plasma adding a toroidal (azimuthal) magnetic field to the plasma gun (Figure 4.3 a). A $\bar{J} \times \bar{B}$ force associated with the toroidal field and the radial current flow allows the toroidal field to act as a “piston” pushing the magnetized plasma down the axial length of the plasma gun. Because the radial field is frozen into the plasma, it becomes elongated and poloidal (with ends being embedded into the conducting walls since the poloidal field has had time to penetrate them) as the plasma is forced towards the muzzle of the gun (Figure 4.3 b).

The upper end, or muzzle, of the coaxial plasma gun opens up into a larger area defined by a wider separation between inner and outer conducting walls. This region is often called the expansion or formation region and takes the place of the flux conserver in traditional spheromak experiments [43]. As the field-embedded plasma is pushed into this region, it expands forming a magnetized plasma bubble, i.e., plasma toroid, with the poloidal field lines at its base stretching back into the gun region where they remain attached to the gun electrodes. This shear field configuration in the gun region, along with the non-zero resistivity of the plasma, causes the field lines in this region to reconnect. The reconnection of the poloidal field lines close the magnetized bubble, thus forming a compact toroid (Figure 4.3 c).

Without the occurrence of magnetic reconnection, a self-contained compact toroid could not be formed using a plasma gun/expansion configuration. The reconnection process is a three dimensional effect which is associated with the resistive tearing mode instability [44]. This particular instability arises when a plasma current layer becomes unstable as a result of finite plasma conductivity. In the later stage of formation, a current sheet is produced in the region of null field where the stretched poloidal magnetic field in the gun region changes

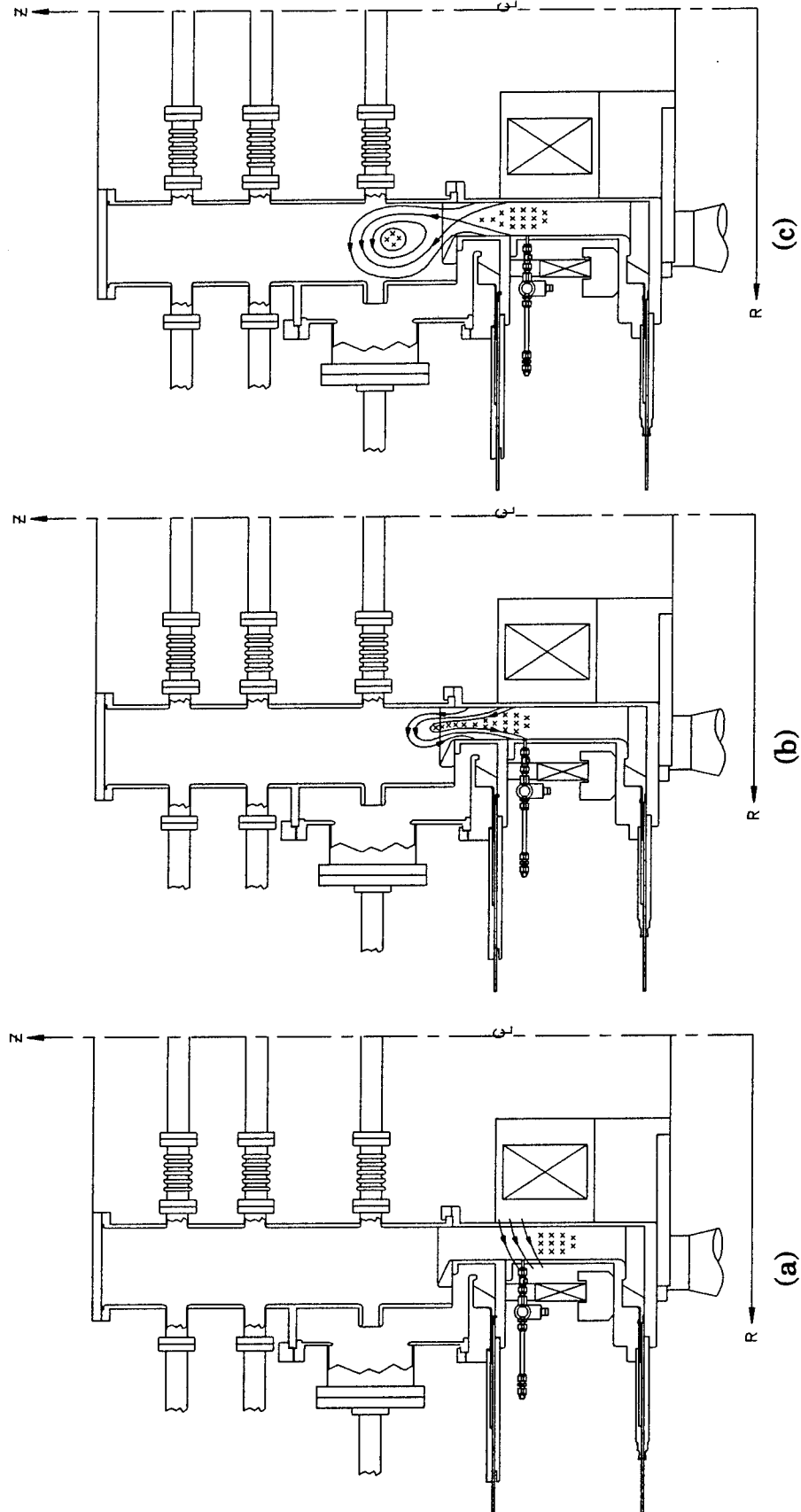


Figure 4.3. A schematic of the formation process. (a) Initial bias field and toroidal field. (b) Expansion into the expansion region. (c) Formation of compact toroid with reconnection of poloidal field lines [42].

direction. For the discharge and field energies indicative of MARAUDER formation shots, the field and plasma conditions are such that magnetic reconnection of the field lines in this region occurs naturally. This spontaneous reconnection can also be driven to take place on a faster timescale by applying an acceleration discharge near the base of the toroidal bubble. This introduces an additional toroidal magnetic field which pushes the poloidal magnetic field lines closer together, increasing the rate of reconnection [43].

Once formed and in the expansion region, the compact toroid is often allowed to relax toward a force free, minimum energy, equilibrium state referred to as a Woltjer-Taylor state. Force free configurations are described classically by the relationship $\bar{J} \times \bar{B} = \nabla p = 0$ which leads to the eigenvalue equation $\nabla \times \bar{B} = \lambda \bar{B}$ with λ constant [45,46]. In the lowest energy mode, the force free configuration can be shown to be stable to MHD instabilities [46,47]. Thus, by allowing the compact toroid to relax to this minimum energy state, the toroid will remain stable and resilient under subsequent conditions of acceleration.

In the MARAUDER experiment, the plasma gun consists of a coaxial conductor with inner wall at 44.8 cm from the center line and outer wall at 52.4 cm, creating an electrode gap of 7.6 cm. The inner electrode is the anode, and neutral gas is puffed through the outer electrode into the gun region via an array of 60 equally spaced gas valves. At present, between 0.5 and 2 mg of gas is believed to be injected into this region with a gas species typically of Nitrogen or Argon [40,43]. (Neon, Krypton, and Xenon are designated as future possibilities.) Both experimental measurement of the gas distribution in the gun region and 2-D hydrodynamic computations of the mass injection process give a qualitative picture of the transient gas distribution up to the time of the formation discharge current.

The initial bias radial field is produced by solenoids driven in series by a 15mF, 200 μ H, 1.5 - 2.0 kV capacitor bank with a 10 ms current rise time [48]. The two solenoids are located on either side of the plasma gun and reach a peak current of ~ 3 kA for a 2 kV discharge. This results in a radial-axial field of 0.1 to 0.5 Tesla in the gas puff region which reaches its peak value at ~ 12 ms. Computationally predicted initial gas distributions along with initial injected field configurations for representative formation shots are shown in Figure 4.4 and Figure 4.5, respectively.

The formation discharge is produced by a portion of the Phillips Laboratory Shiva Star capacitor bank. The Shiva Star capacitor bank consists of 36 fast capacitor bank modules and can be configured to allow the use of 3, 6, 12, or all 36 modules. Three of the modules are used for the formation discharge resulting in a 110 μ F, 40 - 100 kV gun bank. The bank discharges through a transmission line that connects to the bottom of the coaxial cylindrical conductors. Once the neutral gas is ionized within the gun and a current path is established, the current discharge determines the magnitude of the piston $\bar{J} \times \bar{B}$ force pushing the plasma-embedded radial field up into the expansion region. The expansion region has an ever evolving geometry since it serves two purposes - first to aid in the formation of the compact toroid, and second to provide the necessary transition to an acceleration and/or compression stage. The most current expansion region geometry is shown in Figure 4.2. Here the outer wall of the conductor is at 62.6 cm. Figure 4.6 (a) - (c) displays a MACH2 computational simulation of the formation process, starting from the time of the formation discharge leading up through the formation of the compact toroid in the expansion region. This calculation was carried out using a variation on the expansion region depicted in Figure 4.2.

One can imagine a large number of compact toroid applications that

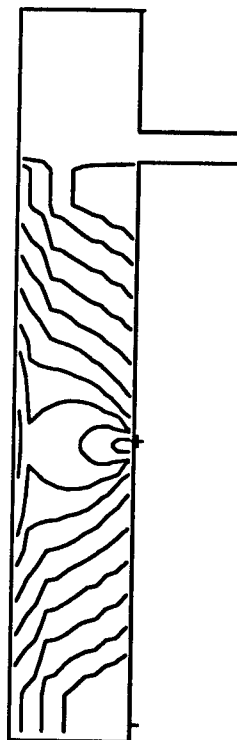


Figure 4.4. Computationally predicted 2-D mass distribution prior to the formation discharge. This is arrived at by superimposing the gas distributions resulting from all 60 gas valves using a MACH2 calculation modelling the mass distribution from a single valve. The superposition of the 60 distributions is averaged over the azimuthal angle to obtain the 2-D mass contours shown above. The contours are logarithmic, ranging from approximately $5.0 \times 10^{16} / \text{cm}^3$ in the region adjacent to the nozzle and thinning out to $1.0 \times 10^{11} / \text{cm}^3$ in the outermost gun regions [49].

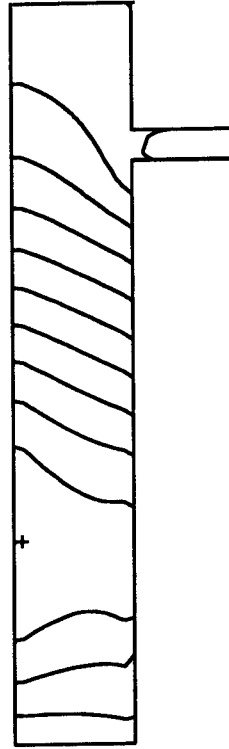


Figure 4.5. Initial magnetic field configuration shown above as poloidal magnetic flux contours. This is derived from a time-dependent electromagnetic code which calculates the diffusion of magnetic flux produced by currents in the solenoid coils exterior to the gun through the gun electrodes [49].

require toroids with directed kinetic energies in the MJ range. This is particularly true for the use of the compact toroid in radiation production. As discussed in Section 2 of Chapter 1, the impact of a high velocity, high energy compact toroid against a stationary target has the potential of being a significant source of keV range radiation. The ability of a stagnating compact toroid to provide the desired radiation yield depends upon the density of the material and the electron temperature during the stagnation process. It is these parameters which determine the spectral distribution of radiation and the radiative power output.

For the plasma temperatures and densities typical of MARAUDER formation stage compact toroids, and the accelerating discharges which can be applied to them, the stagnation process is not sufficient to drive the density and temperatures to the level of efficient radiation production. To overcome this problem, the stable nature of the compact toroid is utilized to accelerate the toroid to a large directed kinetic energy. This is done with the intent of converting a large fraction of the plasma kinetic energy into internal energy upon stagnation. This conversion is efficient for supersonic compressions, where shock physics enhances the increase in plasma density and material temperature. Such supersonic compressions require large toroid velocities, hence, compact toroids with kinetic energies in the MJ range.

To obtain the large specific kinetic energies necessary for high energy density radiation production, a mg-range compact toroid must be accelerated to a velocity on the order of a 100 cm/ μ s or more. This requires large accelerating forces. The piston, or accelerating, force is proportional to the azimuthal magnetic field which is given by:

$$B_{\theta} = \frac{\mu_o I_z}{2\pi r} , \quad (55)$$

where I_z is the bank discharge current and r is the distance from the center line of the coaxial conductors. The field has a radial dependence making the piston force nonuniform across the conducting gap and thus along the back of the toroid. Specifically, the piston force is preferentially stronger at the inner electrode. It has been shown both computationally [50] and experimentally [51] that when the magnitude of the piston field exceeds that of the compact toroid, the larger accelerating force on the inner conductor pushes the toroid to the outer electrode, allowing the piston field to flow past the compact toroid. This effect is called “blowby” [51] and for the purpose of compact toroid acceleration is undesirable. To prevent the occurrence of blowby, but still retain the capability of applying a large accelerating force, the toroid magnetic field is increased through the process of self-similar compression. The maximum accelerating force which can then be applied to the toroid is given by:

$$B_\theta = \frac{\mu_o I_z}{2\pi r_c} \quad (56)$$

where r_c is the radius of compression.

Although compact toroid compression is used to circumvent the blowby phenomenon associated with the acceleration of the compact toroid, it also has other benefits in terms of final radiative output. Compression provides the additional advantage of increasing the plasma density. This has a number of effects on the confined plasma properties. The increase in density leads to a decrease in photon mean free path and also electron-ion interaction distance. This improves the overall efficiency of the coupling and aids in the conversion of kinetic energy to material heating to radiation during the stagnation.

The plasma beta, which is the ratio of the plasma pressure to the field pressure, describes the ability of the magnetic field to confine the plasma. As the compact toroid is compressed, the plasma density, and subsequently,

temperature increases. This results in an increase in plasma pressure which competes with the increased magnetic field pressure. If the assumption of a self-similar, quasistatic compression [52] is made, then the compression is considered to be an isentropic process, i.e., one that is adiabatic and reversible [53]. Under such conditions and assuming a monatomic gas, values of plasma pressure and magnetic field after compression are related to the corresponding precompressed values in the following manner (See Appendix A for a derivation of these relationships.):

$$\frac{p}{p_o} = \left(\frac{r_o}{r_c}\right)^5, \quad \frac{B}{B_o} = \left(\frac{r_o}{r_c}\right)^2 \quad (57)$$

With

$$\beta = \frac{p}{B^2/(2\mu_o)} = \frac{n_s k T_s}{B^2/(2\mu_o)}, \quad (58)$$

$$\frac{\beta}{\beta_o} = \frac{r_o}{r_c} \quad (59)$$

Here r_o is the radius prior to compression and T_s , n_s correspond to the temperature and density, respectively of the particular species. Equation (59) states that the plasma beta increases with compression, reducing the ability of the field to confine the plasma. However, as the plasma radiates, it keeps the plasma temperature from increasing rapidly and a lower plasma beta can be maintained.

Compression may be performed simultaneously with acceleration or alone followed by acceleration. Generally speaking, the idea is to use an initial compression to aid in acceleration, and after acceleration, a final focusing (compression) of the toroid to reach a desired density. In this manner, the radiation losses are kept at a minimum throughout the compact toroid travel time,

increasing the density of the toroid just prior to impact. Because radiative emission in many cases (i.e. Bremsstrahlung) goes as n^2 , an increase in density results in a good radiator.

The first MARAUDER compression geometry is displayed in Figure 4.2. The compact toroid is compressed by a factor of three in radius while simultaneously undergoing acceleration. Beyond the compression cone, the compact toroid is pushed upstream into the stovepipe region, eventually stagnating against a target. A MACH2 simulation of the compression and the journey down the stovepipe for this experimental configuration is displayed in Figure 4.6 (d), (e), and (f). Future experimental designs which are under consideration include a factor of 5, 9, and 10 radial compression, variations on an additional focusing cone or an extended stovepipe, and further acceleration - all with the goal to maximize the radiation production during the stagnation process.

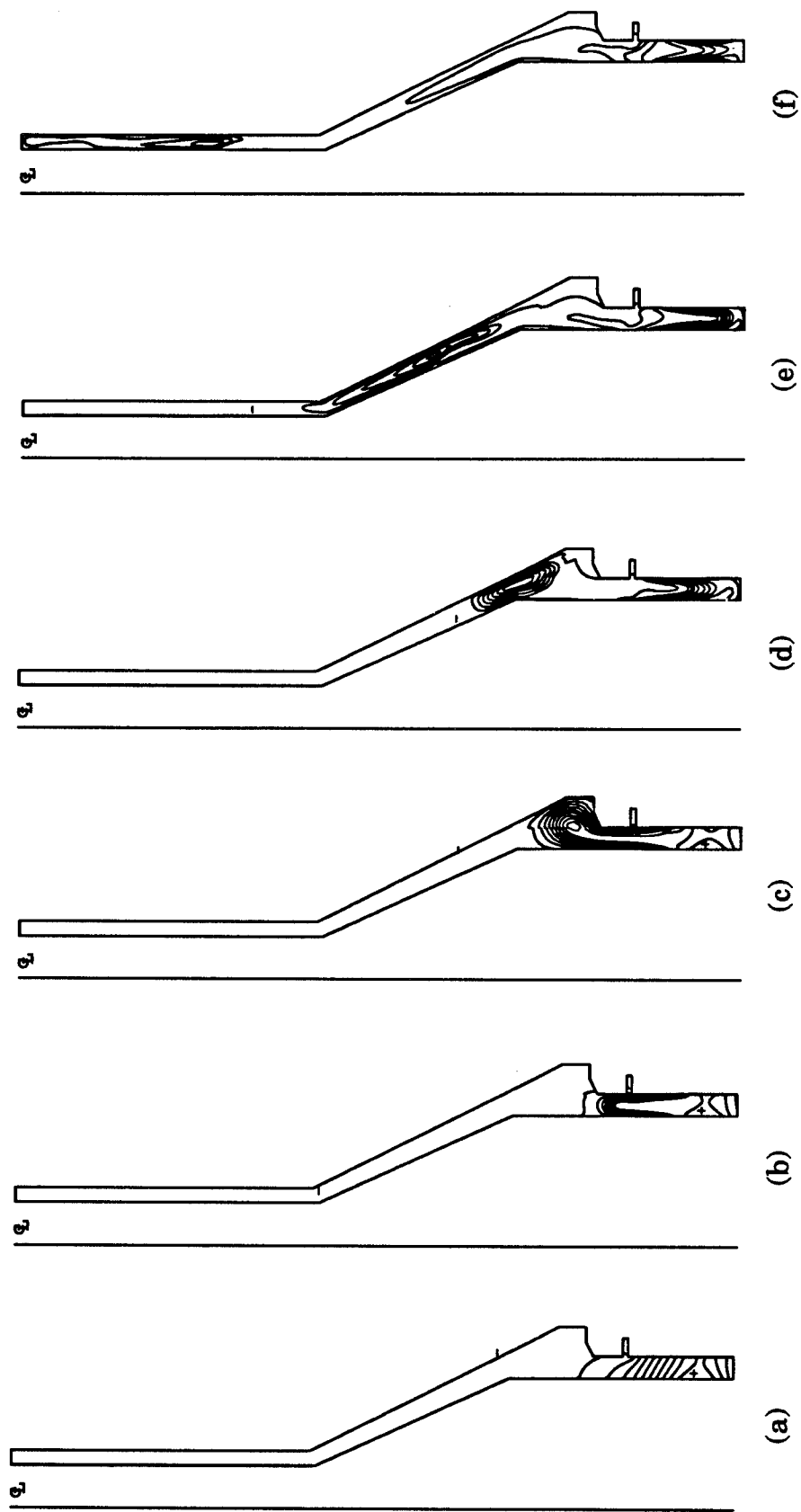


Figure 4.6. A MACH2 simulation showing the formation, compression, and acceleration down the stovetube region of a compact toroid. Pictured are the poloidal magnetic flux lines at (a) 0 ms, (b) 4 ms, (c) 6 ms, (d) 15 ms, (e) 17 ms, and (f) 20 ms [54].

CHAPTER 5. BENCHMARKING

Testing, or benchmarking, newly implemented code against known analytical solutions or documented computational solutions is a necessary stage of code development. While benchmarking can provide a means of debugging and improving algorithms, its primary function is to validate the ability of an algorithm to simulate physical problems effectively. The continuous partial differential equations which constitute the radiation MHD equations are approximated by discrete, coupled finite difference equations. The solutions to these finite difference equations are determined through algebraic manipulation and numerical techniques. The resulting algorithms often have limitations associated with them. Benchmarking reveals the accuracy with which the algorithms exhibit the expected physical behavior and defines regions and parameters where the algorithms fail to do so. This aids in the proper simulation of complex problems and in user discernment over potential unphysical results arising from purely numerical effects.

The test problems which are presented in this chapter are designed to specifically investigate the simulation of radiation-electron coupling and radiation diffusion both separately and together. Because there is no well defined set of radiation MHD test problems, these are based on and include a combination of personal choice, examples in the literature, or suggestions by others working with radiation hydrodynamic codes. The advection of the radiation field, radiation pressure-volume work, and the effect of radiation acceleration on the material has also been benchmarked, but on a qualitative level. These terms were found to produce the numerically correct behavior for both optically thick and thin physical regimes and exhibit qualitatively correct behavior in the transition region. No further remarks will be made concerning these terms.

5.1 Numerical Stability and Accuracy

The radiation MHD equations are a set of partial differential equations which describe the time evolution of a radiating fluid. In general, the numerical solution to any time-dependent partial differential equation involves rewriting the equation in an algebraic "difference" form with physical variables defined at discrete locations on a finite grid. This leads to a set of algebraic equations coupled through values at neighboring grid locations. With initial conditions and/or boundary conditions, these coupled algebraic equations can then be solved at any subsequent time. This can be a straightforward process when using known values of the dependent variable (fully explicit method), or can involve solving a set of coupled algebraic equations when taking either time advanced values of the dependent variable (fully implicit method), or a combination of known and time advanced values.

The solution that is obtained for the difference equation is clearly an approximation to the true solution of the differential equation. The degree to which these two solutions compare with each other depends on the algebraic formulation of the differential equation, i.e. truncation errors which occur from the discretisation of derivatives, and any errors to the exact solution of the difference equation stemming from computer roundoff, irregular grid zoning [14], boundary effects [14] and applied equation solvers. The manner in which the partial differential equation is structured into an algebraic expression can yield values which are grossly different from those of the true solution, and this dissimilarity can grow with time. This condition is referred to as numerically unstable and is commonly manifest in nonphysical oscillatory behavior which increases at each calculational timestep. A finite difference form is defined as unstable when a perturbation, i.e. error, to the exact solu-

tion of the difference equation continues to grow until it becomes the dominate term in the solution. This perturbation can be introduced at any stage of the computation and typically depends on cell size, timestep, and physical parameters. A finite difference form is referred to as unconditionally unstable if the algorithm is unstable to all values of cell size and timestep, and conditionally unstable if it exhibits stable behavior for only certain values of cell size and timestep. If a finite difference equation is stable for all values of timestep and cellsize, then it is defined as unconditionally stable.

Stability criteria for a difference equation can be established using a number of stability analysis techniques. One of the more common techniques which is found in the literature is the von Neumann stability analysis [36]. This analysis is applicable to linear difference equations with constant coefficients and defines necessary conditions for stability. It can also generally be applied to more complicated difference equations which are indicative of practical physical problems. For example, nonlinear equations can be linearized and this analysis performed, while variable coefficients are addressed by treating the analysis as local; the coefficients are then considered constant.

To illustrate the von Neumann stability analysis, the evolution equation for the diffusion of radiant energy is examined. Recall from Section 3.3 that the diffusion equation for the radiation energy density in one dimension, assuming a constant diffusion coefficient:

$$\frac{\partial E}{\partial t} = \kappa \frac{\partial^2 E}{\partial y^2} , \quad (60)$$

can be written explicitly in difference form as

$$\frac{E_j^{n+1} - E_j^n}{\Delta t} = \kappa \frac{E_{j+1}^n - 2E_j^n + E_{j-1}^n}{(\Delta y)^2} . \quad (61)$$

Here the subscript i as it appears in Equation (48) has been omitted for simplicity. In this case, the spatial second derivative of the energy density in expression (61) is written in terms of known values at timestep n . This is referred to as explicit differencing of the differential equation. Alternatively, this second derivative could have been written in terms of the values of E at the $n+1$ timestep (as in Section 3.3), defined as implicit differencing, or some mixture of values between the two timesteps often denoted as a time-centered differencing. As will be shown below, the time differencing scheme chosen can effect the stability of the algorithm differently.

One interpretation of the von Neumann stability analysis considers a perturbation introduced at each grid point during any time level and represents this as a finite Fourier series [36, 55]. This Fourier series is then substituted into the discretized linear equation and stability is determined by considering whether separate Fourier components of the perturbation decay or amplify in progressing to the next time level. For a linear algorithm, it is sufficient to consider just one term of the Fourier series [36]. Thus, with the perturbation defined by

$$E_p = \xi^n e^{ikj\Delta y} , \quad (62)$$

where k is a real spatial wave number and ξ is an amplitude factor which depends on k , a difference equation is said to be stable when substitution of E_p leads to a relationship in which

$$\left| \frac{\xi^{n+1}}{\xi^n} \right| \leq 1 . \quad (63)$$

Substituting Equation (62) into equation (61):

$$\frac{\xi^{n+1} e^{ikj\Delta y} - \xi^n e^{ikj\Delta y}}{(\Delta t)} = \kappa \xi^n \frac{[e^{ik(j+1)\Delta y} - 2e^{ikj\Delta y} + e^{ik(j-1)\Delta y}]}{(\Delta y)^2} , \quad (64)$$

or

$$\frac{\xi^{n+1} - \xi^n}{\Delta t} = \kappa \xi^n \frac{[e^{ik\Delta y} - 2 + e^{-ik\Delta y}]}{(\Delta y)^2} . \quad (65)$$

Expressing the exponential terms in trigonometric form and rearranging, the above equation becomes

$$\xi^{n+1} = \xi^n \left[1 - \frac{2\kappa\Delta t}{(\Delta y)^2} (1 - \cos k\Delta y) \right] . \quad (66)$$

Dividing through by ξ^n and rewriting the term in brackets:

$$\frac{\xi^{n+1}}{\xi^n} = 1 - \frac{4\kappa\Delta t}{(\Delta y)^2} \sin^2\left(\frac{k\Delta y}{2}\right) . \quad (67)$$

Applying the stability criterion as defined by Equation (63),

$$\frac{1}{2} \frac{4\kappa\Delta t}{(\Delta y)^2} \sin^2\left(\frac{\kappa\Delta y}{2}\right) \leq 1 . \quad (68)$$

Since

$$\sin^2\left(\frac{\kappa\Delta y}{2}\right) \leq 1 ,$$

this states that the explicit formulation of the radiation diffusion equation (or any diffusion equation for that matter) is conditionally stable when

$$\frac{1}{2} \frac{4\kappa\Delta t}{(\Delta y)^2} \leq 1 \quad \text{or} \quad \frac{2\kappa\Delta t}{(\Delta y)^2} \leq 1 . \quad (69)$$

This stability condition can be physically interpreted [33] by considering the diffusion time across a cell size of width Δy :

$$t_{diffusion} \sim \frac{(\Delta y)^2}{\kappa} \quad (70)$$

Then equation (69) states that the maximum allowed timestep that can be used before the solution displays any unstable behavior is on the order of the

diffusion time across a cell.

If an implicit differencing scheme is considered, then the values of the radiation energy density on the right hand side of Equation (61) are evaluated at timestep $n+1$ and

$$\frac{E_j^{n+1} - E_j^n}{\Delta t} = \kappa \frac{E_{j+1}^{n+1} - 2E_j^{n+1} + E_{j-1}^{n+1}}{(\Delta y)^2} . \quad (71)$$

Substituting in the expression (62),

$$\begin{aligned} \frac{\xi^{n+1} - \xi^n}{\Delta t} &= \kappa \xi^{n+1} \frac{[e^{ik\Delta y} - 2 + e^{-ik\Delta y}]}{(\Delta y)^2} , \\ \xi^{n+1} \left[1 + \frac{2\kappa\Delta t}{(\Delta y)^2} (1 - \cos k\Delta y) \right] &= \xi^n , \end{aligned} \quad (72)$$

or

$$\frac{\xi^{n+1}}{\xi^n} = \frac{1}{1 + \frac{4\kappa\Delta t}{(\Delta y)^2} \sin^2 \left(\frac{k\Delta y}{2} \right)} . \quad (73)$$

Using the stability criteria (Equation (63)), it is apparent that this finite difference form of the diffusion equation is unconditionally stable since the magnitude of the above expression cannot exceed unity for any positive k and Δt . This eliminates the need for a time restriction as imposed in the explicit scheme. Thus, as far as stability alone is concerned, this fully implicit method is preferable to the explicit method.

It should be noted that even if an explicit difference expression is numerically stable in that the amplitude of an existing (or introduced) perturbation does not increase with time, it can still lead to unacceptable physical results. One example in which this is numerically evident is in the difference representation of the electron-radiation coupling equation. For an explicit, or

backward, time differencing formulation of the electron-radiation coupling, the computational solutions will oscillate about the equilibrium values of the material temperature and the radiation energy density under certain conditions. In particular, the oscillations will occur if the calculational timestep becomes too large. In this case, the oscillations are not caused by the growth of any numerical error present, but by overshooting the solution because of the large timestep. This is very different from a solution which is increasingly diverging with each timestep. For the purpose of this work, the nonphysical oscillatory behavior exhibited with this difference form is also considered a numerical instability of sorts.

From the above discussion, it is evident that the manner in which a difference form is constructed can influence the stability of its solution. Unfortunately, the condition of stability does not insure accuracy (or convergence) of the difference solution to that of the differential equation it is approximating. For example, in implicit formulations, the solution can be unconditionally stable but still be inaccurate for certain timesteps and cell size. This is because implicit differencing schemes tend to drive the variables of interest to their equilibrium (steady state) values, neglecting the details of the small timescale evolution. If the timesteps are too large, the time evolution of the solution will not accurately depict that of the real solution.

The chosen structure of a difference form basically depends on the physics in which one is interested. In cases where an explicit formulation leads to conditional instability, the timestep can be reduced to produce a stable solution. If the timestep is computationally taxing, or the explicit method is unconditionally unstable, an implicit formulation or a time-centered treatment might be an alternate form of choice. A fully implicit scheme requires no timestep limitations for stability, but accuracy may be sacrificed at large

timesteps. A higher accuracy can be attained if smaller timesteps are taken. If the details of the small timescale evolution are of interest, either an explicit scheme, or an implicit scheme with small timesteps can be used.

The accuracy with which the approximate solution to the difference equation compares to the real solution of the differential equation is an important issue regardless of the differencing scheme being used. All methods, whether explicit, implicit, first order in Taylor expansion, or a higher order scheme, have associated with them some degree of error. In general, the behavior of the approximate solution should approach that of the real solution in the limit of infinitesimal cell size and time step. However, when solving a set of equations, the accuracy is also related to the accuracy of the equation solver. In many instances, the method of solution entails iterating to convergence. The convergence criterion, along with the leading term in the truncation error, should algebraically provide a measure of the difference solution error.

The accuracy of a particular algorithm on a finite grid can often be assessed computationally by its application to a simple problem which has a known or exact solution. Manipulation of the convergence criteria (if used), grid size, and timestep should provide a measure of the accuracy and conditions under which such convergence is reached. For successive grid refinement, stricter convergence criteria, and increasingly smaller timestep, the difference solution is typically found to approach some value and maintain this value to within a predetermined accuracy. When this occurs, the difference solution is said to converge to the exact solution.

The issues presented in this section are important in obtaining the correct time evolved solutions of the radiation MHD equations. The issue of accuracy and the importance of timestep, cell size and convergence criteria will be addressed specifically in the discussion of the benchmarking of the radiation

diffusion term. In this case, the accuracy of the solution is visibly dependent on these parameters. The difficulties which can arise from numerical instability, as well as accuracy, will become apparent in the following section with the discussion of the electron radiation coupling.

5.2 Radiation Diffusion

In an optically thick regime, radiation is transported through the process of diffusion. Photons interact with surrounding material on the order of a photon mean free path, exchanging energy and momentum with nearby electrons. The electrons, in turn, emit radiation indicative of the absorbed or scattered photons, and the interaction process is repeated. In this manner, radiation energy is transferred throughout the material. As the optically thin regime is approached, the photon mean free path grows increasingly larger, becoming comparable to characteristic structural lengths in the material. Under these conditions, radiation is no longer transported through the material via diffusion, and the standard diffusion approximation leads to physically unacceptable results. In particular, the rate of transport of radiative energy exceeds the speed of light (Refer to Section 2.4 for a complete discussion). Nonetheless, the diffusion approximation is often maintained in the thin limit, using algebraic prescriptions to force the proper physics in this regime. In such cases, it is not only important to test the radiation diffusion algorithm under opaque material conditions, but also under conditions where the material is transparent to radiation.

In this section, the radiation diffusion algorithm in the MACH2 code is examined using a set of test problems which cover a range of physical regimes. The test problems are initially quite simple, simulating only the physical process of radiative diffusion in an optically thick medium where the diffusion approximation is valid. Further benchmarking entails more complicated test runs in which both electron-radiation coupling and fluid motion are permitted in addition to diffusion. For these calculations, the material properties are defined such that both opaque and transparent mediums are addressed. A

description of these problems will be deferred to Section 5.4 after the discussion of the electron-radiation coupling. The test problems which are found on the following pages involve the one and two dimensional linear diffusion of radiation in a static, opaque medium. These problems have corresponding analytic solutions with which they can be directly compared.

It should be noted that the diffusion algorithm in MACH2 solves a time centered difference equation given by [34]:

$$E_{i,j}^{n+1} = E_{i,j}^n + (\Delta t \kappa) [\theta \nabla^2 E_{i,j}^{n+1} + (1 - \theta) \nabla^2 E_{i,j}^n] , \quad (74)$$

or

$$E_{i,j}^{n+1} - \theta \Delta t \kappa \nabla^2 E_{i,j}^{n+1} = E_{i,j}^n + (1 - \theta) \Delta t \kappa \nabla^2 E_{i,j}^n , \quad (75)$$

where θ is a time centering parameter which defines the type of differencing being performed. For $\theta = 1$, the above equation becomes

$$E_{i,j}^{n+1} - \Delta t \kappa \nabla^2 E_{i,j}^{n+1} = E_{i,j}^n , \quad (76)$$

and the differencing is fully time implicit. On the other hand, $\theta = 0$ results in a fully explicit difference form, while for $0 < \theta < 1$, the differencing is of mixed type; the preferred value for θ in this case is $1/2$, i.e., time-centered. In MACH2, the implicit formulation given by Equation (76) is used unless otherwise specified by the user. For the purpose of this dissertation, this is always the case, and radiation diffusion in all calculations is done implicitly. The time-implicit, finite volume difference representation of the radiation diffusion equation is written out in Section 3.3, Equation (44). A discussion of the iterative solution techniques used to solve the set of implicit algebraic equations is also found in that section.

As shown previously (Section 5.1), the implicit difference form of the diffusion equation is stable under all parameter conditions. However, implicit

formulations in general, are known to decrease in solution accuracy at large timesteps and cell size. The first benchmarking test is thus used to investigate this issue and to insure that the diffusion algorithm works properly. The test involves the penetration of radiation from a "hot" radiating wall into a cold static material. This is modelled numerically by defining a block of hydrogen in which $T_R = 0$ eV and the fluid temperature is 5 eV. The hydrogen is bounded by radiatively insulating walls on all sides except the top and bottom, which are defined to have a radiation temperature of 10 eV and 0 eV, respectively. Taking the diffusion coefficient as constant throughout the simulation, the radiation field is then allowed to diffuse through the medium from the hot boundary. Eventually a steady state radiation temperature (energy density) distribution is reached. To isolate the diffusion algorithm for benchmarking purposes, the physical processes involving electron-radiation coupling and pressure gradients were neglected.

A series of calculations were performed with the described initial conditions for a range of cell resolutions along the flow direction and a range of timesteps. In particular, the number of cells used in the calculation varied from 4 to 32, and two timesteps were essentially considered, 10^{-3} s and 10^{-6} s. The computational region was defined by a 2 m x 2m x 1m box, with 4 cells specified in the direction perpendicular to the flow. The material density was assigned a value of 1 kg/m^3 , and the diffusion coefficient a value of $100 \text{ m}^2/\text{s}$. With this value for the radiative conductivity, the photon mean free path was $1 \text{ } \mu\text{m}$, substantially smaller than the box length of 2 m. Thus for the system being considered, the material was optically thick and the diffusion approximation was accurate in describing the transport of radiation. For the iterative solving procedure, a relaxation weighting factor of 1.0 was taken and the tolerance was set to 10^{-6} . This latter value provides a user-defined measure

for ending the iteration process; when the algorithm makes changes in the field that are smaller than 10^{-6} times the largest value of the field, the iteration stops. The results from the test runs can be compared directly to the analytic solution:

$$E(y, t) = \frac{E_o}{l}y + \frac{2E_o}{\pi} \sum_{n=1}^{\infty} \frac{(-1)^n}{n} \sin\left(\frac{n\pi}{l}y\right) e^{-\kappa \frac{n^2 \pi^2}{l^2} t}, \quad (\text{B25})$$

where

$$E_o = a_R T_R^4 = 1.37 \times 10^5 \text{ J/m}^3 ,$$

and l is the vertical length of the box. A detailed derivation of this solution is given in Appendix B.

The complete set of calculations is shown in Table 5.1. Each calculation is defined in terms of the number of cells which span the region parallel to the radiation flow and the computational timestep. For each case, a diffusion Courant number is also given. This value is determined by:

$$N_{C_D} = \frac{\kappa \Delta t}{(\Delta y)^2} .$$

This number is useful because it contains both timestep and cell size, and is therefore a convenient way to place a measure on solution accuracy.

Table 5.1. N_C for cell size and timestep

Δt #of cells	10^{-3}s	10^{-6}s
4	0.18	1.8×10^{-4}
8	1.6	1.6×10^{-3}
16	6.4	6.4×10^{-3}
32	25.6	0.0256

Figures 5.1 through 5.4 display plots of the radiation energy density for the above test runs. In each plot, the analytic solution is represented by a solid

line while the numerical solution is depicted by open circles. The circles are drawn at cell-center locations on the numerical grid since the radiation energy density calculated by MACH2 is a cell-centered value. In all cases, the right edge of the figures correspond to the hot wall boundary temperature of 10 eV, while the left edge corresponds to the cold wall boundary temperature of 0 eV.

An examination of Figures 5.1 through 5.4 leads to a number of conclusions concerning the stability and accuracy of the implicit radiation diffusion algorithm. As expected, the numerical solution is stable, while its accuracy is clearly dependent on cell size and computational timestep. The influence of the cell size, or cell resolution, on solution accuracy can be seen by inspecting the calculated runs made with the smaller timestep, 10^{-6} s. At the earlier times in these calculations, the numerical solution has not converged to the analytic solution of the differential equation for the coarse grids comprised of 4 and 8 cells. (For this problem, 4 zones correspond to a cell size of 0.5 m, while 8 zones correspond to a cell width of 0.25 m.) The grids containing 16 and 32 cells have converged though, consistent with the supposition that as $\Delta y \rightarrow 0$, the approximate difference solution should approach that of the differential equation. By the time 1×10^{-3} s is reached, the numerical solution in both the 4 and 8 zone cases coincides with the analytic solution.

While finer grid resolution results in improved accuracy of the difference solution, increasing the calculational timestep typically leads to a corresponding decrease in accuracy. This can be seen by comparing the test results at the two different timesteps, 10^{-6} s and 10^{-3} s for the same cell resolution. It is particularly evident in the cases involving 16 and 32 cells, where the energy distribution at 1×10^{-3} s has converged at the smaller timestep, but has diverged somewhat at a timestep of 10^{-3} s. Regardless of the timestep taken, or the cell size considered, it is clear from Figures 5.1 through 5.4, that the com-

putational solutions always converge to the analytic steady state solution at later times. This is indicative of any implicit differencing scheme which tends to drive the numerical solution to the steady state or equilibrium solution.

A relationship between the accuracy of the difference algorithm and the diffusion Courant number can be inferred from Table 5.1 and the above observations. For Courant numbers less than one and reasonable cell resolution, the diffusion algorithm produces stable, accurate, time evolved solutions. For Courant numbers greater than one, the solution still remains stable, but cannot be assumed accurate at early times. The requirement for sensible cell resolution arises from the fact that the diffusion algorithm will always transport radiation into adjacent cells as long as a gradient in radiation energy is present and the radiative conductivity is nonzero. In the hot wall problem, for example, the diffusion algorithm will deposit energy into the first real cell even if radiation is unable to propagate across the cell in the time being considered. Recall from Section 5.1, the diffusion time across a cell of width Δy :

$$t_{diffusion} \sim \frac{(\Delta y)^2}{\kappa} \quad (70)$$

For the 4 zone case, this value is 2.5×10^{-3} s, and for the 8 zone case, 6.25×10^{-4} s. Prior to these times, i.e., at 5×10^{-4} s, the radiation field has not had time to diffuse across the spatial scale of a cell size. The diffusion algorithm is unable to discern this physical restriction; consequently, the computed radiation energy profile will consist of unrealistic results. This is seen in Figures 5.2 (a) and 5.3 (a), where the radiation energy distribution at 5×10^{-4} s in both instances is higher in the cell (or cells) closest to the hot boundary.

Although this discussion of solution accuracy has focused solely on the issues of cell resolution and timestep, the user defined level of convergence for the implicit equation solver also plays an important role. If the convergence

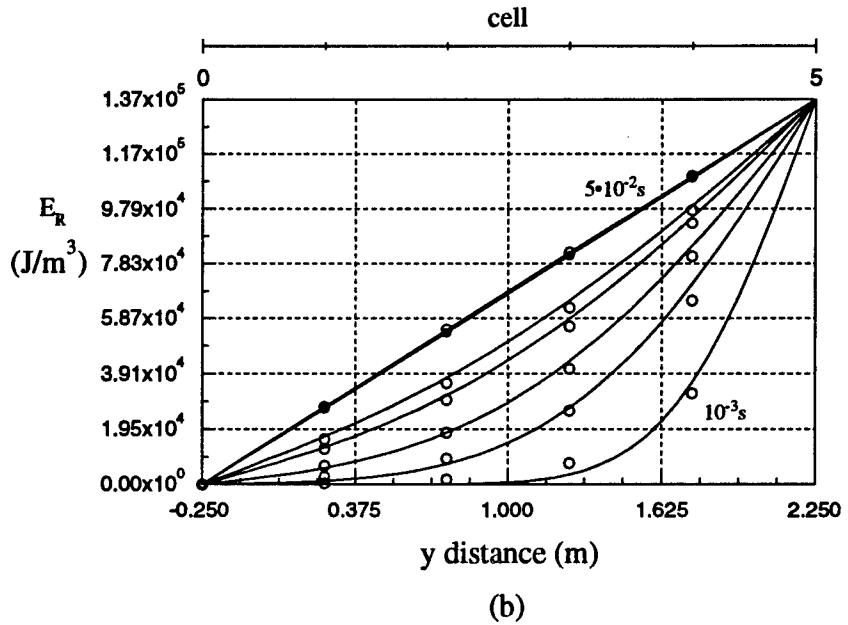
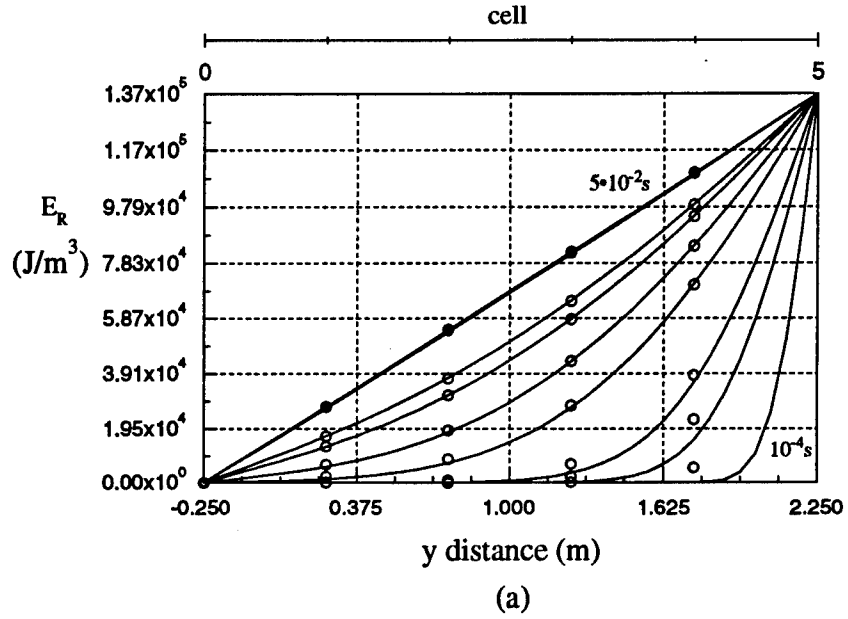
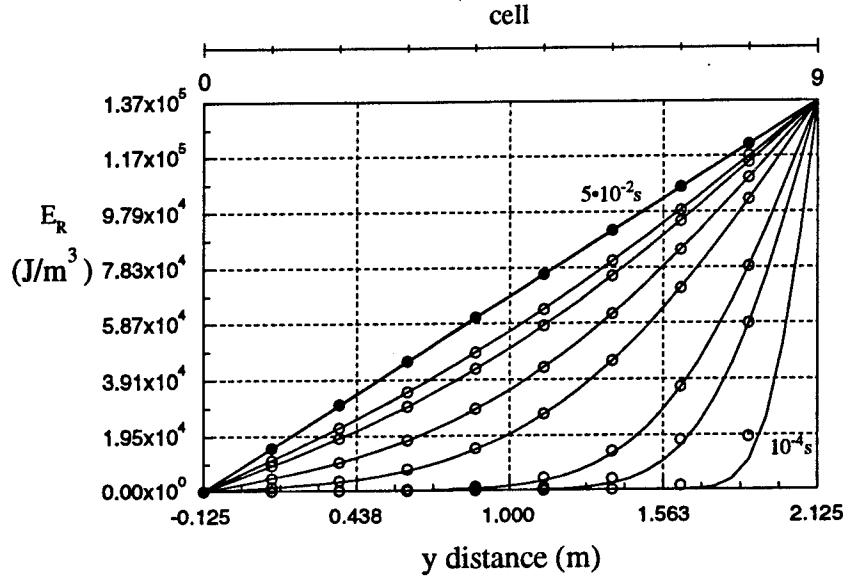
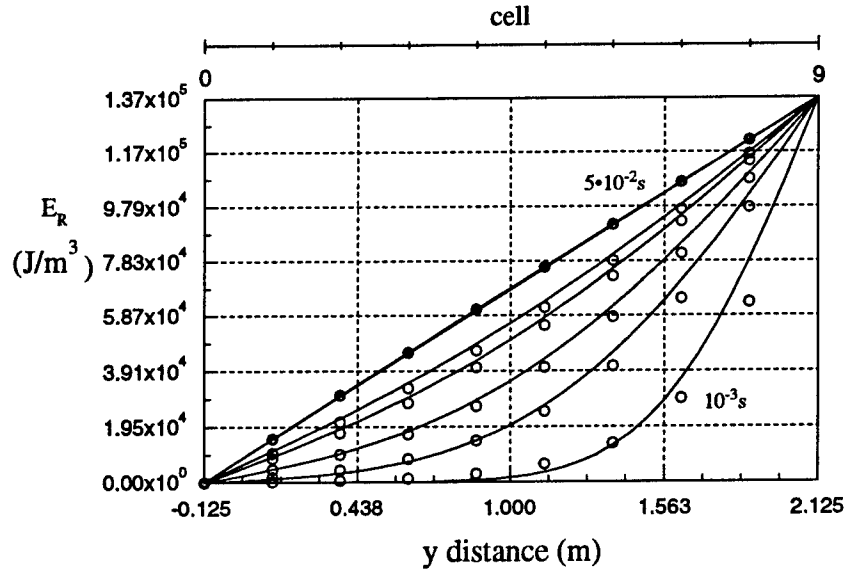


Figure 5.1. Radiation energy distribution for one dimensional radiation diffusion in the y -direction with 4 cells. Curves plot the energy as a function of vertical distance for $1 \times 10^{-4}\text{s}$, $5 \times 10^{-4}\text{s}$, $1 \times 10^{-3}\text{s}$, $3 \times 10^{-3}\text{s}$, $5 \times 10^{-3}\text{s}$, $8 \times 10^{-3}\text{s}$, $1 \times 10^{-2}\text{s}$, $3 \times 10^{-2}\text{s}$, and $5 \times 10^{-2}\text{s}$ using a calculational timestep of (a) 10^{-6}s and (b) 10^{-3}s . The solid lines represent the analytic solution, while the open circles represent the numerical solution.

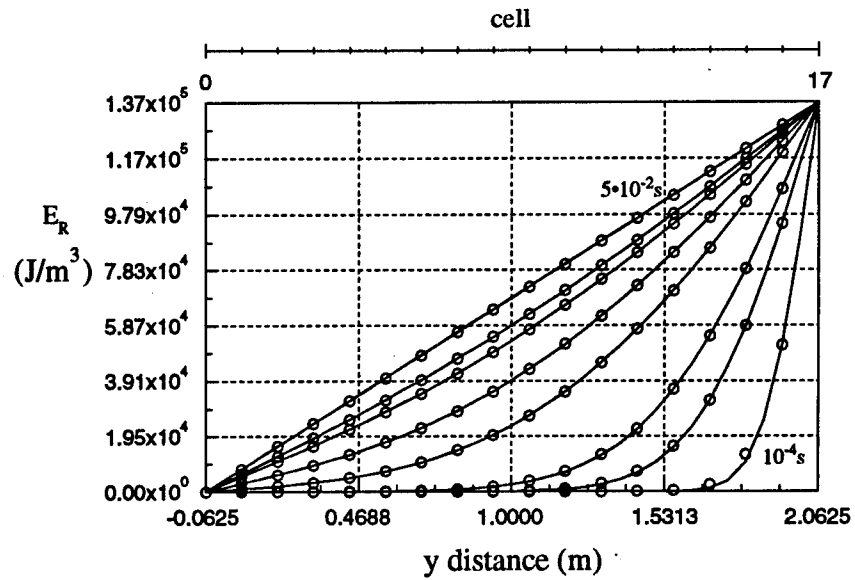


(a)

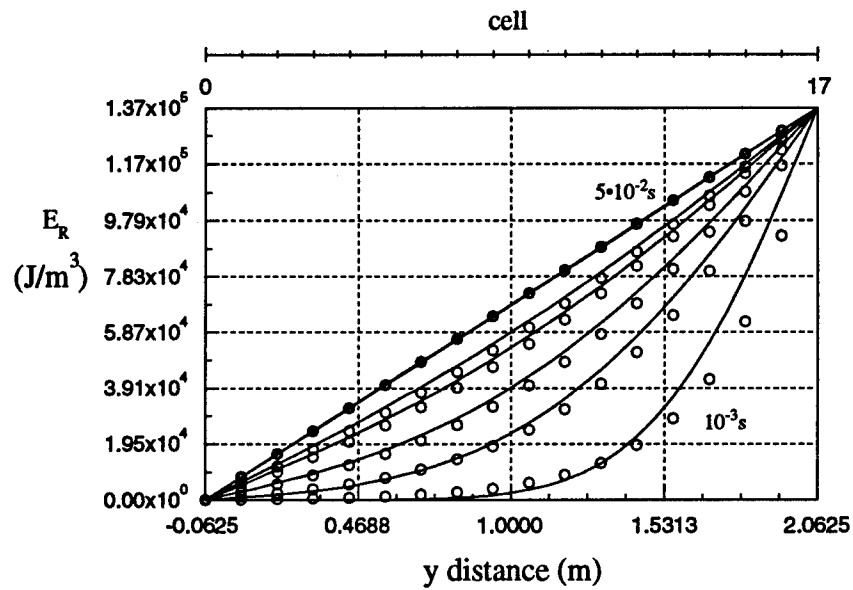


(b)

Figure 5.2. Radiation energy distribution for one dimensional radiation diffusion in the y-direction with 8 cells. Curves plot the energy as a function of vertical distance for 1×10^{-4} s, 5×10^{-4} s, 1×10^{-3} s, 3×10^{-3} s, 5×10^{-3} s, 8×10^{-3} s, 1×10^{-2} s, 3×10^{-2} s, and 5×10^{-2} s using a calculational timestep of (a) 10^{-6} s and (b) 10^{-3} s. The solid lines represent the analytic solution, while the open circles represent the numerical solution.

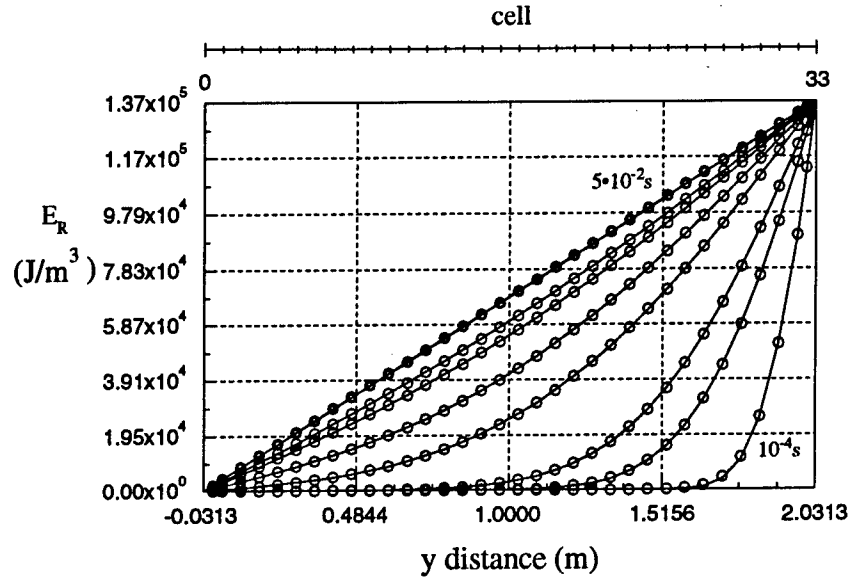


(a)

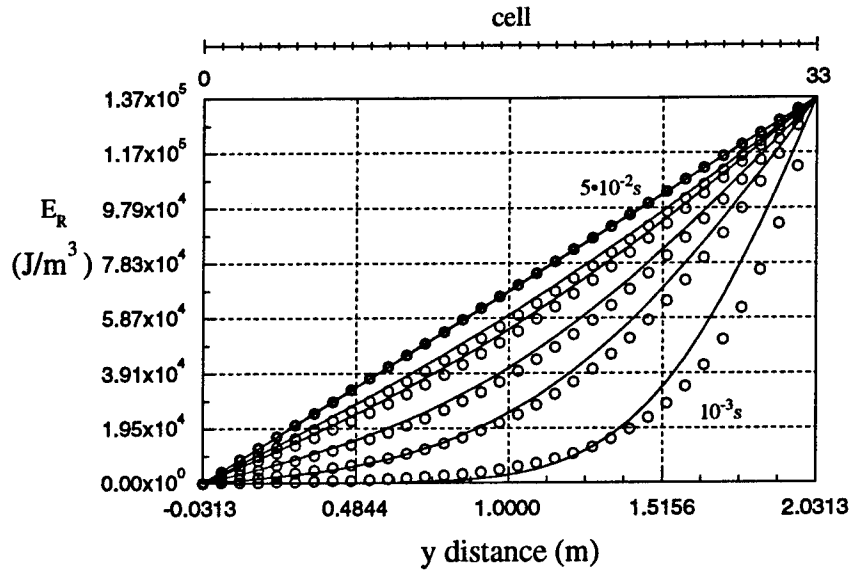


(b)

Figure 5.3. Radiation energy distribution for one dimensional radiation diffusion in the y -direction with 16 cells. Curves plot the energy as a function of vertical distance for $1 \times 10^{-4} \text{ s}$, $5 \times 10^{-4} \text{ s}$, $1 \times 10^{-3} \text{ s}$, $3 \times 10^{-3} \text{ s}$, $5 \times 10^{-3} \text{ s}$, $8 \times 10^{-3} \text{ s}$, $1 \times 10^{-2} \text{ s}$, $3 \times 10^{-2} \text{ s}$, and $5 \times 10^{-2} \text{ s}$ using a calculational timestep of (a) 10^{-6} s and (b) 10^{-3} s . The solid lines represent the analytic solution, while the open circles represent the numerical solution.



(a)



(b)

Figure 5.4. Radiation energy distribution for one dimensional radiation diffusion in the y-direction with 32 cells. Curves plot the energy as a function of vertical distance for $1 \times 10^{-4}s$, $5 \times 10^{-4}s$, $1 \times 10^{-3}s$, $3 \times 10^{-3}s$, $5 \times 10^{-3}s$, $8 \times 10^{-3}s$, $1 \times 10^{-2}s$, $3 \times 10^{-2}s$, and $5 \times 10^{-2}s$ using a calculational timestep of (a) $10^{-6}s$ and (b) $10^{-3}s$. The solid lines represent the analytic solution, while the open circles represent the numerical solution.

criterion is not tight enough, the numerical solution will not converge to the solution of the difference equation. The results can be quite different from that of the differential equation and often effect radiation energy transport and energy conservation. For the diffusion problems considered in this work, a convergence criterion of 10^{-5} provided acceptable solutions.

To test the two dimensional radiation diffusion capability of the diffusion algorithm, the loss of radiation from a radiatively "hot" confined fluid to its surroundings was considered. This was modelled numerically by defining a block of uniform radiation energy density bounded by cold surfaces ($T_R=0$ at boundary walls). The radiation was then allowed to leave the system, governed by a constant radiative conductivity of $100 \text{ m}^2/\text{s}$. The original material conditions were the same as in the one dimensional benchmarking problem, with hydrogen at 5 eV and $\rho = 1 \text{ kg/m}^3$. Two different geometries were considered, one that is square in the computational plane (a $2 \text{ m} \times 2 \text{ m} \times 1 \text{ m}$ box) and one that is rectangular (a $2 \text{ m} \times 4 \text{ m} \times 1 \text{ m}$ box). The cell resolution in the square geometry was 16 cells by 16 cells, and in the rectangular geometry, 16 cells by 32 cells. The convergence criteria was again set to 10^{-5} and a computational timestep of 10^{-6} s was used. The analytic solution is given by (refer to Appendix B)

$$v(x, y, t) = E_0 \Psi(x, l_x, t) \Psi(y, l_y, t)$$

where

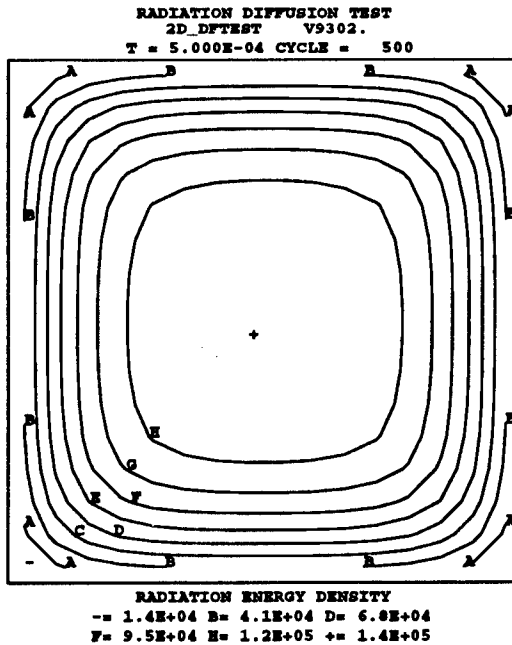
$$\Psi(z, l, t) = \frac{4}{\pi} \sum_{n=0}^{\infty} \frac{(-1)^n}{(2n+1)} e^{-\kappa(2n+1)^2 \pi^2 t / 4l^2} \cos \frac{(2n+1)\pi z}{2l}, \quad (\text{B27})$$

and

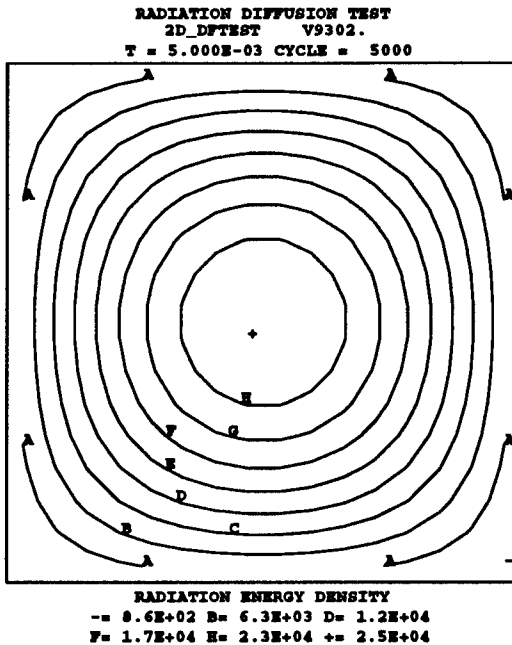
$$E_0 = 1.37 \times 10^5 \text{ J/m}^3, \quad -l_x \leq x \leq l_x, \quad -l_y \leq y \leq l_y.$$

Figures 5.5 through 5.8 display the results of these two test runs. Figures

5.5 and 5.7 are MACH2 contour plots of the radiation energy distribution for the two different geometries at 5×10^{-4} s and 5×10^{-3} s. Slice plots of the computational solution and the analytic solution are shown in Figure 5.6 and Figure 5.8. In both cases, the energy density is measured along a path which not only spans the system but crosses through its center. For the square geometry this corresponds to a vertical distance along the y-axis, while the rectangular geometry considers both a horizontal distance along the x-axis and a vertical distance along the y-axis. In these latter figures, the analytic solution is defined by the solid line and the numerical solution by open circles. Clearly, the computational solution converges to the differential solution in both cases.



(a)



(b)

Figure 5.5. MACH2 radiation energy density profiles for the square 2 dimensional diffusion problem at (a) 5×10^{-4} s and (b) 5×10^{-3} s. Initial conditions are a uniform interior radiation temperature of $T_R=10$ eV, and $T_R=0$ at boundaries. Cell resolution is 16 cells x 16 cells.

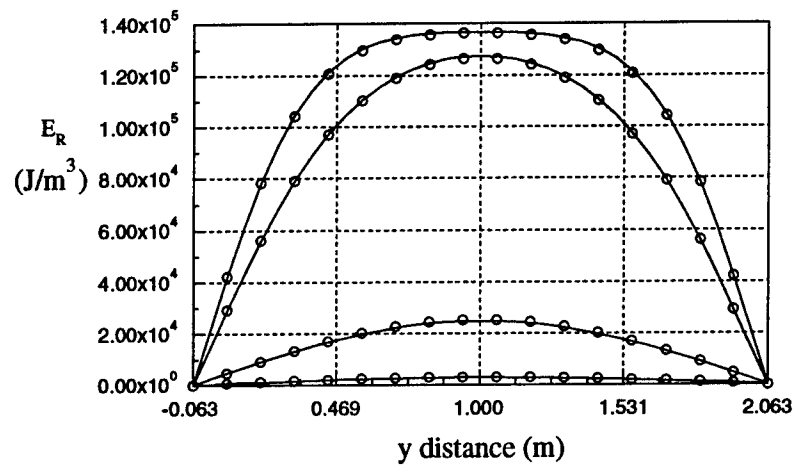


Figure 5.6. Radiation energy density profile for the square two dimensional diffusion problem. Curves plot the energy as a function of vertical distance along the y-axis for 5×10^{-4} s, 1×10^{-3} s, 5×10^{-3} s, and 1×10^{-2} s. The solid lines represent the analytic solution, while the open circles represent the numerical solution.

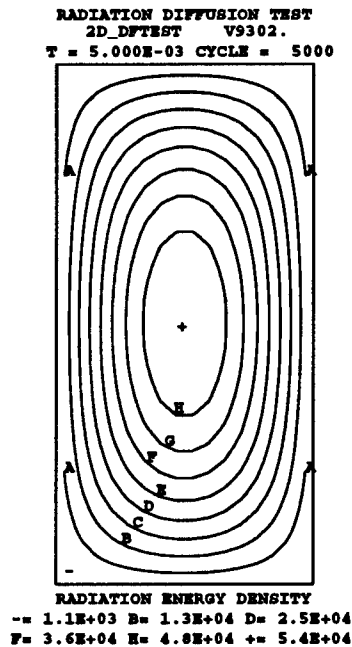
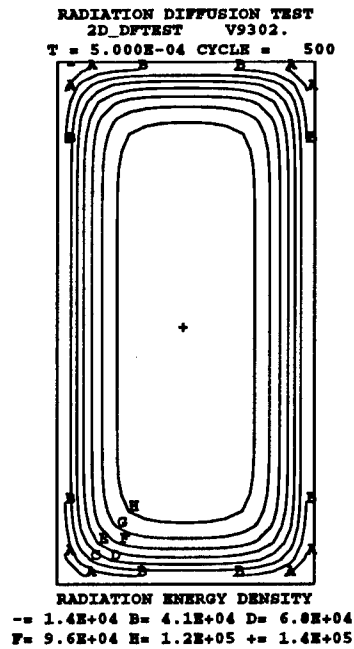
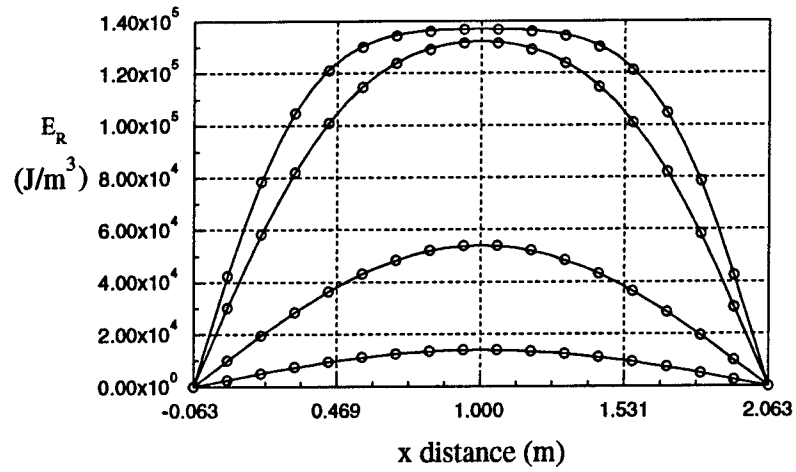
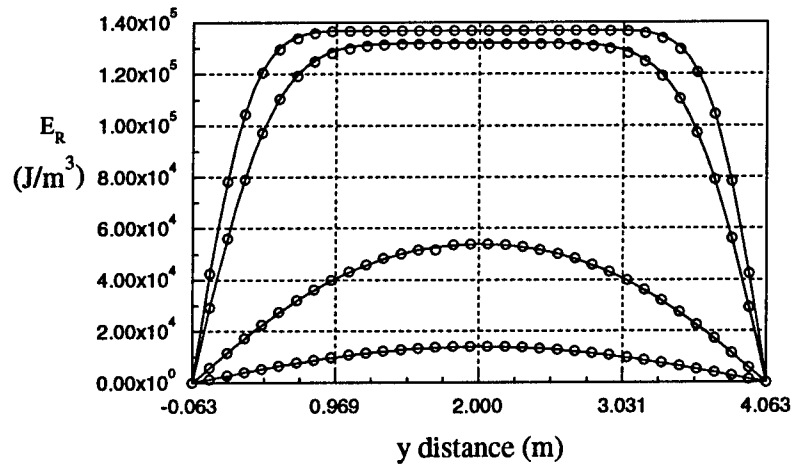


Figure 5.7. MACH2 radiation energy density profiles for the rectangular 2 dimensional diffusion problem at (a) 5×10^{-4} s and (b) 5×10^{-3} s. Initial conditions are a uniform interior radiation temperature of $T_R=10$ eV, and $T_R=0$ at boundaries. Cell resolution is 16 cells x 32 cells.



(a)



(b)

Figure 5.8. Radiation energy density profile for the rectangular two dimensional diffusion problem. Curves plot the energy as a function of (a) horizontal distance along the x-axis for vertical position at cell 16 (b) vertical distance along the y-axis for horizontal position at cell 8, for 5×10^{-4} s, 1×10^{-3} s, 5×10^{-3} s, and 1×10^{-2} s. The solid lines represent the analytic solution, while the open circles represent the numerical solution.

5.3 Electron-Radiation Coupling

The exchange of energy between a radiation field and a material is carried out primarily through the interactions of photons with electrons. Under thick material conditions where electron-photon interaction rates are large, the electron-radiation coupling plays a significant role in energy exchange. As a material transitions from a thick to thin regime, this coupling is expected to become less important, typically playing a negligible role when the material is thin. For certain conditions in the thin limit, however, coupling may be of consequence for specific radiation lines; electron-photon collision rates may be substantial for a given photon energy or a range of photon energies, allowing for some degree of coupling. In any event, it is necessary to accurately depict the electron-radiation interaction process in numerical simulations.

The testing of the electron-radiation coupling term is accomplished by defining a static medium with initial temperatures of the material and the radiation field held at different values. The system is then allowed to evolve with the electron-radiation coupling turned on. Physically, the two temperatures will reach a steady state value based on characteristic time scales given by the governing differential equations. This should be observed numerically with the difference algorithm. This algorithm should also be structured such that energy is conserved in the system at each calculational timestep. The requirement of energy conservation, along with a steady state solution on proper timescales, is necessary to insure the correct modelling of the coupling term.

In this section, two finite difference representations of the electron radiation coupling equation are examined in light of the above requirements. The first representation is an explicit form of the coupling equation, while the

second is an implicit form. Recall the partial differential equations describing the electron-radiation coupling (Section 3.2):

$$\rho c_{v_e} \frac{\partial T_e}{\partial t} = -\kappa_p \rho c (a_R T_e^4 - E) , \quad (77)$$

$$\frac{\partial E}{\partial t} = \kappa_p \rho c (a_R T_e^4 - E) . \quad (78)$$

An explicit difference formulation of these equations can be written as:

$$E^{n+1} = E^n + \kappa_p \rho c \Delta t (a_R (T_e^4)^n - E^n) , \quad (79)$$

$$T_e^{n+1} = T_e^n - \frac{\kappa_p c}{c_{v_e}} \Delta t (a_R (T_e^4)^n - E^{n+1}) , \quad (80)$$

Here the known values of radiation energy density and material temperature at timestep n are used to update the radiation energy density at timestep $n+1$. This updated energy density is then used to determine the new value of the material temperature at time $n+1$. An implicit difference form of the coupling equations was given in Section 3.3:

$$E_{i,j}^{n+1} = \frac{1}{1 + (k_{eff})_{i,j}^n} [E_{i,j}^n + (k_{eff})_{i,j}^n a_R (T_e)_{i,j}^n] , \quad (41)$$

$$e_{i,j}^{n+1} = e_{i,j}^n - (k_{eff})_{i,j}^n (a_R (T_e)_{i,j}^n - E_{i,j}^{n+1}) / \rho_{i,j}^n , \quad (42)$$

$$(k_{eff})_{i,j}^n = \frac{(\kappa_P)_{i,j}^n \rho_{i,j}^n c \Delta t}{1 + \frac{4 a_R (\kappa_P)_{i,j}^n c}{(c_v)_{i,j}^n} (T_e^3)_{i,j}^n \Delta t} . \quad (43)$$

Again, old values of the material temperature and the radiation energy density are used to determine the energy density at time $n+1$, which is substituted

into Equation (42) to find the updated material temperature.

For a given set of initial conditions, these two difference representations can be benchmarked against the steady state solution, testing whether the solutions reach the steady state value within a few characteristic coupling timescales, and if energy is conserved during this process. A statement of energy conservation for the electron-radiation coupling can be found by adding Equations (77) and (78) together

$$\frac{\partial}{\partial t} (\rho c_{v_e} T_e + E) = 0 ,$$

or

$$\rho c_{v_e} T_e + E = C_o , \quad (81)$$

where C_o is a constant defined by the initial conditions of the system. At any point in the calculation, this can be used to verify that the values of the electron temperature and the radiation energy density satisfy this equation and conserve energy.

If the specific heat capacity and Planckian mean opacity are assumed to be constant for a closed system of interest, then a steady state solution implies that

$$-\rho c_{v_e} \frac{\partial T_e}{\partial t} = \kappa_p \rho c (a_R T_e^4 - E) = 0 .$$

Substituting the expression (81) for E:

$$\kappa_p \rho c (a_R T_e^4 - E) = \kappa_p \rho c (a_R T_e^4 - C_o + \rho c_{v_e} T_e) = 0 ,$$

or

$$T_e^4 + \frac{\rho c_{v_e}}{a_R} T_e - \frac{C_o}{a_R} = 0 . \quad (82)$$

Thus, for constant ρ , c_{v_e} , and an initial value of T_e , this quartic equation can be solved to find the steady state value of the material temperature and the radiation temperature. A characteristic timescale over which the material and radiation field relax toward a steady state solution is determined by the coefficient in front of the difference term $(a_R T_e^4 - E)$. Rewriting the material coupling Equation (77) with $e = \rho c_{v_e} T_e$,

$$\frac{\partial e}{\partial t} = -\kappa_p \rho c (a_R T_e^4 - E) .$$

This equation has the same form as the coupling equation for the radiation field:

$$\frac{\partial E}{\partial t} = \kappa_p \rho c (a_R T_e^4 - E) .$$

Thus, the material specific internal energy and the radiation energy density go to their steady state solutions on the same timescale which is given by

$$\tau_c \sim (\kappa_p \rho c)^{-1} . \quad (83)$$

To investigate the nature of the difference algorithms, Equations (79) to (80) and Equations (41) to (43), a series of calculations were performed on a rectangular system of hydrogen numerically defined on a 16 x 16 grid in Cartesian geometry. For each calculation, the material temperature was initially assigned a value of 100 eV and the radiation field a value of 10 eV. A set of solutions to these difference expressions were then obtained for a range of densities and calculational timesteps. The density spanned four orders of magnitude, with values of 0.01 kg/m³, 1 kg/m³, and 100 kg/m³. At each density, three different timesteps were used: one of the same order as the radiation characteristic time found from Equation (83), one two orders of magnitude lower, and one two orders of magnitude larger.

For the purpose of testing, both the specific heat capacity and the Plankian

mean opacity were considered constant and assigned values using the LTE SESAME tables accessed by MACH2. The specific heat capacity was defined as 2.8×10^8 J/kg-eV, while the opacities were density dependent and taken as the tabular value given at 100 eV (at 100 eV, hydrogen is fully ionized and the specific heat capacity is essentially the same value for all three densities in the temperature range of interest). The densities, corresponding timesteps, Plank mean opacities, characteristic timescales, and the steady state temperatures for the test runs are shown in Table 5.2. The value of the steady state temperature was found solving Equation (82) for the initial parameters using MATHEMATICA [56,57].

Table 5.2. Electron-Radiation coupling parameter survey

ρ (kg/m ³)	Δt (s)	κ_p (m ² /kg)	τ_c (s)	T_{ss} (eV)
.01	10^{-2}	2.23×10^{-3}	1.49×10^{-4}	55.3
	10^{-4}			
	10^{-6}			
1.0	10^{-6}	0.218	1.53×10^{-8}	95.9
	10^{-8}			
	10^{-10}			
100	10^{-10}	16.7	2.0×10^{-12}	100
	10^{-12}			
	10^{-14}			

Figures 5.9 through 5.14 plot the temperature profiles of the material and radiation field as a function of time for the timesteps given in the above table using both the explicit and implicit difference methods. In Figures 5.9, 5.11, and 5.13, where solutions are found from the explicit difference form, the solution is observed to oscillate about the steady state value for the largest computational timestep. This oscillatory behavior is caused by the multiplication term containing Δt in the difference Equations (79) and (80). If Δt has too great a value, this multiplication causes overshooting of the solution. Oscilla-

tions then arise at subsequent times from the opposite signs of the coupling term, $(a_R T_e^4 - E)$, in Equations (79) and (80). For a density of 1 kg/m^3 and 100 kg/m^3 , this behavior has disappeared at the next smaller timestep which is on the order of the relaxation time. (See Figures 5.11 (b) and 5.13 (b).) Physically, the disappearance of the oscillations in going from a timestep two orders of magnitude larger than the relaxation time to a timestep of the same order as the relaxation time, can be interpreted as a stability constraint - computational timesteps should not exceed the characteristic time at which the radiation field relaxes to the steady state solution.

Although the explicit solutions in Figures 5.11 (b) and 5.13 (b) are stable at smaller timesteps, there exists an artificial sharp transition in the solution at the first calculational time. This inaccurate behavior is removed as seen in Figures 5.11 (c) and 5.13 (c) when an even smaller timestep is taken. For all three densities investigated, the solutions are the most accurate at the smallest timesteps as evidenced by Figures 5.9 (c), 5.11 (c), and 5.13 (c). Plots of the material and radiation energy densities are shown in Figure 5.15 for all three material densities at the smallest timestep. Clearly in all cases, steady state solutions are reached within a few characteristic timescales. With increasing material density, the ratio of fluid energy density to radiation energy density becomes higher allowing the material to maintain a larger store of energy. This is observed in Figure 5.15 (c) where the energy density of the material remains at its initial level, while the radiation field energy density increases substantially.

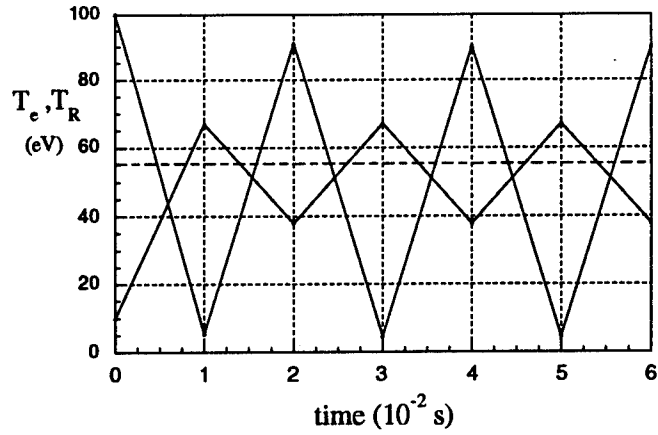
Comparing the solutions to the implicit difference equation at large timesteps with those from the explicit expression, the oscillations found with the explicit solutions are not present. However, it can be seen from Figures 5.10 (a), 5.12 (a), and 5.14 (a) that the implicit solution is unable to resolve the

early radiation temperature at such timesteps, with a discrete, large transition from the initial value of the radiation temperature to a new value at the first calculation time. In all three cases, the final steady state solution is approached within a few timesteps. As the timestep decreases, the implicit solution improves in accuracy, approaching the explicit one as the timestep becomes ever smaller. This can be seen in Figures 5.10 (c), 5.12 (c), and 5.14 (c) which mirror the corresponding explicit solutions.

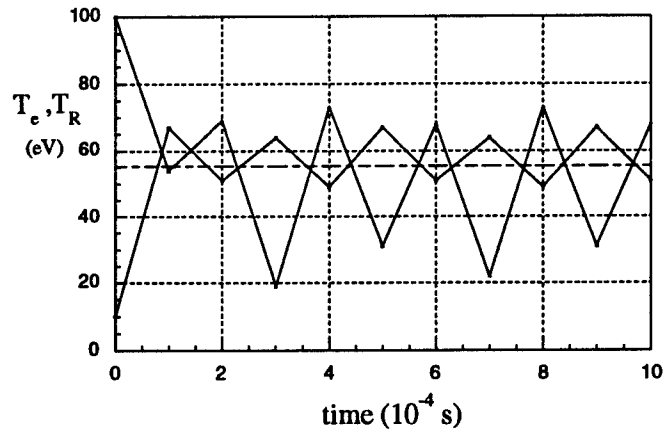
The results of this study indicate that the implicit method is stable regardless of the timestep used. Although accuracy is sacrificed at large timesteps, it can be improved by moving to smaller timesteps. The explicit method requires timesteps smaller than the characteristic time for the solution to be stable. At the smaller timesteps already required for stability, accuracy is not a problem; the explicit solution is accurate. An examination of the total energy of the system indicates that energy conservation is an issue at larger timesteps in the explicit formalism. The energy in many cases was not conserved. In the implicit method, the energy of the system was always conserved to within 1% each cycle. Based on the above information, the difference representation of choice for this work was the implicit difference form. With an implicit difference scheme for the electron-radiation coupling, the possibility of instability is always avoided, producing the correct steady state solutions on adequate timescales. Furthermore, energy is conserved throughout the time evolution of the system. If the temporal evolution of the temperature profiles is important, the timestep can be decreased as needed.

Two additional test problems were simulated using the implicit difference form. The results are shown in Figures 5.16 and 5.17. Here the material was again hydrogen and the density was taken to be $5 \times 10^{-2} \text{ kg/m}^3$. Figure 5.16 represents the implicit solution with initial material temperature of 100 eV

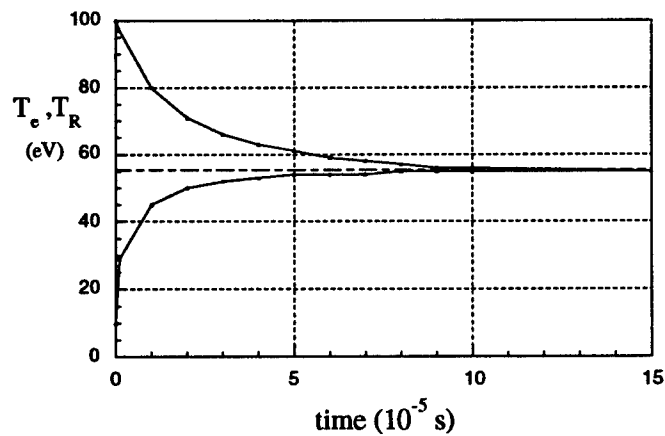
and radiation temperature of 10 eV. The Plankian opacity was defined as $0.0103 \text{ m}^2/\text{kg}$. The steady state temperature was determined from Equation (82) to be 72.9 eV, and the characteristic time was calculated as $6.5 \times 10^{-6} \text{ s}$. Figure 5.17 plots the implicit solution for initial material temperature of 10 eV and radiation temperature of 100 eV. The Plank opacity here was taken as $103 \text{ m}^2/\text{kg}$. The steady state temperature was 75 eV with a relaxation time of $6.5 \times 10^{-10} \text{ s}$. In both cases the solutions reach the steady state value on the characteristic timescales.



(a)

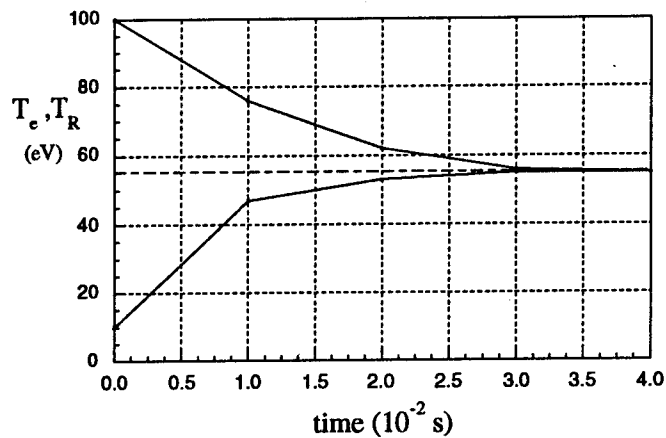


(b)

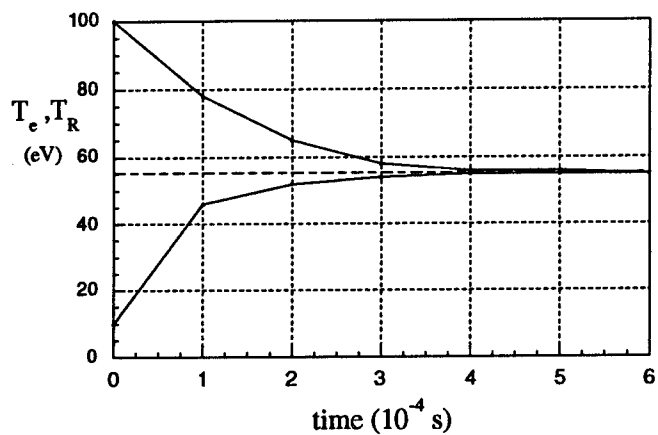


(c)

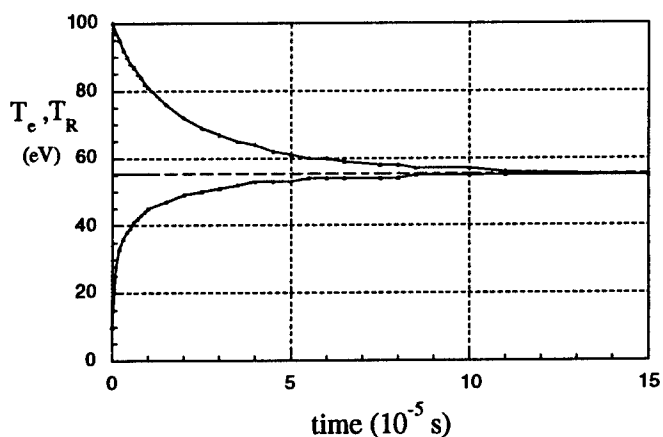
Figure 5.9. Material, Radiation temperature vs. time for a density of 10^{-2}kg/m^3 using the explicit difference form given by Eqns. (79) and (80) with timesteps of (a) 10^{-2} s, (b) 10^{-4} s, and (c) 10^{-6} s.



(a)

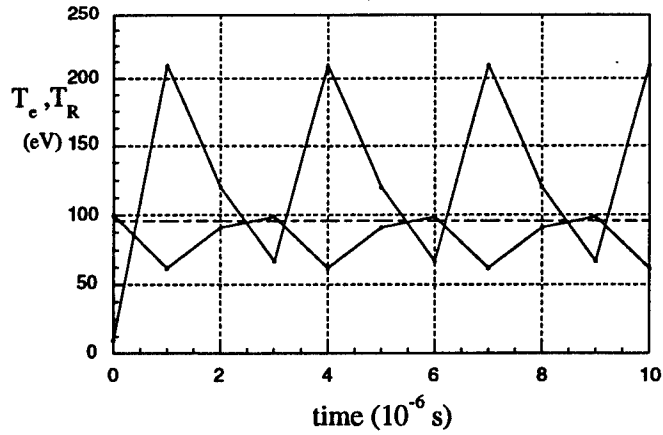


(b)

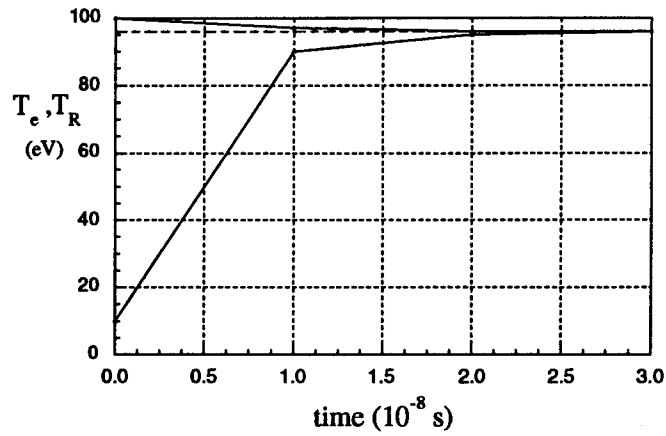


(c)

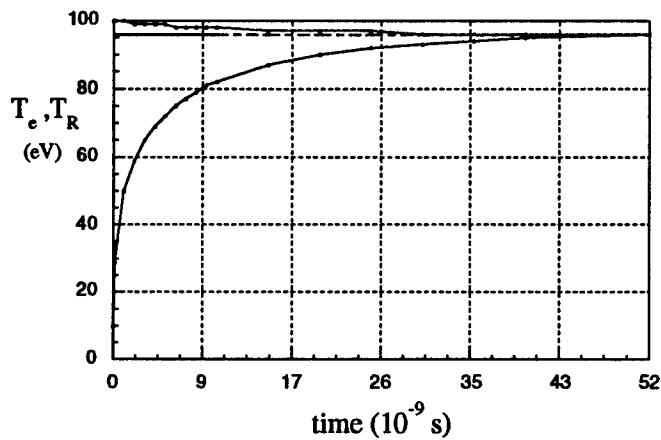
Figure 5.10. Material, Radiation temperature vs. time for a density of 10^{-2} kg/m^3 using the implicit difference form given by Eqns. (41), (42) and (43) with timesteps of (a) 10^{-2} s, (b) 10^{-4} s, and (c) 10^{-6} s.



(a)

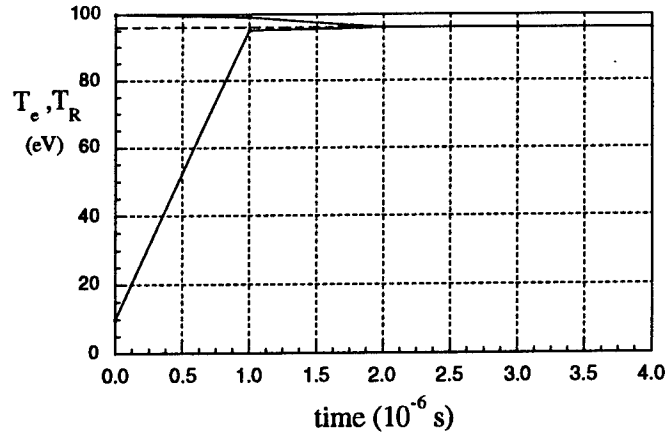


(b)

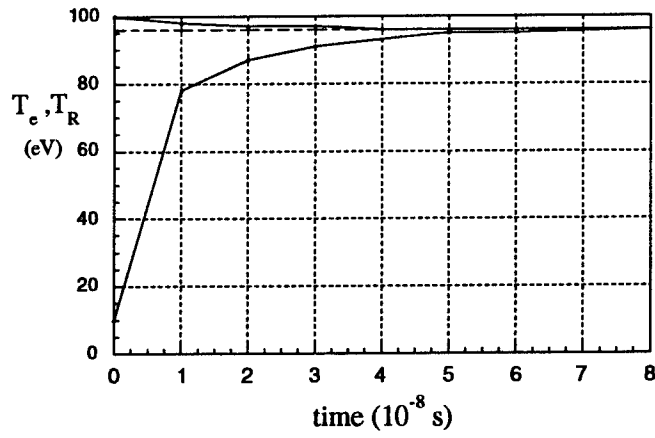


(c)

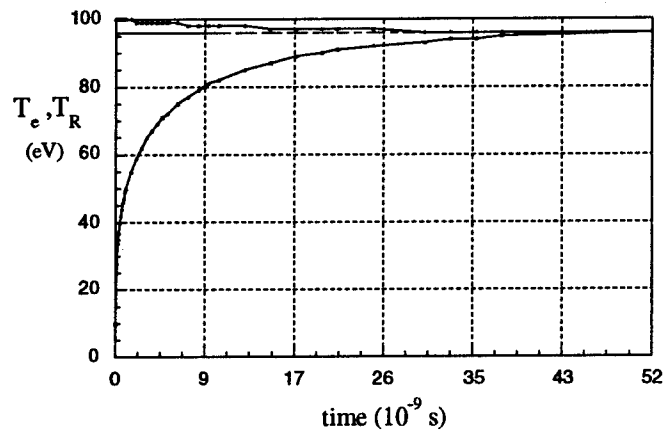
Figure 5.11. Material, Radiation temperature vs. time for a density of 1 kg/m^3 using the explicit difference form given by Eqns. (79) and (80) with timesteps of (a) 10^{-6} s, (b) 10^{-8} s, and (c) 10^{-10} s.



(a)

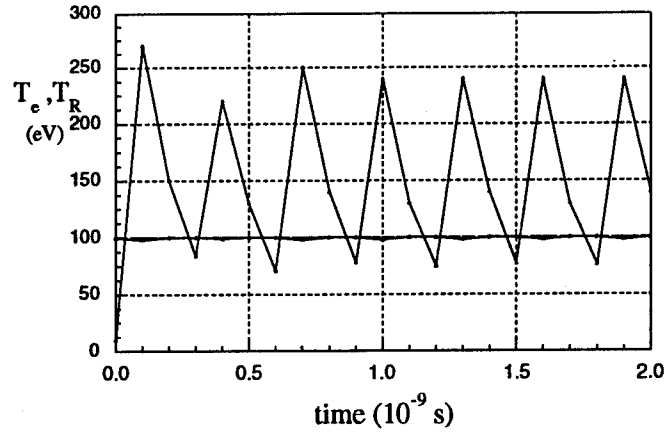


(b)

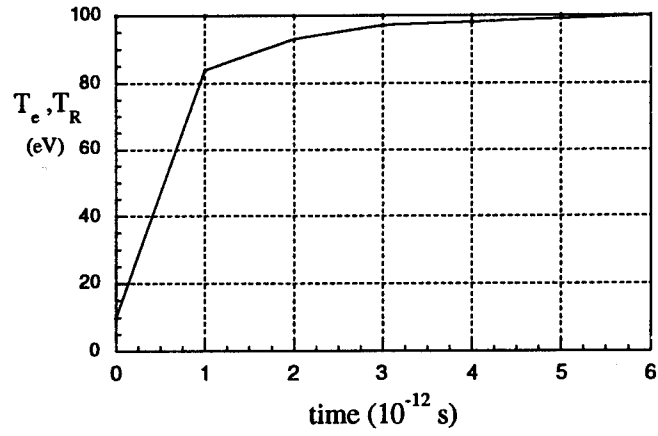


(c)

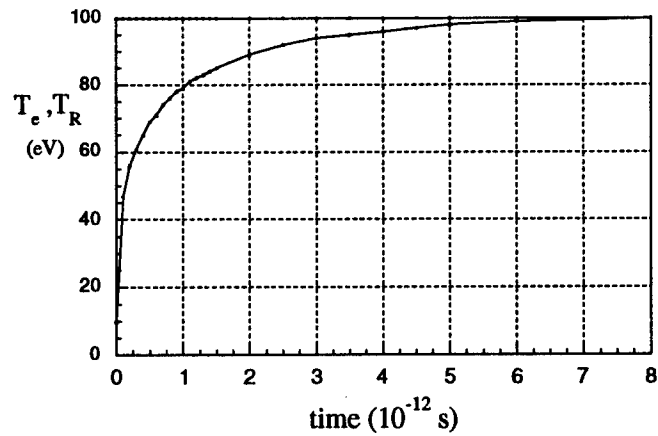
Figure 5.12. Material, Radiation temperature vs. time for a density of 1 kg/m^3 using the implicit difference form given by Eqns. (41), (42) and (43) with timesteps of (a) 10^{-6} s, (b) 10^{-8} s, and (c) 10^{-10} s.



(a)

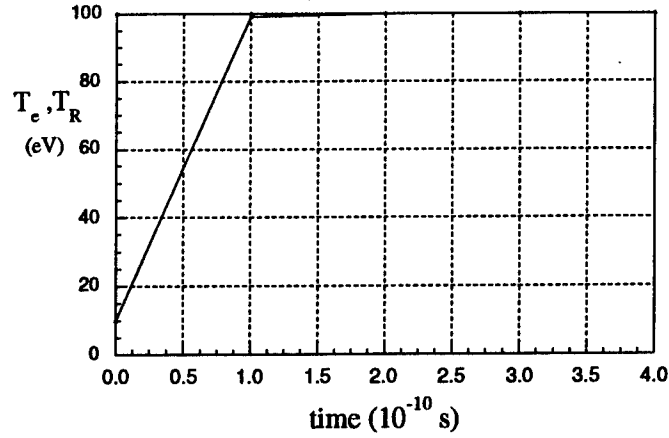


(b)

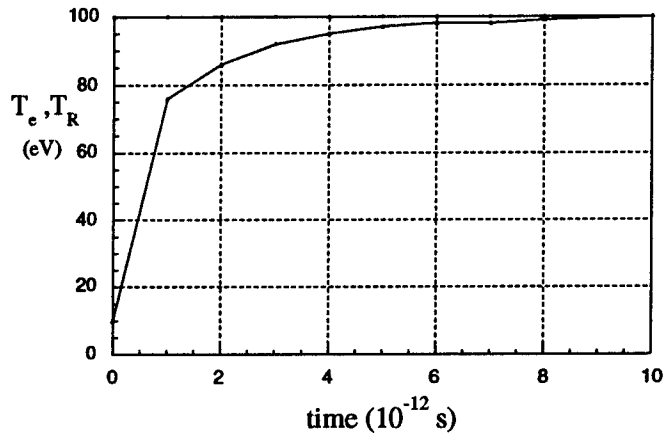


(c)

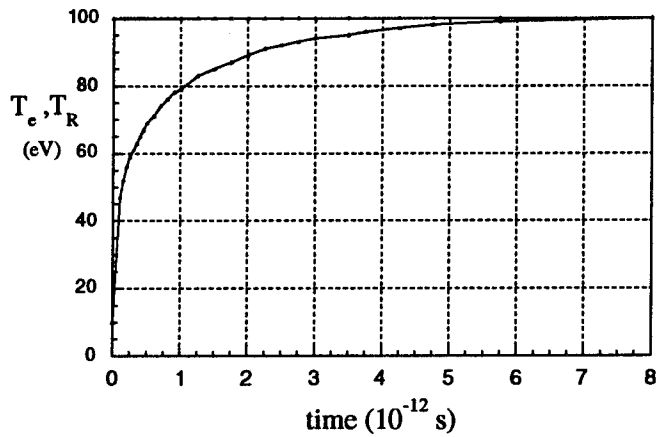
Figure 5.13. Material, Radiation temperature vs. time for a density of 10^2 kg/m^3 using the explicit difference form given by Eqns. (79) and (80) with timesteps of (a) 10^{-10} s, (b) 10^{-12} s, and (c) 10^{-14} s.



(a)



(b)



(c)

Figure 5.14. Material, Radiation temperature vs. time for a density of 10^2 kg/m^3 using the implicit difference form given by Eqns. (41), (42) and (43) with timesteps of (a) 10^{-10} s, (b) 10^{-12} s, and (c) 10^{-14} s.

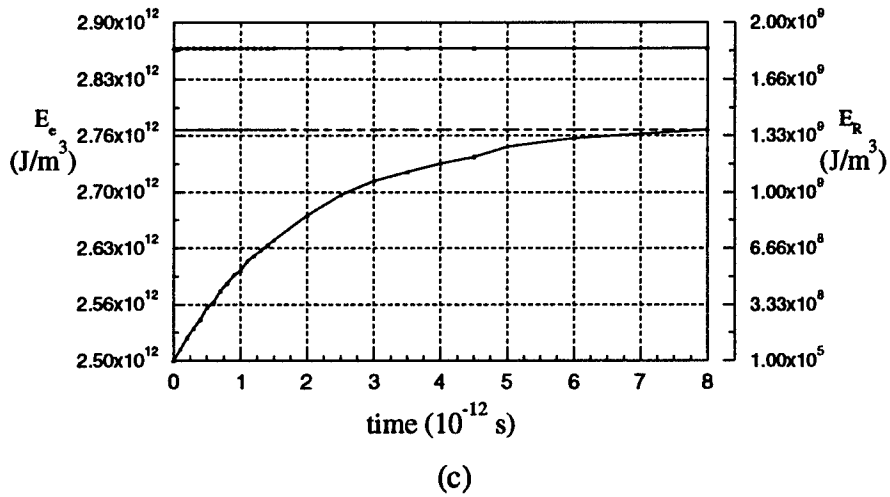
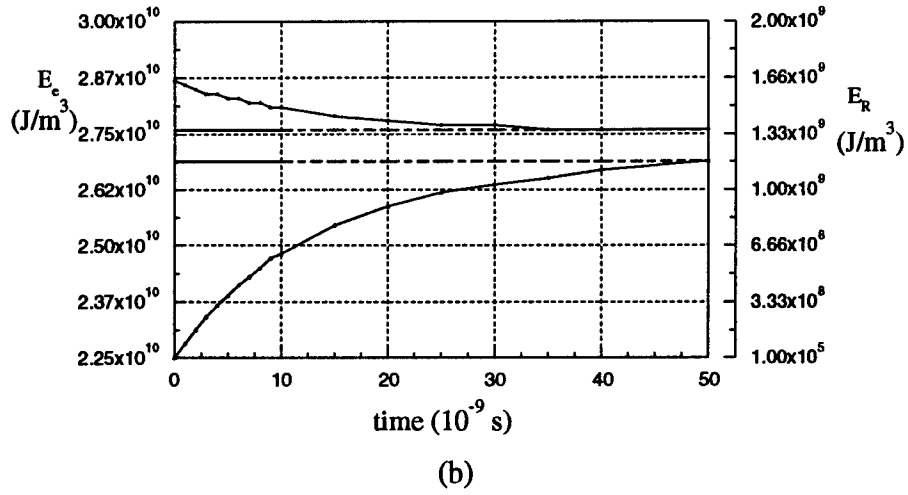
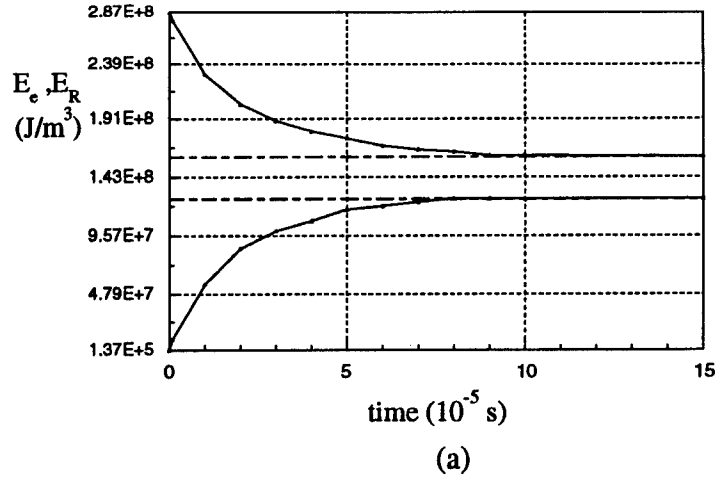
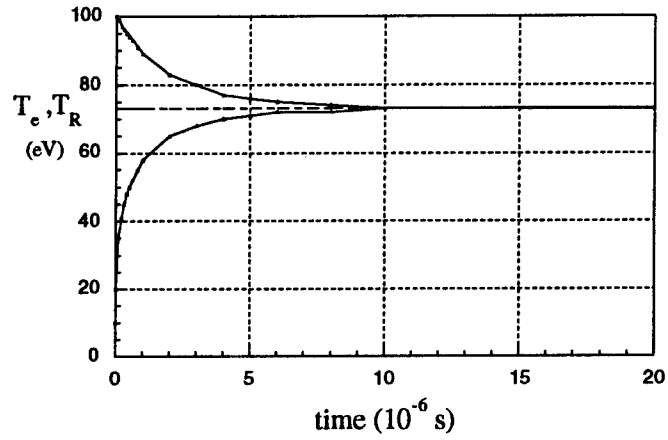
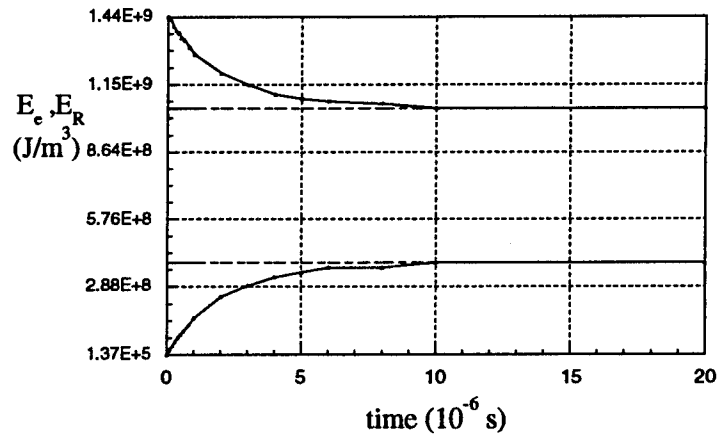


Figure 5.15. Material, Radiation energy density vs. time for (a) density of 10^{-2} kg/m^3 at a timestep of 10^{-6} s , (b) density of 1 kg/m^3 at a timestep of 10^{-10} s , and (c) density of 10^2 kg/m^3 at a timestep of 10^{-14} s for the explicit difference form given by Eqns. (79) and (80).

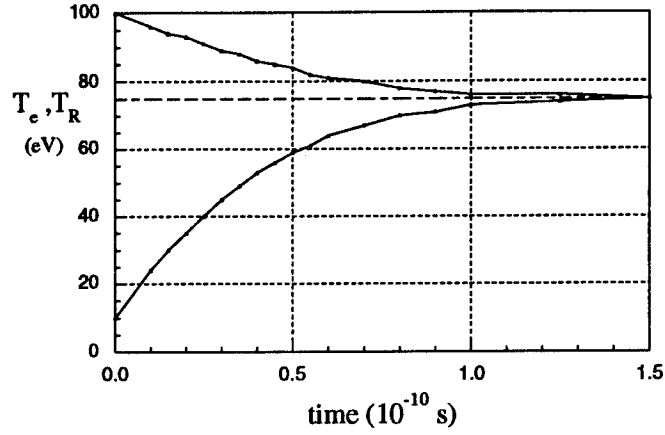


(a)

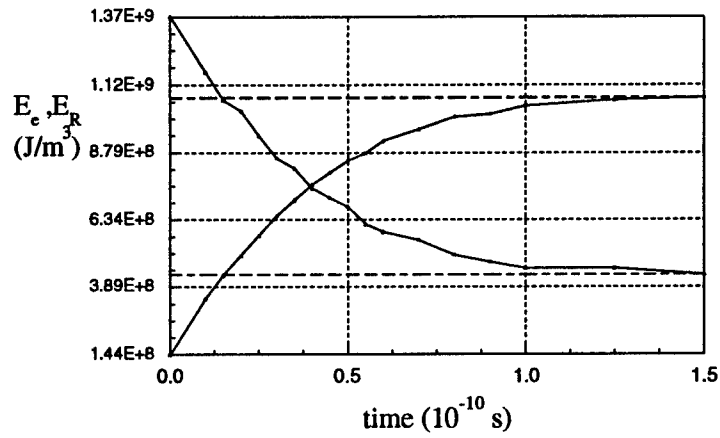


(b)

Figure 5.16. Time evolution of Material, Radiation (a) temperatures and (b) energy densities for initial material temperature of 100 eV, initial radiation temperature of 10 eV, timestep 10^{-14} s for the implicit difference form given by Eqns. (41), (42) and (43). Material density is $5. \times 10^{-2} \text{ kg/m}^3$.



(a)



(b)

Figure 5.17. Time evolution of Material, Radiation (a) temperatures and (b) energy densities for initial material temperature of 10 eV, initial radiation temperature of 100 eV, timestep 10^{-14} s for the implicit difference form given by Eqns. (41), (42) and (43). Material density is $5. \times 10^{-2} \text{ kg/m}^3$.

5.4 Additional Benchmarking

In the last two sections, the physical processes of radiation diffusion and electron-radiation coupling were examined separately for a static medium. Further benchmarking involves treating these two processes together and taking into account the actual dependence of the radiative conductivity on material temperature. Additional complexity can be introduced by permitting pressure gradient effects which generate fluid motion. Such test problems, along with those in section 5.2, demonstrate the ability of the code to model the correct physics in a regime where radiation diffusion is most applicable - the thick regime. It is also important to examine the flux-limited form of the radiation diffusion algorithm in a regime where the material is transparent to radiation. Each of these issues are addressed in this section using the one-dimensional "hot" wall problem. Specifically, the following test calculations will be considered: (1) nonlinear one dimensional diffusion with electron-radiation coupling in a static opaque medium, i.e., a radiation analog to the Marshak wave, (2) nonlinear radiation diffusion with electron-radiation coupling and hydro in an opaque, originally static material, and (3) nonlinear radiation diffusion in an optically thin, static material.

The first test problem was designed to simulate the diffusion of a radiation field into a lower temperature material in which electron-photon interactions are considered as well as the temperature dependence of the radiative conductivity. This type of problem is often referred to as a Marshak Wave [2]. The problem setup was defined by a rectangular $25 \times 10 \times 1$ m grid containing hydrogen at an initial uniform density of 10 kg/m^3 and a temperature of 100 eV. At this temperature, hydrogen is fully ionized so that the electron-photon interaction process is based purely on Bremsstrahlung (free-free) collisions. In

this case, the Rosseland mean opacity has the form [58]

$$\chi_R \sim \rho T^{-3.5} ,$$

and the radiative conductivity is related to the material temperature via

$$\kappa_D \sim \frac{c}{3\rho} T^{3.5} .$$

The driving radiation field was positioned at the left boundary of the computational domain with a radiation temperature of 150 eV. The radiation temperature was set to 100 eV within the grid and at the right boundary. For these conditions and physical domain, the material remained thick throughout the simulation, as required for the Marshak class of problems. Furthermore, the material energy density and radiation energy densities were initially within three orders of magnitude ($3.1 \times 10^{11} \text{ J/m}^3$ and $1.37 \times 10^9 \text{ J/m}^3$, respectively). This enabled the material to reach its maximum absorbed radiation capacity in minimal time, permitting the Marshak wave to propagate on a timescale related to the diffusion time based on a material temperature of 100 eV.

The computational grid was comprised of 32 by 16 zones, giving a cell size of 0.781 m in the direction of radiation flow. For the original material conditions, the photon mean free path was 0.87 m, just over a cell length in distance. Throughout the calculation, this value never exceeded two cell widths - at 150 eV, the photon mean free path is $1.54 \sim 2(0.781)$. A timestep on the order of the radiation diffusion time across a cell, 10^{-9} s, was taken.

Figure 5.18 displays the time evolution of the radiation energy density for the Marshak Wave problem. These plots, along with those in the figures that follow, were produced using the MACH2 graphics slice capability and graph the cell-centered energy density as a function of position. The solution depicted in Figure 5.18 compares favorably on a qualitative basis with computational solutions and the analytic Marshak-wave similarity solution

described in Mihalas and Mihalas [2]. The radiation field at a given location diffuses at a rate dependent upon the local material temperature, reaching a steady state distribution by 3.0×10^{-5} s. Slice plots of the radiation temperature and the material temperature at $10 \mu\text{s}$ are shown in Figure 5.19. These profiles are exactly the same, indicating that the radiation field and electron fluid are in equilibrium as expected in an opaque static material. Here the electron-radiation coupling time is on the order of 10^{-11} s as compared to the cell diffusion time of 10^{-9} s. Also shown in this figure are the photon mean free path and the radiative flux. Clearly, the photon mean free path remains under 1.54 m.

In reality, electron-radiation coupling will also heat a material, building a pressure gradient which induces a fluid flow. This was observed to occur in the above problem by allowing the hydrodynamic effects caused by a material pressure gradient to be included in the simulation. (Radiation pressure was neglected in this calculation.) Figure 5.20 displays the radiation energy density, the photon mean free path, and the material density and velocity at $10 \mu\text{s}$ for such a problem. A comparison of the energy density profile with the corresponding profile in Figure 5.19 shows that the radiation energy distribution is not substantially effected in this case. However, the material now has a net flow to the right with a peak velocity of 9 km/s, and the density in the region adjacent to the wall has decreased somewhat. The maximum value of the mean free path has increased slightly to 1.6 m in correspondence to the density drop near the wall.

To test the flux-limited form of the diffusion coefficient, the above problem was modified to provide material conditions which were transparent to radiation. This was accomplished by lowering the initial density three orders of magnitude to 0.001 kg/m^3 . At this density, the photon mean free path in the

material was 2.5×10^5 m, substantially larger than the box size. All other conditions were kept the same and a computational timestep of 1.0×10^{-10} s was taken. With the flux-limiter on, the radiation ceiling was set to 1.0×10^{-50} so that this term was essentially neglected in the determination of the radiation diffusion coefficient (Refer to Section 3.2). Thus, the diffusion coefficient in this problem was defined by

$$\kappa_{rad} \cong \frac{c}{3\chi_R\rho + \frac{|\nabla E|}{E}} \quad (37')$$

Figures 5.21 and 5.22 display the results of this calculation. With little interaction between material and radiation, the radiation field should propagate through the material at the speed of light. This is observed in Figure 5.21 where the radiation front, defined by large $|\nabla E|$, travels through the material at a velocity close to 3×10^8 m/s. In the regions preceding the front and behind the front, the gradient in radiation energy density is small, and the radiation diffuses through the problem domain with a diffusion coefficient defined by the dominant of the two terms in Equation (37')

$$\frac{3\chi_R\rho}{c}.$$

This dependence of the diffusion coefficient on the size of the gradient in radiation energy density can be seen in Figure 5.22 (a) and (c). From Figure 5.22 (a), the radiative flux at the radiation front can be calculated and compared to that found in Figure 5.22 (d). Comparisons show that this value is cE , the value of the radiation flux in the thin material limit. This is approximately two orders of magnitude larger than the maximum flux of the Marshak Wave problem shown in Figure 5.19 (d). From the above discussion, and the poor material-radiation coupling indicated by little change in the material temperature, it is evident that the flux-limiting portion of the code works properly

under thin material conditions. This will become important in the stagnation calculations of the next chapter where the outer regions of the toroid are typically considered thin.

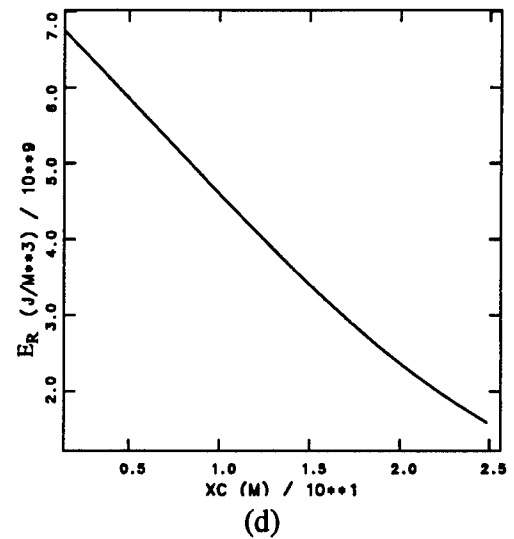
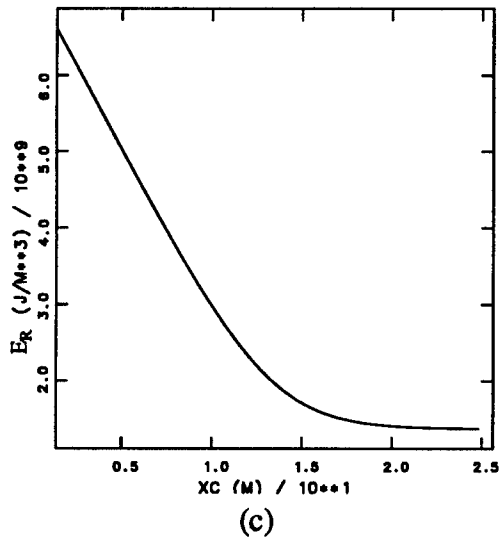
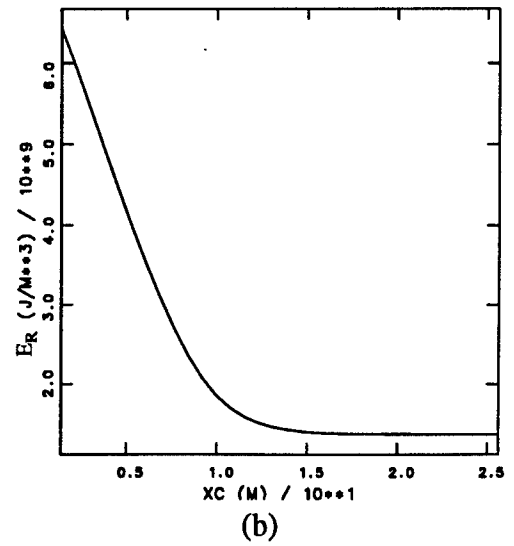
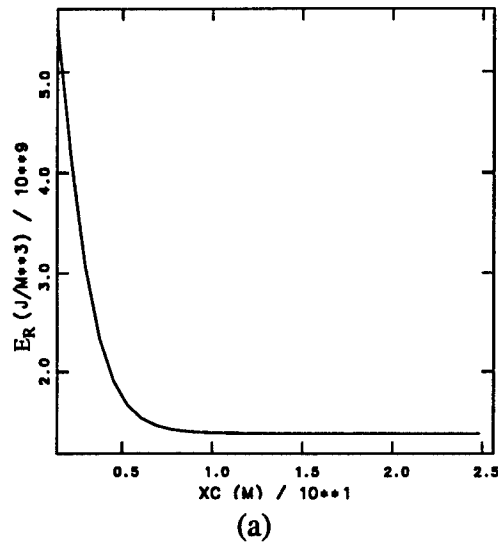


Figure 5.18. Distribution of radiation energy density along a slice in the x-direction at (a) 1.0×10^{-6} s, (b) 5.0×10^{-6} s, (c) 1.0×10^{-5} s, and (d) 3.0×10^{-5} s for the Marshak Wave problem. Material density is 10 kg/m^3 and the material temperature is initially 100 eV. The wall is at a radiation temperature of 150 eV.

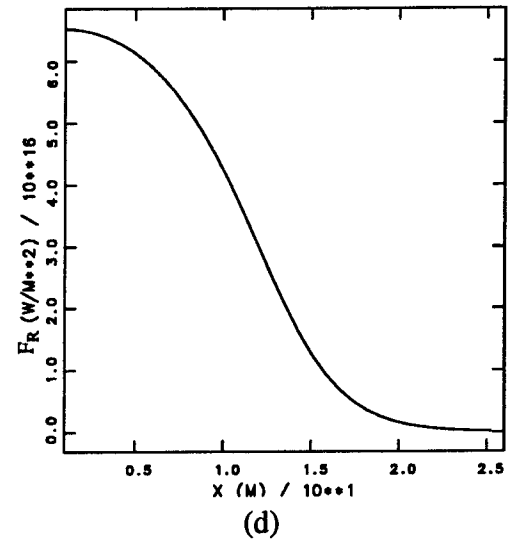
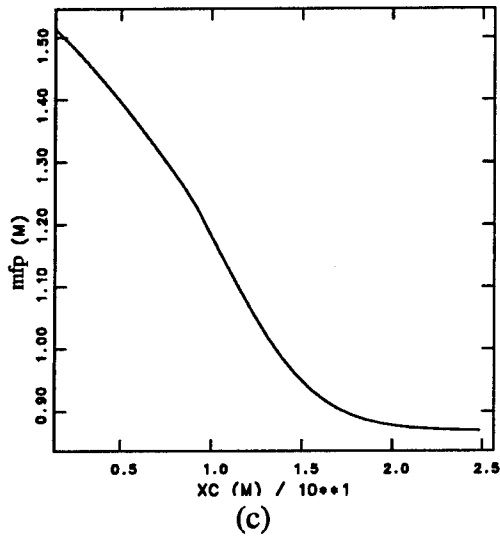
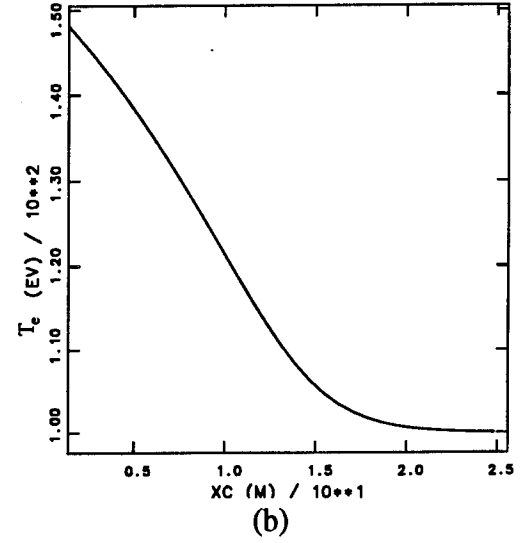
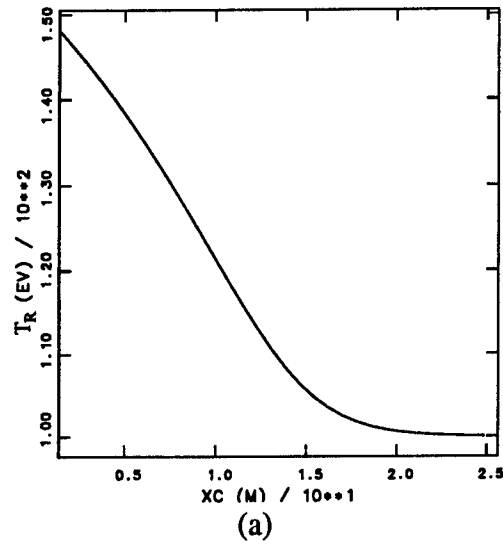


Figure 5.19. Slice plots of (a) the material temperature, (b) the radiation temperature, (c) the photon mean free path, and (d) the radiative flux at 1×10^{-5} s for the Marshak Wave problem. Material density is 10 kg/m^3 and the material temperature is initially 100 eV. The wall is at a radiation temperature of 150 eV.

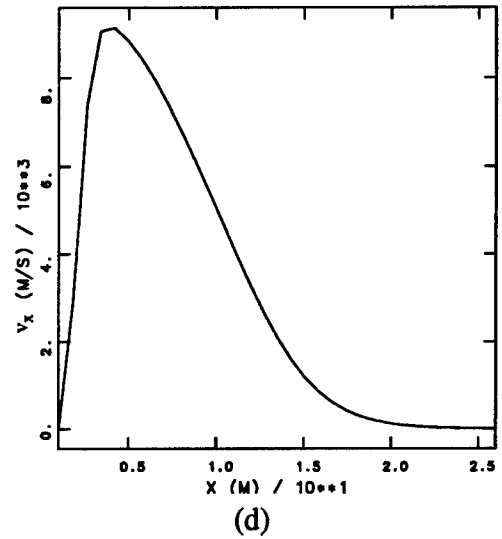
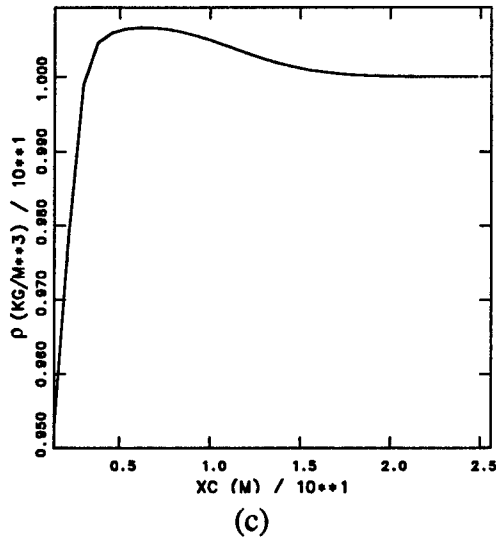
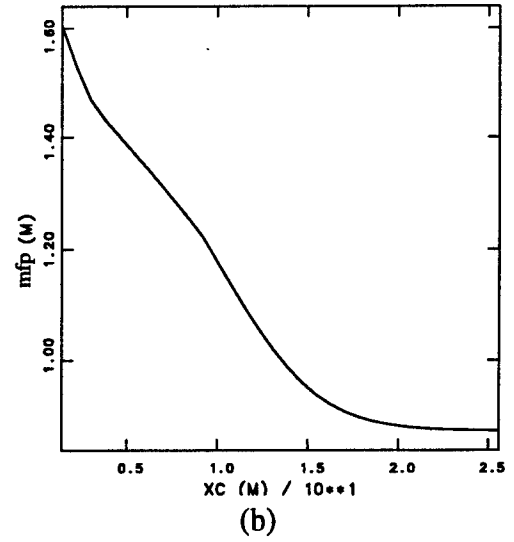
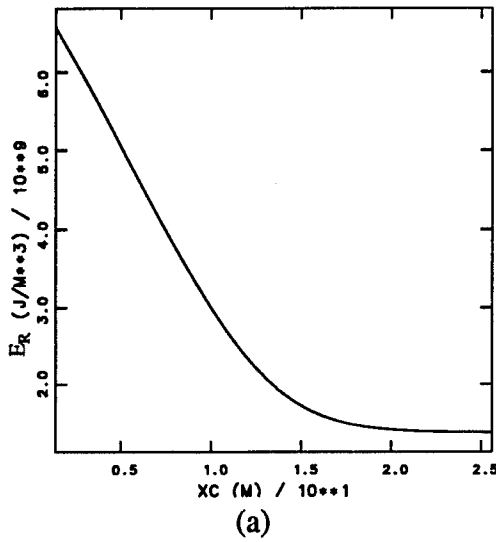


Figure 5.20. Slice plots of (a) the radiation energy density, (b) the photon mean free path, (c) the material density, and (d) the material velocity along the direction of the diffused radiation field, at 1×10^{-5} s for the "Marshak wave" problem allowing for dynamic fluid effects. Material density is 10 kg/m^3 and the material temperature is initially 100 eV. The wall is at a radiation temperature of 150 eV.

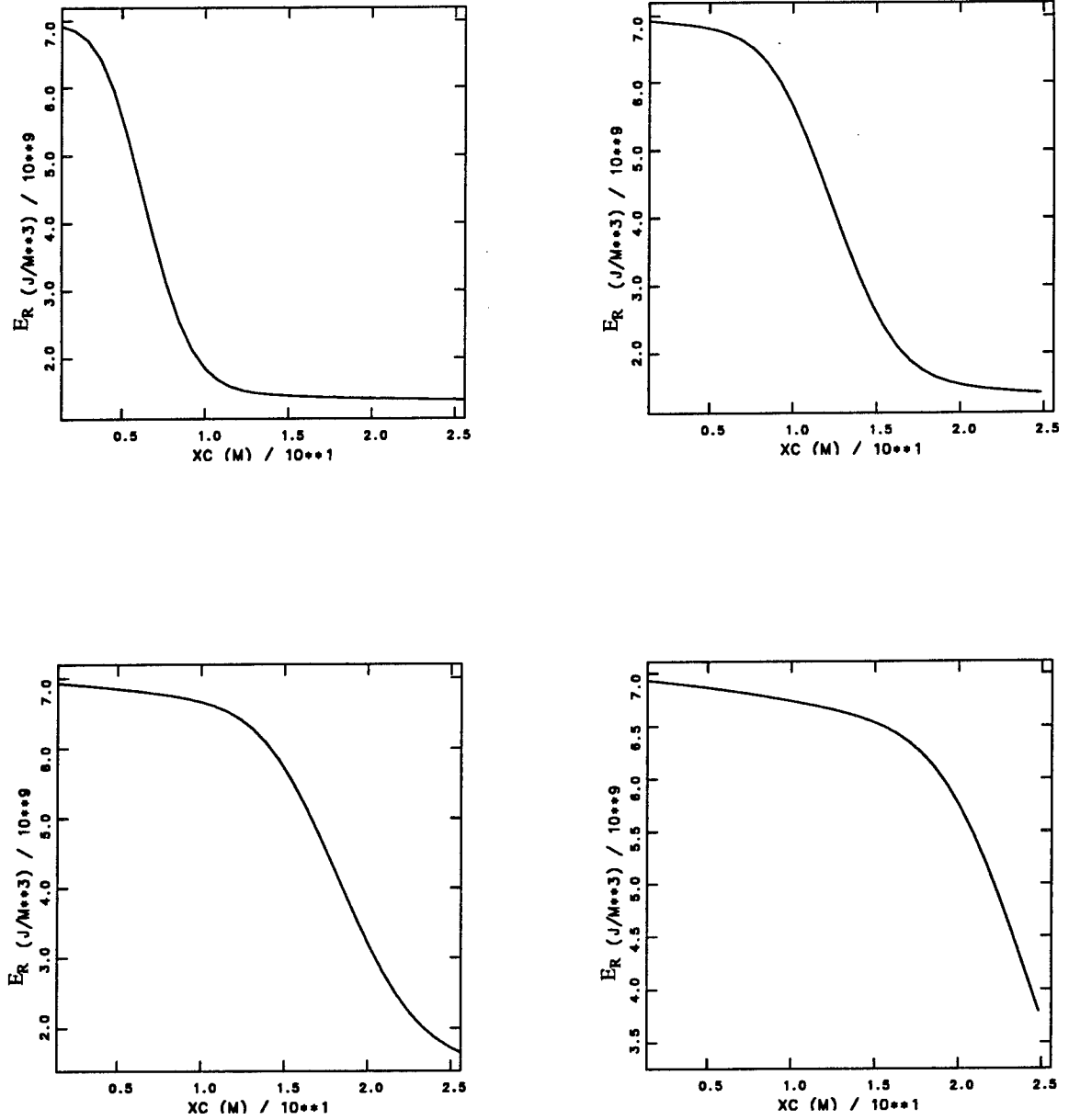


Figure 5.21. Radiation profiles showing the propagation of radiation through a thin material with the initial conditions defined using the Marshak Wave problem but with a fluid density of 0.001 kg/m^3 . The plots are at (a) 2.0×10^{-8} s, (b) 4.0×10^{-8} s, (c) 6.0×10^{-8} s, and (d) 8.0×10^{-8} s. The radiation and material temperature are originally set to 100 eV. The wall is at a radiation temperature of 150 eV.

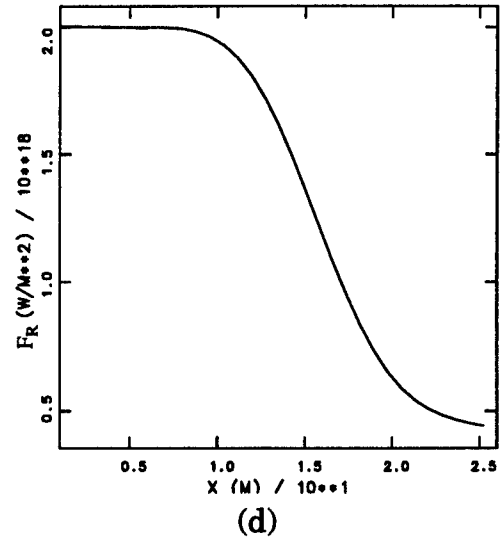
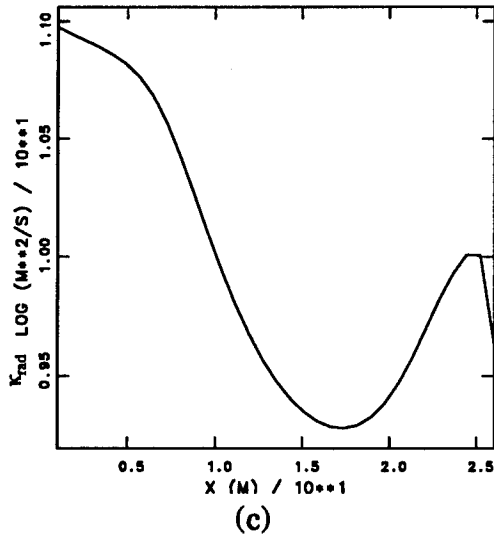
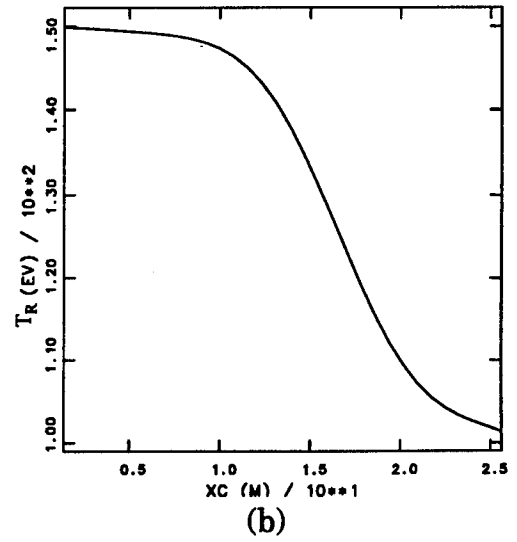
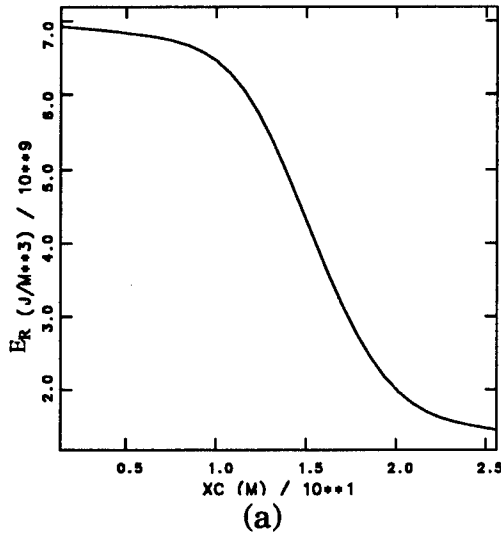


Figure 5.22. Slice plots of (a) the radiation energy density, (b) the radiation temperature, (c) the flux-limited diffusion coefficient, and (d) the radiative flux at 5.0×10^{-8} s for the thin problem illustrated in Figure 5.21. The material density is set to 0.001 kg/m^3 with the initial material and radiation temperatures at 100 eV. The wall is at a radiation temperature at 150 eV.

CHAPTER 6. COMPACT TOROID STAGNATION

In Section 1.2, the concept of using a compact toroid as a possible radiation source in the keV to 100 keV range was introduced. Under suitable conditions, the stagnation of a high velocity, high Z (high atomic number) toroid against a stationary target will result in the conversion of a large fraction of the directed kinetic energy into internal material energy and radiation. The spectrum of radiation produced and total radiated energy will depend on the post stagnation density and temperature of the material (determined primarily by shock strength), and the ratio of ion-electron and electron-radiation coupling times to the dynamic timescale of the stagnation process. In general, these values are affected by a variety of parameters, including field strength, velocity, and initial density. Understanding the role of such parameters upon the stagnation process and hence radiation production is of great interest if this application is to be successful.

In this chapter, a detailed analysis of a standard stagnation calculation is presented. This analysis includes not only an examination of the physics occurring during stagnation, but also additional simulations which explore the numerical aspect of modelling the stagnation process. In particular, these latter calculations involve varying cell resolution, adaptive grid control, computational domain and radiation boundary conditions. This discussion will then be followed by a parameter study in which the defined set of initial conditions for the standard calculation, including experimental geometry, are varied. These calculations will aid in clarifying the role of such parameters on toroid compressibility and conversion efficiency of directed kinetic energy into radiative yield.

6.1 Numerical Simulations: Baseline Calculation

At present, there are many unanswered questions and unverified predictions concerning the influence of various prestagnation toroid properties on the radiative productivity of the stagnation process. As mentioned in Section 1.2, previous calculations on compact toroid stagnation involved one dimensional slab simulations with a single component of the magnetic field, time-dependent atomic physics, and multigroup radiation diffusion. These calculations neglected the two and three dimensional nature of the toroid, which arise from the existence of three components of the magnetic field and velocity, and the nonuniform distribution of density and magnetic field. The calculations on the following pages include such multi-dimensional characteristics while addressing the role of toroid mass, directed kinetic energy, magnetic field strength, and geometry on radiative output. This is accomplished through a parameter study which should indicate the range for optimal prestagnation conditions, and verify qualitatively predicted trends.

The initial conditions chosen for the calculations presented in this chapter provide both an experimentally feasible set of prestagnation values and an optical regime in which the nonequilibrium diffusion approximation is most applicable. In the MARAUDER compact toroid experiment, present and near future capabilities of the experimental apparatus place the injected mass in the 0.1 to 10 mg mass range, a factor of 3 to a factor of 20 radial compression from an initial outer radius of 62.6 cm, and acceleration velocities in the 10 to 200 cm/ μ s range. For a mass of 10 mg and a compression of 20, conditions are obtained in which the photon absorption mean free path is on the order of the toroid dimensions. This describes a physical regime in which radiation diffusion is appropriate. Based on this, an initial set of parameters can thus be

defined. The corresponding values of other prestagnation quantities such as temperature and magnetic field can be inferred from formation values assuming isentropic compression (See Appendix A).

The parameters for a standard baseline calculation are given in Table 6.1. The simulation begins just prior to impact, with a Xenon-filled toroid already having undergone a factor of 20 compression from its original state in the MARAUDER expansion region and having been accelerated to velocities on the order of tens to a few hundred cm/ μ s. From the experimental geometry, a factor of 20 compression results in a toroid diameter of 0.89 cm with inner conducting wall at 2.24 cm and outer conducting wall at 3.13 cm. This degree of compression has not yet been attained in the present experiment. However, values indicative of prestagnation temperatures and magnetic field can be estimated using experimentally measured formation values and qualitative considerations concerning the physical processes that occur during the compression phase. The initial magnetic field configuration is taken as force free, defined by $\nabla \times \bar{B} = \lambda \bar{B}$ (This was discussed in Chapter 4). This is based on the assumption that the compact toroid is allowed to relax to a Woltjer-Taylor [46,47] state at formation and maintains this structure during volumetric compression and acceleration [43]; this ideal configuration is a reasonable approximation to the magnetic field. The peak magnetic field is determined from the experimental formation value of 0.5 Tesla (at ~ 1 m initial diameter) using isentropic relations.

The temperatures of the electrons and ions as given in Table 6.1 have been determined using experimental measurements of the electron temperature within the initially formed toroid. For a formation temperature of 5 eV [61], a factor of 20 compression leads to a prestagnation temperature of 2 keV. This value was calculated assuming the compression stage involves an adiabatic,

reversible process. In reality, the compression of the toroid will be accompanied by a loss in toroid energy through escaping radiation. (Interaction with the bounding conducting walls which cause energy loss through thermal conduction and friction effects are small and will be neglected in this discussion.) Free electrons interact with ions and neutrals through bound electron excitation, ionization of bound electrons, and bremsstrahlung transitions. As the toroid compresses, the material gains energy, each constituent of the material increasing in random kinetic energy dependent on the particular species. As the free electron population increases in energy, it simultaneously loses energy through collisional excitation and ionization processes, and photon production caused by free-free interactions. Since the toroid plasma is essentially transparent to radiation during the compression stage, any radiation which is produced leaves the toroid, lowering the electron temperature. Because there is some coupling between ions and electrons, the ion temperature will also decrease. Thus, the temperatures given in Table 6.1 are representative values which correspond physically to a decrease in energy through radiative loss. These temperatures relate closely to those used in the one dimensional calculations by M. Gee, et. al [12,13].

Figure 6.1 depicts the stagnation geometry used for most of the calculations presented in this chapter. Prior to impact, the toroid has been compressed and accelerated, travelling up toward the end of a stovepipe construct which has been capped by a solid wall. The structure of the out-of-plane component of the magnetic field is shown to provide the spatial extent and position of the toroid at the stagnation time. The three dimensionality of the problem can be visualized by rotating the stovepipe area out of the computational plane about the axis of symmetry. This forms two concentric cylinders. The box drawn about the end region of the stovepipe to the right of the center

Table 6.1. Initial parameters for 5 MJ baseline case

parameter	initial value at t=0
toroid mass	10.0 mg
toroid velocity	100 cm/ μ s
ρ_{peak}	1.85 kg/m ³
$(B_{\theta})_{\text{peak}}$	2.0 MG
T_i	1.0 keV
T_e	100 eV
T_R	50 eV
kinetic energy	5.0 MJ
magnetic energy	112 kJ
Stagnation geometry $r_{\text{inner}} = 2.24 \text{ cm}$ $r_{\text{outer}} = 3.13 \text{ cm}$	

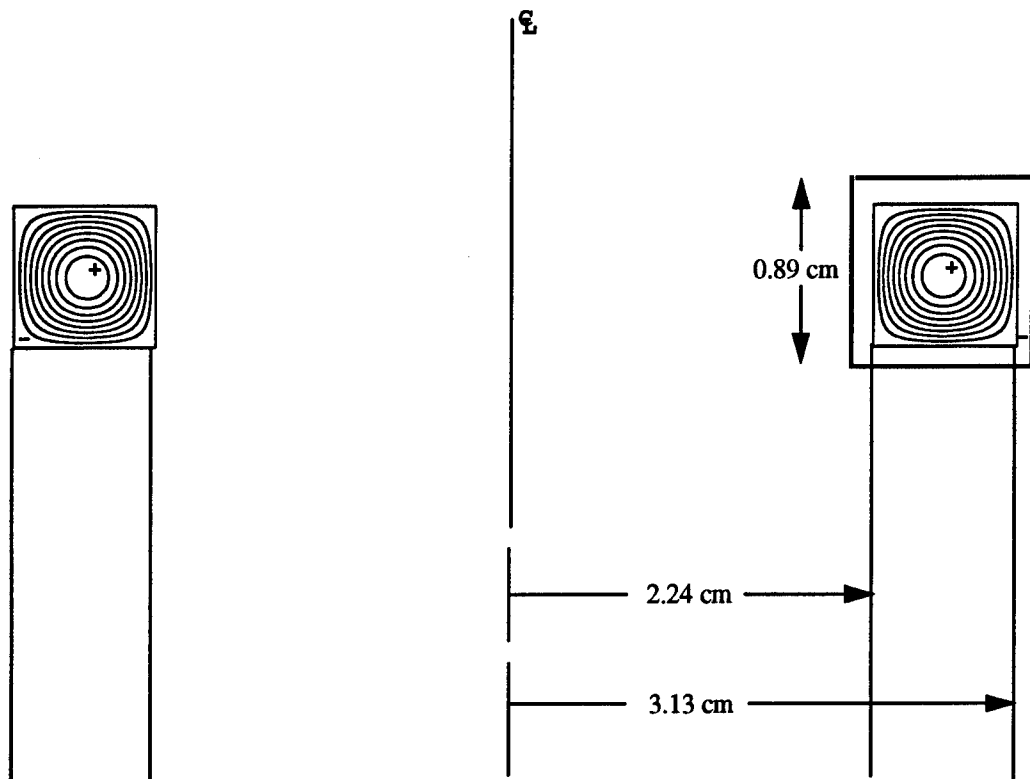
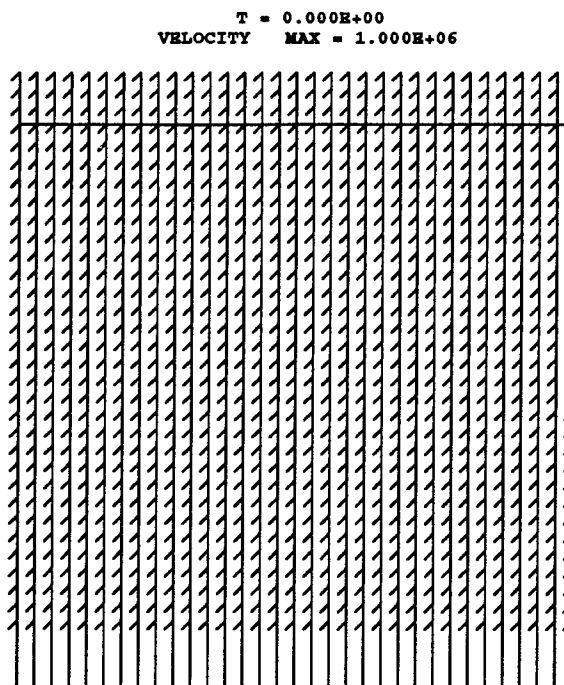


Figure 6.1. Compact Toroid Stagnation Geometry. Prior to stagnation, the compact toroid has been compressed and/or focused down to an 0.89 cm diameter. Depicted is the toroid at the end of the stovepipe ready to impact the end wall. The compact toroid spans the annular region formed by extending the conducting walls out of the computational plane about the centerline. This produces a structure consisting of concentric cylinders. The box at the upper right of the diagram shows the region contained in the simulations.

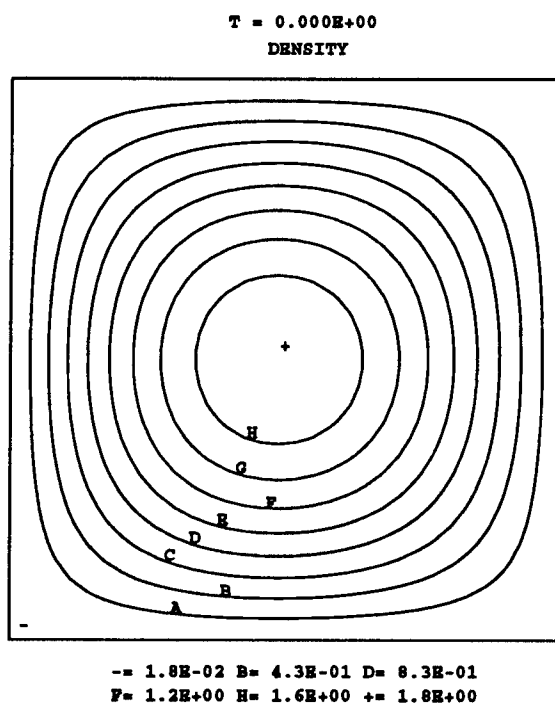
line illustrates the region that was numerically simulated. In the calculations, the electrode walls and the end wall were assumed to be perfectly conducting, reflecting, ideal boundaries. Specifically, the perpendicular component of the magnetic field was defined as zero at the walls, and neither mass nor radiation was permitted to flow across such boundaries. Any interaction, or physical process occurring with or within the end wall itself, such as ablation was ignored. The bottom boundary from which the toroid would have physically originated was considered open, providing a surface through which mass, magnetic field, and radiation could enter or leave the computational domain.

Figures 6.2 and 6.3 show the initial conditions for the baseline case. (Here the values which are found with these figures and those that follow are in units of MKSA-eV, unless otherwise noted.) The total mass of the toroid, 10 mg, was distributed such that the density isocontours follow the poloidal magnetic flux lines. Consequently, the density peaks in the center region of the toroid at 1.85 kg/m^3 and decreases toward the edges. The magnetic field configuration was force free, with the maximum magnitude of the toroidal field at 2.0 MG (200 T). The toroid was travelling towards the target wall at a velocity of $100 \text{ cm}/\mu\text{s}$. With 10 mg of mass at this velocity, the directed kinetic energy of the compact toroid was 5 MJ.

The stagnation process was numerically modelled using the three temperature capability of the MACH2 code. Each component of the fluid, including the radiation field, is described by a separate energy evolution equation. The physical processes which were accounted for in the simulation included thermal conduction, radiation diffusion, magnetic field diffusion, joule heating, ion-electron coupling, electron-radiation coupling, and of course, the hydrodynamics (evolution of fluid flow and changes resulting from fluid flow). The

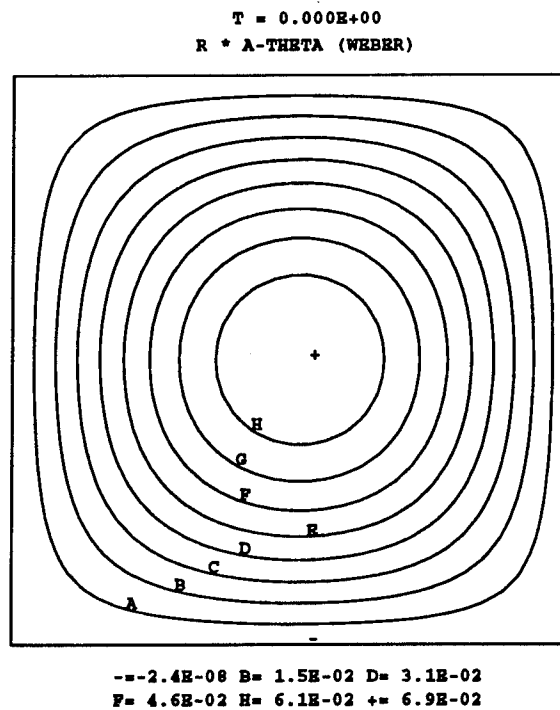


(a)

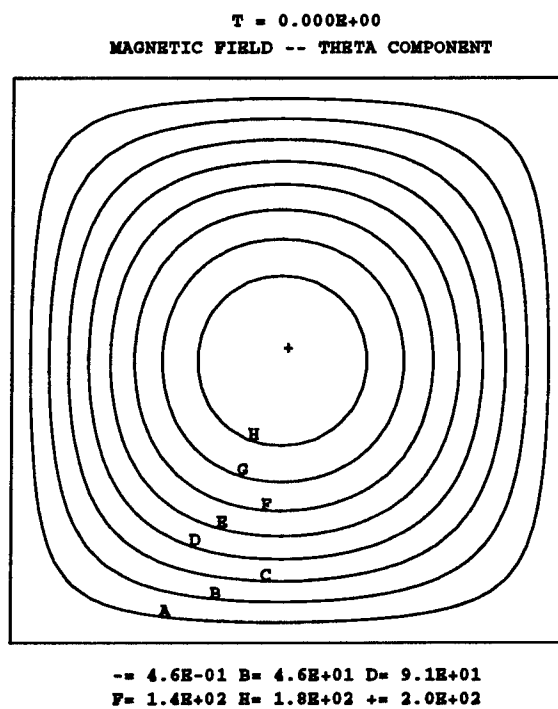


(b)

Figure 6.2. Initial conditions of compact toroid prior to stagnation, (a) directed velocity, (b) density.



(a)



(b)

Figure 6.3. Initial conditions of compact toroid prior to stagnation, (a) poloidal magnetic flux, (b) out of plane component of magnetic field.

material properties were determined from the SESAME LTE [25] equation of state tables accessed by MACH2. The thermal conduction and radiation diffusion were carried out using a relaxation factor of 0.5 and multigrid acceleration with the converge option. A convergence criteria of 1.0×10^{-5} was used to determine the accuracy of the iterated solution. The radiation diffusion was flux-limited throughout the calculation with a user-given radiative diffusion ceiling of 1.0×10^6 (See Section 3.2). The magnetic diffusion was accomplished using a relaxation factor of 0.5 and the multigrid converge acceleration technique. The convergence criteria here was set to 1.0×10^{-4} .

In general, the motion of the fluid upon impact is complex and cannot be modelled in a purely Lagrangian fashion. As a consequence, the simulations were performed using either a purely Eulerian grid treatment or Eulerian treatment with some amount of grid adaptivity. Thus a Lagrangian step was initially executed, followed by grid movement, if any, and convective transport of fluid variables. A relative error of 1.0×10^{-3} was used to define an acceptable solution to the implicit hydrodynamic portion of the code and an artificial viscous pressure was included in the velocity equation to aid in modelling shock conditions. The variables after the Lagrangian step were chosen to be centered in time, i.e., the physical quantities going into the transport are advanced by half the difference between the updated Lagrangian value and the value prior to the Lagrangian step. The advection of these quantities was then carried out using a van Leer [26] interpolation scheme for determining fluxes at cell edges.

By default, the specific internal energy, as opposed to the total energy, is the energy quantity that is advected in MACH2. Previous calculations indicated that numerical inaccuracies caused the energy to be insufficiently conserved during the stagnation process (See Appendix C for more discussion). To

overcome this difficulty, the option of convecting a total energy, defined as the electron internal plus kinetic plus magnetic, was utilized. Upon transport, the electron internal energy is extracted from the advected value of the total energy. This procedure allowed any energy loss caused by the inaccurate advection of magnetic flux and fluid momentum to be placed back into the energy of the electron fluid, solving the problem of global total energy loss.

The stagnation of the baseline case is illustrated in Figure 6.4, displaying the evolution of the out-of-plane component of the magnetic field. As the toroid initially strikes the end wall of the stovepipe, the material density increases at the impact surface; individual particles adjacent to the wall prior to stagnation upon impact reflect off the wall and into the incoming stream of particles constituting the forward edge of the prestagnated portion of the toroid. This increase in density is accompanied by a rise in internal energy as the directed kinetic energy of the particles is converted into random thermal energy. On a microscopic scale, this conversion occurs through collisional processes over a small region of space adjacent to the wall. The energetic, high velocity particles disperse their kinetic energy in this region through primary and secondary collisions. The size of this region remains small compared to toroid dimensions, since the particle momentum is randomized over a few mean free paths.

The rise in internal energy is manifested in a dramatically sharp increase in macroscopic fluid temperatures and pressure in this region. Thus, a discontinuity in the thermodynamic variables, or a shock, is formed at the toroid-wall interface. Initially, it is the ion component of the fluid which preferentially gains thermal energy as the toroid passes through the shock region. This is evident by looking at the ratio of the relaxation, or equilibration, times

for the electron and ion fluids [6]:

$$\frac{\tau_{eq}^{ee}}{\tau_{eq}^{ii}} = 0.0235 \frac{Z^4 n_i}{A^{1/2} n_e} \left(\frac{T_e}{T_i} \right)^{3/2} . \quad (84)$$

Here the variable Z stands for the ion charge, and A , the atomic weight. Making the assumption that the pre-stagnation temperatures for the most part are approximately equal at 100 eV (this is actually not a bad assumption as will be seen shortly), and taking an average ionization state of the Xenon plasma as 25, $n_e \approx 25n_i$:

$$\frac{\tau_{eq}^{ee}}{\tau_{eq}^{ii}} \approx 700 .$$

This shows that the ions equilibrate on a much faster timescale than the electrons under the defined conditions. With energy relaxation times functionally similar to momentum relaxation times [6], it is clear that the ions respond faster overall to their surroundings over a shorter distance. The ions thus exhibit thermal heating caused by the conversion of kinetic energy to thermal energy before the electrons. Numerically in MACH2, this process is treated as a heating of the ion fluid followed by subsequent heating of the electrons through ion-electron coupling.

The energy gain in the ions is lost to the electron fluid despite the fact that the coupling is poor due to the low material density at the early stages of the stagnation; there is so much energy in the ion fluid, that even a small amount of coupling results in a large energy exchange between the two species almost instantaneously. The same phenomenon occurs with the electron-radiation coupling. Hence, at the onset of stagnation, a substantial fraction of the directed kinetic energy of the incoming plasma is converted into thermal energy and subsequent radiation: the ions lose a portion of their energy to the

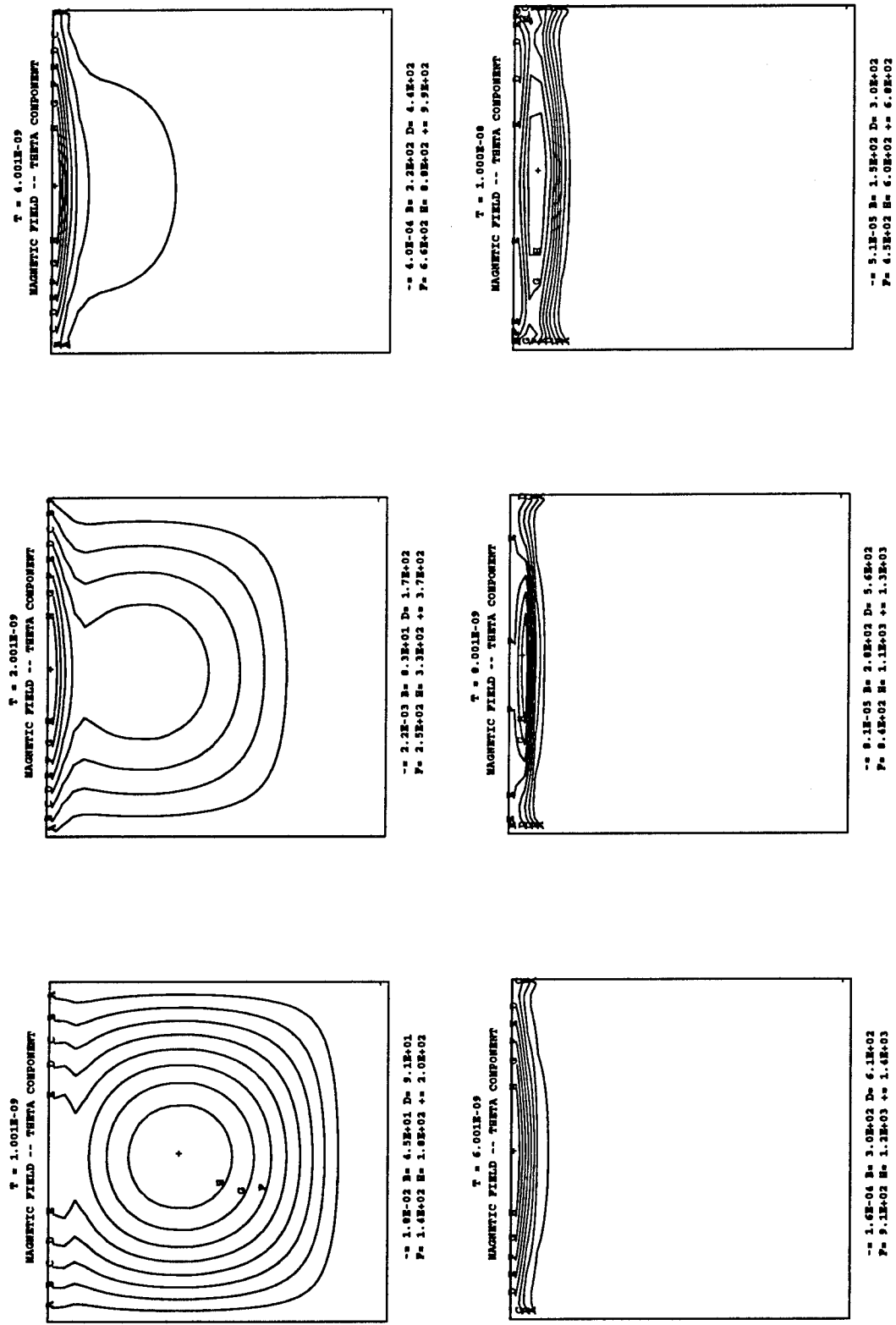
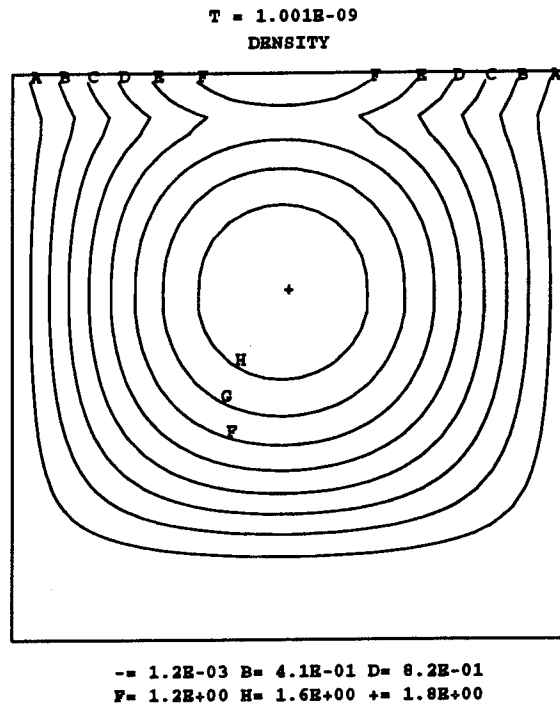


Figure 6.4. Evolution of stagnation process for 5 MJ compact toroid baseline case. Shown are out-of -plane magnetic field lines.

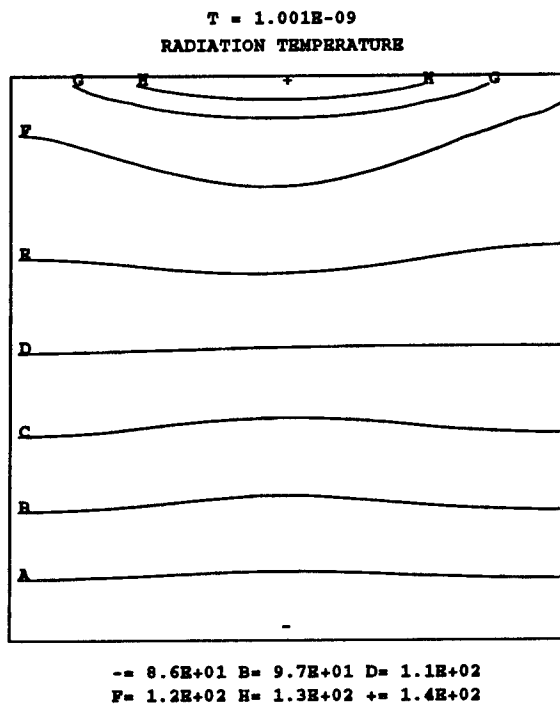
electrons, the electrons, in turn, lose most of the energy gained from their interaction with the ions to the radiation field, and the toroid radiates. The amount of radiation emitted as a result of these processes monotonically increases as the toroid continues to undergo compression, fueled by additional mass and further enhanced by improved coupling as the material there cools via radiative losses.

Figures 6.5 (a) and (b) are contour plots of the material density and radiation temperature, respectively, at 1.0 ns. Slice plots of the density, pressure, electron and ion temperatures are also shown for this time in Figure 6.6. The slices were taken vertically along the direction of motion through the middle of the toroid. The right boundary of the plot defines the target wall and the left boundary, the bottom of the computational box of Figure 6.1. The temperatures have been plotted on a logarithmic scale. From Figures 6.5 and 6.6, it can be seen that a large fraction of the toroid has not yet compressed at 1.0 ns. The shock region is very distinct and extends over a 0.5 mm distance adjacent to the wall as shown in the slice plot of the material pressure. The ion temperature ranges from 63 keV along the wall in the shocked region decreasing rapidly down to approximately 100 eV in the prestagnation material. The electron temperature along the wall is 130 eV, but ranges from 100 eV in the section of the toroid furthest from the impact region to 125 eV near the shock interface.

An examination of the ion and electron slice plots indicate that even before a large portion of the toroid has been compressed, the ions have cooled substantially from 1 keV down to 100 eV, equilibrating with the electron fluid. This suggests that the initial value of 1 keV for the ion temperature was chosen somewhat large for the other physical conditions assumed. As the leading edge of the toroid passes through the shock, a radiation front propagates



(a)



(b)

Figure 6.5. Contour plots of the (a) density and (b) radiation temperature at 1.0 ns.

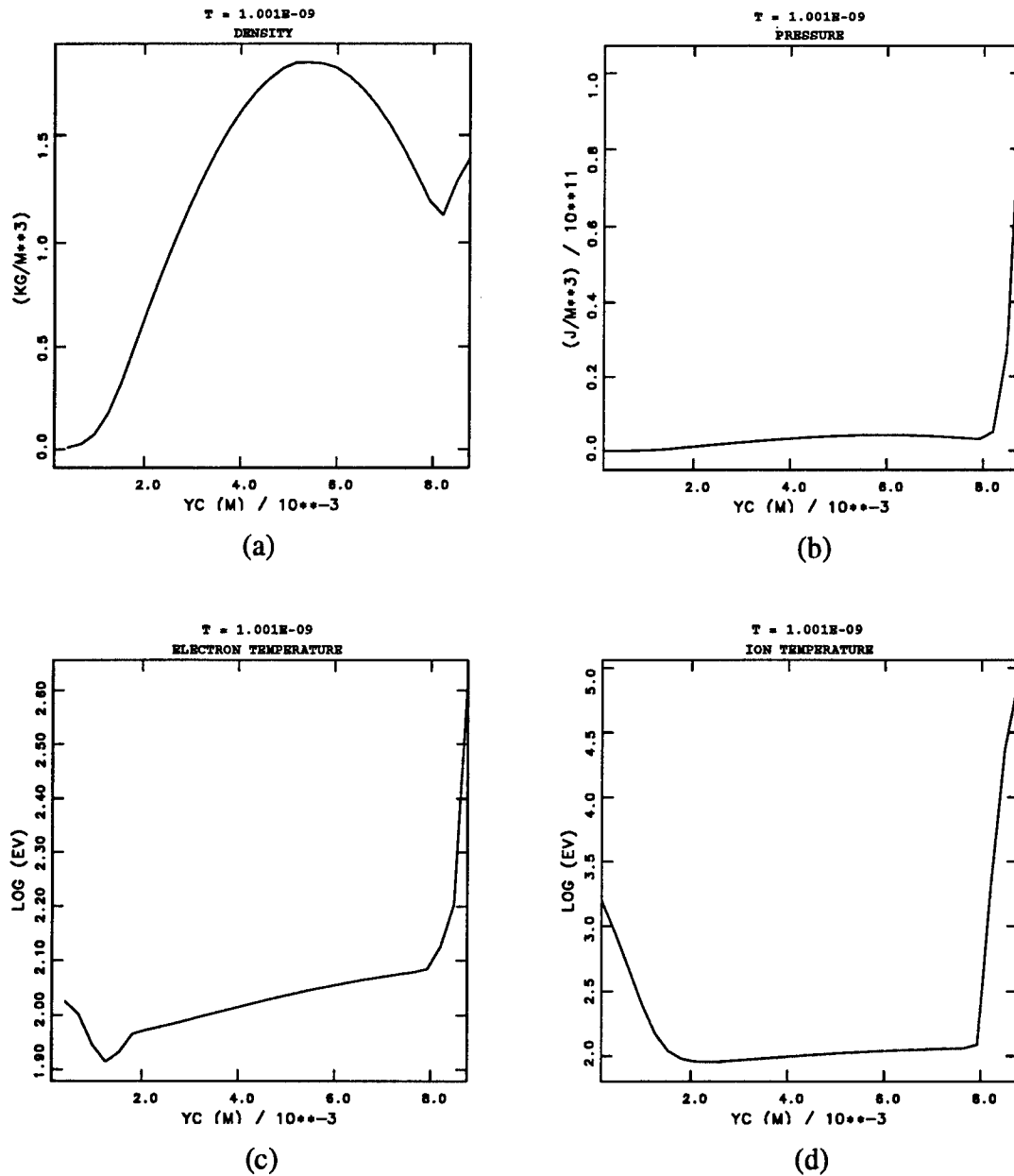


Figure 6.6. Slice plots of the (a) density, (b) pressure, (c) electron temperature, and (d) ion temperature at 1.0 ns. The slices are taken along the direction of motion through the center of the toroid. The right boundary defines the target wall, while the left boundary is the open boundary at the bottom of the computational box of Figure 6.1.

outward from the wall toward the backside of the plasma ring. The radiation front moves through the prestagnated material, coupling with the electrons and raising the electron temperature slightly across the toroid. Since the electrons near the shock interface interact with the radiation front initially, they absorb most of the energy available through coupling. As a result, their temperature is somewhat higher than that of the electron fluid at the rear of the toroid. This was mentioned above and is observed in the slice plot of the electron temperature. The Plankian mean free path, which is a measure of the ability of the radiation field to couple with the electrons, is approximately 3.0 mm over the prestagnated region which spans a length of 6.0 mm.

Peak compression occurs at about 6.2 ns. Figure 6.7 shows the density, toroidal magnetic field, radiation temperature, and radiation flux profiles at this time. Slice plots of the density, pressure, electron temperature, and ion temperature are also displayed in Figure 6.8. At peak compression, the density has a maximum value of 19 kg/m^3 at the wall, more than a factor of 10 larger than the initial peak density in the toroid. The ion temperature in the stagnation region has now dropped, ranging from approximately 200 eV in the neighborhood immediately adjacent to the wall to 10 keV at the back edge of the fully compressed toroid. The corresponding electron temperature varies from 145 eV at the wall to 160 eV at the low density toroid edge, while the radiation temperature maintains approximately 145 eV throughout the shocked region.

The decrease in ion temperature has taken place gradually during the stagnation process as more material gathers in the vicinity of the impact region. Up to a density of about 3.5 kg/m^3 , the ion-electron coupling is relatively poor and only a certain fraction of the ion energy can be lost through coupling with the electron fluid. This is observed through the large differences

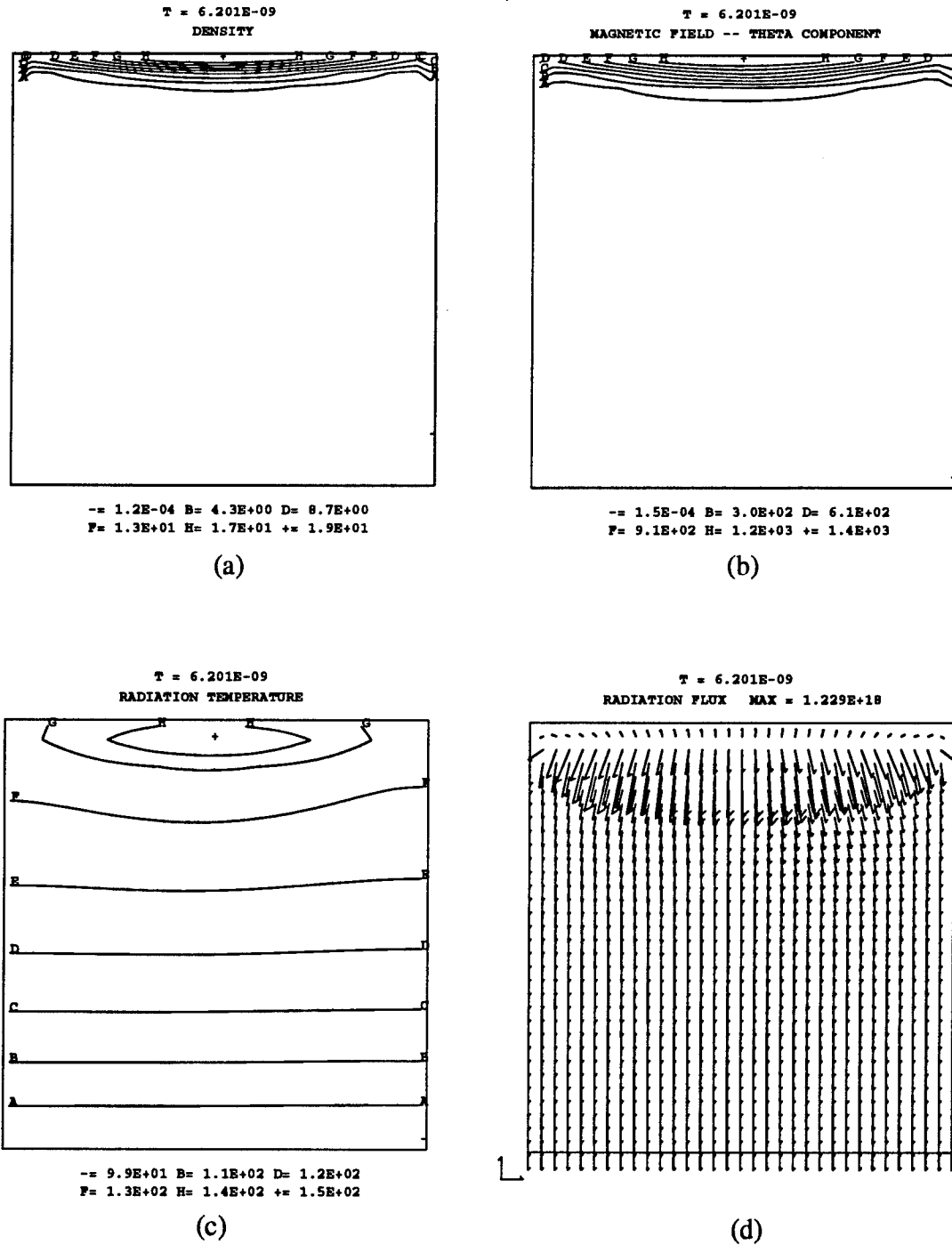


Figure 6.7. Contour plots of the (a) density, (b) out-of -plane component of the magnetic field, (c) radiation temperature, and (d) radiation flux at peak compression - 6.2 ns.

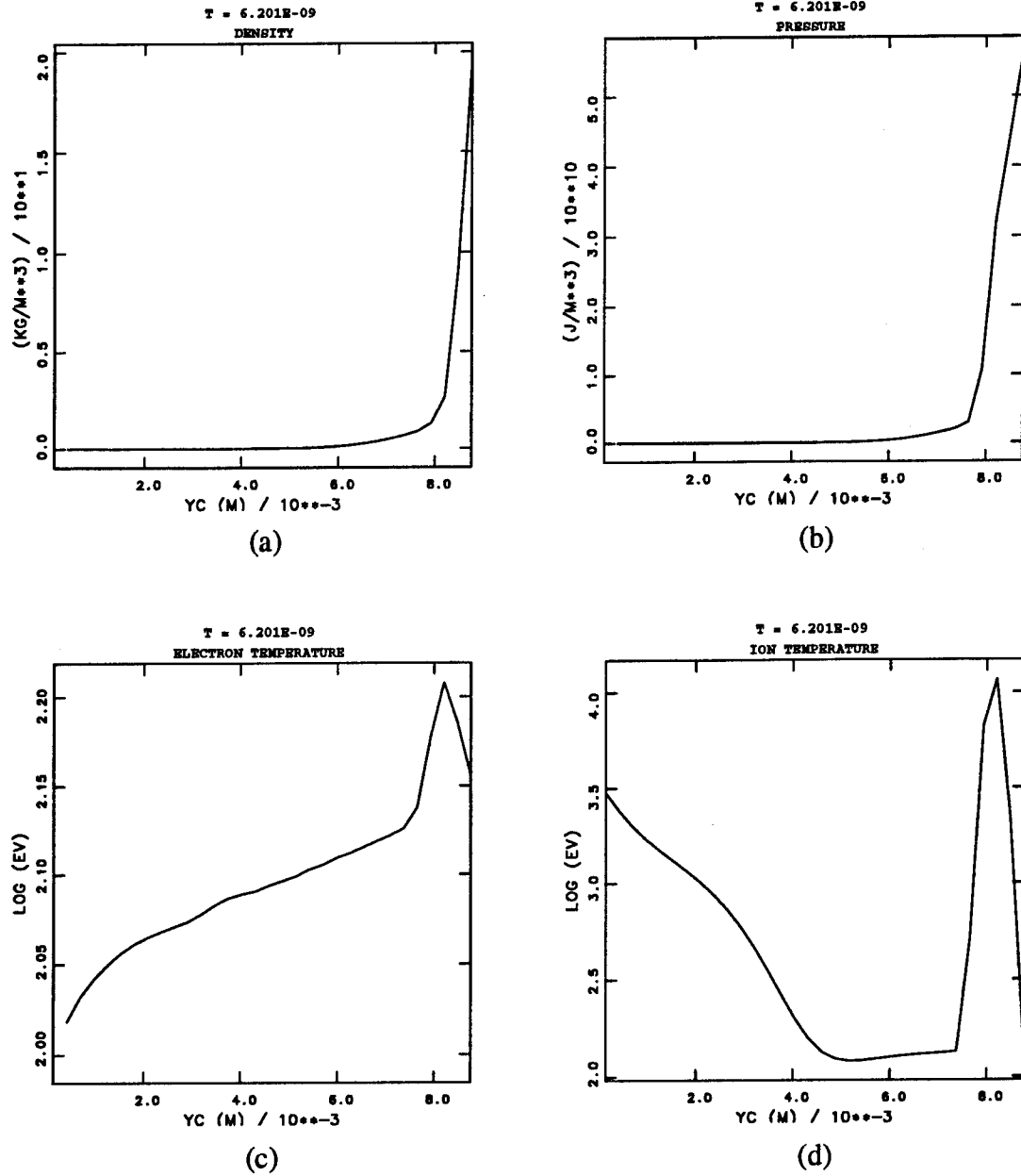


Figure 6.8. Slice plots of the (a) density, (b) pressure, (c) electron temperature, and (d) ion temperature at 6.2 ns. The slices are taken along the direction of motion through the center of the toroid.

in ion and electron temperatures. At higher densities, the ion-electron coupling becomes sufficiently strong so that by peak compression, the ion temperature has been reduced to within a factor of 1.5 of the electron temperature. However, at the back edge of the compressed toroid, where the density is close to 1.0 kg/m^3 , the coupling is still fairly weak and the ions maintain a much larger temperature. Inspection of the magnetic field contour reveals that the magnetic field strength has peaked to a value of 14.0 MG (1400 T), a factor of 7 larger than the prestagnation value. The radiated power is $1.6 \times 10^{14} \text{ W}$ and the total radiated yield at this time has reached 3.7 MJ.

An estimate of the shock Mach number can be made for this problem using prestagnation conditions and the perfect gas equation of state. The Mach number is defined as [62]

$$M = \frac{v_s}{c_s}, \quad (85)$$

where v_s is the shock velocity and c_s is the sound speed, or acoustic speed, of the prestagnated material. The shock speed is essentially the velocity of the compact toroid, $100 \text{ cm}/\mu\text{s}$ or 10^6 m/s . This is the speed that an observer sitting in the toroid frame would measure as the shock moves outward from the wall and toward the observer. For a perfect gas, the sound speed can be written as [53]

$$c_s = (\gamma R T_e)^{1/2}, \quad (86)$$

with γ a dimensionless quantity defined by the ratio of specific heats, R the specific gas constant for Xenon ($R \sim 63 \text{ J/kg-deg kelvin}$), and T_e the electron temperature (deg kelvin) in the prestagnated region of the toroid. From kinetic theory, γ is equal to $5/3$ for a monatomic gas such as Xenon. Using this information and an electron temperature of 100 eV, the sound speed is then

calculated as 10^4 m/s. The value, along with the shock speed, gives a Mach number of 100, indicating that the shock is quite strong.

For a perfect gas and uniform planar one dimensional flow, the strong shock condition leads to a simple relationship between the shocked (compressed) material density and preshocked (prestagnated) material density given by [62]

$$\frac{\rho_s}{\rho_o} = \frac{\gamma + 1}{\gamma - 1} , \quad (87)$$

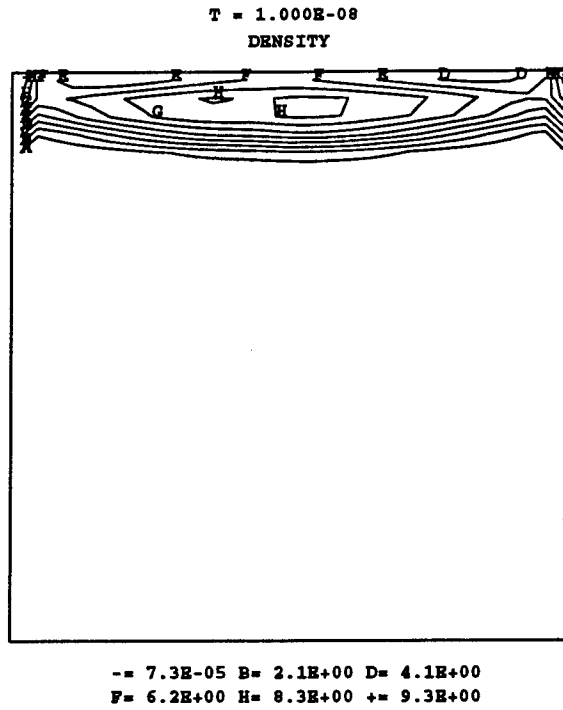
where ρ_o is the initial toroid density. For a monatomic gas in which ionization and radiation effects do not appreciably contribute to the internal energy (and hence specific heat), γ is 5/3 and this ratio is 4. In the simulation of the baseline case, this ratio is approximately 10, over a factor of two greater than that predicted by Equation (86) with $\gamma = 5/3$. (Peak density reached by the material component of the stagnating toroid is 19 kg/m^3 compared to 7.4 kg/m^3 .) This leads to an "effective γ " [18] of 11/9 or 1.22 and is a direct consequence of the ionization and excitation of Xenon electrons as the material passes through the shock, together with the radiative cooling of the stagnation region. Any initial kinetic energy that goes into the ionization and excitation of the plasma is no longer directly available for thermal energy. This keeps the material pressure at a lower value than it would otherwise have, and further compression can occur. Radiative cooling also prevents the material pressure from increasing as rapidly, thereby allowing even additional compression.

Clearly radiation losses will play an important role in the degree to which a compact toroid compresses during stagnation. The formal relationship given by Equation (86) is based on treating the shock as a adiabatic discontinuity. In this derivation, the energy conservation equation does not include any sink or source terms. Specifically, a radiative loss term is not accounted for in the

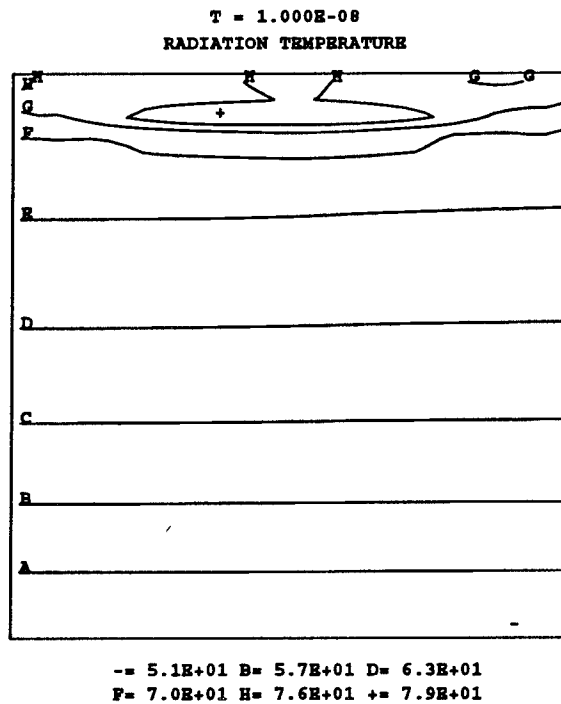
equation. The inclusion of such a term would lead to a higher compression ratio than that predicted from the strong shock condition (86) with a γ of 5/3. As the toroid radiates, the material components cool, losing thermal energy and thus pressure. As long as the total pressure (material + magnetic) in the stagnation region is smaller than the dynamic pressure exerted on it by the incoming flow, the toroid will continue to collapse, increasing in density. It is the fact that the toroid radiates significantly during compression that contributes to further collapse leading to higher densities. This, in turn, leads to greater radiation rates and overall higher radiative yield. It is interesting to note that for the stagnation parameters of the baseline case, it is actually the magnetic pressure which halts the toroid compression; the magnetic pressure is over a factor of twenty greater than the material pressure at peak compression ($1.5 \times 10^{12} \text{ J/m}^3$ compared to $5.6 \times 10^{10} \text{ J/m}^3$).

By 10 ns, the toroid has expanded to twice the size it had at peak compression and is beginning to move away from the target wall. The peak density in the toroid has now dropped to 8 kg/m^3 , while the material and radiation temperatures within the toroid have cooled substantially, equilibrating at approximately 80 eV. Figure 6.9 shows the contour plots of the density and radiation temperature at this time. A comparison between the density profile in Figure 6.9 (a) and the magnetic field contour at 10 ns in Figure 6.4 reveal that the material distribution and magnetic field structure are closely coupled, i.e., the material is frozen to the field lines. This is the case throughout the whole stagnation process, suggesting that the magnetic field could play a significant role in effecting the degree of toroid compression. The influence of magnetic field strength on stagnation will be investigated later in this chapter.

The bulk of the radiation emitted during the stagnation process occurs within a time span of 10 ns, basically the time it takes for the toroid to fully



(a)



(b)

Figure 6.9. Contour plots of (a) density and (b) radiation temperature at 10 ns.

compress and then expand outward to a quarter of its original size. The total radiation energy output computed by 10 ns is 4.77 MJ. In terms of the initial directed kinetic energy of 5.0 MJ, this gives a conversion efficiency - conversion of kinetic energy into thermal energy into radiation - of 96%, indicating that at these initial conditions, the toroid is a very efficient radiator. The kinetic energy that is not converted directly into thermal energy goes into compressing the magnetic field (magnetic pressure resists the compression) and into the rotational velocity of the toroid ($(\bar{J} \times \bar{B})_{\theta}$ force), which develops as the toroid impacts the wall. An estimate of the energy utilized for this latter process can be obtained by looking at the total rotational kinetic energy. From numerical diagnostics, this value is 28.3 kJ, and is a small percentage of the directed kinetic energy. An additional loss mechanism is also provided by joule heating. Diagnostics indicate that the energy associated with this process is about 164 kJ, again a small percentage of the kinetic energy.

A plot of the radiated power, as measured from the bottom boundary of the computational domain, is displayed as a function of time in Figure 6.10 (a). Initially, the toroid is emitting radiation because (1) the electron fluid has a predefined non zero temperature and (2) the electrons are also radiating any additional energy obtained through coupling with the ions. As the electron temperature decreases through radiative losses, the available energy in the electron fluid is lowered and a decrease in radiated power is observed. Around 0.4 ns, the radiation caused by the impact of the leading edge of the toroid with the wall reaches the back boundary and begins to dominate the radiation rate. The radiated power is then observed to turn over and increase monotonically with time.

During the early stages of compression, the material density and electron temperatures within the stagnation region are such that the ion-electron and

electron-radiation coupling is not very efficient. At 1 ns into the stagnation, the ion temperature is 63 keV, the electron temperature 398 eV, and the radiation temperature, 133 eV. The large difference in electron and radiation temperatures at this time can be attributed to the poor coupling. The Plank mean free path at this time is 8 cm, over 8 times the length of the prestag-nated toroid. Thus, it is difficult for the electrons to radiate any of their energy away (via coupling with the radiation field), and the radiation that is produced at T_R , is much lower than that of the electrons; the fraction of the toroid which has undergone compression radiates as a volume radiator [18].

Even though the coupling is initially poor, some of the energy in the ion fluid is still transferred to the electrons. The electron temperature consequently rises, and a portion of the associated energy goes into the radiation field. Because of the energy storage capacity (i.e., large specific heat) of the electrons, the amount of energy gained from the ions and lost to the radiation field does not significantly change the electron temperature. As a result, any increase in density leads to improved coupling. This is particularly true for the electrons and radiation field, and an increase in the radiation rate is observed as the stagnation progresses.

At 1.4 ns into the stagnation, the density has increased further and the Plank mean free path in the compression region has gone from a value of 8 cm to approximately 1 cm. This improved coupling can be seen in the values of the electron and radiation temperatures, 172 eV and 142 eV, respectively. (Within 0.4 ns, the temperature difference went from a factor of 3 down to 30 eV.) This jump in the coupling efficiency has been traced to the Xenon equation of state tables and is speculated to be a real effect caused by the change in absorption-emission properties as the outer bound electron distribution shifts from a filled L shell to a partially filled M shell. This is illustrated in Figures 10 (c) and (d).

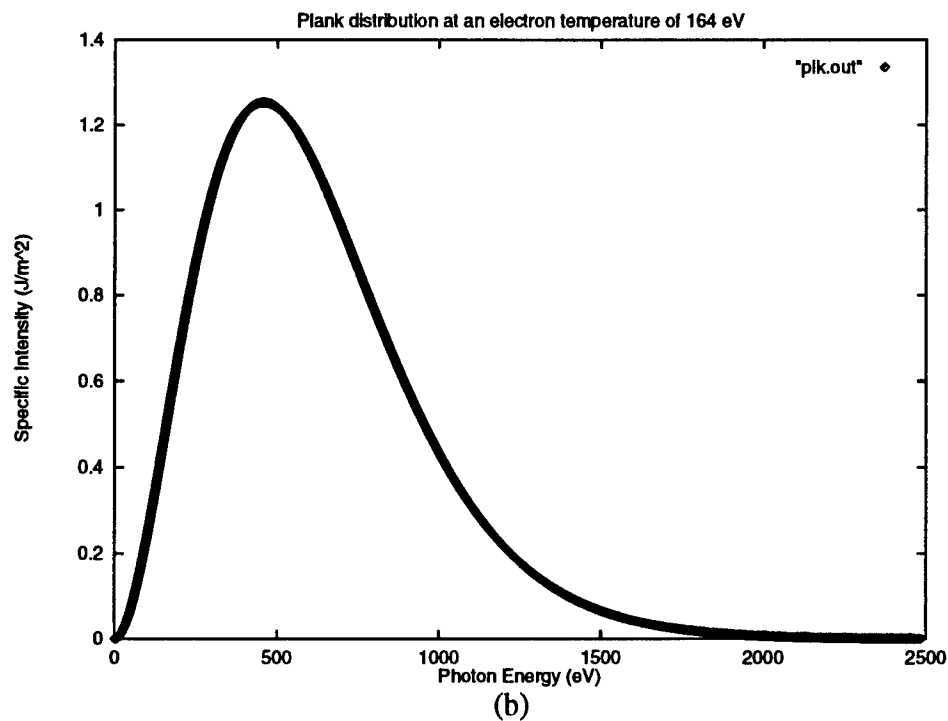
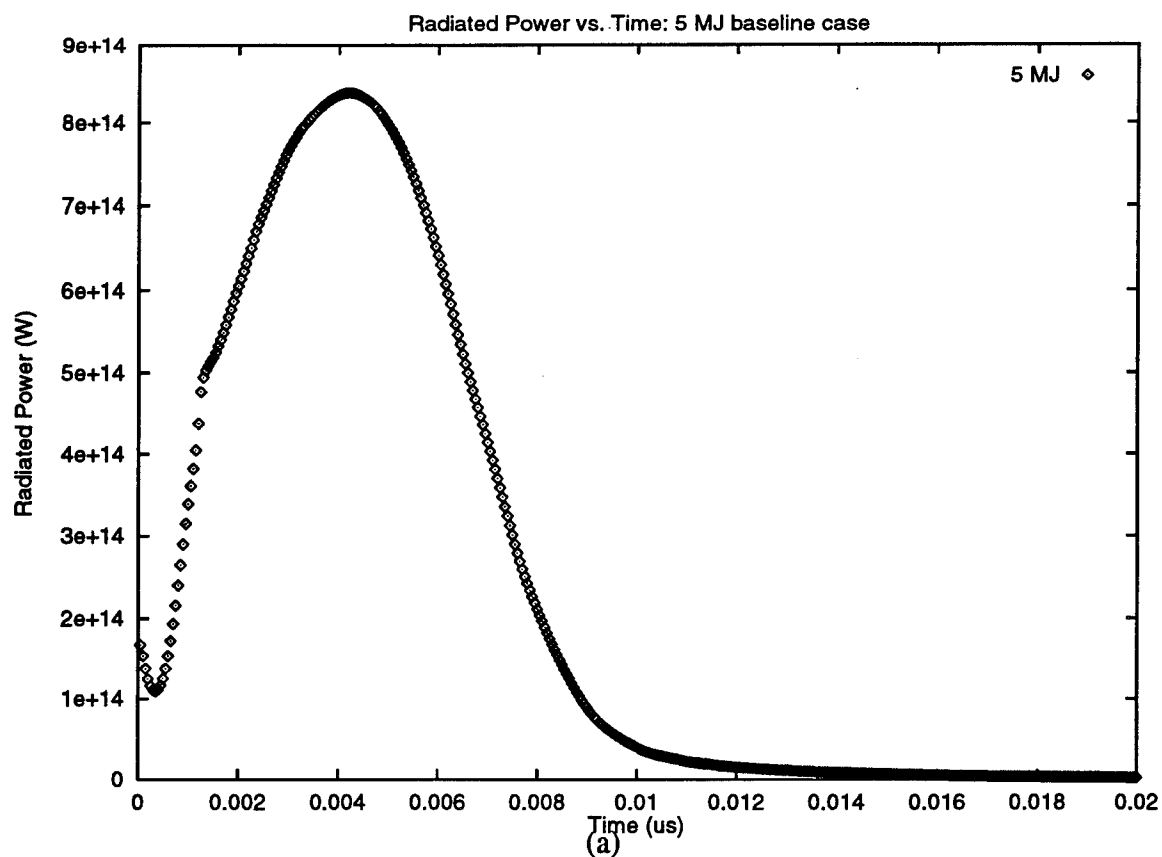


Figure 6.10.(a),(b). Plot of (a) Radiated Power vs. Time for the 5 MJ kinetic energy baseline case and (b) Plank distribution at 4.2 ns, time at which radiated power peaks. Electron temperature here is 164 eV.

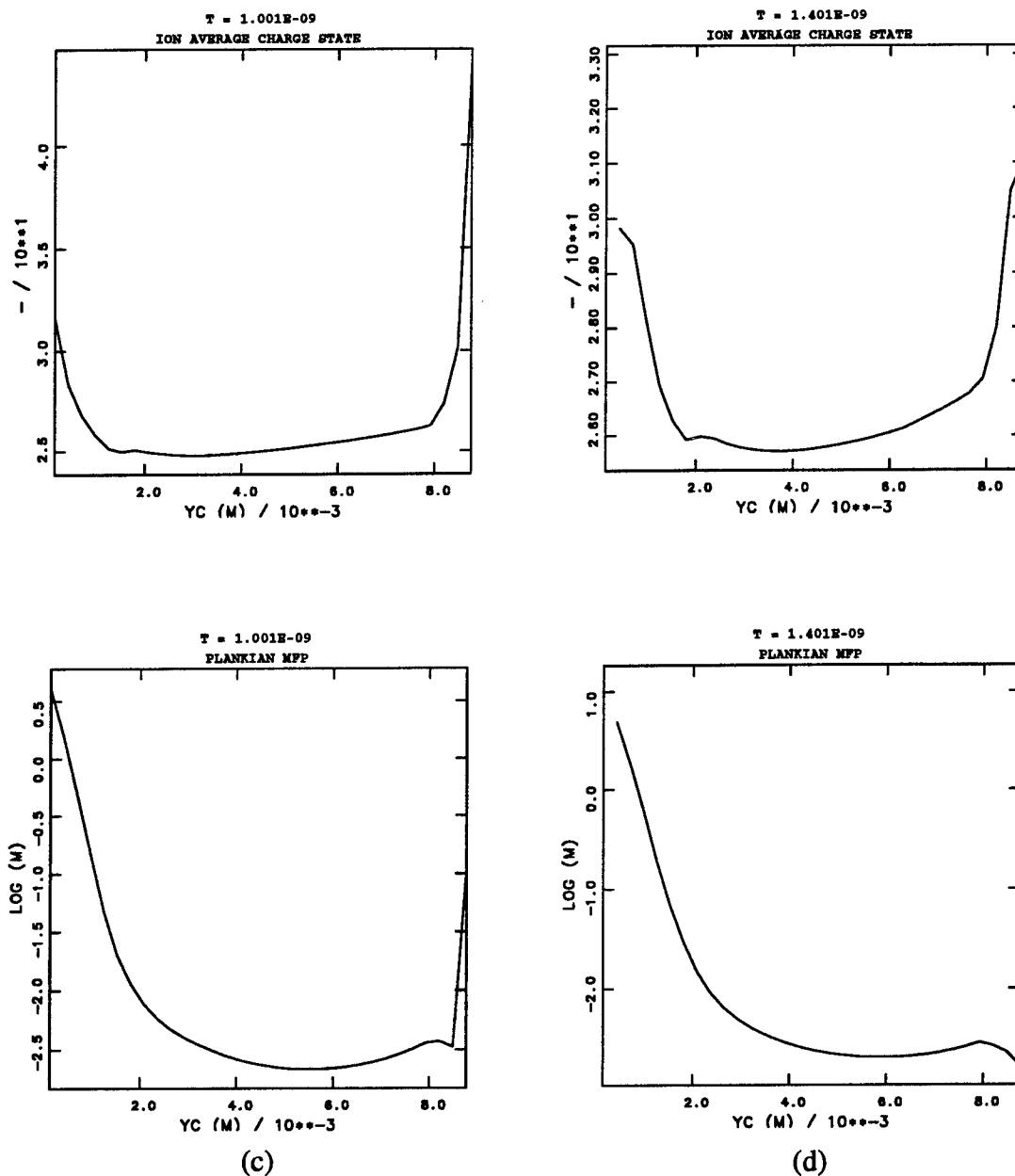


Figure 6.10 (c),(d). Slice plots of the ion average charge state and Plank mean free path at (c) 1 ns and (d) 1.4 ns into stagnation. The slices are through the center of the toroid with the right side of the figures defining the stagnation wall and the left side, the open flowthru boundary. The plots indicate that in going from an ionization state of $\bar{Z} \sim 43$ to a state with $\bar{Z} \approx 31$ (from a filled L shell to a partially filled M shell), the bound electron distribution significantly modifies (increases) the opacity and the Plank mean free path drops rapidly from 8 cm down to 1 cm.

In any event, the improved coupling forces the electron and radiation temperatures to rapidly move closer together. This leads to a decrease in the rate of change in radiation energy density and is responsible for the visual transition in the slope of the radiated power curve.

With improved coupling, the electrons are able to share more of their energy with the radiation field, and as noted, the electron temperature drops. As the toroid continues to compress, the density increases and the Plank mean free path becomes correspondingly smaller. By 2 ns the Plank mean free path is on the order of the stagnation region. The photons originating within this region are thus more likely to be absorbed, re-emitted, and scattered as they travel, and the stagnation region becomes more like a surface emitter radiating at a temperature $T_R = T_e$. With further compression, this value becomes even lower, reaching a minimum of about 0.1 mm at peak compression. Throughout the rest of the stagnation, i.e., up to 20 ns, the Plank mean free path never gets above 1 mm, and the compressed toroid continues to resemble a surface emitter.

As shown in Figure 6.10 (a), the peak in radiated power occurs at 4.2 ns and is 8.37×10^{14} W. By this time, a large fraction (~ 95%) of the toroid mass has been compressed, and the source of converting directed kinetic energy to thermal energy depleted. In addition, a large portion of the energy contained in the ion fluid has already been transferred to the electrons and radiated away. Hence, as the stagnation proceeds, the energy remaining in internal energy becomes increasingly smaller and the amount of emitted radiation begins to decline. The radiation rate has dropped to 5% of the peak value by the time the toroid's outward expansion is visually significant at 10 ns. The full width of the radiation pulse at half-maximum value is 5.8 ns.

At peak radiated power, the electrons and radiation field are essentially in

equilibrium and to first order, the photon distribution can be determined using the Planck function evaluated at the electron temperature. Figure 6.10 (b) plots the Planck distribution at 4.2 ns using an electron temperature of 164 eV. The peak in the distribution occurs at a temperature of 457 eV. The amount of energy being emitted above 1 keV can be calculated by integrating the Planck distribution over the related frequencies (energies). This value has been estimated as 114 kJ.

Within the first few ns of stagnation, the absorption mean free path throughout the toroid is typically two to three times larger than either the prestagnation region or the shocked region at the wall. As a result, radiation leaves the system via flux-limited diffusion at essentially cE [2,14]. Around peak compression, however, the absorption mean free path in the neighborhood of the wall is comparable to the compressed toroid dimensions there. Under these conditions, the radiative conductivity has a significant contribution from the absorption opacity term of Equation (37). At even later times, after the toroid has begun to expand, this opacity term becomes even more important. The decrease in the absorption mean free path in these instances, indicates that in the latter stages of stagnation the radiation is transported via diffusion in some parts of the computational domain.

From the above discussion, it is evident that the material-radiation coupling and the radiation transport both move through different regimes during stagnation. Early in compression, the density is low and the ion-electron, electron-radiation coupling are poor. The ion, electron, and radiation temperatures are not equal. At the same time, the low density and high electron temperatures result in a large absorption mean free path and the radiation is free streaming. Later in the compression, the density is high enough that the electrons and radiation field have come into equilibrium and the absorption

mean free path is about the length of the stagnation region. In this case, the radiation travels through the stagnation region somewhere between free streaming and being diffused. By expansion, the mean free path has finally become smaller than the toroid dimensions, and an equilibrium diffusion regime is approached. Because of these various stages, modelling the physics in the stagnation process requires a model which can extend across all of these regimes. This can be accomplished using a flux-limited nonequilibrium diffusion model.

As already mentioned, the prestagnation temperatures chosen to initialize the numerical simulation of the stagnation process were based on a number of assumptions and qualitative arguments concerning volumetric compression. The results of the baseline case, imply however, that these values may not accurately depict the conditions just prior to impact. This seems to be particularly true for the ion temperature. An examination of the temperature profiles reveal that within the first ns, before a significant fraction of the stagnation has taken place, the ions have rapidly cooled to 100 eV and the electrons to 90 eV. This suggests that these latter values might be more appropriate in defining the starting conditions of the simulation. This information also brings up the question of how strongly the choice of (reasonable) initial temperatures influence the outcome of the physics in the stagnation region and the subsequent radiation properties. To answer this question, a number of compact toroid stagnation calculations were run with varying initial temperatures. Table 6.2 list the stagnation runs and the temperatures assigned to the ions, electrons, and radiation field. For all of the calculations except ct4 and ct5, the electron temperature is taken to be 100 eV.

Table 6.3 shows the total radiated yield at 1 and 10 ns into each run. Clearly, the range in assigned values of temperatures change the radiated

Table 6.2. Initial temperatures for each run

simulation	$(T_e)_{\text{init}}$	$(T_i)_{\text{init}}$	$(T_R)_{\text{init}}$
ct1	100 eV	1 keV	50 eV
ct2	100 eV	100 eV	50 eV
ct3	100 eV	10 keV	50 eV
ct4	70 eV	1 keV	50 eV
ct5	70 eV	100 eV	50 eV
ct6	100 eV	1 keV	100 eV

Table 6.3. Total radiated yield for each run

simulation	$E_{\text{tot}}(1.0 \text{ ns})$	$E_{\text{tot}}(10.0 \text{ ns})$
ct1	173 kJ	4.77 MJ
ct2	164 kJ	4.76 MJ
ct3	270 kJ	4.87 MJ
ct4	132 kJ	4.73 MJ
ct5	123 kJ	4.72 MJ
ct6	191 kJ	4.79 MJ

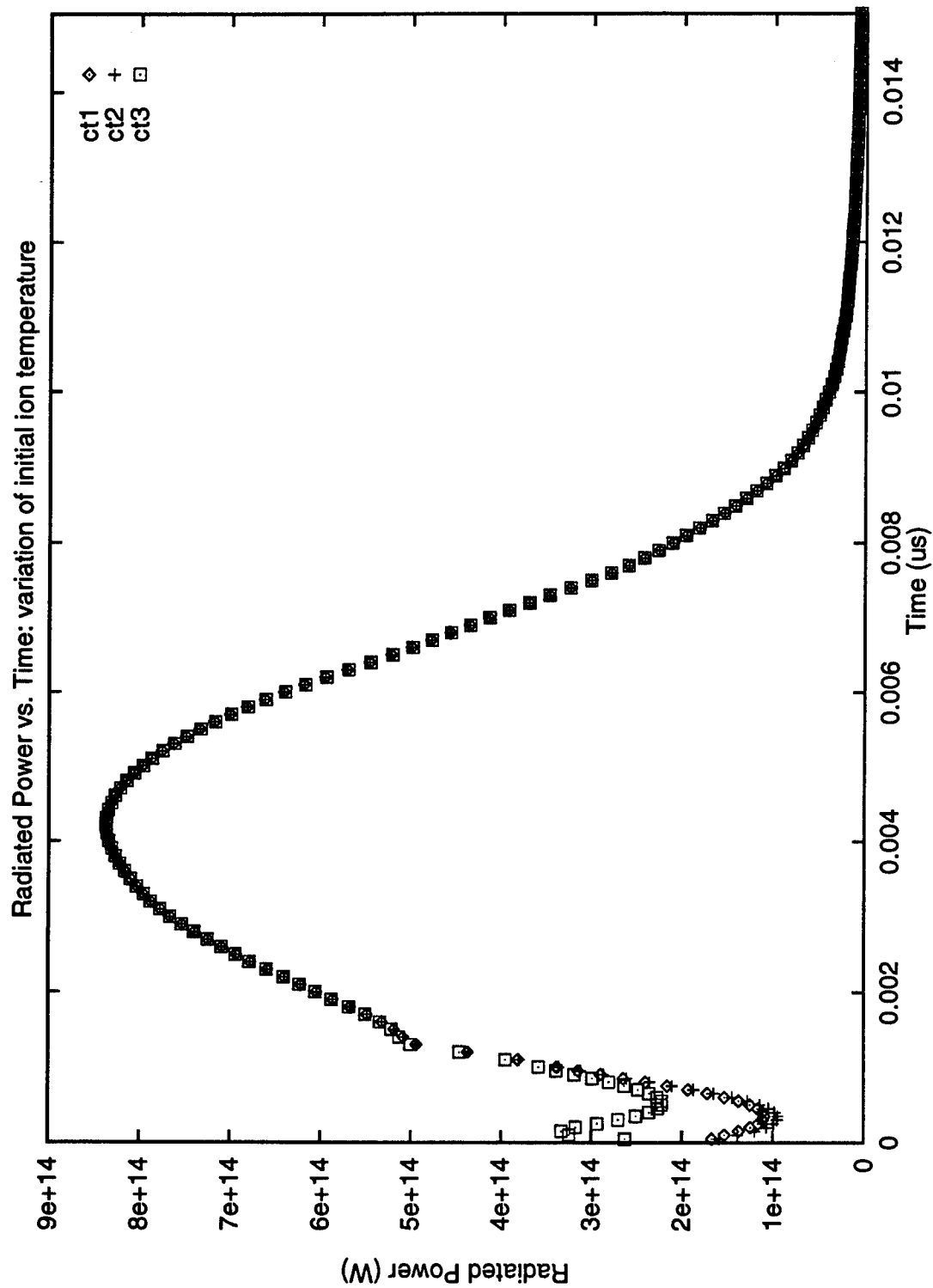


Figure 6.11. Plot of the Radiated Power vs. Time for the runs ct1, ct2, and ct3.

yield by 10 ns only slightly. This small difference originates early in the simulation as can be seen from the radiation output at 1 ns. The higher the temperatures, the larger the internal energies, making available more energy that could be initially radiated away. Figure 6.11 is a plot of the radiated power as a function of time for the ct1, ct2, and ct3 runs. From this figure, it is evident that for most of the stagnation the radiated power is the same. The discrepancy in the power curve occurs within the first 2 ns where the radiation rate is governed by the predefined values of temperature.

The details of the radiation loss in the first ns or so is an artifact of the initial temperatures, and as such, merits some discussion. In the first three calculations described in Table 6.2, the ion temperature is permitted to vary between 100 eV and 1 keV. In each case, a decline in the radiation rate is observed before the radiation emitted from the stagnation process takes over and the radiation rate rises. As indicated in the discussion of Figure 6.10 (a), this corresponds to the fact that the initial temperatures are set to an artificially large value and the electrons continue to radiate the associated energy away. As the electrons radiate, they lose internal energy. If they are not supplied with enough energy from the ion component of the fluid, they will continue to radiate less and less. This results in a decrease in the radiated power. With the ion temperature at 1 keV, the electrons have a source of energy and the radiation rate is somewhat larger than in the ct2 calculation. In the run of ct3, the radiated power rapidly increases then begins to drop (refer to Figure 6.11). This initial increase is caused by the 10 keV ion temperature heating the electron fluid faster than it can radiate the energy away. Note that the radiated power does not decrease as much as in the ct1 and ct2 runs. As with the ct1 calculation, this can be attributed to the continual addition of energy from the ions to the electrons.

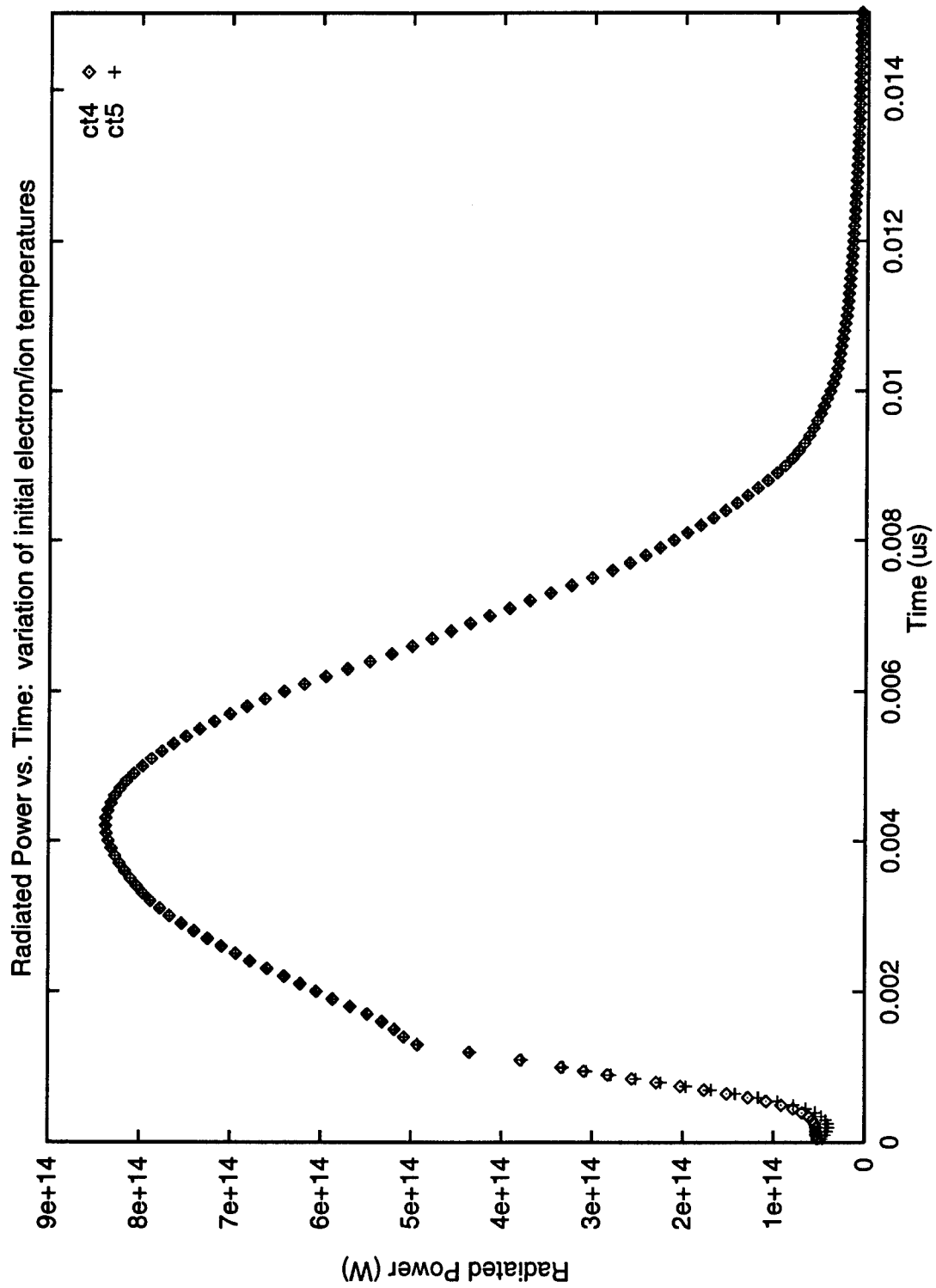


Figure 6.12. Plot of the Radiated Power vs. Time for the runs ct4 and ct5.

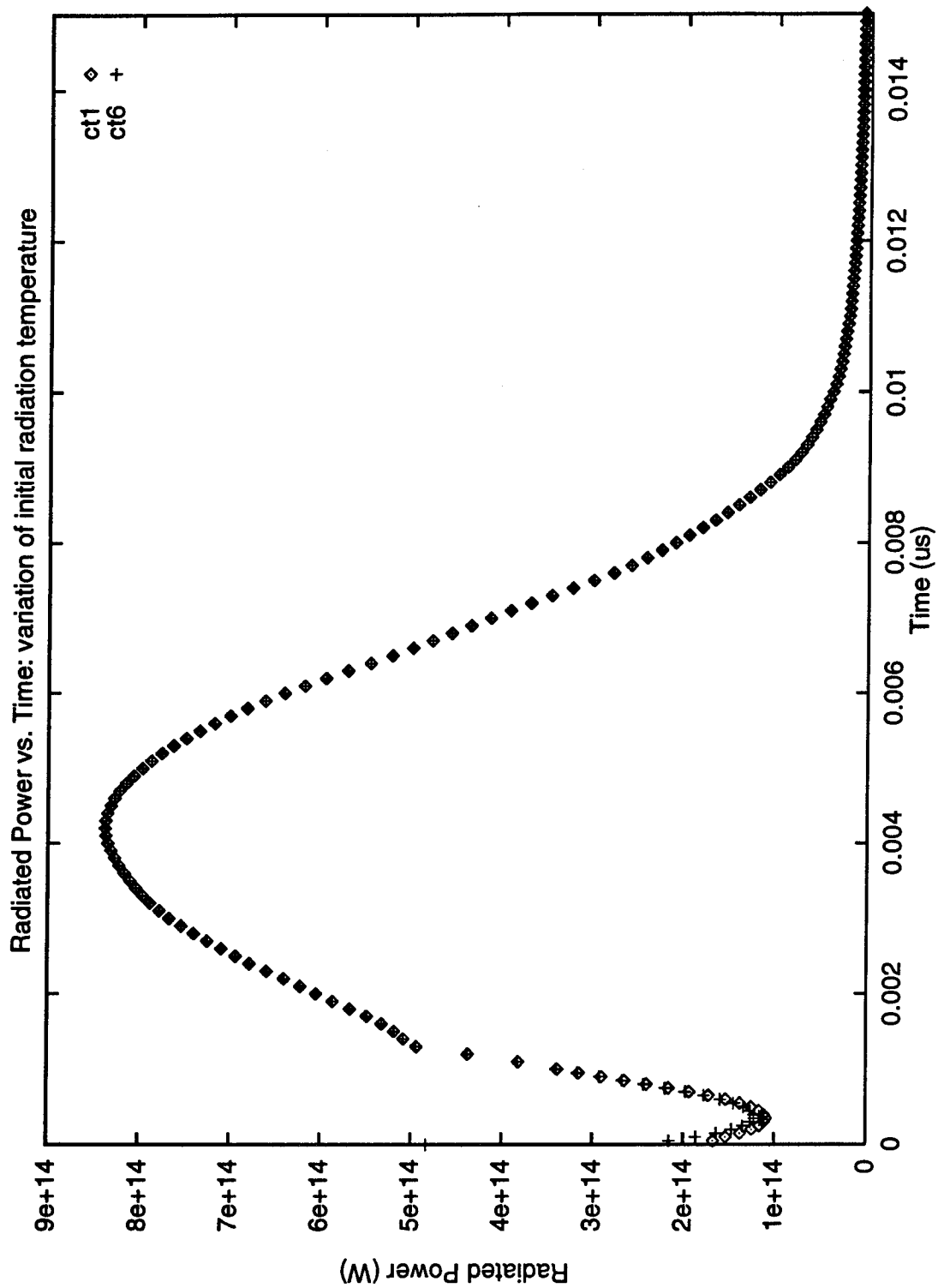
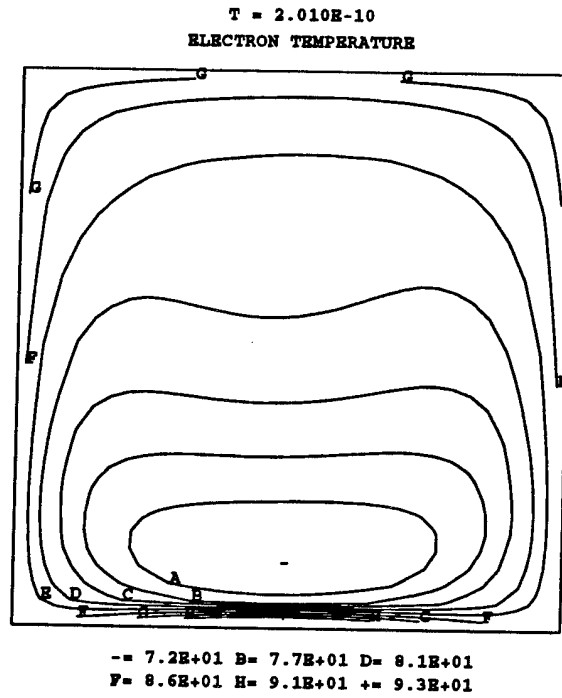


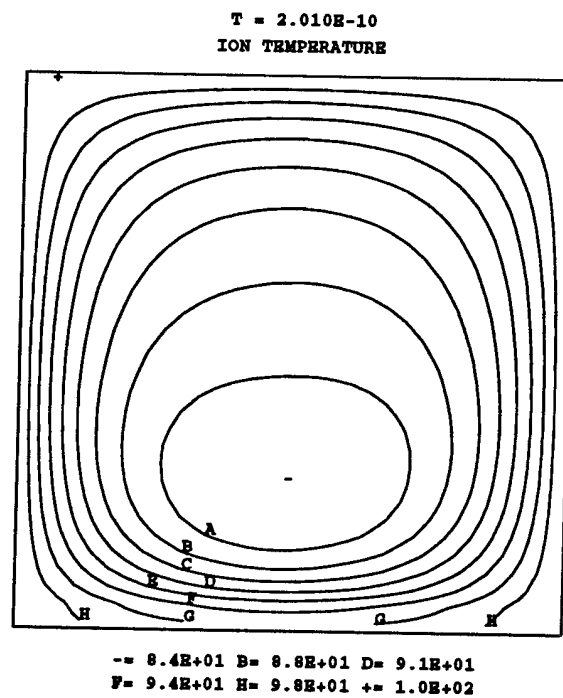
Figure 6.13. Plot of the Radiated Power vs. Time for the runs ct1 and ct6.

The dip in the radiated power curve found in the first three calculations can be removed by setting the input value of the electron temperature to 70 eV. This has been done in the ct4 and ct5 runs and is shown in Figure 6.12. Here the ion temperatures of 100 eV and 1 keV made only a small difference in the amount of initial radiated power, with the larger ion temperature giving a slightly overall higher radiation rate. Out of curiosity, a final calculation, ct6, was performed with a radiation temperature of 100 eV as opposed to 50 eV. This is compared with the baseline calculation in Figure 6.13. Initially, the radiated power is over a factor of two larger than that in the baseline case (485 TW as opposed to 180 TW). This indicates that a radiation temperature of 100 eV is unrealistically large.

The temperature survey considered above reveals that the range of temperatures examined did not strongly influence the values of the radiated yield or the radiated power. This also holds true for the material and magnetic properties in the stagnation region and was observed in the plot and slice files at 1, 6 (near peak density), and 10 ns. For this reason, the original choice of temperatures was kept in the calculations which follow, with the understanding that these values were overestimated. Another means of approximating the prestagnated temperatures can be obtained by simulating the evolution of a zero velocity toroid at the baseline conditions. Figure 6.14 shows the electron and ion temperature profiles at 0.2 ns, close to the time the stagnation begins. In this case, the calculation prescribes an initial temperature of about 85 eV for the electrons and 95 eV for the ions, rather than the 100 eV and 1 keV considered.



(a)



(b)

Figure 6.14. Contour plots of (a) electron and (b) ion temperature at 0.1 ns.

6.1.1 Role of Numerical Resolution in the Baseline Case

An investigation into the role that numerical resolution plays in modelling the stagnation physics has been carried out on the baseline calculation. Table 6.4 lists a set of computations performed using the baseline conditions but varying the number of cells across the toroid. For each run, the same number of cells were defined along both spatial directions. In the first three calculations, the grid was kept fixed throughout the simulation, while in the last calculation, ct9, the grid was allowed to adapt to the material density. In this latter case, the number of cells remained constant, but the cell shape and size were permitted to vary, expanding or compressing depending on the density distribution. The calculation represented as ct1 in Table 6.4 is the standard stagnation run which has been analyzed up to this point. This simulation has been based on a resolution of 32 x 32 zones.

Table 6.5 presents the values of the density and time at peak compression for each run, and the total radiated yield at 10 ns. These results indicate that with decreasing resolution (fewer number of cells), peak compression occurs later in time and the compression itself becomes less severe. However, this trend does not appear to effect the overall radiated yield. The degree of compression observed throughout each simulation is related to the cell size and is a direct consequence of the finite differencing of the divergence of velocity term in the mass continuity equation:

$$\frac{d\rho}{dt} = -\rho \nabla \cdot \bar{v} . \quad (88)$$

This can be seen by writing a simple finite difference form of Equation (87). For uniform flow in the y-direction and a forward difference approximation to $\nabla \cdot \bar{v}$:

$$\rho_{i,j}^{n+1} = \rho_{i,j}^n - \frac{\rho_{i,j}^n \Delta t}{\Delta y} (v_{i,j+1}^n - v_{i,j}^n) . \quad (89)$$

Table 6.4. Resolution parameters for each run

simulation	# of cells	grid motion
ct7	16 x 16	stationary
ct1	32 x 32	stationary
ct8	64 x 64	stationary
ct9	32 x 32	adaptive

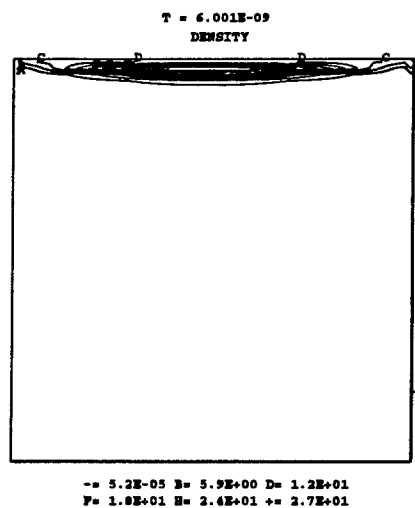
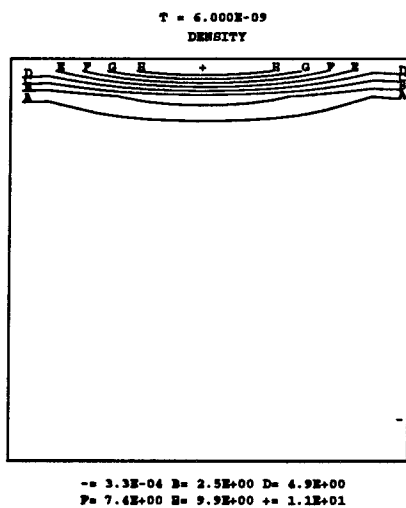
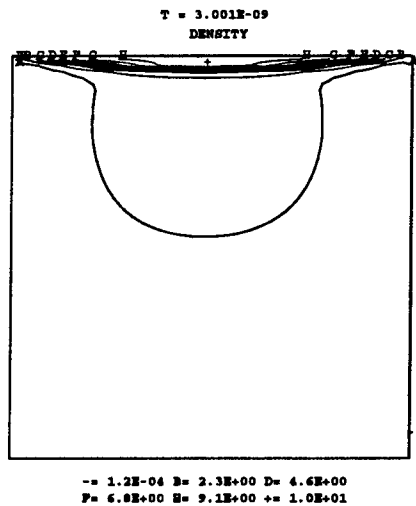
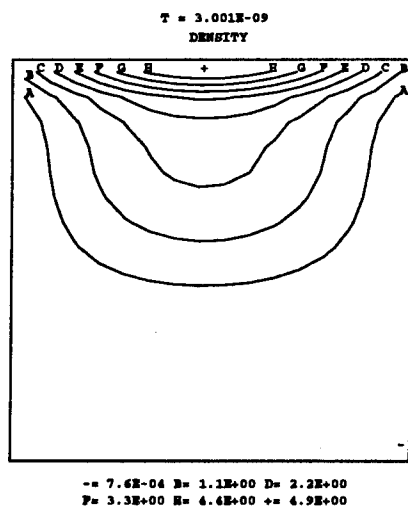
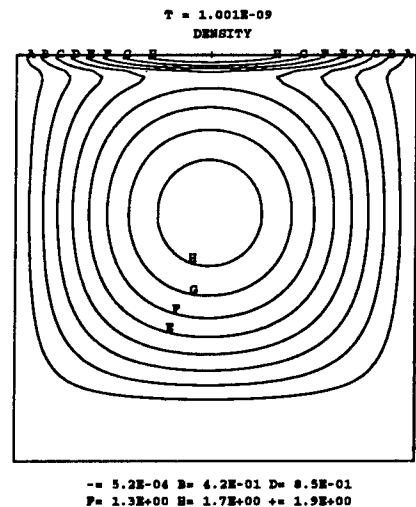
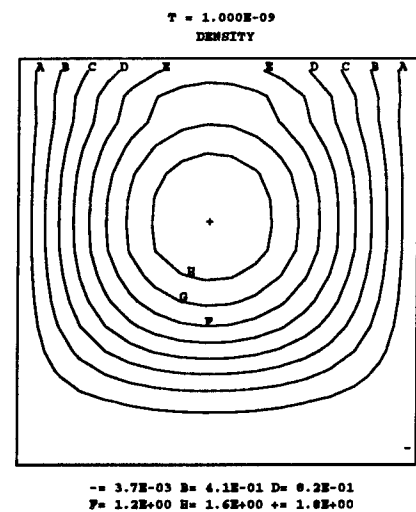
Table 6.5. Results of resolution calculations

simulation	(ρ)	t_p	$E_{tot}(10 \text{ ns})$
ct7	12 kg/m ³	8.4 ns	4.776 MJ
ct1	19 kg/m ³	6.2 ns	4.768 MJ
ct8	28 kg/m ³	5.6 ns	4.773 MJ
ct9	19 kg/m ³	6.0 ns	4.779 MJ

During the first half of the stagnation, $v_{i,j+1} < v_{i,j}$ in the vicinity of the wall and from the above equation, the updated density is always increasing. The amount by which the density is incremented is indirectly proportional to the cell size Δy . Thus as the cell size becomes increasingly smaller, i.e., the grid becomes more refined, the density becomes correspondingly higher for fixed Δt . On the other hand, as the cell size is made larger, i.e., the number of cells decreases, the region near the wall is not as well resolved and the density there is underestimated.

The delay in peak compression observed in going to lower resolutions is directly related to the amount of compression the material undergoes with each calculational timestep. A coarser grid will naturally take longer to reach maximum compression, since in this case, the density at the wall increases at a slower rate than its higher resolution counterpart. In addition, the larger cell size contains more mass. As a result, the density at peak compression is smaller at lower resolutions. Figure 6.15 illustrates the influence of cell resolution on compression by displaying the density profiles at 1.0, 3.0, and 6.0 ns for the runs of ct7 and ct8. The difference in the amount of compression between the two calculations is noticeable.

A comparison of the output from the ct9 calculation with that of ct1 shows little variation in stagnation values. This is most likely due to the fact that in the former case the cell concentration in the region adjacent to the wall was not sufficiently higher than that of ct1. Stated another way, the resolution was not significantly modified at the degree to which the grid was allowed to adapt and the calculations therefore produced similar results. In moving to 64 cells, however, the stagnation region contains a larger number of cells and the compression values are much higher. Clearly the improved resolution gives a somewhat different picture of the physics in this region. The physics is, of



(a)

(b)

Figure 6.15. Density profiles at 1.0, 3.0 and 6.0 ns for (a) 16 and (b) 64 cell resolution.

course, related to the shock formed near the wall and the real numerical issue under these circumstances is the ability to resolve the shock over a small grid scale.

Typically a fluid code such as MACH2, tends to spread a shock over three or four zones in an Eulerian calculation [14]. This smearing is caused by an artificial viscosity model. Under steady state conditions, the Rankine-Hugoniot relations are satisfied across the shock and the modifications made by the shock to the material is given correctly. Within the shock structure itself, no attempt is made to model the physics precisely, but only to provide a smooth qualitative transition in material properties across the interface region between upstream and downstream flows [2]. As a consequence, the higher the resolution, the smaller the spatial width of the shock, and the narrower the region where the physics may not be quantitatively correct.

In the stagnation problem, the shock is very close to the wall and the transition region may actually extend up to the wall boundary. It is therefore reasonable to believe that the values being reported in the cells adjacent to the wall become increasingly inaccurate as the resolution in this region decreases. Inevitably, this relates back to the hydrodynamic terms of the finite difference equations for the evolution of the mass, momentum, and energy. With increasing resolution, these terms should numerically change the thermodynamic properties of the material by even larger amounts over even smaller regions. This is exactly what is observed in the runs of Table 6.4.

From the above discussion, improved resolution should lead to a more accurate description of the physics in the stagnation region. However, such resolution comes with a demand for extensive cpu time. For a single calculation this is not much of an issue. But with a parameter survey, where multiple calculations are required, this can be time consuming and may not be the

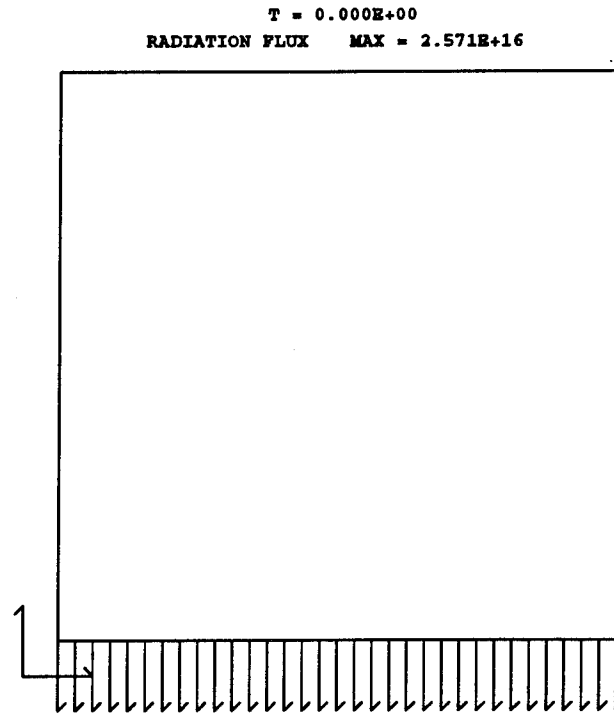
most efficient approach. As already noted, the effect of the shock in the stagnation region on the overall large scale structure of the problem is always modelled correctly. This is evidenced in the radiated yield for each calculation. If the radiated yield and other properties of the entire system are of the most interest, then a lower resolution may be appropriate. This is the point of view taken in this dissertation. For the calculations which follow, a grid resolution of 32 by 32 cells is assumed. This resolution has been found to provide reasonable results with a relatively quick computational turnaround time.

6.1.2 The Role of Radiation Boundary Conditions and Computational Geometry on the Baseline Case

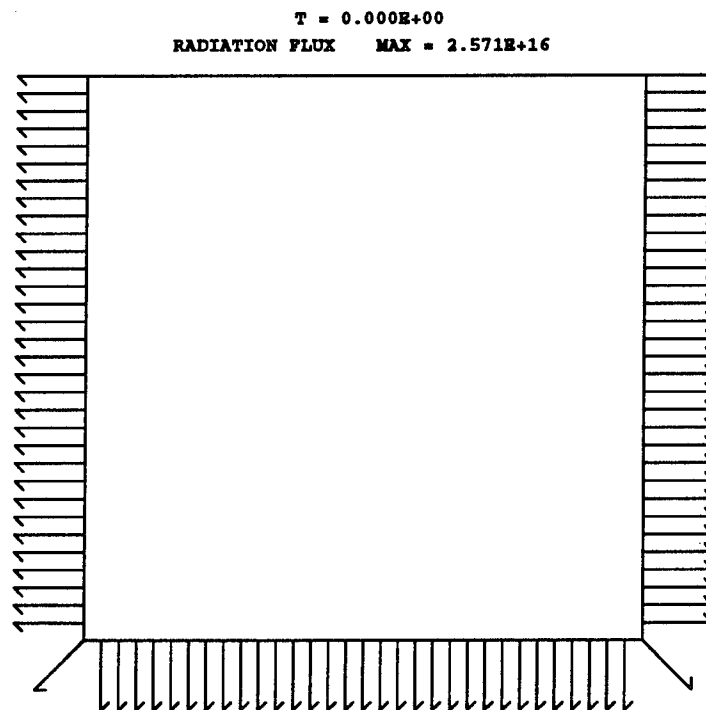
The last calculations of this section consider the influence that radiation boundary conditions and computational geometry have on the outcome of the simulations. In the previous calculations of the baseline case, the radiation field was permitted to flow only through the bottom boundary, the other three boundaries being reflective. This suggests that some fraction of the radiation may be prevented from escaping the problem as rapidly. In addition, the stagnated material is confined by the geometry specified in the initialization of the calculation. In all likelihood the compressed toroid, if not bounded by the inner and outer conducting walls, would extend further along the impact wall. This might lead to a change in compression and radiated yield. In any event, both of these issues could numerically influence the radiating ability of the stagnation process.

Figure 6.16 (a) illustrates the radiation boundary conditions used in previous calculations of the baseline case. In these calculations, only the bottom boundary of the computational box is open to radiation flow as indicated by the radiation flux vectors pointing outward from that location. Figure 6.16 (b) depicts the radiation boundary conditions of a calculation in which the bottom boundary and side boundaries are each considered to be open to radiation. In this instance, the wall is the only boundary which is reflective. A comparison of this calculation with that of the one radiating boundary shows they both produce essentially the same stagnation results. Peak compression in the two cases occurs at the same time with a peak density of about 19 kg/m^3 . The other thermodynamic variables evolve in much the same manner.

Figure 6.17 plots the radiated power as a function of time for the two calcu-



(a)



(b)

Figure 6.16. Plots of the radiative flux indicating radiation boundary conditions with (a) one radiating boundary and (b) three radiating boundaries.

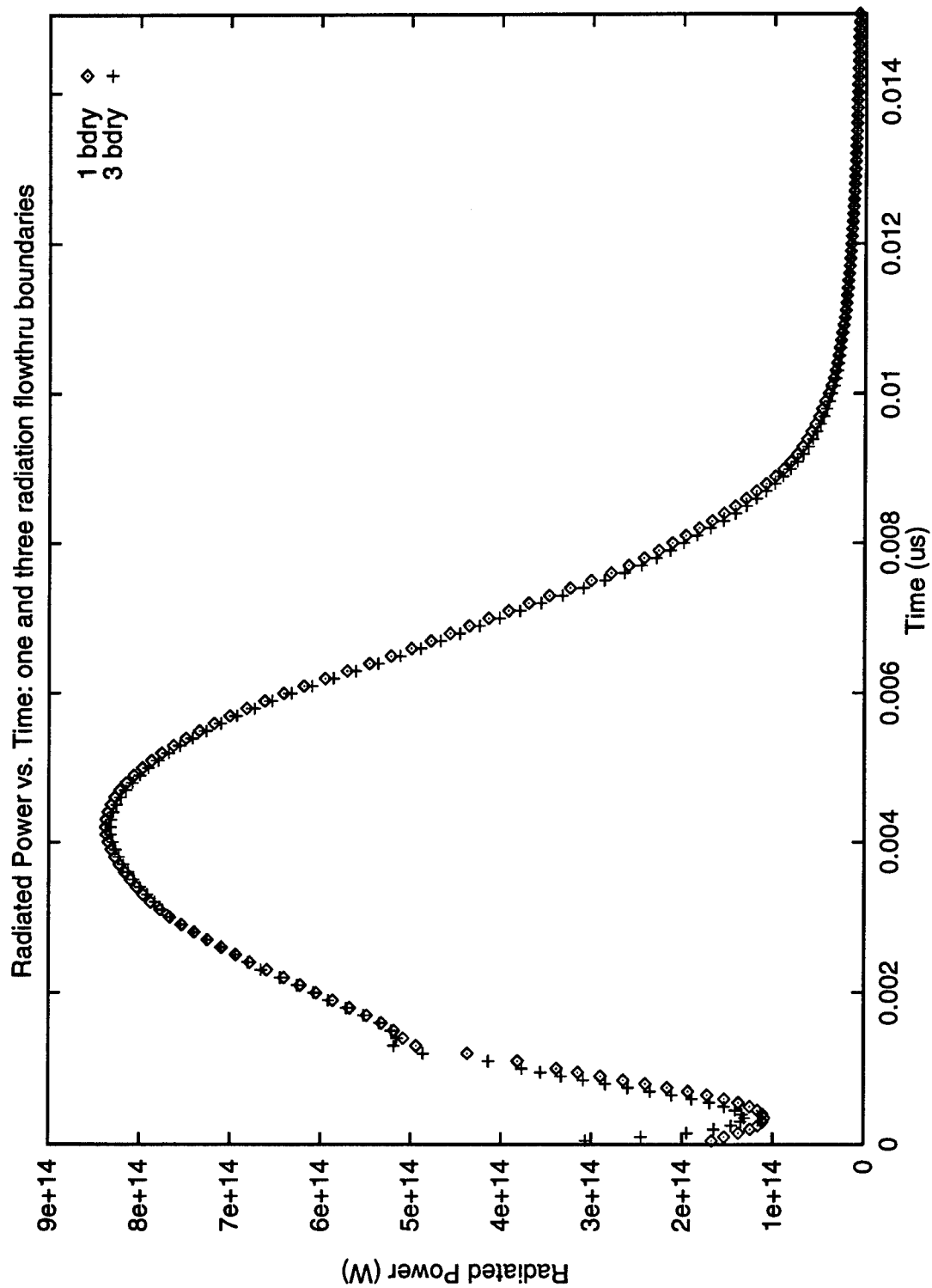


Figure 6.17. Plot of the Radiated Power vs. Time for the calculation of the baseline case with one flowthru radiating boundary and the calculation with three flowthru radiating boundaries.

lations. There is only a small difference between the two curves, caused by the initially higher radiation rate in the three boundary problem. Because more radiation can leave through three boundaries as opposed to one, the three boundary problem cools more rapidly. At later times, this evidenced in a lower radiation rate. Here the total radiated yield at 10 ns is 4.774 MJ as opposed to 4.768 MJ calculated in the one boundary case. This simulation plainly demonstrates that the stagnation properties along with the radiated output were not appreciably influenced by the inclusion of two additional radiation flowthru boundaries.

To estimate the effect the original "restrictive" geometry has on the stagnation process, the inner conducting wall was extended to the center axis, a distance of 2.24 cm. The outer conducting wall was also extended by the same amount. This provided ample space for expansion perpendicular to the direction of motion. Figure 6.18 depicts the revised stagnation geometry and the boundaries that are open to radiation flow. Both the top boundary and the left boundary, as defined by the centerline, are considered to be perfectly reflecting to radiation. The position of the toroid at the beginning of the simulation is indicated in Figure 6.19, along with the field configuration. It should be noted that the only difference in this calculation and those discussed above involves the width of the stagnation region and the area through which the radiation can flow out of the computational domain; neither the location of the toroid with respect to the centerline or its physical dimensions has changed.

A comparison of this run to the one boundary and three boundary calculations, illustrated by Figure 6.16, shows relatively close agreement in stagnation properties and total radiated yield. Figure 6.20 displays the density and radiation temperature at peak compression. From the density profile, it can be seen that the compressed toroid has extended a little beyond the original posi-

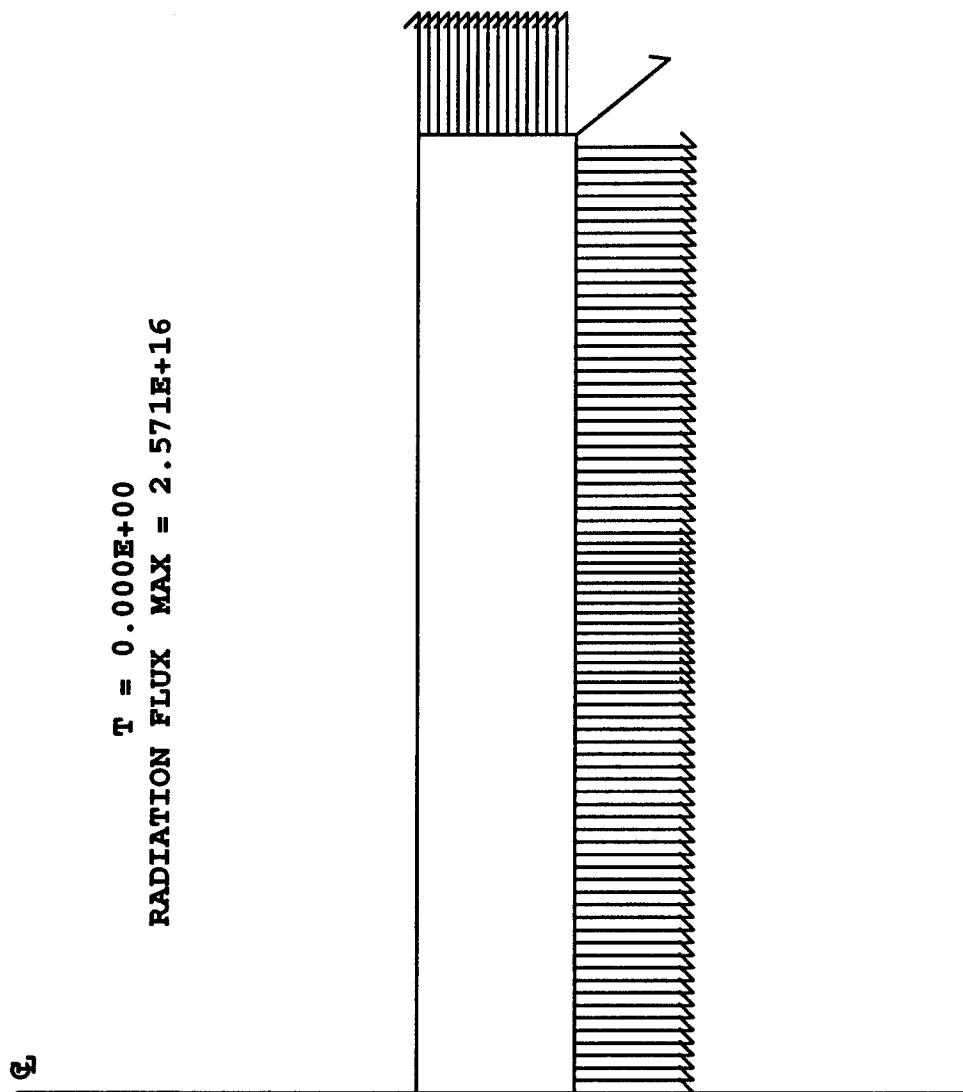


Figure 6.18. Stagnation geometry in which the inner and outer conducting walls have been extended an additional 2.24 cm. The plot also illustrates the boundaries through which radiation is permitted to flowthru.

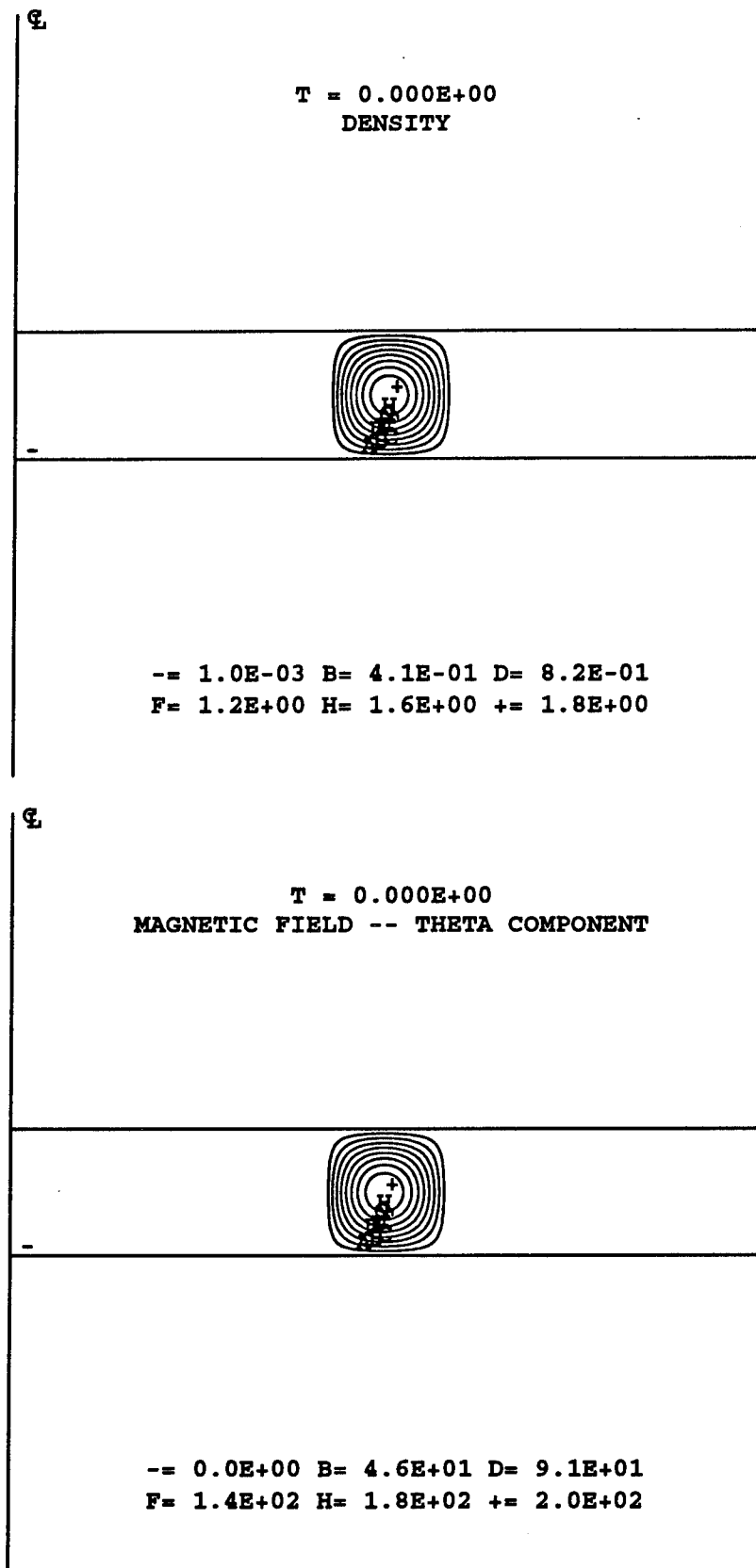


Figure 6.19. Plot of the (a) initial density and (b) initial toroidal field profiles for the calculation using the extended stagnation geometry.

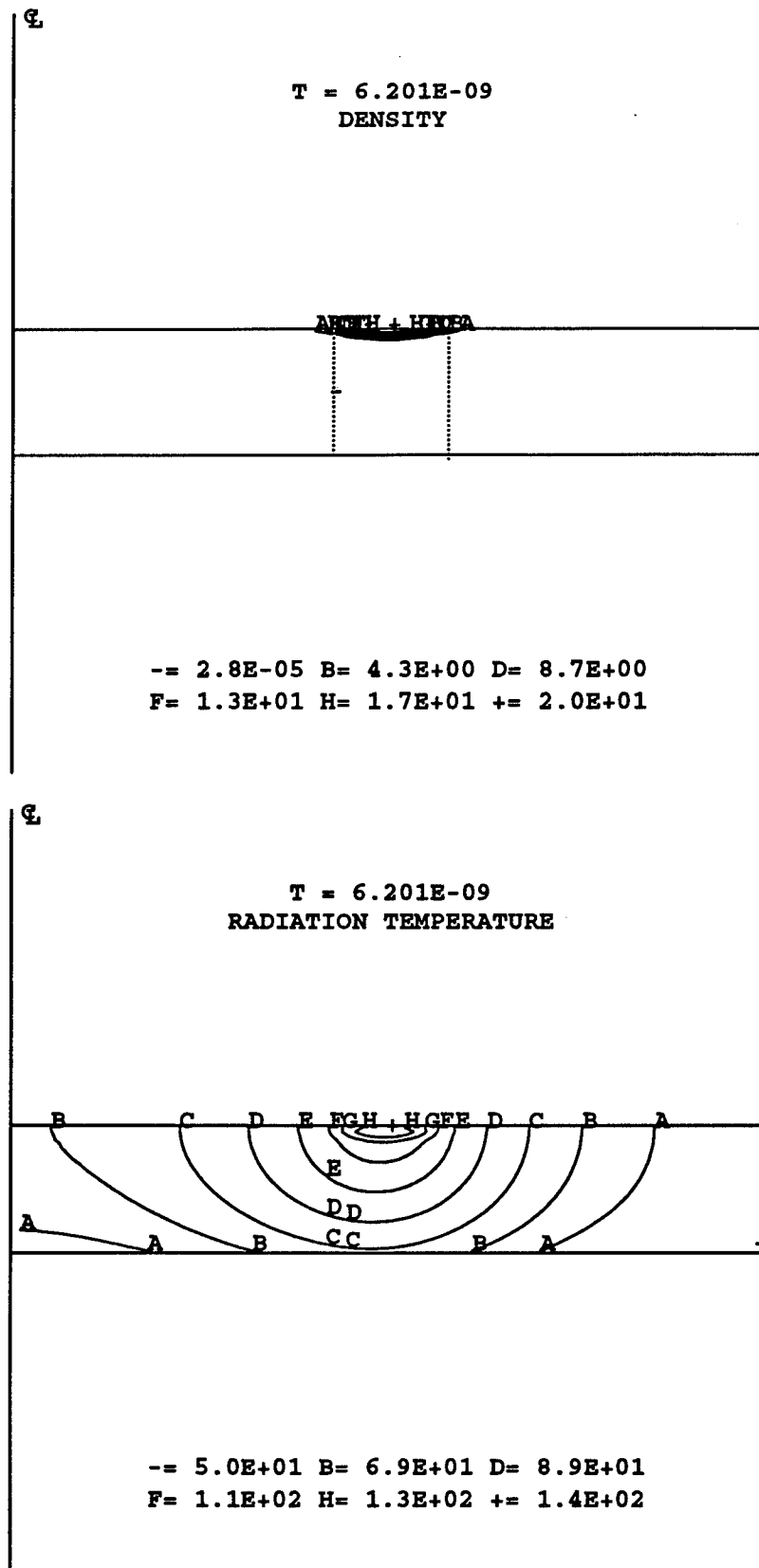


Figure 6.20. Plot of the (a) density and (b) radiation temperature at peak compression for the calculation using the extended stagnation geometry.

tion of the boundary walls (denoted by the dotted lines), and the peak density is slightly higher. This does not appear, however to produce any large changes in material properties within the stagnation region. The radiation temperature at this time is lower overall by about 10 eV (140 eV compared to 150 eV).

The radiated power curve for this calculation along with that of the standard (one radiating boundary) calculation is shown in Figure 6.21. In this case, denoted as "3block", the radiation rate peaks at a 4% lower value. This occurs because some portion of the initial directed kinetic energy actually goes into spreading the compressed toroid outward along the stagnation wall instead of increasing its internal energy. This is compounded by the fact that radiation can leave the computational domain through the bottom and right boundaries. Thus, not only can the toroid cool faster, but some fraction of kinetic energy that would have led to increased thermal energy and then radiation is no longer available.

Based on the information presented in the above two paragraphs, the extension of the inner and outer conducting walls, like the added radiating boundaries, has only a small effect on the stagnation process. This might not be true for higher velocity toroids, which could spread over a broader area allowing for further compression. Nonetheless, these two calculations suggest that their incorporation into the initial problem makes little difference in the outcome of the stagnation physics.

This concludes the study of the baseline case. The rest of the chapter is devoted to a parameter survey which covers a range of projectile velocities, field strengths, and mass. A change in the stagnation geometry will also be considered. The analysis provided in this section will then be used to interpret these findings and enable conclusions to be reached concerning the influence of these parameters on the stagnation process and radiation properties.

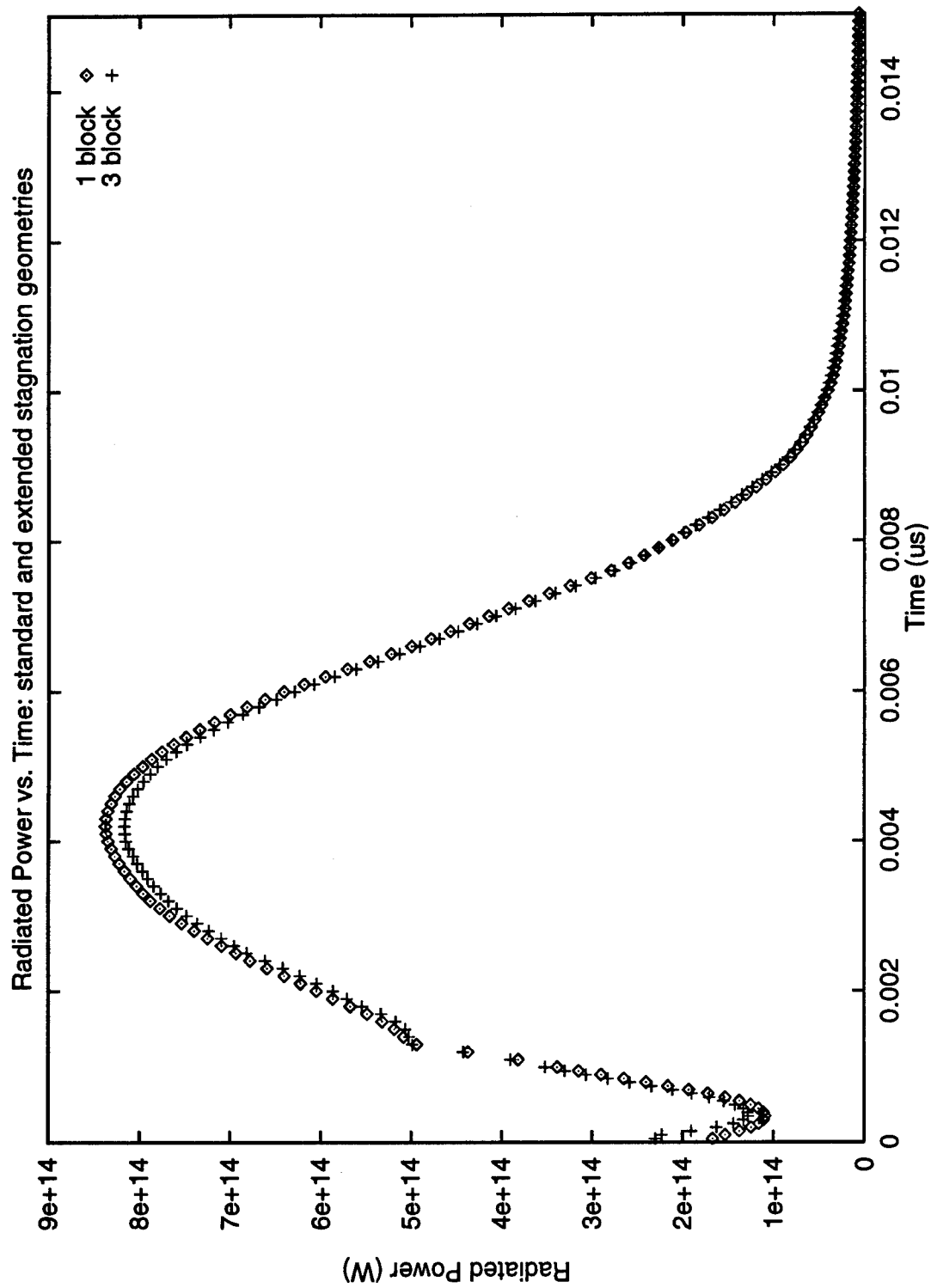


Figure 6.21. Plot of the Radiated Power vs. time for the calculation of the baseline case with both the standard stagnation geometry and the extended geometry (denoted as 3 block since three computational blocks were used to model this problem)

6.2 Numerical Simulations: Parameter Survey

The results of the baseline calculation presented in the last section demonstrated the radiative capability of a stagnating, 5 MJ Xenon compact toroid. From that discussion, the radiation production was described in terms of the total amount of radiation energy output, the radiated power with time, and the radiation pulse width. Such properties, along with the photon energy distribution, ultimately depend upon the prestagnation conditions in the toroid.

Prior to impact, the toroid has a substantial amount of energy stored in the form of directed kinetic energy. During stagnation, this can be converted into thermal energy which can then be radiated away. The initial amount of energy available for conversion is given by the kinetic energy per particle and the number of particles available. As the shock interface is encountered, this energy is partitioned into internal energy of the ions and electrons, magnetic field, radiation field, and ionization. The degree of partitioning depends on the hydrodynamics and the ion-electron, electron-radiation coupling. For the stagnation problem, the velocity of the material upstream of the shock (i.e., region adjacent to the wall) is essentially at rest and the kinetic energy in this region is zero. At this point, the ion temperature is substantially increased, and the final radiated yield depends upon the ability of the ions to efficiently couple with the electrons, and the electrons with the radiation field. In both instances, the coupling is a function of stagnation densities and temperatures. These, in turn, are related to the initial density of the toroid and the shock strength.

To investigate the effects of various toroid parameters on the stagnation process, and hence, radiation production, a number of calculations have been carried out. These are presented on the following pages and have been struc-

tured around the baseline case. The calculations include altering the magnetic field strength, the initial directed velocity, the toroid mass, the toroid material, and the stagnation geometry.

6.2.1 Magnetic Field Strength Variation

The first set of calculations to be discussed concern varying the initial magnetic field strength. As mentioned in Chapter 4, the magnetic field structure is necessary as it provides stability to the compact toroid, allowing it to be accelerated to high velocities. However, the presence of a magnetic field also introduces magnetic pressure which can be influential in retarding compression and draining kinetic energy from the toroid. Simulations of the baseline calculation indicated that for the conditions and timescales of stagnation, the magnetic field lines are frozen into the plasma. As the material compresses, so do the field lines, and the magnetic pressure increases in this region. The magnetic pressure acts as an additional force against the incoming flow of material, in effect, producing a "stiffer" toroid. Under these conditions, some of the initial kinetic energy must go into compressing magnetic field. This causes the spatial region over which the toroid is decelerated to broaden, and the material velocity may be decreased before it encounters the shock. As the magnetic contribution to the total pressure in the stagnation region rises, the pressure there can exceed the dynamic pressure at lower densities. Thus the stagnation can be halted at lower densities and is manifest in less toroid compression.

Clearly, less overall compression will influence the coupling efficiency in the stagnation region. The radiated yield should decrease, as well as the radiation rate. To determine the extent to which the magnetic field strength influences the stagnation process, calculations were performed using the prestagnation conditions of the baseline case, but with increasing initial values for the toroidal magnetic field. In the baseline calculation, the peak toroidal field was at 2.0 MG (200 T). For the standard toroid configuration, this

resulted in a magnetic energy of 112 kJ, approximately 2% of the directed kinetic energy. With this in mind, peak values of magnetic field were chosen such that the corresponding magnetic energy was at 10%, 30% and 50% of the directed kinetic energy. Table 6.6 lists the peak initial value of toroidal magnetic field, the corresponding magnetic energy, and the ratio of magnetic energy to kinetic energy for each calculation.

Figure 6.22 shows the effect of the magnetic field strength on the stagnation process by displaying the density and toroidal magnetic field contours at peak compression for both the baseline case and with the prestagnation magnetic energy at 50% of the kinetic energy. From these plots, it is evident that the magnetic field influences the amount of compression that the toroid undergoes during stagnation. With the larger magnetic field, peak compression occurs earlier in time, at 4.2 ns, and the peak density is 5.8 kg/m^3 . This is approximately a factor of three lower in density than in the baseline case. In a similar manner, the peak value of the magnetic field at this time, 25 MG (2500 T), indicates only a factor of 2.6 in magnetic compression as compared to a factor of 7 in the baseline case.

The influence of the magnetic field is further illustrated in Table 6.7 which provides values of the density, magnetic field, and temperatures at peak compression for this set of calculations. With increasing field strength, the toroid does not compress as much and peak compression occurs at earlier times and lower densities. The temperatures, which are measured in the region of highest density, are correspondingly lower. The smaller ion temperatures suggest that by peak compression, some of the kinetic energy has been lost in compressing against the additional force of increased magnetic pressure, making less available to heat the ion fluid.

The effect that the magnetic field strength has on the radiation properties

Table 6.6. Initial field parameters for magnetic field strength survey

simulation	$(B_\theta)_{\text{initial}}$	Initial Mag. E.	Mag.E./ Kinetic E.
ct1	2.0 MG	112 kJ	.02
ct10	4.3 MG	500 kJ	.10
ct11	7.5 MG	1.5 MJ	.30
ct12	9.7 MG	2.5 MJ	.50

Table 6.7. Results at peak compression for magnetic field strength survey

simulation	t	ρ_{max}	B_{max}	T_e, T_R	T_i
ct1	6.2 ns	19 kg/m ³	14.0 MG	145 eV	180 eV
ct10	5.0 ns	12 kg/m ³	21.0 MG	145 eV	158 eV
ct11	4.8 ns	7.3 kg/m ³	24.0 MG	133 eV	133 eV
ct12	4.2 ns	5.8 kg/m ³	25.0 MG	133 eV	133 eV

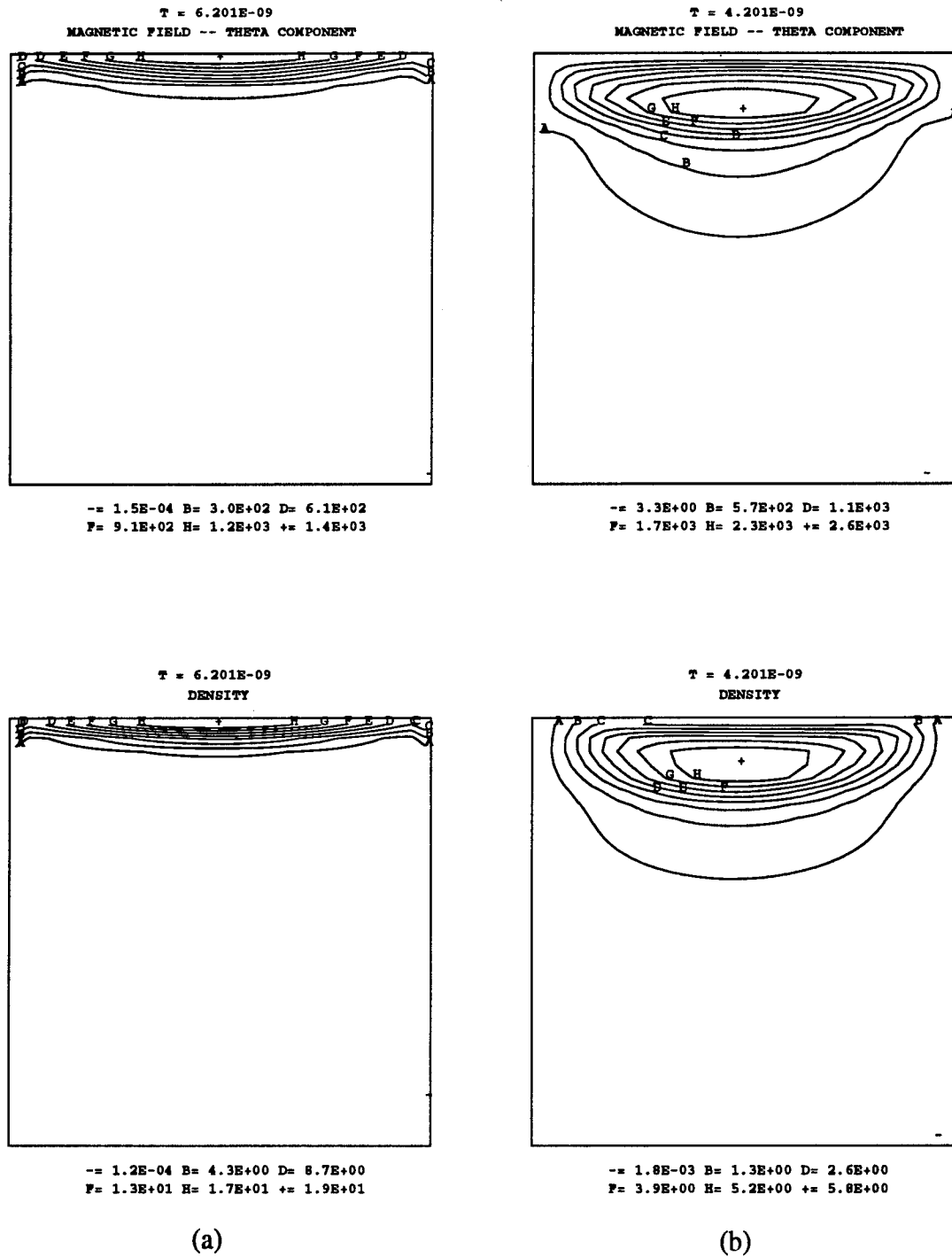


Figure 6.22. Toroidal Magnetic field and density contours at peak compression for (a) the baseline case where the magnetic energy is 2% of the kinetic energy and (b) the case where the magnetic energy is 50% of the kinetic energy.

is shown in Table 6.8. The pulse width was obtained as in the last section, defined by the full width at half max value of the peak radiated power. The total radiated yield was measured at the time in which the radiated power had dropped to 5% of the peak value. In terms of energy conversion, the baseline case is unquestionably the most efficient with a total radiated yield of 4.768 MJ. Here the conversion efficiency is 94% as opposed to 64%, when the magnetic energy is at half of the kinetic energy. The decline in conversion efficiency as a function of increasing field strength, and hence, magnetic energy, is depicted graphically in Figure 6.23. The radiated power over time is displayed in Figure 6.24. As noted in Table 6.8, the radiated power peaks at a lower value as the initial field strength is made larger. This is observed in the profile of the radiation rate. The pulse width, which gives an idea of the length of time over which significant radiation is emitted, is also shorter.

These results imply, as expected, that the conversion efficiency and radiated power depend upon the magnetic field strength, or more specifically, the amount of magnetic energy present as compared to kinetic energy. In the case of the compact toroid, a magnetic field is required to contain the plasma and maintain toroid resiliency. However, too high of a magnetic field can lead to degradation in radiation production. Based on these simulations of the 5 MJ baseline case, a magnetic energy that is approximately 10% or less of the initial directed kinetic energy is necessary to obtain conversion efficiencies above 80%. It should be noted that even with the higher magnetic energies, where the conversion efficiency has dropped to 60%, the radiated yield is still large for this problem; in the worst case, 3.2 MJ is emitted. This is certainly a respectable amount of radiation.

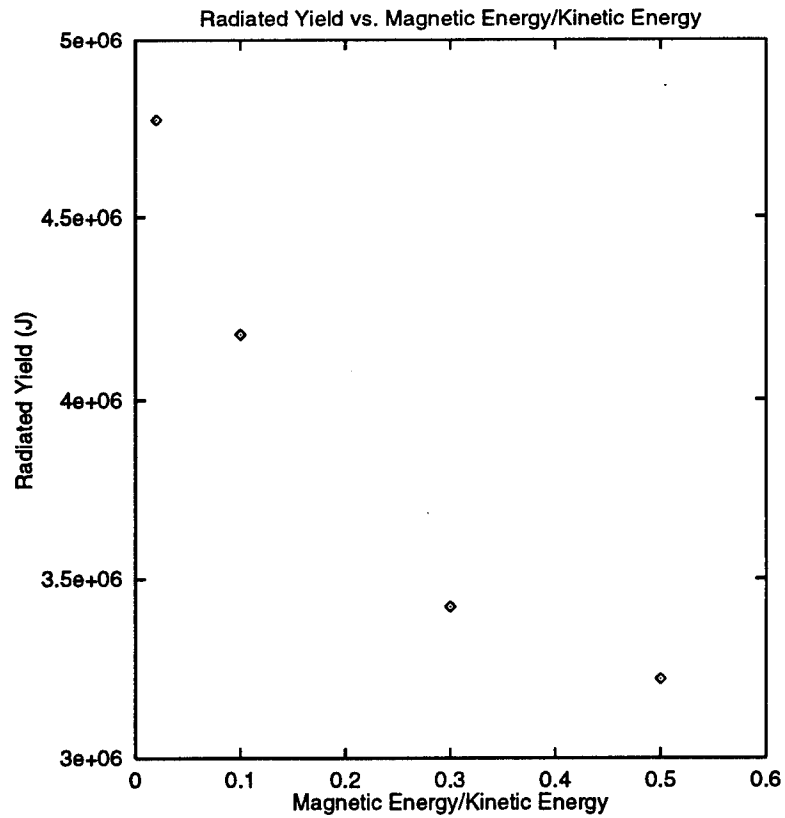


Figure 6.23. Radiated Yield as a function of magnetic energy to kinetic energy.

Table 6.8. Results of radiation production from magnetic strength survey

simulation	peak power	pulse width	Total yield (5% of peak power)	conversion efficiency
ct1	837 TW	5.8 ns	4.768 MJ	96%
ct10	783 TW	5.3 ns	4.181 MJ	84%
ct11	665 TW	4.5 ns	3.423 MJ	68%
ct12	602 TW	4.1 ns	3.221 MJ	64%

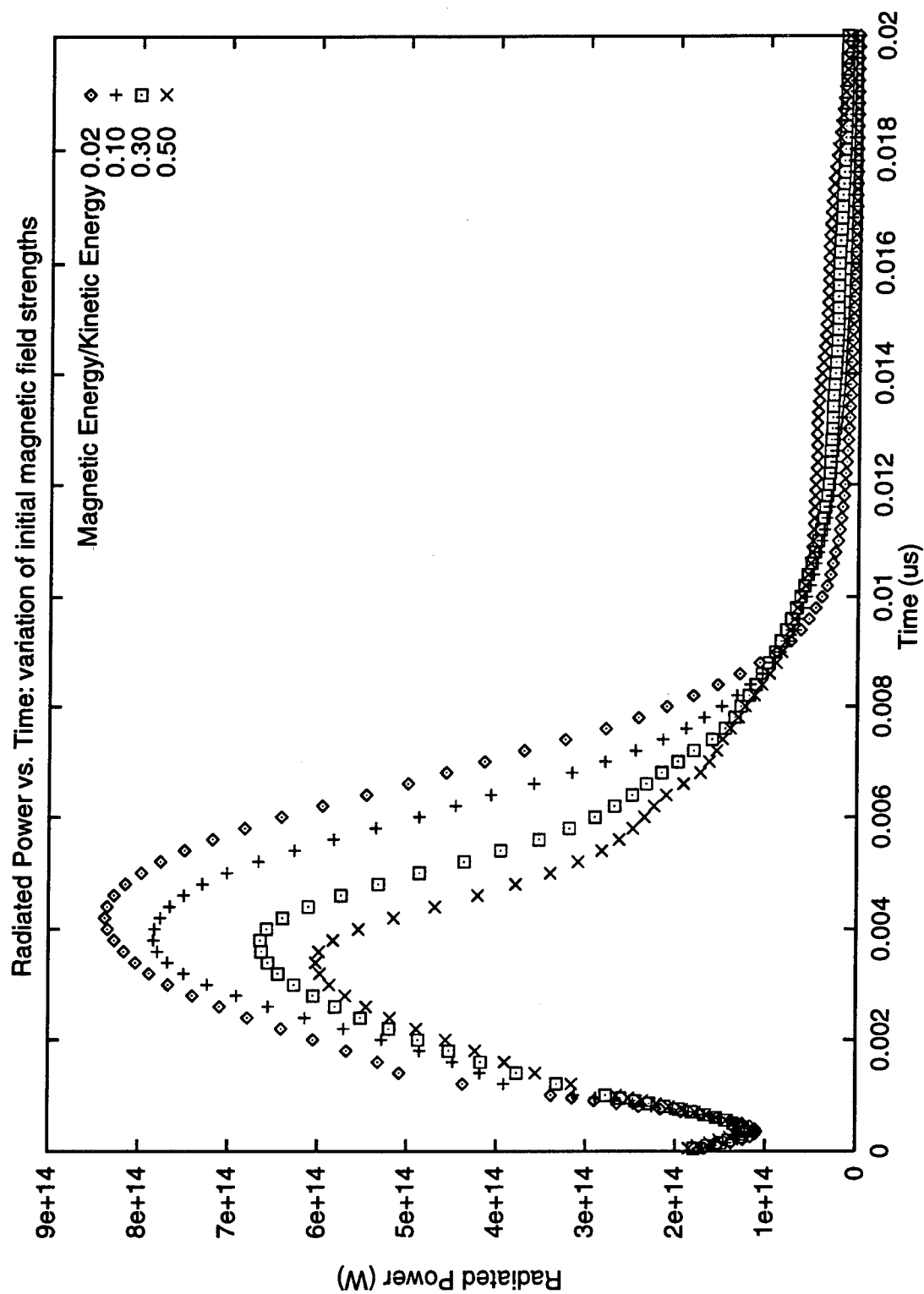


Figure 6.24. Plot of the Radiated Power vs. time for varying initial magnetic field strengths, and thus magnetic energies.

6.2.2 Constant Mass, Velocity Variation

One approach to improved radiation production in the sense of higher radiation output, radiation rates, and photon energies, is to increase the initial kinetic energy per particle. Thus as the toroid stagnates, there is more energy available to put into the internal energy of the ion fluid. If the conversion mechanisms are efficient during this process, the larger kinetic energies will be reflected in the emitted radiation - a larger radiated yield, radiation rate, and photons at higher energies will be achieved. This effect has been examined by taking both a smaller and a larger value of the initial velocity (than that of 100 cm/ μ s), keeping all other parameters defined as in the baseline calculation. For the same amount of mass, an increase in velocity will then lead to an increase in the kinetic energy per particle, and an increase in the total kinetic energy available for eventual radiation. Table 6.9 lists the two velocities chosen and the associated kinetic energies. As a reminder, the baseline calculation is also included in this table.

Table 6.10 contains the time of peak compression, the maximum density at peak compression, the peak radiated power, the pulse width, and the total radiated output for each simulation. In going from a velocity of 45 cm/ μ s (corresponding to a kinetic energy of 1 MJ), to a velocity of 145 cm/ μ s (kinetic energy of 10 MJ), the total radiated yield has been increased by a factor of 10. The peak radiated power has jumped by over a factor of 40, while the time over which the radiated power is above 5% of the peak has been shortened by approximately 7 ns. In all three of the simulations presented here, the overall conversion efficiency was above 90%. For these cases, the more kinetic energy prior to stagnation, the more energy that was produced in the form of radiation.

Table 6.9. Initial parameters for velocity survey

simulation	initial velocity	kinetic energy
ct13	45 cm/ μ s	1.0 MJ
ct1	100 cm/ μ s	5.0 MJ
ct14	142 cm/ μ s	10.0 MJ

Table 6.10. Results from velocity survey: peak compression, radiation production

simulation	(t) _{peak comp.}	(ρ) _{peak comp.}	peak power	pulse width	Total Yield (5% of peak power)
ct13	11.0 ns	12.0 kg/m ³	74.6 TW	11.4 ns	.9591 MJ
ct1	6.2 ns	19.0 kg/m ³	837 TW	5.8 ns	4.768 MJ
ct14	5.2 ns	25.0 kg/m ³	3186 TW	3.75 ns	9.703 MJ

With increasing velocity, the compression occurs on a faster timescale. The material stagnates at a faster rate, and is compressed to higher densities and reaches higher temperatures than its lower velocity counterparts. As a result, the pressure (material + magnetic) necessary to stop compression and begin expansion is obtained soon after the initial stagnation. By the time the toroid does begin to expand outward, a substantial amount of energy has already been radiated away. (This is the case with all of the simulations examined to this point.) These factors together contribute to the large radiation rates and narrower radiation pulses observed at the higher velocities.

As discussed above, an increase in toroid velocity is accompanied by higher ion and electron temperatures. As the velocity becomes greater, the amount of energy that can be imparted to the ion fluid becomes larger, and the ion temperature subsequently rises. This is clear in the early stages of stagnation. At 1 ns into the simulations, the ion temperature for the 142 cm/ μ s calculation is 398 keV, for the baseline calculation, 63 keV, and for the 45 cm/ μ s run, 10 keV. This behavior is also seen in the electrons, and is attributed to the ion-electron coupling. By peak compression, the ions have cooled significantly and the electron fluid and radiation field are in thermal equilibrium. Even at this time, the signature of higher velocities is still evident in the electron temperatures: 237 eV for ct14, 145 eV for ct1(baseline calculation), and 89 eV for ct13.

The radiated power with time for both velocity calculations is shown in Figure 6.25. The difference in the two radiation rates is quite obvious. The rapid climb in power observed at the front of the 10 MJ pulse is the result of a sudden increase in the electron-radiation coupling within the stagnation region. During the initial compression, the ion and electron temperatures are very large and both the ion-electron and electron-radiation coupling is low. Even by 1.6 ns, the ions are at 100 keV and the electrons at 1.8 keV ($T_R=195$

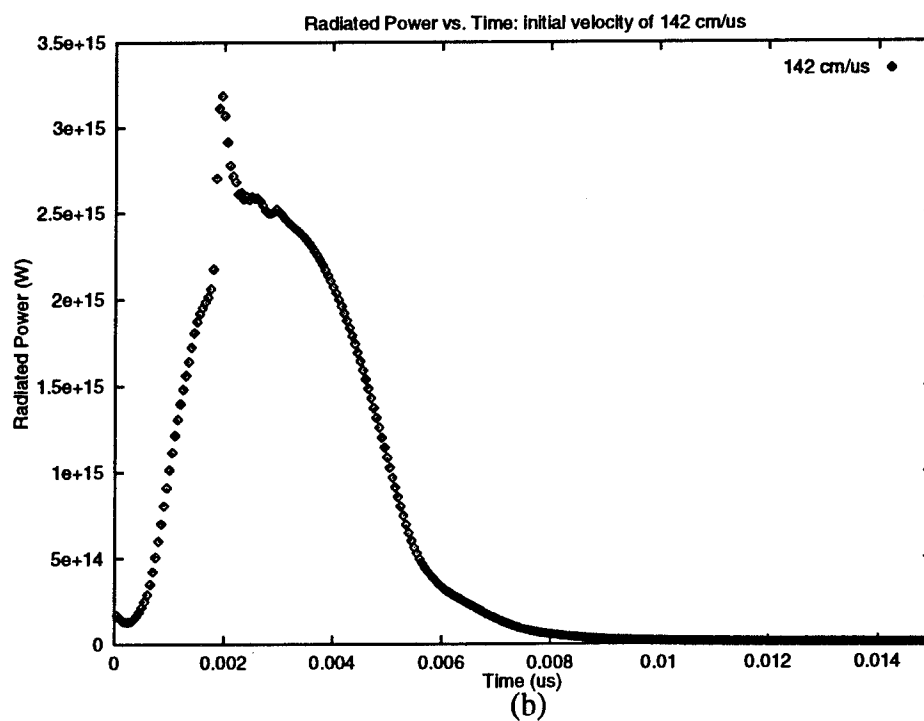
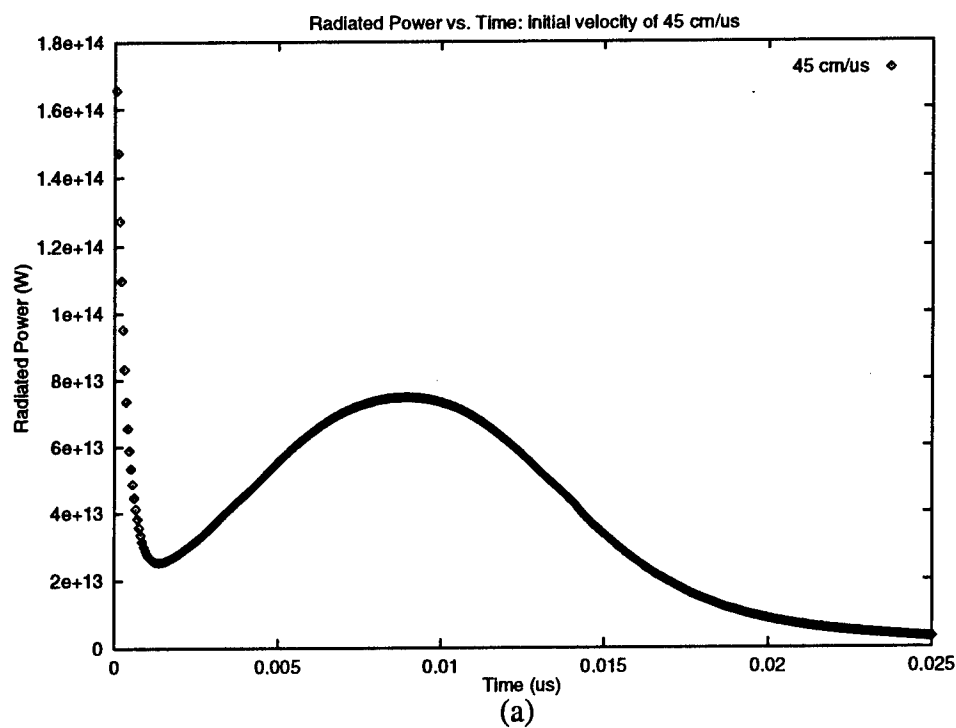


Figure 6.25. Radiated Power vs. Time for the (a) 45 cm/ μ s velocity run, 1 MJ directed kinetic energy and (b) 142 cm/ μ s run, 10 MJ directed kinetic energy.

eV). At this electron temperature and a density of 4.5 kg/m^3 , the mean free path for electron-radiation coupling is 13 m. As the density in this region increases, the interaction between the electrons and radiation field continually improves and the large reservoir of energy that is available in the electron fluid can be more easily radiated away and shared with the radiation field. At 1.8 ns, just before the abrupt change in the radiation rate occurs, the Plank mean free path has decreased to 1 m. By 2 ns, on the downside of the peak, it has dropped dramatically to 0.79 mm. During this time interval, the electrons are strongly coupled with the radiation field and a rapid rise in radiated power is observed. This is further evidenced in the electron temperature at 2 ns which has dropped to 234 eV. The ion temperature at this time has decreased to 2.8 keV.

6.2.3 Constant Velocity, Mass Variation

As shown, increasing the toroid velocity increases the kinetic energy per particle, which in turn increases the total amount of kinetic energy accessible for conversion into thermal energy and then radiation. A larger kinetic energy can also be obtained by adding more mass to the toroid. In this case, the directed kinetic energy per particle remains the same, but the number of particles has changed. The ions will be heated to the same temperature, but there will be more of them. If the transfer of energy between the material components and the radiation field is significant on the timescale of stagnation, the resulting radiated energy will be correspondingly greater as will the radiation rates. For the same toroid dimensions, a larger mass will produce higher densities. It should be noted that this can have a bearing on the coupling properties in the stagnation region and could alter the radiated yield, the shape of the radiated power curve and the photon distribution.

Table 6.11 list a set of calculations in which the initial mass of the toroid has been varied. Also contained in the table are the peak densities and energies affiliated with the given mass. As usual, the baseline case values have been included for reference. Table 6.12 shows the time and density at peak compression and the various radiation quantities. As more mass is put into the system, the density becomes higher and the coupling is enhanced. The toroid can cool more efficiently, and the pressure takes longer to build allowing for greater compression. Because of this, peak compression occurs later in time. For the 2 mg toroid, the peak density is a factor of 6.2 greater than the initial peak value. For the 40 mg case, this has increased to 14.

As with increasing velocity, the higher kinetic energy obtained through additional mass results in a higher peak power and total radiated yield. In

Table 6.11. Initial parameters of mass survey

simulation	initial mass	initial peak density	kinetic energy
ct15	2.0 mg	0.37 kg/m ³	1.0 MJ
ct1	10.0 mg	1.8 kg/m ³	5.0 MJ
ct16	20.0 mg	3.7 kg/m ³	10.0 MJ
ct17	40.0 mg	7.4 kg/m ³	20.0 MJ

Table 6.12. Results from mass survey: peak compression, radiation production

simulation	(t) _{peak comp.}	(ρ) _{peak comp.}	peak power	pulse width	Total Yield (5% of peak power)
ct15	5.0 ns	2.3 kg/m ³	157 TW	5.0 ns	0.840 MJ
ct1	6.2 ns	19.0 kg/m ³	837 TW	5.8 ns	4.768 MJ
ct16	7.0 ns	46.0 kg/m ³	1713 TW	5.8 ns	9.668 MJ
ct17	7.5 ns	100.0 kg/m ³	3521 TW	5.8 ns	19.57 MJ

going from 2 mg to 40 mg, the total radiated yield went from 0.84 MJ to 19.57 MJ. This corresponds to over a factor of 20 difference in total radiated energy. The conversion efficiency in these two instances is 84% and 97%, respectively. This observed improvement in efficiency is a consequence of better coupling at the larger densities. Figure 6.26 displays the radiated power as a function of time for the runs ct15, ct16, and ct17. The 2 mg, 1MJ calculation was plotted separately from the other two simply because of the scaling.

An inspection of the radiated power curve for the 2 mg calculation reveals that it is very similar to that of the baseline case. Initially, the Plank mean free path is on the order of 1 m in the stagnation region. At 1.8 ns, the electron-radiation coupling improves substantially and this value drops to approximately 1 cm. The electron temperature changes from 310 eV to 130 eV within 0.2 ns bringing it much closer to the radiation temperature of 98 eV. As a result, a change in slope is seen in the radiation rate. This change occurs later than in the baseline case because there is less material (lower densities) to start off with originally and it takes longer to reach the required densities (and temperatures). By peak compression, the Plank mean free path has decreased to around 2 mm in the stagnation region. At this time, the ion temperature is at 100 eV, the electron temperature at 98 eV and the radiation field, 95 eV.

The abrupt change in the slope of the radiated power observed in the 2 mg and baseline calculations is also present at 20 mg. A comparison of these simulations indicate further that this change occurs earlier in time with increasing toroid mass. By the 40 mg calculation, this discontinuity appears to have completely vanished. With the ct15 run of 20 mg, the transition in slope occurs at 1.4 ns, and, similar to the lower mass calculations, the Plank photon mean free path in the stagnation region is approximately 1 cm. This value of 1 cm

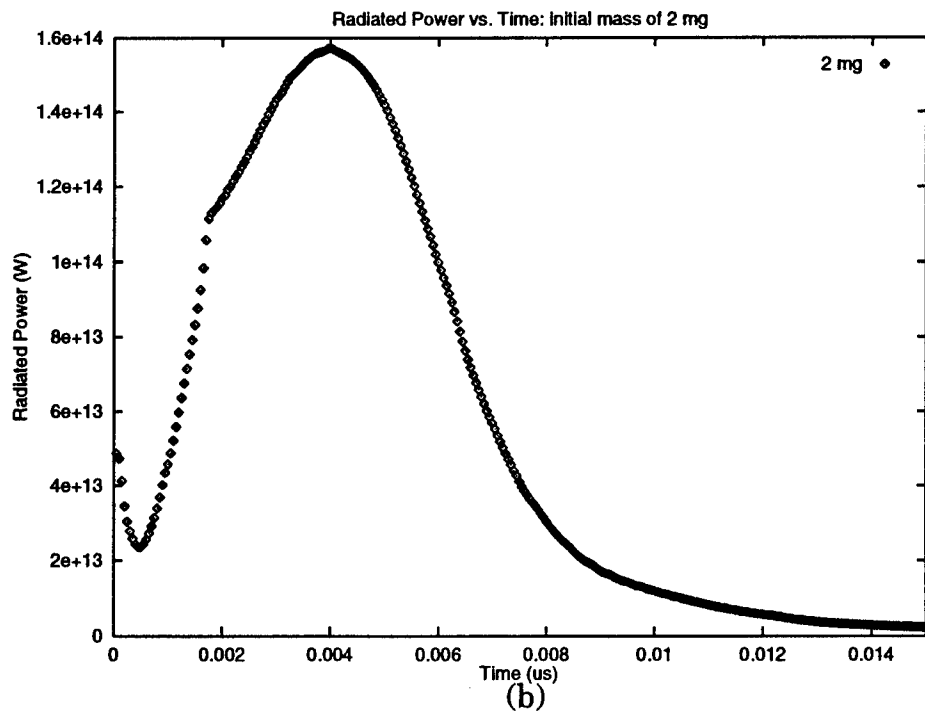
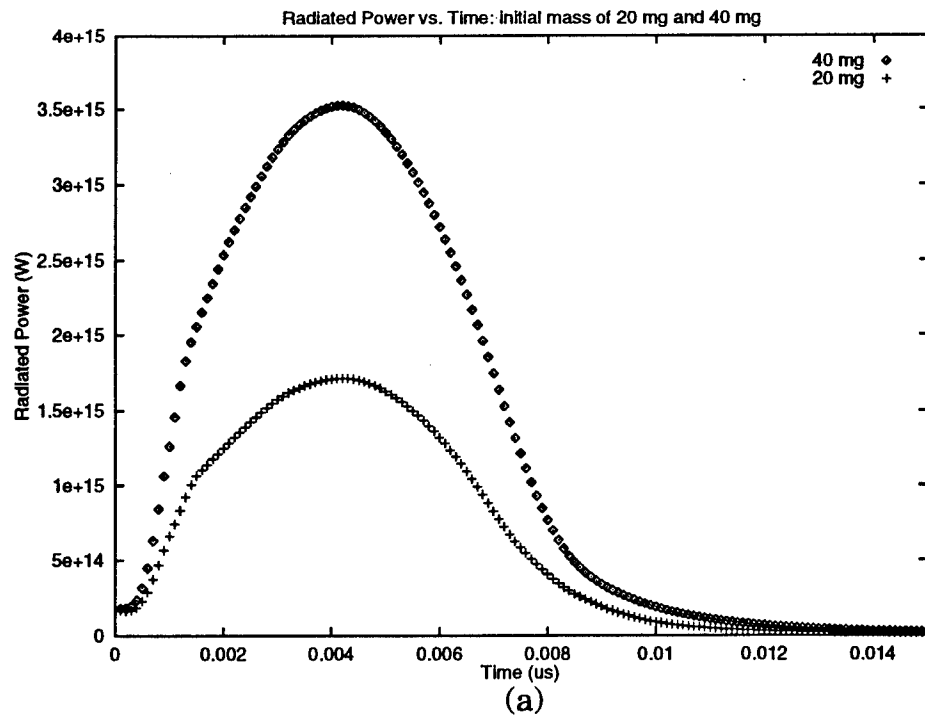


Figure 6.26. Radiated Power vs. Time for the (a) 20 mg and 40 mg runs at 10 MJ and 20 MJ directed kinetic energy, respectively, and (b) 2 mg run at 1 MJ directed kinetic energy.

seems to be a defining number as far as the electron-radiation coupling is concerned, implying that there is a density threshold at which the coupling (albeit an artifact of the equation of state tables) really "turns on". In the 40 mg simulation, the photon mean free path is already 1 cm at 1 ns into the stagnation. Thus, there is no regime in coupling efficiency to cross over in this case.

At 40 mg, the density is high enough that by 2 ns the mean free path for the electron-radiation coupling is on the order of the stagnation region: the Plank mean free path at the wall is 0.6 mm compared to the 0.5 mm size of the compression zone. As the toroid continues to compress, the Plank mean free path continues to decrease and by peak compression is at 0.03 mm. Under these conditions, the stagnation region, which produces the large fraction of emitted radiation, closely resembles a surface emitter. This is most certainly the case by peak compression. At this time the ion temperature is 230 eV and the electrons and radiation field are at 219 eV.

The absorption mean free path, which determines the transport of the radiation field, ranges from 3 mm to 6 mm in the prestagnated material for the first 4 ns of stagnation. Since this value remains smaller than the uncompressed toroid dimensions, the radiation in this region is transported by diffusion using the rosseland mean opacity term in the radiative conductivity. During the early part of stagnation, the absorption mean free path at the wall is typically larger than the stagnation region, but smaller than the size of the entire toroid. This value continues to decline and has dropped to 0.1 mm by peak compression. An examination of the output indicates that actually by 3 ns, the stagnation region is in the diffusion regime with the mean free path at 0.3 mm. For the 20 mg calculation the diffusion regime is reached at approximately 6.5 ns into the stagnation. (In the prestagnated material the mean free path is 10 mm.) As for the 2 mg problem, the radiation is always flux-limited

as the absorption mean free path is larger than the characteristic dimensions of the toroid throughout the entire stagnation.

A comparison of the 1 MJ and 10 MJ simulations to their velocity counterparts (ct13 and ct14 calculations, respectively) reveal that the calculations having the same initial total kinetic energy produce similar radiated yields. The 2 mg, 100 cm/ μ s calculation has a somewhat lower yield than that of the 10 mg, 45 cm/ μ s run. This is caused by the lower coupling efficiency resulting from the smaller densities and higher temperatures in the 2 mg problem. Although the radiated yields are close in both cases for the two separate energies, the radiated power and pulse widths are quite different. Take for instance the two 10 MJ calculations. As the velocity is increased to 142 cm/ μ s and the mass is kept at 10 mg, the pulse width naturally becomes shorter. Because of the increasing velocity, the photon energy distribution is shifted to higher energies (the ion temperature is higher, resulting in higher electron and radiation temperatures). The amount of higher energy photons leaving the system in this case, surpasses that of the 20 mg case where there may be more photons emitted, but at lower energies. The radiated power is subsequently larger for the 142 cm/ μ s simulation. The peak value of radiated power is further enhanced in this run by the transition in material-radiation coupling at around 1.8 ns.

6.2.4 Mass Variation, Velocity Variation

In the two previous sets of calculations, either the mass or the velocity of the toroid was varied, thereby changing the amount of initial directed kinetic energy. In the next two calculations, both of these parameters have been varied simultaneously, and in such a manner that the kinetic energy is kept at a constant value of 5 MJ. Table 6.13 list the initial mass and velocity in these calculations. In the first run, the mass is lower than in the baseline case and the velocity has correspondingly increased. In the second run, the opposite is true. The results of the two simulations along with that of the baseline calculation are shown in Table 6.14. The radiated power curve for each run is displayed in Figure 6.27.

The information provided in Table 6.14 indicates that decreasing the mass to 5 mg and increasing the velocity to 142 cm/ μ s leads to a narrower pulse width and a larger radiation rate. These characteristics are consistent with those observed in the velocity survey. At a higher velocity, the compression occurs at a faster rate and the time over which substantial radiation is emitted is reduced. In addition, at higher velocities there is more energy available per particle. The ion temperature is larger, which raises the electron temperature, and consequently the radiation rate can increase. In accordance with the higher ion temperature, the photon energy distribution will also be shifted to larger energies. At 1 ns into the stagnation, the ion temperature has reached 398 keV, the same as in the 10 mg, 142 cm/ μ s calculation. This further illustrates that it is the kinetic energy per particle which governs the maximum energy that can be put into ion thermal motion.

The physics in the stagnation region, is of course, also dependent on the density. This, along with the temperature, is what defines the ability of the

Table 6.13. Initial parameters for 5 MJ survey: varying initial mass and velocity

simulation	initial mass	initial peak density	initial velocity
ct18	5.0 mg	0.92 kg/m ³	142 cm/μs
ct1	10.0 mg	1.85 kg/m ³	100 cm/μs
ct19	40.0 mg	7.4 kg/m ³	50 cm/μs

Table 6.14. Results from 5 MJ survey: peak compression, radiation production

simulation	(t) _{peak comp.}	(ρ) _{peak comp.}	peak power	pulse width	Total Yield (5% of peak power)
ct18	4.4 ns	9.7 kg/m ³	1729 TW	3.5 ns	4.716 MJ
ct1	6.2 ns	19.0 kg/m ³	837 TW	5.8 ns	4.768 MJ
ct19	12.0 ns	71.0 kg/m ³	424 TW	11.0 ns	4.924 MJ

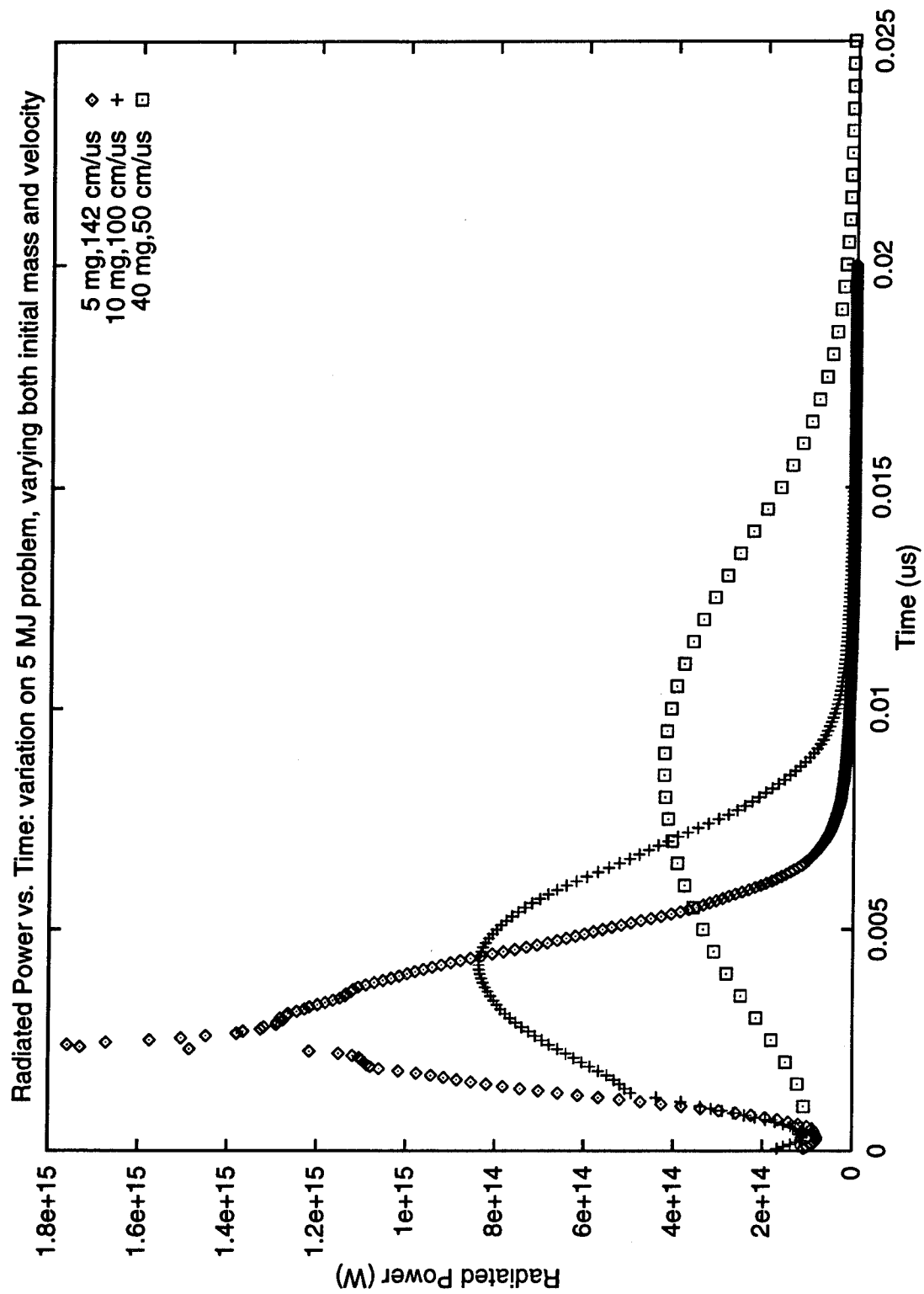


Figure 6.27. Plot of the Radiated Power vs. Time for a 5 MJ toroid with varying initial mass and velocity.

ions and electrons and subsequently the electrons and radiation field to couple with each other. The coupling can in turn effect the degree of compression and the conversion of initial kinetic energy into thermal energy and then radiation. For this run, the density is lower than in the baseline case but the temperatures are higher. As a result, the coupling efficiency is expected to decrease and the conversion efficiency to be lower. An examination of the table shows, however, that the conversion efficiency has not been substantially effected. The lower mass, higher velocity simulation is almost as efficient a radiator as the baseline case.

An explanation for this unexpected improvement in conversion efficiency can be found by looking at the radiated power curve. From Figure 6.27, the radiation rate exhibits a sharp rise at the front end of the pulse which is not observed in the smooth curves of the other two calculations. This feature is similar to that observed in the ct14 run at 10 mg, 142 cm/ μ s and is caused by an equation of state related transition in the electron-radiation coupling. In this case the Plank mean free path drops from a value of 10 m just prior to the observed spike to 1 mm on its downside. The amount of radiated energy produced as a result of this coupling effect can be estimated from the radiated power curve and is found to be approximately 400 kJ. Thus, without this contribution to the coupling, the total radiated yield would decrease to 4.316 MJ.

The influence of the density and temperature on the conversion efficiency is apparent in going from the baseline calculation to the 40 mg, 50 cm/ μ s calculation. The conversion efficiency in this latter case is 97% as opposed to the baseline and ct18 runs of 94%. Again, the results in this case are consistent with the velocity and mass surveys. Because of the low velocity, the stagnation process occurs slowly and the associated pulse width is quite broad. With decreasing velocity there is also less kinetic energy per particle and the ion

temperature does not get as high (The ion temperature at 1 ns is 8.9 keV). The radiated power is therefore not as large as in the baseline calculation and the radiation spectrum should consist of more lower energy photons. With the larger mass, the density in the stagnation region has increased. This factor, together with the smaller temperatures, will improve the coupling and an increase in conversion efficiency will be observed.

In all of the calculations considered thus far, the coupling was sufficient at least during some part of the stagnation to extract most of the energy originally stored in the directed kinetic energy of the toroid. Based on previous discussions, one could envision initial conditions where the coupling becomes essentially non-existent within the stagnation region and the radiation production would severely deteriorate. Obvious candidates for influencing coupling are the initial mass and velocity. With increasing velocity or decreasing mass (or both), the degree of coupling will gradually decline and the radiative yield will become correspondingly limited. For the 5 MJ toroid, where both mass and velocity are varied, the lower mass, higher velocity calculations will eventually exhibit lower radiation production.

6.2.5 Stagnation Geometry and Toroid Material Variation

The last two simulations presented here investigate separately the influence of stagnation geometry and toroid material on radiation production. In the first calculation, a more compact geometry was considered in which the inner conducting wall has been removed and the outer conducting wall brought in closer to the centerline at 0.89 cm. This geometry is representative of that found in the calculations of M. Gee et. al. [12,13] and uses the highest degree of focusing (focusing down to the axis). The initial values of mass and velocity were the same as in the baseline case and the directed kinetic energy of the toroid was 5 MJ. The peak value of the toroidal component of the magnetic field was set to 11 MG (1100 T). This value is less than that determined from isentropic conditions for a compression down to 0.89 cm outer radius (25 MG, 2500 T) and is based on the fact that there may be some losses in magnetic energy due to diffusion and nonadiabatic compression. The corresponding magnetic energy for this configuration is 500 kJ, 10% of the initial kinetic energy. With these values, the kinetic and magnetic energies in this problem are about the same as in the ct10 simulation discussed earlier.

At a smaller radius and hence smaller volume, the density in this calculation is larger than in the baseline case. As a consequence, the coupling is expected to be more efficient throughout the stagnation. However, for this problem, the magnetic energy is also larger and the deleterious effects of magnetic pressure will compete with the improved coupling. If the coupling is not sufficiently improved, then the additional energy gained through coupling is not enough to offset or overcome that lost to magnetic pressure. Under these circumstances, the results of this calculation may be no better than that of ct10 (magnetic energy 10% of kinetic energy) and the baseline case may be

more adequate in supplying the desired radiation production.

The maximum compression in this simulation occurs at 5.0 ns with a peak density of 74 kg/m^3 . Compared to the initial density of 11 kg/m^3 , this is a factor of 6.7 in compression and is slightly larger than that of 6.5 observed in the ct10 calculation. The total radiated yield is 4.12 MJ, producing a conversion efficiency of 83%, while the radiated power has a peak value of 787 W and a pulse width of 5.1 ns. These values are very close to those of the ct10 calculation and are consequently lower than the baseline case. This indicates that for the parameters chosen, focusing to a smaller volume in an attempt to gain higher conversion efficiencies and radiation rates does not work. In this case, it is better to go with less compression, smaller fields for the same amount of mass. This is actually desirable since the latter puts less demands on the experimental system. The radiated power as a function of time is displayed in Figure 6.28 (a). Note that the transition in coupling efficiency which appears in the curve for the ct10 and baseline calculation (Figure 6.24) has almost disappeared.

For the final calculation of this section, a lower Z (atomic number) material, in this case Argon, was chosen instead of Xenon to examine the effects that complete ionization has on the radiation production during stagnation. In the baseline calculation, the Xenon in the stagnation region is never fully ionized reaching its highest ionization fraction, \bar{Z} , of 43 in the first ns of stagnation. ($Z = 54$ for Xenon). As the density increases, this fraction decreases, and by peak compression $\bar{Z} = 25$, the value it had initially in the prestagnated material. Thus, throughout the stagnation, there are always Xe ions with bound electrons. Contributions to the emitted radiation will then result not only from free-free interactions but also from bound-bound and bound-free electron transitions. (In a fluid code, where the radiation field couples strictly

through the electron temperature, the effect of bound electrons is folded into the opacities.) In addition, the interaction of the radiation field in terms of the scattering and absorption of photons also depends upon both the free and bound electron distributions. In particular, heavier elements with many inner shell electrons can provide substantial opacity to energies below about 10 keV [4].

To investigate the effect that these properties have on radiation production, the Xenon plasma was replaced with Argon. For the same initial conditions, the Argon becomes fully stripped almost immediately in the stagnation region and remains so throughout the compression. Figure 6.28 (b) shows the radiation rate for the Argon calculation. The radiated power peaks at 219 TW substantially lower than the 837 TW of the baseline calculation. Because the radiated power curve gradually drops off, it is difficult to approximate a pulse width. As a first estimate, this is measured from the point where the radiation rate actually starts to rise, at about 2 ns, out to 10 ns. Here the 10 ns is taken from the baseline calculation, and is the time at which the radiated power has dropped to 5% of the peak value there. With this, the pulse width is 8 ns. The radiated yield at 10 ns is 1.31 MJ. This is quite low compared to that of the baseline case and relates to a conversion efficiency of 26%. By this time, the radiation being emitted is occurring during expansion. As a result, the material is cooling very rapidly and the radiation conversion is even less efficient. Even by the end of the simulation, 25 ns, this has only increased to 2.117 MJ.

These results imply that the material comprising the toroid can strongly influence its ability to be a good radiator. In moving from Xenon to Argon, the plasma went from partially ionized to fully ionized, a process characterized as "burn through ". In this case, the ion-electron and the electron-radiation coupling decreased considerably (i.e., $\tau_{eq}^{ie} \propto Z^{-2}$) [6] and not much energy could be

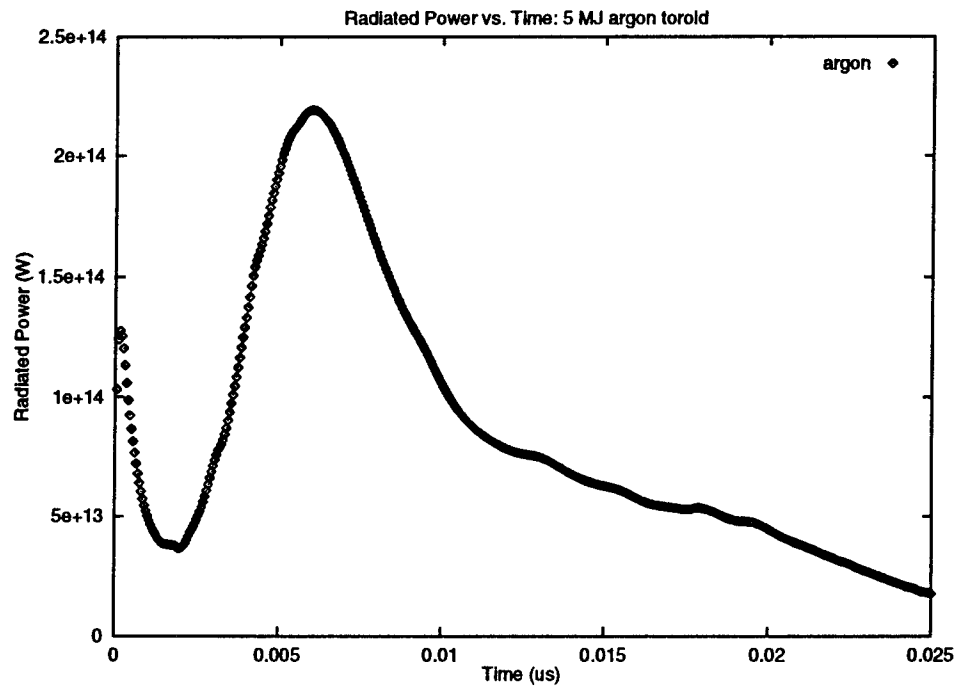
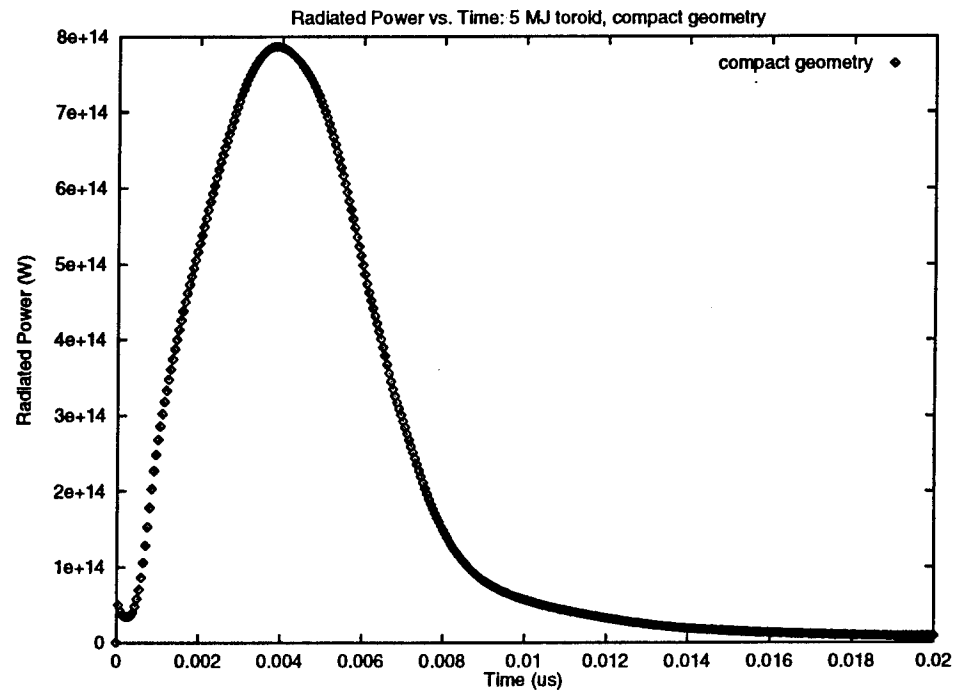


Figure 6.28. Radiated Power vs. time for (a) more compact geometry with outer conducting wall only, and (b) Argon filled toroid.

transferred to the radiation field. This is evident in the temperatures at peak compression: 10 keV for the ions, 5 keV for the electrons, and 87 eV for the radiation field. Clearly, this is very different than the close temperatures observed at peak compression in the baseline case. The very low radiation temperature is directly related to the poor coupling characterized by a large Plank mean free path observed in the Argon calculation and is indicative of a volumetric emitter - this never drops below a km! Furthermore, because the Argon has burned through, any radiation that can be emitted is bremsstrahlung and tends to consist of low energy photons [6]. It is the poor coupling and low energy photons combined that lead to the decrease in radiation production making Argon a poor choice for the stagnation plasma. In the same token, it is the efficient coupling and high energy line emission that is a consequence of partial ionization and large Z that makes Xenon a better choice.

CHAPTER 7. SUMMARY AND CONCLUSIONS

In this dissertation a flux-limited nonequilibrium radiation diffusion model was incorporated into the MHD code MACH2, and extensively benchmarked. This three temperature radiation MHD code was then used to simulate the complex physics of stagnating compact toroids including radiation production. A summary of the work performed and the conclusions reached concerning the stagnation process is presented below.

MACH2 is a 2 1/2-dimensional, nonideal magnetohydrodynamics code which has been utilized to model a variety of laboratory experiments. The equations that are solved by the code include the dynamic equations for the material density, electron and ion specific internal energies, momentum, and magnetic field. An equation of state is used to supplement these evolution equations and may be evaluated analytically or extracted from pre-generated tables which are based on LTE (local thermodynamic equilibrium) material conditions. With the addition of the nonequilibrium radiation diffusion model to the code, the radiation field is treated as a separate entity described by a Plankian distribution at the radiation temperature T_R . This implementation introduced a dynamic equation for the radiation field and modified the momentum and energy equations - a radiation pressure term in the momentum equation and a electron-radiation coupling term in the electron energy equation.

The nonequilibrium radiation diffusion model is most accurate in the diffusion regime where the absorption mean free path is much smaller than a characteristic dimension of interest. To extend this model to an optically thin regime, where the diffusion approximation is no longer valid, a flux-limited version of the radiative conductivity was formulated. This modified conductiv-

ity provided the proper values of the radiation flux in both the thick and thin limits (cE) and enabled a qualitative smooth transition between these limits.

The coding of this radiation model into MACH2 was followed by rigorous testing of the various algorithms. Detailed benchmarking of the electron-radiation coupling and the radiation diffusion was performed using a set of radiation MHD test problems. This benchmarking had the purpose of not only verifying that the associated algorithms were correct, but ensuring the implemented algorithms were stable and robust. This latter issue became important in the electron-radiation coupling, and resulted in changing the initial explicit difference form of the coupling equation to an implicit form. The radiation diffusion test problems were extensive and covered a range of physical regimes. The first calculations involved one and two dimensional diffusion of radiation in a static, opaque material with a constant diffusion coefficient. Additional calculations allowed for more complexity by including electron-radiation coupling and pressure gradient effects which generated fluid motion (dynamic diffusion). These latter problems examined both optically thick and thin regimes. The advection of the radiation field, radiation pressure-volume work, and the effect of radiation acceleration on the material were also benchmarked on a qualitative level.

With the flux-limited nonequilibrium radiation diffusion model in the code, MACH2 was used to simulate the stagnation of compact toroids against stationary targets and the subsequent evolution of the radiation field. Compact toroids, which are magnetically confined plasma rings, can be accelerated to large velocities, and thus large directed kinetic energies. At high enough densities and velocities, they have the capacity to become effective radiation sources upon stagnation, producing photons above 1 keV. The compact toroids considered in this work are approximately 1 cm in diameter and have kinetic

energies in the MJ range with masses between 5 mg and 40 mg, and velocities between 50 cm/ μ s and 142 cm/ μ s.

A baseline case of 10 mg at 100 cm/ μ s, corresponding to a directed kinetic energy of 5 MJ, was analyzed in detail. For the defined prestagnation conditions, this toroid was found to be an efficient radiator upon stagnation, producing 4.768 MJ of radiated yield with a peak radiated power of 837 TW and a pulse width at half max of 5.8 ns. The stagnation region was also found to evolve through different radiation regimes related to electron-radiation coupling and radiation transport. Poor coupling in the early stages of stagnation led to three separate temperatures in the compression region. The low densities and high temperatures during this time also resulted in a large absorption mean free path and the radiation was free streaming. In the latter stages of compression and into expansion, the material was observed to transition to higher densities and lower temperatures. Consequently, the electrons and radiation field had reached thermal equilibrium by peak compression at 5.2 ns. The absorption mean free path, which was on the order of the toroid dimensions at peak compression, continued to decrease into expansion and the radiation field was transported in a diffusion-like manner. In terms of the electron-radiation coupling, the stagnating toroid is observed to move from a volumetric emitter towards a surface emitter during the stagnation process.

A parameter study was also performed using the baseline case as a starting point. This study examined varying the prestagnation magnetic energy to kinetic energy ratio, the initial mass, the initial velocity, both mass and velocity together keeping the kinetic energy the same, the stagnation geometry, and finally, the toroid material. There are a number of conclusions which can be reached based on the results of this parameter survey. The magnetic energy to kinetic energy ratio, if too large, can cause a reduction in total radiated yield

and radiated power; the magnetic field introduces magnetic pressure effects which can deter toroid compression. For the 5 MJ calculations which were examined here, the radiated yield was still significant even when the magnetic field effects were influential in the stagnation. In the most extreme case, where the prestagnated magnetic energy was 50% of the kinetic energy, the radiated yield was 3.2 MJ. Although this was only a conversion efficiency of 64%, the radiated energy was still high.

With a change in initial directed velocity, the total kinetic energy of the toroid is varied as is the kinetic energy per particle. In this instance, larger velocities provided more available energy for conversion and the radiated yield increased. In addition, the photon distribution was shifted to higher energies and a rise in radiated power was observed. Higher velocities also led to shorter pulse widths. On the other hand, by varying the mass, the amount of particles is changed but the kinetic energy per particle remains constant. Under these conditions more mass led to larger total kinetic energies and higher initial densities which resulted in improved coupling. Consequently, the radiated energy increased (as a result of larger kinetic energy and higher conversion efficiencies), as did the radiated power.

In the calculations where both the mass and velocity were varied while the directed kinetic energy was maintained at 5 MJ, the results were consistent with those of previous simulations. A mass of 5 mg, velocity of 142 cm/ μ s produced a short pulse of 3.5 ns with large radiation rates - peak power of 1729 TW. At the other extreme, a mass of 40 mg, velocity of 50 cm/ μ s produced a wide pulse of 11 ns with a smaller peak radiated power of 424 TW. In both cases, the total kinetic energy was the same, but the kinetic energy per particle different. The conversion efficiency was slightly better with the higher mass because of improved coupling. This latter study indicated that for a spec-

ified amount of kinetic energy, one can construct the desired photon distribution, radiated power, and pulse width by varying either or both of these parameters. Of course, varying these parameters also influences the coupling efficiency in the stagnation region and thus the amount of radiation energy that can be extracted. This must be kept in mind.

In an attempt to obtain higher conversion efficiencies and radiation rates, a more compact geometry with 5 MJ directed kinetic energy at 10 mg, 100 cm/ μ s was simulated. In this case, the toroid was focused down to 1 cm in diameter at the axis, physically causing the density to increase as well as the magnetic field. The results of the simulation indicated that this does not improve the radiation production because the effect of the higher magnetic strength prevails over the increase in coupling caused by higher densities. This is important in that it provides evidence that higher compression with the same mass and velocity does not always lead to improved radiation production. This permits less stringent requirements on the experimental system.

To examine the effect that partial ionization of material in the stagnation region has on the radiation production, a calculation was carried out which used Argon gas instead of Xenon as the material comprising the compact toroid. At the same initial densities, temperatures, and fields as in the baseline case, the Argon toroid was found to be fully stripped during most of the stagnation. This resulted in a poor radiator indicating that bound electrons can drastically influence the coupling properties and photon energies in the stagnation region.

There is always more work that can be done to develop a more accurate picture of compact toroid stagnation, either by improving the modelling of the stagnation process, and in particular, the radiation treatment, or by further calculations which span a broader parameter space than was addressed here.

The calculations presented in this dissertation were based on LTE atomic physics and mean opacities were used to describe the electron-radiation coupling and the diffusion of the radiation field. In the initial stages of stagnation, the low density material in the vicinity of the wall reaches large temperatures on a timescale of approximately 1 ns. As a result, the compressed portion of the toroid is most likely non LTE during the first ns or so of the simulation and the LTE atomic physics model is not appropriate to use at this phase of the stagnation. Furthermore, a lower mass or less compressed toroid might not have the prestagnation densities to ever reach an LTE state at any time during the calculation. In this case a non LTE description of the atomic physics is required throughout the entire stagnation to accurately simulate radiation production. An investigation into the non LTE issues of the stagnation process could clarify the importance that such physics plays, whether it occurs in only the first few ns of a calculation, or throughout the simulation. A decision can then be made concerning the necessity of using non LTE physics either in MACH2 or at some point outside the calculation via post processing.

As mentioned, the radiation diffusion is based upon a single mean opacity into which is folded the information contained in line absorption, etc. This is another area which could be improved upon by incorporating multigroup diffusion into the radiation diffusion algorithm. With a multigroup treatment, the radiation spectrum is divided into a number of frequency groups and the group opacities (specifically Rosseland) are obtained by averaging the associated spectrum over its corresponding frequency group. Thus, any spectral information that might have been previously washed out through the averaging, will become more visible. This method becomes increasingly better as the number of groups becomes larger - the details of the weighting procedure are less important. The implementation of such a treatment, however, requires a

separate diffusion equation for each group and for the entire set of equations to then be solved simultaneously. Clearly, such an effort would require a substantial amount of work and would be a reasonable project for a post doctoral position.

The calculations discussed in this dissertation were based on a compact toroid which had undergone a factor of twenty in radial compression. These calculations were limited in the range of parameter space that was simulated, investigating the stagnation physics for a relatively small set of prestagnation properties and geometry. It should be noted that a factor of twenty compression has not yet been attempted in the current experiment at the Phillips Laboratory. In all likelihood, this degree of radial compression will be reached in the near future. At that time, it would be appropriate to benchmark the nonequilibrium radiation diffusion model of MACH2 by simulating the entire compact toroid experiment, from formation through compression to stagnation, based on the experimental geometry.

The parameter survey examined here should be extended to include other possible scenarios which might lead to a realistic optimization of the desired radiation production together with relaxed system requirements. For example, simulations which consider larger masses and larger toroid sizes prior to stagnation, while maintaining the density range of previous calculations, have been suggested [63]. In these instances, the larger size of the toroid would provide a greater extent over which the radiation field can interact with the material. This would keep the photon mean free path in the surface-like emitter regime longer, as well as the diffusion regime, resulting in higher conversion efficiencies. This is of interest experimentally, since it might allow less compression for the required radiation production thus bypassing many of the problems that can arise with extreme compression.

APPENDIX A. ANALYTIC COMPRESSION RATIOS OF PHYSICAL PARAMETERS FOR ISENTROPIC COMPRESSION

A first order approximation to the scaling of physical parameters during compact toroid compression can be derived analytically. Such analytic expressions are informative in that they indicate the effect of compression on the magnitude of physical quantities and provide an intuitive picture of the compression process without requiring the use of sophisticated numerical codes or after-the-fact experimental measurements. Under the assumption of self-similar, quasistatic compression, the compression process can be considered adiabatic and reversible, i.e. isentropic. In this case, physical quantities such as temperature, density, and magnetic field are related in a simple manner to their precompressed counterparts.

Recall the first law of thermodynamics:

$$du = dq - pdv \Rightarrow dq = du + pdv . \quad (A1)$$

where du is the change in the internal energy of an isolated system, pdv is the work done by the system, and dq is the quantity of heat loss from the system. (All quantities are written per unit mass.) Writing dq as Tds and specializing to an ideal gas ($pv = \mathcal{R}T$, $du = c_v dT$, the above equation becomes

$$Tds = c_v dT + \mathcal{R}T \frac{dv}{v} , \quad (A2)$$

or

$$ds = c_v \frac{dT}{T} + \mathcal{R} \frac{dv}{v} . \quad (A3)$$

For an adiabatic process $dq = 0 = ds$ and, upon integration

$$0 = c_v \ln \left(\frac{T}{T_o} \right) + \mathcal{R} \ln \left(\frac{v}{v_o} \right) . \quad (A4)$$

Rearranging,

$$\ln\left(\frac{T}{T_o}\right) = -\frac{\mathcal{R}}{c_v} \ln\left(\frac{v}{v_o}\right) . \quad (\text{A5})$$

Using, $\mathcal{R} = c_p - c_v$ for an ideal gas and the definition $\gamma \equiv c_p/c_v$,

$$\ln\left(\frac{T}{T_o}\right) = -(\gamma - 1) \ln\left(\frac{v}{v_o}\right) , \quad (\text{A6})$$

or

$$T = T_o \left(\frac{v_o}{v}\right)^{(\gamma-1)} . \quad (\text{A7})$$

If the compact toroid is assumed to have a spherical shape, with radial dimension given by R then

$$v = \left(\frac{4}{3}\pi R^3\right)/m , \quad m = \rho \left(\frac{4}{3}\pi R^3\right) = \text{constant} \Rightarrow \frac{v}{v_o} = \left(\frac{R}{R_o}\right)^3 = \frac{\rho_o}{\rho}$$

and

$$T = T_o \left(\frac{\rho}{\rho_o}\right)^{(\gamma-1)} = T_o \left[\left(\frac{R_o}{R}\right)^3\right]^{(\gamma-1)} . \quad (\text{A8})$$

For a monatomic gas (three degrees of freedom), $\gamma = 5/3$, and the temperature after compression is related to the precompression temperature by

$$T = T_o \left(\frac{R_o}{R}\right)^2 . \quad (\text{A9})$$

A similar pressure relationship can be found from (A9) using the equation of state for an ideal gas:

$$T = \frac{pv}{R} = \frac{p}{\rho R} , \quad (\text{A10})$$

$$\Rightarrow \frac{p}{\rho} = \frac{p_o}{\rho_o} \left(\frac{R_o}{R}\right)^2$$

or

$$p = p_o \frac{\rho}{\rho_o} \left(\frac{R_o}{R}\right)^2 = p_o \left(\frac{R_o}{R}\right)^3 \left(\frac{R_o}{R}\right)^2 = p_o \left(\frac{R_o}{R}\right)^5 \quad (\text{A11})$$

To determine the compression ratios for magnetic field, the assumption of a highly conducting material (conductivity is infinitely large) is made. For such material conditions, the magnetic flux is conserved through any surface of a system and [45]

$$\Phi_M = \int_{\Delta S} \vec{B} \cdot d\vec{A} \quad (\text{A12})$$

Using the surface area of a sphere and equating the precompressed flux to the flux at any stage of the compression:

$$B_o R_o^2 = B R^2$$

or

$$B = B_o \left(\frac{R_o}{R}\right)^2 \quad (\text{A13})$$

APPENDIX B: ANALYTIC SOLUTIONS OF THE DIFFUSION EQUATION

Benchmarking recently developed code against known analytic or standard numerical solutions is a common and necessary practice in computational physics. Benchmarking aids in the debugging process of algorithms and provides a measure of the ability of a code to simulate actual physical conditions. It can be useful in determining the regimes, if any, in which numerical solutions diverge from true physical solutions and can assist in identifying the cause of solution error, i.e., whether this divergence results from the finite difference approximation to the differential equations, or in some cases, to the manner in which a set of difference equations are solved.

In this appendix, analytic expressions for the diffusion of a physical quantity in one and two dimensions are derived for specific cases in planar geometry. These solutions are then used to benchmark the radiation diffusion algorithm in MACH2. In particular, solutions that are of interest include the one dimensional linear flow of radiant energy from a boundary into a cold material ($T_R=0$), and the two dimensional cooling of a radiatively "hot" rectangular region by diffusion through its bounding surfaces.

Consider the one dimensional diffusion problem given by:

$$\begin{aligned} \frac{\partial v}{\partial t} &= \kappa \frac{\partial^2 v}{\partial x^2}, & 0 \leq x \leq l & & v = v_1 \text{ at } x = 0 \\ & & & & v = v_2 \text{ at } x = l \\ & & & & v = f(x) \text{ at } t = 0 \end{aligned} \quad (B1)$$

where v is the variable of interest and κ is a constant characteristic of the system in which the quantity v is described. The solution to this problem can be broken into two contributions. One contribution is the solution to the diffusion equation with v at the ends $x = 0, l$ set to zero, while the other contribution is the steady state solution for $v = \text{constant} \neq 0$ at $x = 0, l$. In other words, the

solution to the problem posed by (B1) is a superposition of two solutions. The first solution corresponds to the spatial and temporal evolution of v for a system which tends to a final steady state of $v = 0$ (which occurs when the value of v is zero at $x = 0, l$). The second solution corresponds to a time independent correction term which arises because the end conditions at $x = 0, l$ are some value other than zero, leading to a final steady state value different from zero. Mathematically, this transforms the problem defined by (B1) into an equivalent problem given by the following two equations and their boundary conditions:

$$\frac{\partial u}{\partial t} = \kappa \frac{\partial^2 u}{\partial x^2}, \quad u = 0 \text{ at } x = 0, l \quad t \geq 0, \quad (\text{B2})$$

and

$$\frac{\partial^2 u_c}{\partial x^2} = 0, \quad \begin{aligned} u_c &= v_1 \text{ at } x = 0, \\ u_c &= v_2 \text{ at } x = l, \end{aligned} \quad (\text{B3})$$

where the solutions u and u_c must satisfy

$$v = u + u_c, \quad v = f(x) \text{ at } t = 0. \quad (\text{B4})$$

The general solution to the diffusion equation

$$\frac{\partial u}{\partial t} = \kappa \frac{\partial^2 u}{\partial x^2}, \quad (\text{B5})$$

can be determined using the method of separation of variables [59] with

$$u(x, t) = F(x) T(t). \quad (\text{B6})$$

Substituting this expression into Equation (B5)

$$\frac{1}{F} \frac{\partial^2 F}{\partial x^2} = \frac{1}{\kappa T} \frac{\partial T}{\partial t} \quad (\text{B7})$$

or

$$\frac{1}{F} \frac{\partial^2 F}{\partial x^2} = -\alpha^2, \quad \frac{1}{\kappa T} \frac{\partial T}{\partial t} = -\alpha^2, \quad (\text{B8})$$

where α is the separation constant. With the solutions to these two equations given by

$$\frac{\partial^2 F}{\partial x^2} + \alpha^2 F = 0 \Rightarrow F(x) = \begin{pmatrix} \sin \alpha x \\ \cos \alpha x \end{pmatrix}, \quad (\text{B9})$$

and

$$\frac{\partial T}{\partial t} = -\alpha^2 \kappa T \Rightarrow T(t) = e^{-\alpha^2 \kappa t}, \quad (\text{B10})$$

the basic solution takes the form

$$u = [A \sin \alpha x + B \cos \alpha x] e^{-\alpha^2 \kappa t}. \quad (\text{B11})$$

Applying the boundary conditions defined for Equation (B2),

$$A \sin 0 + B \cos 0 = 0 \Rightarrow B = 0 \quad (\text{B12})$$

$$A \sin \alpha l = 0 \Rightarrow \alpha l = n\pi \Rightarrow \alpha = \frac{n\pi}{l},$$

the solution becomes the series

$$u = \sum_{n=1}^{\infty} A_n \sin\left(\frac{n\pi}{l}x\right) e^{-\kappa \frac{n^2 \pi^2}{l^2} t}. \quad (\text{B13})$$

To find the coefficients A_n , the initial condition $v = f(x)$ at $t = 0$ is used along with the definition $v = u + u_c$ to obtain

$$v - u_c = f(x) - u_c = \sum_{n=1}^{\infty} A_n \sin\left(\frac{n\pi}{l}x\right). \quad (\text{B14})$$

Multiplying both sides of the above equation by $\sin(n\pi x/l)$ and averaging over $2l$:

$$A_n = \frac{2}{l} \int_0^l [f(x') - u_c(x')] \sin\left(\frac{n\pi}{l}x'\right) dx'. \quad (\text{B15})$$

Using the solution given by Equations (B13) and (B15), and the steady state

solution to Equation (B3):

$$\begin{aligned} \frac{\partial^2 u_c}{\partial x^2} = 0 &\Rightarrow \frac{du_c}{dx} = C \Rightarrow \int_{v_1}^{v_2} du'_c = C \int_0^l dx' \Rightarrow C = \frac{v_2 - v_1}{l} \\ \therefore \frac{du_c}{dx} = \frac{v_2 - v_1}{l} &\Rightarrow \int_{v_1}^{u_c} du'_c = \frac{v_2 - v_1}{l} \int_0^x dx' \text{ or } u_c = v_1 + \frac{v_2 - v_1}{l} x \end{aligned} \quad (B16)$$

an expression for v , the solution to the original problem, can be written as

$$\begin{aligned} v = u + u_c &= v_1 + \frac{v_2 - v_1}{l} x \\ &+ \sum_{n=1}^{\infty} \left(\frac{2}{l} \int_0^l [f(x') - u_c(x')] \sin\left(\frac{n\pi}{l} x'\right) dx' \right) \sin\left(\frac{n\pi}{l} x\right) e^{-\kappa \frac{n^2 \pi^2}{l^2} t} \\ &= v_1 + \frac{v_2 - v_1}{l} x \\ &+ \sum_{n=1}^{\infty} \left(\frac{2}{l} \int_0^l \left[f(x') - \left(v_1 + \frac{v_2 - v_1}{l} x' \right) \right] \sin\left(\frac{n\pi}{l} x'\right) dx' \right) \\ &\quad \times \sin\left(\frac{n\pi}{l} x\right) e^{-\kappa \frac{n^2 \pi^2}{l^2} t} \end{aligned} \quad (B17)$$

This expression can be simplified by carrying out the integration of the terms contained in the summation wherever possible. Integrating the second term in the summation:

$$v_1 \int_0^l \sin\left(\frac{n\pi}{l} x'\right) dx' = \frac{l}{n\pi} v_1 (1 - \cos n\pi) \quad (B18)$$

Performing the integration of the third term using integration by parts

$$\left(\frac{v_2 - v_1}{l} \right) \int_0^l x' \sin\left(\frac{n\pi}{l} x'\right) dx' = \left(\frac{l}{n\pi} \right)^2 \left(\frac{v_2 - v_1}{l} \right) [-n\pi \cos n\pi] \quad (B19)$$

Then

$$\begin{aligned}
& \int_0^l \left[f(x') - \left(v_1 + \frac{v_2 - v_1}{l} x' \right) \right] \sin \left(\frac{n\pi}{l} x' \right) dx' \\
&= \int_0^l f(x') \sin \left(\frac{n\pi}{l} x' \right) dx' - \left[\frac{l}{n\pi} v_1 (1 - \cos n\pi) \right. \\
&\quad \left. - \left(\frac{l}{n\pi} \right)^2 \left(\frac{v_2 - v_1}{l} \right) [n\pi \cos n\pi] \right] \\
&= \int_0^l f(x') \sin \left(\frac{n\pi}{l} x' \right) dx' - \left[\frac{l}{n\pi} v_1 - \frac{l}{n\pi} v_1 \cos n\pi \right. \\
&\quad \left. - \frac{l}{n\pi} v_2 \cos n\pi + \frac{l}{n\pi} v_1 \cos n\pi \right], \quad (\text{B20})
\end{aligned}$$

or

$$\begin{aligned}
& \int_0^l \left[f(x') - \left(v_1 + \frac{v_2 - v_1}{l} x' \right) \right] \sin \left(\frac{n\pi}{l} x' \right) dx' \\
&= f(x') \sin \left(\frac{n\pi}{l} x' \right) dx' - \frac{l}{n\pi} (v_1 - v_2 \cos n\pi), \quad (\text{B21})
\end{aligned}$$

and Equation (B17) becomes

$$\begin{aligned}
v = v_1 + \frac{v_2 - v_1}{l} x + \frac{2}{l} \sum_{n=1}^{\infty} \sin \left(\frac{n\pi}{l} x \right) e^{-\kappa \frac{n^2 \pi^2}{l^2} t} & \left[\int_0^l f(x') \sin \left(\frac{n\pi}{l} x' \right) dx' \right. \\
& \left. + \frac{l}{\pi} \frac{(v_2 \cos n\pi - v_1)}{n} \right]. \quad (\text{B22})
\end{aligned}$$

or

$$\begin{aligned}
v = v_1 + \frac{v_2 - v_1}{l} x + \frac{2}{\pi} \sum_{n=1}^{\infty} \sin \left(\frac{n\pi}{l} x \right) e^{-\kappa \frac{n^2 \pi^2}{l^2} t} & \frac{(v_2 \cos n\pi - v_1)}{n} \\
+ \frac{2}{l} \sum_{n=1}^{\infty} \sin \left(\frac{n\pi}{l} x \right) e^{-\kappa \frac{n^2 \pi^2}{l^2} t} & \int_0^l f(x') \sin \left(\frac{n\pi}{l} x' \right) dx'. \quad (\text{B23})
\end{aligned}$$

For the case of a "hot" boundary where

$$\begin{aligned}x &= l, \quad v_2 = V_o \\x &= 0, \quad v_1 = 0 \\f(x) &= 0 \text{ at } t = 0,\end{aligned}\tag{B24}$$

the above equation reduces to

$$\begin{aligned}v &= \frac{V_o}{l}x + \frac{2V_o}{\pi} \sum_{n=1}^{\infty} \sin\left(\frac{n\pi}{l}x\right) e^{-\kappa \frac{n^2\pi^2}{l^2}t} \frac{\cos n\pi}{n} \\&= \frac{V_o}{l}x + \frac{2V_o}{\pi} \sum_{n=1}^{\infty} \frac{(-1)^n}{n} \sin\left(\frac{n\pi}{l}x\right) e^{-\kappa \frac{n^2\pi^2}{l^2}t}.\end{aligned}\tag{B25}$$

For the two dimensional diffusion problem with the conditions

$$\begin{aligned}-l_x \leq x \leq l_x, \quad -l_y \leq y \leq l_y \\v &= f(x, y) = V_o \text{ at } t = 0 \\v &= 0 \text{ at } x = -l_x, l_x, \quad y = -l_y, l_y \quad (t \geq 0),\end{aligned}\tag{B26}$$

the analytic solution is given by [60]

$$v(x, y, t) = V_o \Psi(x, l_x, t) \Psi(y, l_y, t)$$

where $\Psi(z, l, t)$ is the relevant one dimensional solution:

$$\Psi(z, l, t) = \frac{4}{\pi} \sum_{n=0}^{\infty} \frac{(-1)^n}{(2n+1)} e^{-\kappa (2n+1)^2 \pi^2 t / 4l^2} \cos \frac{(2n+1)\pi z}{2l}.\tag{B27}$$

The general one dimensional diffusion solution, Equation (B23), and the two dimensional diffusion solution of Equation (B27) have been incorporated into two computer programs which are listed on the following pages. These programs were used to find analytic solutions for a given set of initial conditions at specific times. These solutions were then used to benchmark the radiation diffusion portion of the MACH2 code.

```

1
2      program dft
3 *
4 * This program determines radiation energy distributions for given
5 * initial conditions resulting from one dimensional radiation flows.
6 *
7 * radtest = hotsrc ---> box=eradi, walls=0
8 * radtest = hotwall ---> 1 wall=eradi, box & other wall=0
9 * radtest = coldwall ---> 1 wall=0, box & other wall=eradi
10 *radtest = inslbdry ---> 1 wall insl, box=eradi, other wall=eradb
11
12      real*8 kappa, lbox, xmin, xmax, xstep, tval, xval,
13      %      tradi, eradi, pi, steph, eval, num1, num2, sum
14      character*8 radtest, input, outfile
15      namelist /input/ radtest,kappa,lbox,nmax,xmin,xmax,xstep,tval
16      %      ,tradi, outfile
17
18 c-----set default values for various parameters
19      kappa = 10.0
20      lbox = 2.0
21      nmax = 100
22      xmin = 0.0
23      xmax = 2.0
24      xstep = 0.5
25      tradi = 10.0
26 c-----read in any change in above parameters
27 c
28 c input data from file
29 c
30      open(8,file='dft.inp',status='old')
31      read(8,input)
32      open(12,file=outfile,status='unknown')
33      close(12,status='delete')
34      open(12,file=outfile,status='new')
35 c
36      steph = 13.7191558
37      pi = 4.0 * atan(1.0)
38      eradi = steph * tradi*tradi*tradi*tradi
39      imax = int((xmax-xmin)/xstep) + 1
40
41      if ( radtest .eq. "hotsrc " ) then
42 c-----calculations for hot source problem
43
44      xval = xmin
45      do 10 i=1,imax,1
46      sum = 0.0

```

```

47      do 20 n = 1,nmax,1
48          num1 = 2.0*real(n-1) + 1.0
49          num2 = num1*pi/lbox
50          sum = sum + (1.0/num1) * sin((num1*pi)*(xval/lbox))
51      %          * exp(-kappa*num2**2*tval)
52  20      continue
53          if (abs(sum) .lt. 1.0d-3) sum = 0.0
54          eval = (4.0*eradi/pi)*sum
55
56 c print out formatted values of x, eval, and t
57
58          print 200, xval, eval, tval
59          write(12,300) xval, eval
60          xval = xval + xstep
61  10      continue
62
63      elseif ( radtest .eq. "hotwall" ) then
64 c-----calculations for hot wall problem
65
66          xval = xmin
67          do 30 i=1,imax,1
68              sum = 0.0
69              do 40 n = 1,nmax,1
70                  num1 = real(n)*pi/lbox
71                  num2 = dsin(num1*xval)
72                  if (abs(num2) .lt. 1.0d-2) num2 = 0.0
73                  sum = sum + dcos(n*pi)/real(n)*num2*
74      %                  exp(-kappa*num1*num1*tval)
75  40      continue
76          eval = (eradi/lbox)*xval + (2.0*eradi/pi)*sum
77          if (eval .lt. 1.0d-1) eval = 0.0
78 c print out formatted values of x, eval, and t
79
80          print 200, xval, eval, tval
81          write(12,300) xval, eval
82
83          xval = xval + xstep
84  30      continue
85
86      elseif ( radtest .eq. "coldwall" ) then
87 c-----calculations for cold wall problem
88
89          xval = xmin
90          do 50 i=1,imax,1
91              sum = 0.0
92              nsum = 0.0

```

```

93      do 60 n = 1,nmax,1
94          num1 = real(n)*pi/lbox
95          num2 = (2.0*real(n-1)+1.0)*pi/lbox
96          sum = sum + cos(n*pi)/real(n)*sin(num1*xval)*
97      %          exp(-kappa*num1**2*tval)
98          nsum = nsum + 1.0/(2.0*real(n-1)+1.0)*sin(num2*xval)
99      %          *exp(-kappa*num2**2*tval)
100  60      continue
101          if (abs(sum) .lt. 1.0d-6) sum = 0.0
102          if (abs(nsum) .lt. 1.0d-6) nsum = 0.0
103          eval = (eradi/lbox)*xval + (2.0*eradi/pi)*sum+
104      %          (4.0*eradi/pi)*nsum
105
106 c print out formatted values of x, eval, and t
107
108          print 200, xval, eval, tval
109          write(12,300) xval, eval
110
111          xval = xval + xstep
112  50      continue
113
114      elseif ( radtest .eq. "inslbdry" ) then
115 c-----calculations for one boundary insulated
116
117          xval = xmin
118          do 70 i=1,imax,1
119              sum = 0.0
120              do 80 n = 1,nmax,1
121                  num1 = 2.0*real(n-1)+1.0
122                  num2 = (num1*pi)/(2.0*lbox)
123                  sum = sum + (eradi*(-1.0)**(n-1) + eradb*(-1.0)**n)
124      %          *cos(num2*xval)/num1* exp(-kappa*num2**2*tval)
125  80          continue
126              if (sum .lt. 1.0d-6) sum = 0.0
127              eval = eradb + (4.0/pi)*sum
128
129              xval = xval + xstep
130  70          continue
131
132      else
133          goto 500
134  500 endif
135  200 format(1x,e13.8,3x,e13.8,3x,e13.8)
136  300 format(1x,e13.8,3x,e13.8)
137      end

```

```

1
2 program dif2t
3 *
4 * This program determines radiation energy distributions for a finite
5 * rectangle with surfaces kept at zero and a given initial constant
6 * temperature in the box.
7 *
8     real*8 kappa, lxbox, lybox, xmin, xmax, xstep, tval, xval,
9     %         tradi, eradi, pi, steph, num1, num2, vals, sum1, sum2,
10    %         eval1, eval2, eval
11    character*8 input, outfile
12    namelist /input/ kappa, lxbox, lybox, nmax, xmin, xmax, xstep, ymin
13    %         , ymax, ystep, tval, tradi, outfile
14
15    steph = 13.7191558
16 c-----set default values for various parameters
17    kappa = 100.0
18    lxbox = 1.0
19    lybox = 1.0
20    nmax = 20
21    xmin = -1.0
22    xmax = 1.0
23    xstep = .5
24    ymin = -1.0
25    ymax = 1.0
26    ystep = .5
27    tval = 1.0
28    tradi = 10.0
29 c-----read in any change in above parameters
30 c
31 c input data from file
32 c
33    open(8,file='dft2.inp',status='old')
34    read(8,input)
35    open(12,file=outfile,status='unknown')
36    close(12,status='delete')
37    open(12,file=outfile,status='new')
38 c
39    pi = 4.0 * atan(1.0)
40    eradi = steph * tradi*tradi*tradi*tradi
41    imax = int((xmax-xmin)/xstep) + 1
42    jmax = int((ymax-ymin)/ystep) + 1
43
44    xval = xmin
45    do 10 i=1,imax,1
46        sum1 = 0.0

```

```

47      do 20 n=1,nmax,1
48 c-- compute series for xval
49      num1 = 2.0*real(n-1) + 1.0
50      num2 = num1 * pi/(2.0*lxbox)
51      vals = dcos(num2*xval)
52      if (vals .lt. 1.0d-2) vals = 0.0
53      sum1 = sum1 + dcos((n-1)*pi)*(vals/num1)
54      %      *exp(-kappa*num2*num2*tval)
55 20    continue
56      eval1 = (4.0/pi)*sum1
57      yval = ymin
58      do 30 j=1,jmax,1
59      sum2 = 0.0
60      do 40 n=1,nmax,1
61 c-- compute series for yval
62      num1 = 2.0*real(n-1) + 1.0
63      num2 = num1 * pi/(2.0*lybox)
64      vals = dcos(num2*yval)
65      if (vals .lt. 1.0d-2) vals = 0.0
66      sum2 = sum2 + dcos((n-1)*pi)*(vals/num1)
67      %      *exp(-kappa*num2*num2*tval)
68 40    continue
69      eval2 = (4.0/pi)*sum2
70      eval=eradi*eval1*eval2
71 c
72 c print out formatted values of x, y, eval
73 c
74      print 200, xval, yval, eval
75      write(12,200) xval, yval,eval
76
77      yval = yval + ystep
78      if (abs(yval) .lt. 1.d-3) yval=0.0
79 30    continue
80      xval = xval + xstep
81      if (abs(xval) .lt. 1.d-3) xval=0.0
82 10    continue
83 200 format(1x,e13.6,3x,e13.6,3x,e13.8)
84      end

```


APPENDIX C: CONSERVING ENERGY IN THE STAGNATION PROBLEM

The earliest calculations of the stagnation process, including that of the baseline case, indicated that the total energy of the system was not conserved throughout the simulation; energy losses of up to 30 % were observed in some instances. As a result, the radiation production was proportionally lower in these calculations. It was suggested [64] and later confirmed that this loss occurred during the transport in the stagnation region and was related to the fact that the internal energy, and not the total energy, was transported in these calculations. This loss was also observed in simpler problems, where large gradients in velocity were present and the radiation physics and magnetic fields were excluded, i.e, shock tube, pressure pulse.

One way to overcome this problem, is to transport the total energy rather than the internal energy, thus forcing the total energy to be conserved [65]. This option is available in MACH2 and can be carried out by setting the input parameter `conserv` to a value of 1. With this option, the total energy, which includes the electron specific internal energy, the ion specific internal energy, the magnetic energy and the kinetic energy, is advected. After this and all other fundamental quantities have been transported, new values of magnetic energy and kinetic energy are determined from the advected momentum and magnetic fluxes. These new energies are then subtracted from the advected total energy to yield a new electron plus ion specific internal energy. In this way, any energy loss which is introduced by advecting momentum and magnetic flux, as opposed to transporting the energies themselves, is added back into the electron fluid as internal energy.

Figure c1 shows the total energy and radiated power as a function of time for both the total energy scheme (`conserv` = 1) and the transport of the internal

energy only (conserv = 0) for the baseline case. Here the total energy in Figure c1 (a) includes the energy lost by radiation leaving the system through the bottom boundary of the computational domain. Clearly, these figures illustrate the significant energy loss that can occur in this problem and the improvement which results from using the total energy, or conservative, scheme. A comparison of the two calculations indicates that in the non-conservative case, the peak radiation rate drops by approximately 50 % from that of the conservative case, and the total radiated yield at 10 ns is only 3.2 MJ, a conversion efficiency of 64 %. In the conservative case, the total energy remains within ± 2 % of its original value. Based on this analysis, all the calculations presented in this dissertation used the total energy transport option. A more detailed discussion of this problem and an estimate of kinetic energy loss during transport can be found in [34].

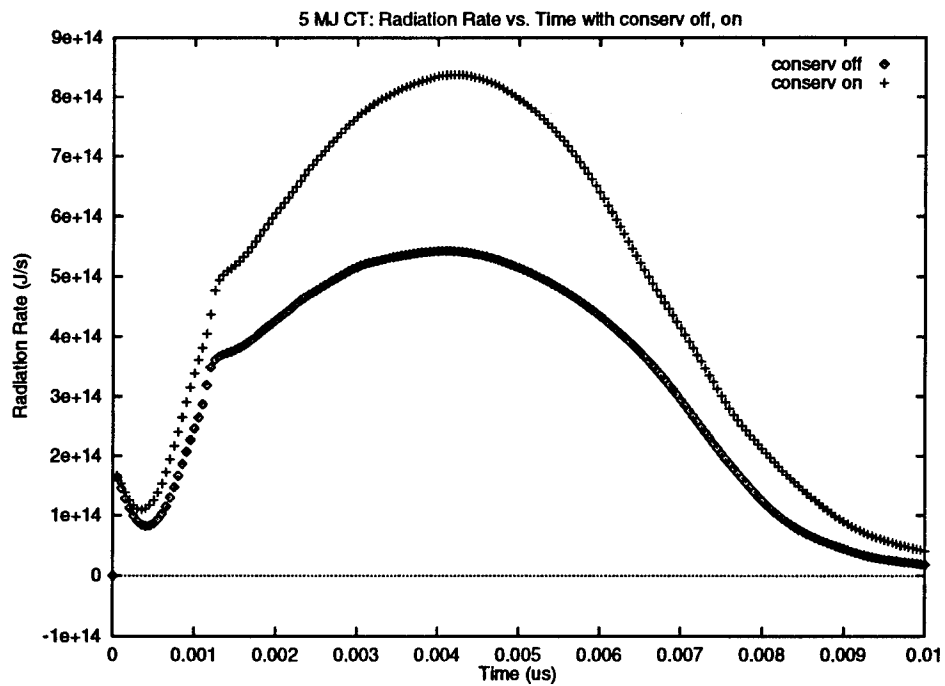
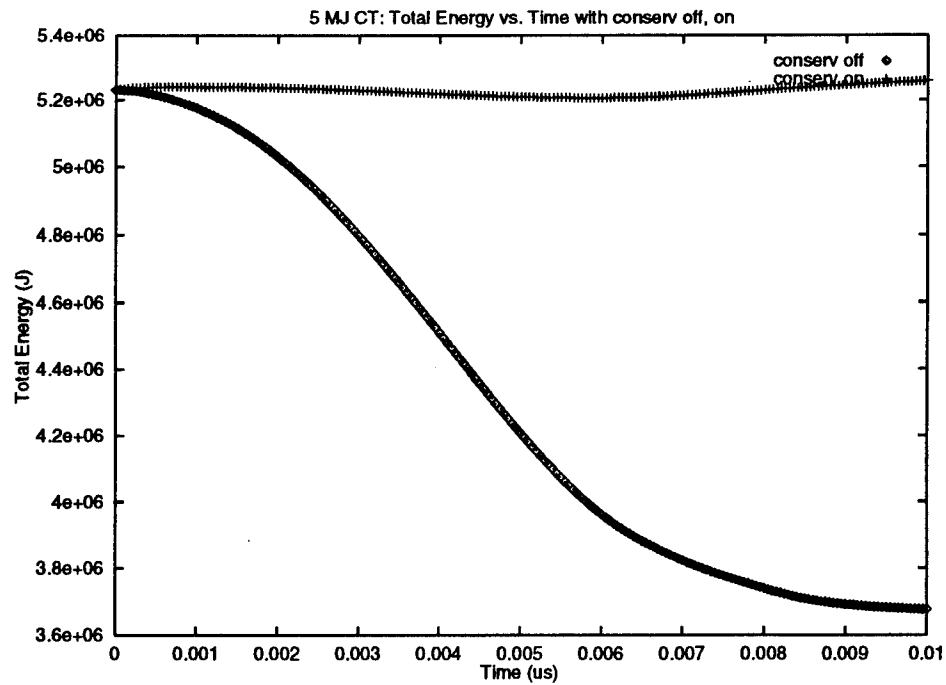


Figure C.1. Plots of (a) the total energy (including radiation energy leaving the bottom boundary of the problem) vs. time and (b) radiated power (radiation rate) vs. time for the baseline 5 MJ calculation.

REFERENCES

- [1] Pomraning, G.C., *The Equations of Radiation Hydrodynamics*, Pergamon Press, 1973.
- [2] Mihalas, D. , and B.W. Mihalas, *Foundations of Radiation Hydrodynamics*, Oxford University Press, 1984.
- [3] Stone, Jim, Ph.D. Thesis, Numerical Simulations of Mass Outflows from Star Forming Regions, University of Illinois, Urbana-Champaign, 1990.
- [4] Shu, Frank H., *The Physics of Astrophysics, Vol.1: Radiation*, University Science Books, 1991.
- [5] Alfven, H., Magnetohydrodynamics and the Thermonuclear Problem, in *Proceedings of Second United Nations International Conference on the Peaceful Uses of Atomic Energy*, Geneva, Switzerland, **31**: 3, 1958.
- [6] Gross, Robert A., *Fusion Energy*, John Wiley & Sons, Inc., 1984.
- [7] *Physics through 1990's, Plasmas and Fluids*, National Academy Press, 1986.
- [8] Hartman, Charles W., and James H. Hammer, New Type of Collective Accelerator, *Physical Review Letters*, **48**: 929-932, 1982.
- [9] Hartman, C.W., and J.H. Hammer, Acceleration of a Compact Torus Plasma Ring: A Proposed Experimental Study, Technical Proposal, LLL-PROP-191, Lawrence Livermore National Laboratory, Lawrence, California, 94551, April 1984
- [10] Courtesy of Uri Shumlak. Theory and Computation Group, WSP Division, Phillips Laboratory, Albuquerque, NM.
- [11] Krall, Nicholas A., and Alvin W. Trivelpiece, *Principles of Plasma Physics*, San Francisco Press, Inc., 1986.
- [12] Gee, M., P. Nowak, and G. Zimmerman, Computational Analysis of a Compact Toroid X-Ray Source, Technical Report UCRL-53951, Lawrence Livermore National Laboratory, Lawrence, California, 94551, August 1989.
- [13] Gee, M., J.H. Hammer, P.F. Nowak, C.W. Hartman, G.B. Zimmerman, A Computational Analysis of a Compact Toroid X-Ray Source, Technical Report UCID-21514, Lawrence Livermore National Laboratory, Lawrence, California, 94551, September 1988.

- [14] Bowers, Richard L., and James R. Wilson, *Numerical Modeling in Applied Physics and Astrophysics*, Jones and Bartlett Publishers, 1991.
- [15] Buchler, Robert J., Radiation Hydrodynamics in the Fluid Frame, *Journal of Quant. Spectroscopy and Radiative Transfer*, **22**: 293-300, 1979.
- [16] Muir, Alan, and Robert Weaver, Radiation Transfer in the Fluid Frame: A Covariant Formulation Part II: The Radiation Transfer Equation, *Computer Physics Report*, **3**, 170-208, 1986
- [17] Castor, John I., Radiative Transfer in Spherically Symmetric Flows, *Astrophysical Journal*, **178**: 779-792, 1972.
- [18] Zel'dovich, Ya. B. and Yu. P. Razer, *Physics of Shock Waves and High Temperature Hydrodynamic Phenomena, Volume I.*, Academic Press, 1966.
- [19] Sanchez, Richard and G.C. Pomraning, A Family of Flux-Limited Diffusion Theories, *Journal of Quant. Spectroscopy and Radiative Transfer*, **45**: 313-337, 1991.
- [20] Alme, Marvin L. and James R. Wilson, Numerical Study of X-Ray Induced Mass Transfer in the HZ Herculis/Hercules X-1 Binary System, *Astrophysical Journal*, **194**: 147-164, 1974.
- [21] Lund, C. M., Radiation Transport in Numerical Astrophysics, in *Numerical Astrophysics*, Symposium Proceedings in honor of James R. Wilson, ed., J. Centrella, J. LeBlanc, and R. Bowers, Jones and Bartlett Publishers, 1985.
- [22] Peterkin, R.E., Jr., Anthony J. Giancola, and Judy E. Sturtevant, MACH2: A Reference Manual- Fifth Edition, MRC/ABQ-R-1490 Mission Research Corporation, Albuquerque, NM 87106, July 1992.
- [23] Peterkin, R.E., Jr., and M.H. Frese, A Material Strength Capability for MACH2, Technical Report MRC/ABQ-R-1191, Mission Research Corporation, Albuquerque, NM 87106, October 1989.
- [24] Peterkin, Robert E., Jr., A Two-Temperature Model for MACH2, Technical Report MRC/ABQ-R-1260 Mission Research Corporation, Albuquerque, NM 87106, February 1990.
- [25] Holian, K.S., ed., *T-4 Handbook of Material Properties Data Base, Vol. Ic: EOS*, LA-10160-MS, Los Alamos National Laboratory, Los Alamos, NM, November 1984.
- [26] Van Leer, Bram, Towards the Ultimate Conservative Difference Scheme. IV. A New Approach to Numerical Convection, *Journal of Computational*

Physics, **23**: 276-299, 1977.

[27] Sovinec, Carl R., The Van Leer Advection Algorithm in the MACH2 Computer Code, Technical Report PL-TR-91-1051, Phillips Laboratory, KAFB, Albuquerque, NM 87117, August 1991.

[28] Evans, C. and J.F. Hawley, Simulation of Magnetohydrodynamic Flows: A Constrained Transport, *Astrophysical Journal*, **332**: 659-677, 1988.

[29] Davidson, R. C., and N. A. Krall, Anomalous Transport in High-Temperature Plasmas with Applications to Solenoidal Fusion Systems, *Nuclear Fusion*, **17**: 1313-1372, 1977.

[30] Bowers, R.L., private communication, 1992.

[31] Frese, M.H., private communication, 1992.

[32] Richtmyer, Robert D., and K.W. Morton, *Difference Methods For Initial-Value Problems*, 2nd edition, John Wiley & Sons, Inc., 1967.

[33] Press, William H., Brian P. Flannery, Saul A. Teukolsky, and William T. Vetterling, *Numerical Recipes*, Cambridge University Press, 1986.

[34] Frese, Michael H., *MACH2: A Two-Dimensional Magnetohydrodynamic Simulation Code for Complex Experimental Configurations*, NumerEx, Albuquerque, NM 87106, September 1986.

[35] Gerald, Curtis F. and Patrick O. Wheatley, *Applied Numerical Analysis*, Addison-Wesley Publishing Co., 1970.

[36] Fletcher, C. A., *Computational Techniques for Fluid Dynamics, Volume I*, Springer-Verlag, 1991.

[37] Burden, Richard L. and J. Douglas Faires, *Numerical Analysis*, Prindle, Weber & Schmidt Publishers, 1985.

[38] Briggs, William L., *A Multigrid Tutorial*, Society for Industrial and Applied Mathematics, 1987.

[39] Brandt, Achi, Multi-Level Adaptive Solutions to Boundary-Value Problems, *Mathematics of Computation*, **31**: 333-390, April 1977.

[40] Dearborn, M.E., D.E. Bell, J.H. Degnan, G.F. Kiuttu, R.E. Peterkin, Jr., and E. L. Ruden, Mass Estimates for Deuterium Compact Toroids, submitted to *Journal of Applied Physics*.

- [41] Courtesy of Don Gale, Maxwell Laboratory, Albuquerque, NM.
- [42] Courtesy of Dave Dunlap, Maxwell Laboratory, Albuquerque, NM.
- [43] Degnan, J.H., et. al., Compact toroid formation, compression, and acceleration, *Physics of Fluids:B*, **5**: 2938-2958, 1993.
- [44] Furth, Harold P. , John Killeen, and Marshall N. Rosenbluth, Finite-Resistivity Instabilities of a Sheet Pinch, *Physics of Fluids*, **6**: 459-484, 1963.
- [45] Nicholson, Dwight R., *Introduction to Plasma Theory*, John Wiley & Sons, Inc., 1983.
- [46] Woltjer, L., A Theorem on Force-Free Magnetic Fields, in *Proceedings of the National Academy of Sciences of the United States of America*, National Academy of Science, **44**: 489-491, 1958.
- [47] Taylor, J.B., Relaxation of Toroidal Plasma and Generation of Reverse Magnetic Fields, *Physical Review Letters*, **33**: 1139-1141, 1974.
- [48] Degnan, J.H., et. al., Compact Toroid Formation Experiments, IEEE International Conference on Plasma Science - Abstracts, 166, 1990.
- [49] Courtesy of R. E. Peterkin, Jr., Theory and Computation Group, WSP Division, Phillips Laboratory, Albuquerque, NM, calculation ct245.
- [50] Peterkin, R.E., Jr., D.E. Bell, J.H. Degnan, M.R. Douglas, T.W. Hussey, B.W. Mullins, N.F. Roderick, and P.J. Turchi, A Long Conduction Time Compact Torus Plasma Flow Switch, in *Proceedings of the Ninth International Conference on High-Power Particle Beams*, D. Mosher and G. Cooperstein, eds., NTIS, 1992.
- [51] Eddleman, J.L, J.H. Hammer, and C.W. Hartman, Numerical Modelling of the Race Experiment, Bulletin of the American Physical Society - Abstracts **32**: 1912, 1987.
- [52] Molvik, A.W., J. L. Eddleman, J.H. Hammer, C.W. Hartman, and H.S. McLean, Quasistatic Compression of a Compact Torus, *Physical Review Letters*, **66**: 165-168, 1991.
- [53] Liepmann, H.W. and A. Roshko, *Elements of Gasdynamics*, John Wiley & Sons, Inc., 1957.
- [54] Courtesy of R. E. Peterkin, Jr. Theory and Computation Group, WSP Division, Phillips Laboratory, Albuquerque, NM, calculation ct251.

- [55] Potter, David, *Computational Physics*, John Wiley & Sons, Inc., 1973.
- [56] Wolfram, Stephen, *Mathematica: A System for Doing Mathematics by Computer*, Addison-Wesley Publishing Co., 1992.
- [57] Blachman, Nancy, *Mathematica: A Practical Approach*, Prentice Hall, Inc. 1992.
- [58] Bowers, Richard L. and Terry Deeming, *Astrophysics I*, Jones & Bartlett Publishers, Inc., 1984
- [59] Boas, Mary L., *Mathematical Methods in the Physical Sciences*, John Wiley & Sons, 1983.
- [60] Carslaw, H.S., and J.C. Jaeger, *Conduction of Heat in Solids*, Oxford University Press, 1959.
- [61] Kiuttu, Gerald, private communication, 1993.
- [62] Harlow, Francis H., and Anthony A. Amsden, *Fluid Dynamics*, Los Alamos Scientific Laboratory LA-4700, June 1971.
- [63] Duric, Nebojsa, private communication, 1994.
- [64] Peterkin, R.E., Jr., private communication, 1994.
- [65] Brackbill, Jeremiah U. and William E. Pracht, An Implicit Almost-Lagrangian Algorithm for Magnetohydrodynamics, *Journal of Computational Physics*, 13:455-482, 1973.